

Study of brain metabolic dysfunctions in animal models of mood disorder using magnetic resonance spectroscopy

Présentée le 24 janvier 2020

à la Faculté des sciences de base
Laboratoire Leenaards-Jeantet d'imagerie fonctionnelle et métabolique
Programme doctoral en neurosciences

pour l'obtention du grade de Docteur ès Sciences

par

Antoine Timothée CHERIX

Acceptée sur proposition du jury

Prof. R. Schneggenburger, président du jury
Prof. R. Gruetter, Dr J.-R. Cardinaux, directeurs de thèse
Prof. S. R. Williams, rapporteur
Prof. C. Stagg, rapporteuse
Prof. P. Magistretti, rapporteur

To my parents

Abstract

Mood disorders, in particular depression, are a major burden of our society. Due to the poor knowledge of the biological basis of these diseases, classification remains based on arbitrary symptomatic parameters. As a result, the existing pharmacological treatments have difficulties targeting relevant pathophysiological processes leading to high level of non-responding patients. Magnetic resonance spectroscopy (MRS) provides an outstanding means of measuring biochemical processes *in vivo* and can help identifying metabolic pathways that are associated with a given pathological condition. In this thesis, we have taken advantage of state-of-the-art MRS technologies at high field for studying metabolic dysfunctions associated with behavioral impairments in animal models of mood disorder. The overall goal consisted in finding potential biomarkers and endophenotypes (i.e. heritable biomarkers) with MRS, associate them with a molecular/physiological mechanism and evaluate the effect of a treatment targeting the observed dysfunction.

We have successfully identified neuroenergetic abnormalities in different limbic regions of the brain in two mouse models of mood disorders; with a genetic or an environmental origin. Genetic deletion of an important metabolic regulator in mouse brain led to hippocampal neuroenergetic impairment and susceptibility to environmental stressors. Treating the animals with ebselen, an energy boosting mood stabilizer, allowed us to reduce the animal's sensitivity to stress. With the same approach, we observed energy-related biomarkers associated with susceptibility to stress in the nucleus accumbens of genetically identical mice. We found that social hierarchy can predict the response to a chronic stressor and that behavioral impairments could be prevented by administering an energy stimulating compound, acetyl-L-carnitine. Finally, in an additional project, we have used MRS in an embryonic model *in ovo* to investigate for markers related to metabolic remodeling during neurogenesis.

Our results support the idea that mood disorders arise from energy metabolism fragility in different regions of the limbic system with both environmental and genetic origin. Due to the high translational potential of MRS into clinics, our findings provide new biological targets or routes to study for a better understanding of mood disorders.

Key words: Mood disorders, Magnetic resonance spectroscopy (MRS), Brain metabolism, Neuroenergetics, Depressive-like behavior, *Crtc1*, Stress, Neurogenesis

Résumé

Les troubles de l'humeur, et en particulier la dépression, sont un enjeu de santé publique majeur de notre société. La compréhension à l'échelle biologique de ces maladies reste limitée et résulte en une classification actuelle relativement arbitraire basée sur des signes et des symptômes. En conséquence, les médicaments existants ne ciblent que des processus pathophysiologiques peu définis, réduisant la chance de réponse favorable des patients au traitement. La spectroscopie de résonance magnétique (SRM) permet la détection de processus biochimiques *in vivo* et permet d'identifier les voies métaboliques associées à une condition pathologique donnée. Dans cette thèse, nous avons tiré profit des avantages de la technologie SRM à haut champ, à la pointe de la technologie, pour étudier les dysfonctions neuro-énergétiques associées aux troubles du comportement qui peuvent être observés chez des modèles animaux de troubles de l'humeur. Notre objectif a consisté à découvrir de potentiels biomarqueurs ou endophénotypes (i.e. biomarqueurs ayant un lien génétique) dans ces animaux en utilisant la SRM, comprendre l'origine moléculaire ou physiologique de ces marqueurs, afin de cibler les dysfonctions comportementales à l'aide d'un traitement approprié.

Nos résultats ont permis d'identifier des anomalies métaboliques dans différentes régions du cerveau de deux modèles murins de troubles de l'humeur; le premier étant induit par génétique, le second, causé par l'environnement. Dans le premier modèle, la suppression d'un gène régulateur métabolique important dans le cerveau de souris a résulté en une détérioration du métabolisme énergétique hippocampal observable en SRM, conduisant à une susceptibilité accrue au stress. L'administration à ces souris d'un stabilisateur d'humeur aux propriétés stimulantes pour le métabolisme énergétique nous a permis de protéger ces animaux des effets délétères du stress. Dans le deuxième modèle, l'application de la SRM sur des souris génétiquement identiques nous a permis d'observer des biomarqueurs neuro-énergétiques, dans le noyau accumbens, liés à une sensibilité au stress. Nous avons identifié que le rang hiérarchique des souris permet de prédire la réponse au stress chronique et que l'administration d'un stimulant énergétique permet de traiter le comportement de type dépressif qui en résulte. Finalement, dans un projet complémentaire, nous avons appliqué la SRM à un modèle embryonnaire *in ovo* pour trouver des marqueurs liés aux adaptations métaboliques lors de la neurogenèse.

Nos résultats supportent l'idée que les troubles de l'humeur peuvent provenir de fragilités du métabolisme énergétique dans différentes régions du système limbique via des causes environnementale et génétiques. Par l'aspect translationnel de la SRM pour le domaine clinique, nos résultats apportent de nouvelles cibles biologiques potentielles, ouvrant la voie à une meilleure compréhension des troubles de l'humeur.

Mots-clefs: Troubles de l'humeur, Spectroscopie de résonance magnétique (SRM), Métabolisme du cerveau, neuro-énergétique, Comportement de type dépressif, *Crtc1*, Stress, Neurogenèse.

Table of contents

Abstract

Résumé

Table of contents **5**

List of Figures and Tables **11**

List of Abbreviations **15**

Outline of the Thesis **17**

Chapter 1: Introduction **19**

1.1 Mood disorders 21

1.1.1 Occurrence and concept 21

1.1.2 Hypotheses of mood disorders 21

1.1.3 Genetic and environmental factors 23

1.2 Brain metabolism..... 25

1.2.1 Definition of metabolism 25

1.2.2 Brain function and metabolism 28

1.2.3 Metabolic dysfunctions in mood disorders 32

1.2.3.1 *Glycolytic dysfunctions* 32

1.2.3.2 *Mitochondrial dysfunctions* 34

1.3 Magnetic resonance spectroscopy to study brain metabolism *in vivo* 37

1.3.1 Basics of nuclear magnetic resonance (NMR) 37

1.3.2 Basics of localization for MRS 41

1.3.3 ^1H -MRS 41

1.3.4 ^{31}P -MRS 44

1.3.5 ^{13}C -MRS 45

1.3.6 Magnetic resonance spectroscopy (MRS) as a tool to study brain energy metabolism dysfunction associated with mood disorder 47

1.4 Aim of the thesis..... 50

Chapter 2: Technical developments **51**

2.1 Introduction..... 53

2.2 Material and methods..... 54

2.2.1	Animals	54
2.2.2	Surgery and animal preparation	55
2.2.3	^1H - ^{13}C -MRS of mouse hippocampus	55
2.2.4	Modelling of hippocampal metabolic fluxes	59
2.2.5	Blood FE measurements	62
2.2.6	^{18}F FDG-PET	63
2.2.7	Statistical analysis	64
2.3	Results.....	64
2.3.1	^1H - ^{13}C -MRS of mouse dorsal hippocampus at 14 Tesla	64
2.3.2	Spectral fitting	65
2.3.3	Quantification of metabolic labelling	66
2.3.4	Mathematical modelling of hippocampal metabolism	67
	2.3.4.1 1-compartment model	67
	2.3.4.2 Pseudo 3-compartment model	69
2.4	Discussion.....	72
2.4.1	Optimization of glucose fitting improves data quality for $[\text{U-}^{13}\text{C}_6]\text{Glc}$ infusion	72
2.4.2	Modelling of brain excitatory/inhibitory metabolic balance	73
2.5	Appendix	78
2.5.1	Supplementary information	78
Chapter 3: MRS in a genetic mouse model of mood disorder		89
3.1	Introduction.....	91
3.2	Material and methods.....	92
3.2.1	Animals	92
3.2.2	Experimental design	93
3.2.3	<i>In vivo</i> ^1H -Magnetic Resonance Spectroscopy (^1H -MRS)	93
3.2.4	<i>In vivo</i> indirect carbon-13 Magnetic Resonance Spectroscopy (^1H - ^{13}C -MRS)	94
3.2.5	<i>In vivo</i> ^{18}F FDG-PET	95
3.2.6	High resolution NMR Spectroscopy	95
3.2.7	Gene expression analysis	96
3.2.8	Mitochondrial DNA copy number and damage quantification	97
3.2.9	Mitochondrial respirometry	97
3.2.10	Open field test	98
3.2.11	Porsolt forced swim test	98

3.2.12	Tail suspension test	99
3.2.13	Repeated open-space forced swim test	99
3.2.14	Ebselen treatment	99
3.2.15	Gas chromatography-mass spectrometry ebselen quantification	99
3.2.16	Statistics	100
3.3	Results.....	101
3.3.1	Neurochemical profile of <i>Crtc1</i> ^{-/-} mice reveals low levels of hippocampal energy metabolites	101
3.3.2	Hippocampal low energy metabolic profile is associated with impaired cerebral metabolic rate of glucose and GABA turnover in <i>Crtc1</i> ^{-/-} mice	104
3.3.3	Hippocampal energetic and GABAergic profile correlate with the depressive-like behavior of <i>Crtc1</i> ^{-/-} mice	107
3.3.4	Hippocampal energetic and GABAergic profile is impaired by stress and can be restored with the mood stabilizer ebselen	110
3.4	Discussion.....	114
3.4.1	Deletion of <i>Crtc1</i> induces neuroenergetic impairments in hippocampus	114
3.4.2	Hippocampal energy impairments result in GABAergic dysfunction	116
3.4.3	Hippocampal vulnerability is challenged by the environment	117
3.4.4	Ebselen protects the hippocampus by stimulating energy metabolism	118
3.4.5	Hippocampal energy metabolites as markers of depression	119
Chapter 4: MRS in an environmental mouse model of mood disorder		123
4.1	Introduction.....	125
4.2	Material and methods.....	126
4.2.1	Animals	126
4.2.2	Experimental design	126
4.2.3	Elevated Plus maze test	127
4.2.4	Open Field test	127
4.2.5	Social confrontation tube test	127
4.2.6	Chronic restraint stress	128
4.2.7	Porsolt forced swim test	128
4.2.8	Social interaction test	129
4.2.9	Acetyl-L-carnitine treatment	129
4.2.10	¹ H-Magnetic Resonance Spectroscopy (¹ H-MRS)	129
4.2.11	Blood metabolite measurements	130
4.2.12	Statistical analysis	130

4.2.13	Factor analysis	130
4.3	Results.....	131
4.3.1	CRS protocol reproduces the behavioral phenotype of CSDS in dominant animals	131
4.3.2	Treatment with LAC reverses the behavioral phenotype induced by stress in dominant mice	133
4.4	Discussion.....	138
4.4.1	Chronic LAC treatment produces antidepressant-like effect in dominant/susceptible animals subjected to CRS	138
4.4.2	Chronic restraint stress reproduces the depressive-like phenotype observed in chronic social defeat stress	139
4.4.3	LAC reverses stress-induced neuroenergetic- and membrane metabolism dysfunctions in NAc: potential astroglial mechanism	140
Chapter 5:	MRS to study metabolic remodeling during neurogenesis	143
5.1	Introduction.....	145
5.2	Material and methods.....	147
5.2.1	Animals	147
5.2.2	Reporter and expression plasmids	147
5.2.3	Retina preparation	147
5.2.4	Fluorescence Activated Cell Sorting	148
5.2.5	Confocal imaging	148
5.2.6	Time-Lapse imaging	148
5.2.7	<i>In vivo</i> proton Magnetic Resonance Spectroscopy (^1H -MRS)	149
5.2.7.1	<i>In vivo</i> measurement	149
5.2.7.2	<i>In vivo</i> spectra quantification	150
5.2.7.3	<i>In vivo</i> pH measurement	150
5.2.8	High resolution ^1H -NMR spectroscopy	151
5.2.8.1	Metabolite extracts measurement	151
5.2.8.2	Metabolite spectra quantification	152
5.2.9	RT-qPCR	153
5.2.10	mtDNA quantification by qPCR	153
5.3	Results.....	153
5.3.1	Mitochondrial metabolism decreases during retinal development	153
5.3.2	Metabolic profile of the eye indicates energetic remodeling at onset of neurogenesis	156

5.3.3	Lactate concentration increases in the vitreous body at onset of neurogenesis	158
5.3.4	A decrease in vitreous citrate parallels lactate and pH increases as the retina undergoes a metabolic switch.	160
5.3.5	Lipid synthesis does not account for the vitreous citrate decrease at the onset of RGC maturation.	162
5.3.6	Temporal modulation of glycolysis regulator expression in the retina suggests that the nature of the metabolic switch is glycolytic	164
5.4	Discussion.....	167
5.4.1	Mitochondria characterization	167
5.4.2	Lactate accumulation is specific to the vitreous body	168
5.4.3	Citrate oxidation drives the glycolytic switch	169
5.4.4	Metabolic regulation and interactions at the retina level	170
5.4.5	Interspecies disparities	172
Chapter 6: General conclusion and perspectives		175
Acknowledgements		179
References		183
Curriculum Vitae		211
Publications and Conference Proceedings		214

List of Figures and Tables

Figure 1. 1 : Glycolysis	26
Figure 1. 2 : Tricarboxylic acid (TCA) cycle	27
Figure 1. 3 : Electron transport chain and mitochondrial ATP synthesis	28
Figure 1. 4 : The tripartite synapse and its metabolic interactions	31
Figure 1. 5 : Effect of an external magnetic field B_0 on magnetic moments of nuclei with $I=1/2$	38
Figure 1. 6 : The population difference between α and β creates a net magnetization M along B_0	39
Figure 1. 7 : Signal detection with a solenoid RF coil	39
Figure 1. 8 : NMR signal acquisition and transformation	40
Figure 1. 9 : Principle of localization in MRS	41
Figure 1. 10 : The neurochemical profile measurable with ^1H -MRS	42
Figure 1. 11 : Metabolic flux analysis based on ^{13}C -MRS	46
Figure 1. 12 : Summary of mitochondrial dysfunction in BPD from Stork & Renshaw (2005)	49
Figure 2. 1 : ^1H - ^{13}C -MRS in mouse dorsal hippocampus	57
Figure 2. 2 : Glucose spectrum dependency on the decoupling efficiency	58
Figure 2. 3 : (^1H - ^{13}C)-Coupled glucose resonances	59
Figure 2. 4 : 1-compartment models of brain metabolism	60
Figure 2. 5 : Pseudo 3-compartment model of brain glucose metabolism	62
Figure 2. 6 : Fitting improvements with a basis set corrected for glucose ^1H - ^{13}C coupling	65
Figure 2. 7 : Quantification improvements with a basis set corrected for glucose ^1H - ^{13}C coupling	66
Figure 2. 8 : Glucose kinetics in brain and plasma	67
Figure 2. 9 : 1-compartment metabolic fluxes correlations	67
Figure 2. 10 : Fitting comparison between the different 1-compartment models	68
Table 2. 1 : Comparison between flux estimation with different 1-compartment models and relevant literature	69
Figure 2. 11 : Validation of fixed parameters from pseudo 3-compartment model	70
Figure 2. 12 : Pseudo 3-compartment metabolic fluxes correlations	71
Figure 2. 13 : Fitting comparison between the different 3-compartment models	71
Table 2. 2 : Comparison between flux estimation with different pseudo 3-compartment models and relevant literature	72
Figure 3. 1 : The neurochemical profile of <i>Crtc1</i> ^{-/-} mice and WT littermates in DH and PFC <i>in vivo</i>	101

Figure 3. 2 : Morphometric analysis of mouse prefrontal cortex	102
Figure 3. 3 : The ^1H -neurochemical profile of <i>Crtc1</i> ^{-/-} mice and WT littermates in DH metabolic extracts	102
Figure 3. 4 : The ^{31}P -neurochemical profile of <i>Crtc1</i> ^{-/-} mice and WT littermates in DH metabolic extracts	103
Figure 3. 5 : Gene expression analysis of <i>Crtc1</i> ^{-/-} mice and WT littermates at 6 weeks	104
Figure 3. 6 : <i>in vivo</i> ^{18}F FDG-PET and ^1H - ^{13}C -MRS in <i>Crtc1</i> ^{-/-} mice and WT littermates at 6 weeks	105
Figure 3. 7 : Fitting of a pseudo 3-compartment model of hippocampal glucose metabolism to the data measured with ^1H - ^{13}C -MRS in <i>Crtc1</i> ^{-/-} mice and WT littermates	106
Table 3. 1 : Hippocampal metabolic fluxes obtained with a 1- or pseudo 3-compartment model of glucose metabolism in <i>Crtc1</i> ^{-/-} mice and WT littermates	106
Figure 3. 8 : Scheme of metabolic fluxes modeled with 3-compartment model in <i>Crtc1</i> ^{-/-} mice	107
Figure 3. 9 : Hippocampal energetic and GABAergic MRS-profile correlates with the depressive-like behavior of <i>Crtc1</i> ^{-/-} mice.	108
Figure 3. 10 : Hippocampal energetic and GABAergic gene expression relate to the depressive-like behavior of <i>Crtc1</i> ^{-/-} mice.	109
Figure 3. 11 : <i>Crtc1</i> ^{-/-} mice depressive-like behavior is impaired by stress and can be restored with the mood stabilizer ebselen.	111
Figure 3. 12: Hippocampal energetic and GABAergic gene expression is impaired by stress and can be restored with the mood stabilizer ebselen.	112
Figure 3. 13 : Effect of chronic stress on the hippocampal MRS-profile	113
Figure 3. 14 : Effect of ebselen on the hippocampal MRS-profile	113
Figure 3. 15 : Proposed neuroenergetic mechanism of <i>Crtc1</i> -related susceptibility	117
Figure 3. 16 : Relationship between hippocampal energetics and GABAergic function	119
Figure 3. 17 : Summary of potential biomarkers related to <i>Crtc1</i> -susceptibility	121
Figure 4. 1 : Determination of mouse hierarchical status	132
Figure 4. 2 : Dominant mice exhibit susceptible phenotype after 21 days of chronic restraint stress	133
Figure 4. 3 : Dominant mice respond to acetyl-L-carnitine treatment after chronic restraint stress	134
Figure 4. 4 : Body metabolic effects of stress and LAC	135
Figure 4. 5 : Factor analysis identified one main factor that accounts for the variance in the metabolic profile of nucleus accumbens	136
Figure 4. 6 : Effect of LAC on the accumbal neurochemical profile of dominant mice after CRS	137
Figure 4. 7 : Associations between blood metabolites and neurochemistry in the nucleus accumbens.	138
Figure 5. 1 : <i>In vivo</i> MRI images of the avian embryo.	150
Figure 5. 2 : Typical spectra obtained from high-resolution ^1H -NMR at 600 MHz	152

Figure 5. 3 : Mitochondrial metabolism decreases as development proceeds in the avian retina	155
Figure 5. 4 : Typical <i>in vivo</i> spectra of the whole avian eye and lactate quantification	157
Figure 5. 5 : Spectral fitting and quantification of remaining metabolites <i>in vivo</i>	158
Figure 5. 6 : Lactate concentration increases in the vitreous body at onset of neurogenesis	159
Figure 5. 7 : High resolution ¹ H-NMR of metabolic extracts confirm the rise of lactate in vitreous body.	160
Figure 5. 8 : Vitreous body citrate drops along with lactate and pH increase at the appearance of the switch	161
Figure 5. 9 : High resolution ¹ H-NMR of metabolic extracts confirm the drop of citrate in vitreous body	162
Figure 5. 10 : Quantification of remaining metabolites from the aqueous phase of retina extracts	163
Figure 5. 11 : Lipidic profile of the retina is increased in chick and in pigeon during development.	164
Figure 5. 12 : Increased glycolysis regulator expression in the retina correlates with appearance of the metabolic switch	166
Figure 5. 13 : Expression of phosphofructokinase 2 (PFK2) increases in the developing retina with a three-day delay between chick and pigeon.	167
Figure 5. 14 : Summary and proposed model of neuroenergetic metabolic switch associated with retinal ganglion cell growth.	172

List of Abbreviations

ACC	anterior cingulate cortex	ETS	electron transfer system
ACLY	ATP-citrate lyase	FACS	fluorescence-activated cell sorting
ADP	adenosine diphosphate	FASTMAP	fast automatic shimming technique by mapping along projections
Ala	alanine	FCCP	carbonyl-cyanide-p-(trifluoromethoxy)phenylhydrazone
AM	amygdala	FDG	fluorodeoxyglucose
AMPA	α -amino-3-hydroxy-5-methyl-4-isoxazolepropionic acid	FE	fractional enrichment
ANLS	astrocyte-neuron lactate shuttle	FID	free induction decay
ANOVA	analysis of variance	fMRI	functional MRI
Asc	ascorbate	FSE	fast spin-echo
Asp	aspartate	FST	forced swim test
AST	aspartate transaminase	FWHM	full width at half maximum
Atoh7	atonal BHLH transcription factor 7	GABA	gamma-aminobutyric acid
ATP	adenosine triphosphate	GAD	glutamate decarboxylase
Bax	Bcl-2-associated X	GC-MS	gas chromatography-mass spectrometry
Bcl-2	B-cell lymphoma 2	GDH	glutamate dehydrogenase
BDNF	brain-derived neurotrophic factor	gDNA	genomic DNA
BHB	beta hydroxybutyrate	GFP	green fluorescent protein
BOLD	blood oxygen-dependent	Glc	glucose
BPD	bipolar disorder	Gln	glutamine
BSA	bovine serum albumin	GLS	glutaminase
CACNA1C	calcium voltage-gated channel subunit alpha 1C	GLUT	glucose transporter
CACT	carnitine-acylcarnitine translocase	Gly	glycine
cAMP	cyclic adenosine monophosphate	GPC	glycerophosphorylcholine
CAT	carnitine O-acetyltransferase	GS	glutamine synthetase
CCC	choline containing compounds	GSH	glutathione
cDNA	complementary DNA	GSK3	glycogen synthase kinase 3
CHCl3	chloroform	GWAS	genome-wide association study
Chrn3	neuronal acetylcholine receptor subunit β 3	HDAC	histone deacetylase
CKB	creatine kinase brain-type	HEPES	(4-(2-hydroxyethyl)-1-piperazineethanesulfonic acid
CKMT	creatine kinase mitochondrial-type	HK1	hexokinase 1
CMRg	cerebral metabolic rate of glucose	HLSVD	Hankel-Lanczos Singular Value Decomposition
CMRg(ox)	oxidative CMRg	HY	hypothalamus
CMV	cytomegalovirus (promoter)	ICD	international classification of disease
CNS	central nervous system	IGF-1	insulin-like growth factor-1
Cr	creatine	IMPase	inositol monophosphatase
CREB	cAMP response element-binding protein	Ins	inositol
CRLB	Cramér-Rao lower bound	iPSC	induced pluripotent stem cell
CRS	chronic restraint stress	KO	knock-out
CRTC1	CREB-regulated transcription coactivator 1	LAC	L-acetyl carnitine
CSDS	chronic social defeat stress	Lac	lactate
CTRL	control	LC	L-carnitine
DG	dentate gyrus	LCModel	linear combination model
DH	dorsal hippocampus	LDH	lactate dehydrogenase
DLPFC	dorsolateral PFC	MAOI	monoamine oxidase inhibitor
DMEM	Dulbecco minimal Eagle's essential medium	MCT	monocarboxylate transporter
DSM	diagnostic and statistical manual of mental disorders	MDD	major depressive disorder
DSS	4,4-dimethyl-4-silpentane-1-sulfonic acid	MeOH	methanol
EAATs	excitatory amino acid transporters	MRI	magnetic resonance imaging
EM	electromagnetic	mRNA	messenger RNA
EPM	elevated plus maze	MRS	magnetic resonance spectroscopy
ETC	electron transport chain		

List of Abbreviations

mtDNA	mitochondrial DNA	qPCR	quantitative polymerase chain reaction
NAA	N-acetyl aspartate	RF	radiofrequency
NAAG	N-acetylaspartyl glutamate	RGC	retinal ganglion cell
NAc	Nucleus Accumbens	RNA	ribonucleic acid
NaDC1	sodium-coupled citrate transporter	RNS	reactive nitrogen species
NADH	nicotinamide adenine dinucleotide	ROS	reactive oxygen species
NADPH	nicotinamide adenine dinucleotide phosphate	rpm	rotations per minute
NCAN	neurocan	Scyllo	scyllo-inositol
Ncor1	nuclear receptor corepressor 1	SEM	standard error of the mean
ND6	NADH dehydrogenase 6	SI	social interaction
nDNA	nuclear DNA	SIK2	salt-inducible kinase
NMDA	N-methyl-D-aspartic acid	SNP	single-nucleotide polymorphism
NMR	nuclear magnetic resonance	SNR	signal-to-noise ratio
NPC	neural progenitor cell	SNRIs	selective noradrenaline reuptake inhibitors
Nrf	nuclear respiratory factor 1	SOD1	superoxide dismutase 1
OAA	oxaloacetate	SPECIAL	spin-echo full intensity acquired localized
ODZ4	teneurin 4	SSRIs	selective serotonin reuptake inhibitors
OF	open field	STZ	streptozotocin
OSFST	open field forced swim test	SUV	standardized uptake value
OVS	outer volume suppression	SZ	schizophrenia
OXPHOS	oxidative phosphorylation	Tau	taurine
PC	pyruvate carboxylase	TBE	TRIS/Borate/EDTA
PCho	phosphocholine	TCA	tricarboxylic acid cycle
PCr	phosphocreatine	TCAs	tricyclic antidepressants
PDH	pyruvate dehydrogenase	TE	echo-time
PDID	2-phenyl-2,3-dihydro-1H-Indole-1,3-dione	TFAM	mitochondrial transcription factor A
PDK	pyruvate dehydrogenase kinase	TMS	tetramethylsilane
PEPCK	phosphoenol pyruvate carboxykinase	TR	repetition time
PET	positron-emission tomography	TrkB	tropomyosin receptor kinase B
PFC	prefrontal cortex	TST	tail suspension test
PFK	phosphofructo kinase	UCP2	uncoupler protein 2
PGC1	PPAR γ coactivator 1	VAPOR	variable power RF pulses with optimized relaxation delays
PK	pyruvate kinase/POCE	VEH	vehicle
POCE	proton-observed/carbon-edited	VH	ventral hippocampus
POLG	polymerase G	VOI	volume of interest
PPARγ	peroxisome proliferator-activated receptor gamma	WHO	World Health Organization
		WT	wild-type
		β2M	beta-2 microglobulin

Outline of the Thesis

This thesis describes the work undertaken to identify metabolic alterations in animal models of mood disorder using magnetic resonance spectroscopy (MRS) at 14 Tesla. After an introductory chapter that situates this thesis in its context, each section describes the findings obtained from a different collaboration and a different project, with the goal of identifying relevant MRS-biomarkers related to mood disorder. More specifically:

Chapter 1 introduces the important concepts and notions required for the overall understanding of the thesis. This chapter starts with a brief description of mood disorders emphasizing the relevance and impact of research in the field. This part is followed by basic introduction to metabolism with focus on energetic aspects. The specificities of brain metabolism are described and known metabolic alterations related to mood disorder are discussed. The third part gives a basic understanding of MRS and its applications to mood disorders. Finally, the **aim of the thesis** is introduced.

Chapter 2 describes the major technical advances produced during the thesis in development and optimization of an existing ^1H - ^{13}C -MRS protocol adapted for the study of excitatory / inhibitory metabolic balance in mouse hippocampus.

Chapter 3 contains the main project of the thesis that aimed at using MRS in a mouse model of mood disorder with a known genetic defect to identify potential biomarkers.

Chapter 4 presents some of the main findings obtained using MRS in a stress-induced mouse model of mood disorder to identify potential biomarkers.

Chapter 5 consists in an alternative study investigating metabolic adaptations related to neurogenesis during embryonic development of the avian retina.

Chapter 6 provides an overall conclusion and presents potential future directions for the understanding of metabolic alterations related to mood disorders using MRS.

Chapter 1

Introduction

Abstract

This chapter summarizes the important concepts required for the understanding of this thesis. A brief introduction of mood disorders provides a contextual understanding and clinical significance of the thesis. In this first part, common disease subtypes and classification are described and the current hypotheses underlying the pathophysiology and etiology of mood disorder are presented. Finally, genetic and environmental risk factors leading to mood disorders are compared. The second part describes basic mechanisms of brain metabolism with focus on energetic aspects. This part covers some basic general concepts of metabolism and the current understanding of how metabolism is coupled to brain function. The end of this section emphasizes on the current knowledge regarding metabolic dysfunction associated with mood disorders. The third part describes magnetic resonance spectroscopic techniques relevant for this thesis, i.e. focusing on proton (^1H), phosphorous (^{31}P) and carbon (^{13}C) detection. Each of the techniques is briefly described after a general introduction of magnetic resonance and the concept of localization for *in vivo* measurements. Emphasis is given on the utilization of MRS techniques to study energy metabolism with a focus on mood disorders. This chapter is concluded with the current problematics in the field of magnetic resonance spectroscopy applied to the study of mood disorders and a description of the aim of this thesis.

1.1 Mood disorders

1.1.1 Occurrence and concept

Mood disorders are one of the leading causes of disability worldwide (Friedrich, 2017; Mathers et al., 2008). Mood disorders are generally classified into major depressive disorder (MDD) and bipolar disorder (BPD), which are both characterized by a strong alteration of the mood. MDD, also called unipolar depressive disorder, is characterized by a single depressed mood state, whereas BPD generally includes fluctuations between depression and mania. Several subtypes or associated specificities exist, which allows a refined description of the disease. Psychiatric classification, or nosology, is mainly based on signs and symptoms that are described by reference books. Currently, two comparable classification systems exist: the Diagnostic and Statistical Manual of Mental Disorders (DSM-5) and the International Classification of Diseases (ICD-10), which are published by the American Psychiatric Association and the World Health Organization (WHO) respectively. For instance, the DSM-5 defines MDD based on whether five or more of the following symptoms have occurred during a 2-week period: 1) depressed mood 2) loss of interest and pleasure 3) a change of more than 5% in body weight 4) sleep alterations 5) psychomotor dysfunction 6) fatigue 7) feeling of worthlessness or guilt 8) difficulty in thinking or concentrating 9) suicidal thoughts. Furthermore, these symptoms should cause clinically significant distress and should not be attributed to the effects of a substance or another medical condition (American Psychiatric Association, 2013).

1.1.2 Hypotheses of mood disorders

The pathophysiology and etiology of mood disorders is poorly understood and results in the current subjective classification method, based on signs and symptoms rather than objective biological parameters. Many hypotheses have been made about the biological substrate of these diseases, but none of them really succeeded in explaining and predicting their appearance, evolution and response to treatments. Among them, monoaminergic dysfunction has been initially proposed to underlie depressed mood, based on the specific stimulation of these neurotransmitter systems by several antidepressants. However, the mismatch between rapid monoamine level rise upon treatment and the delayed improvement of mood has challenged this hypothesis. Several other biological functions have been associated with

depression, like an impaired neuroplasticity or unbalance between excitatory and inhibitory tone in specific brain areas (Liu et al., 2017; Sanacora et al., 2012). Reduced levels in trophic factors in the brain, like BDNF (brain-derived neurotrophic factor) or abnormal prefrontal glutamate concentration have served as a basis for developing these hypotheses (Boku et al., 2018; Luykx et al., 2012). Bipolar disorders have been associated to numerous biological abnormalities ranging from neurotransmitter and plasticity alterations (similar to depression) to neuro-immune, oxidative stress and mitochondrial impairments (Sigitova et al., 2017). For example, alterations of high energy phosphate levels and comorbidity with mitochondrial disorders have led to the mitochondrial dysfunction hypothesis of BPD by Kato & Kato (Kato and Kato, 2000).

Due to the lack of comprehensive understanding of mood disorder pathophysiology, current treatments have arisen from serendipitous discovery. Most of the available drugs for depression target the monoaminergic system by increasing the levels of these neurotransmitters in the synaptic cleft. This mechanism is produced by either reducing the degradation of monoamines, with MAOIs (Monoamine oxygenase inhibitors), or reducing presynaptic reuptake, with reuptake inhibitors. While tricyclic antidepressants (TCAs) and SNRIs (serotonin-noradrenaline reuptake inhibitors) do not differentiate between serotonin and noradrenaline, SSRIs (selective serotonin reuptake inhibitors) are specific to serotonin reuptake and have shown higher efficacy. The role of serotonergic system in depression has been debated and newer generation of treatments start targeting other systems. For instance, stimulating the glutamatergic system with acute ketamine administration has shown rapid and promising results with a strong effect on treatment-resistant depression (Berman et al., 2000; Lener et al., 2017; Zarate et al., 2006). Mood stabilizing agents used for treating BPD have also several biological effects. The gold standard treatment prescribed is lithium chloride, which inhibits inositol monophosphatase (IMPase) and glycogen-synthase kinase 3 (GSK3)(Li et al., 2012a). Whether one or the other enzyme is predominant in the symptom relief is still debated. Valproic acid, which has also known thymoregulator properties, has been shown to modulate glutamate neurotransmission and inhibit histone deacetylases (HDACs). The exact pathological mechanism on which a drug has a beneficial effect is hard to assess given the plethora of neurophysiological consequences of activating or inhibiting a single molecular target. For instance, inhibition of GSK3 by lithium has been shown to enhance neuroenergetics

by reducing insulin resistance and stimulating mitochondrial function (Martin et al., 2018; Toker and Agam, 2014).

1.1.3 Genetic and environmental factors

Several factors can increase the likelihood of developing mood disorders. These risk factors can be segregated into either genetic or environmental. While some people might have a genetic susceptibility to developing mood disorder, the environment plays a central role in the induction or reversal of the disease.

Heritability of MDD has been measured at around 50%, suggesting that a high fraction of variation is due to genetics between individuals (Guffanti et al., 2016; Sullivan et al., 2000). Genome Wide Association Studies (GWAS) have provided a tool to study single nucleotide polymorphisms (SNPs) in high number of samples and in the entire genome. These studies have reported several gene candidates related to depression (Hyde et al., 2017; Ward et al., 2017).

Bipolar disorders are thought to have a stronger genetic component than MDD and higher heritability >50% has been measured (Craddock and Sklar, 2013). For instance, several SNPs have been identified with help of GWAS studies including variants within CACNA1C (Calcium Voltage-Gated Channel Subunit Alpha1 C), ODZ4 (teneurin 4) and NCAN (neurocan core protein). Furthermore, high comorbidity exists between BPD and genetic mitochondriopathies (Fattal et al., 2006). Some genetic studies have pointed towards a possible higher maternal inheritance of bipolar disorder (McMahon et al., 1995), suggesting a mtDNA effect, but these results have been controversial (Grigoriu-Serbanescu et al., 1998; Kato et al., 1996). Mitochondria-related polymorphisms in nuclear and mtDNA have also been identified and linked to BPD (Kato and Kato, 2000; Siciliano et al., 2003). The mitochondrial “common deletion” has been observed in brains (Kato et al., 1997) and in peripheral leukocytes of BPD patients compared to healthy controls (Kato and Takahashi, 1996). It is nevertheless still unclear whether these genetic differences really account for the observed mitochondrial dysfunctions (Fuke et al., 2008; Kato and Takahashi, 1996; Sabunciyan et al., 2007). Probably due to the proximity to reactive oxygen species (ROS) produced in the mitochondrial matrix, mitochondrial DNA (mtDNA) has a mutation rate around 10-20 times that of nuclear DNA (nDNA) (Finsterer, 2004), however >90% of mitochondriopathies are caused by nDNA

mutations (Gillis and Kaye, 2002). Oquendo et al. have shown that parental transmission of mood disorder is more related to the childhood adversity rather than the parental characteristic (Oquendo et al., 2013). In other words, offspring of BPD parents are not more likely to develop BPD than offspring of MDD parents. This suggests that environment plays a key role in the development of mood disorders as well.

Several environmental factors can influence or induce the onset of mood disorders. The underlying mechanism by which environment affects normal brain function can be generalized by “stress”. Stress is a natural response of a living being to an environmental threat, which can be of different kinds. A change in temperature, osmotic pressure, concentration of nutrients or toxins are examples of potential stressors for a cell. The situation is slightly different for more complex organisms like a human, where stress can arise from other experiences like escaping a predator or, more relevant to our current society, managing a social situation. While the stressors can be very different, they all have in common the mobilization of energy resources to give the appropriate biological or behavioral response (Picard et al., 2018). Typically, stress activates the hypothalamo-pituitary-adrenal (HPA) axis in mammals leading to the release of stress hormones, which orchestrate the remodeling of metabolic function. Traditionally, acute stress mediated by adrenaline has been considered to have a positive effect, by improving energetics and providing a quick response to a sudden stress. However, long lasting exposure to stress leads to negative effects, mainly mediated by glucocorticoids. The damaging consequences of chronic stress on a “stressed being” can be understood as a progressive exhaustion of the metabolic resilience mechanisms. The concept of “allostatic load” has been proposed by B. McEwen to describe the burden of repeated active restoration of homeostasis (McEwen, 1998). Under a similar stressful situation, individuals are thus likely to respond differently. Subjects which are able to cope with the stressor are considered to be “resilient”, while the affected ones are “susceptible” to stress. Excessive exposure to stress during early-life or adulthood can induce strong remodeling of gene expression (Bagot et al., 2014). These epigenetic modifications are the result of DNA adaptations to the stress, illustrating the inherent relationship between genetic and environmental factors. Chronic stress is well known to induce neuronal damage through excitotoxic glutamate release (Sapolsky, 1986; Sorrells et al., 2009) or reduce brain plasticity and neurogenesis (Mahar et al., 2014; McEwen, 1999; Schoenfeld et al., 2017) in

hippocampus. Through remodeling of neural architecture, stress has a strong effect on brain function and has been implicated in the development of several psychopathologies including mood disorders (McEwen et al., 2015). Subjecting animals to social or unpredictable environmental stressors can lead to the development of a depressive-like behavior that reflects some aspects of human depression (Chaouloff, 2013).

In summary, mood disorder are complex multifactorial diseases that result from both genetic and environmental influences. The underlying pathophysiology and etiology remain to be elucidated in order to establish accurate biomarkers of the disease. Due to the current symptom-based diagnosis, there is a need for defining objective biological measures to help developing new therapeutic strategies (Lenzenweger, 2013).

1.2 Brain metabolism

1.2.1 Definition of metabolism

Metabolism is the set of chemical reactions maintaining an organism alive. Intermediates of a metabolic pathway are referred to as metabolites. The chemical reactions required for life can either be anabolic, that is leading to the synthesis of new compounds, or catabolic, leading to the breakdown of molecules. Typically, anabolic reactions require energy but are fundamental for synthesizing the plethora of complex compounds required for cellular structural and functional organization. At a thermodynamic point of view, the low level of entropy contained in these highly ordered molecules requires an input of energy for their production. This energy is generally provided by the catabolism of other molecules with high chemical potential provided by food. As such, metabolism can be seen as the chemical process by which a living organism maintains its low level of entropy (Schrödinger, 1951). Catabolic reactions typically degrade high energy carbon-based substrates like glucose, triglycerides or eventually proteins. This molecular breakdown produces adenosine triphosphate (ATP) and nicotinamide adenine dinucleotide (NADH), which are the “carrier” units of free energy and reducing equivalents, respectively. Anabolic reactions include several synthetic pathways producing proteins, nucleic acids, lipids, etc. While catabolic reactions generally produce ATP, anabolic reactions consume it. Reducing equivalents for anabolic reactions are however generally carried by nicotinamide adenine dinucleotide phosphate (NADPH) rather than NADH.

The ability of producing ATP and NADH is fundamental for the survival of an organism as it is the driving force of any kind of adaptation to an environment challenge, which can be described as stress. Two main pathways are responsible for the production of ATP and NADH: glycolysis and oxidative phosphorylation (OXPHOS). Glycolysis is the process by which glucose is oxidized in pyruvate, producing 2 moles of ATP and 2 moles of NADH per mole of glucose (Fig 1.1).

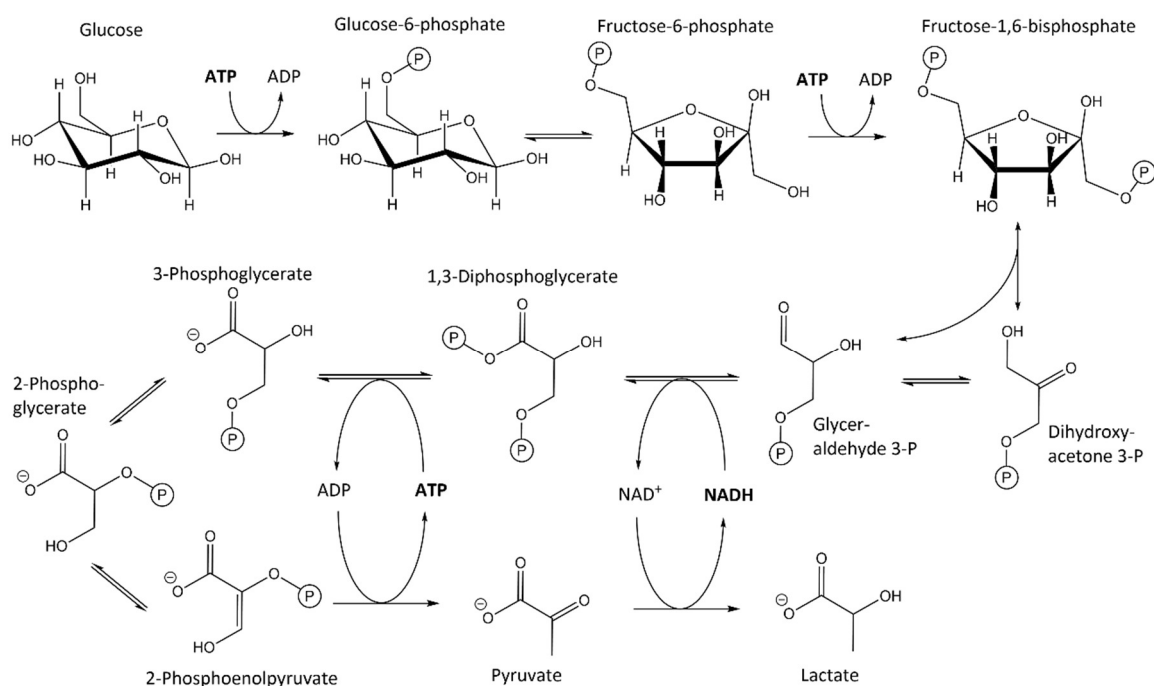


Figure 1. 1 : Glycolysis

Breakdown of glucose in pyruvate provides one of the main catabolic cellular reaction. This glycolytic process produces 2 molecules of ATP per glucose and leads to pyruvate, which can then be further oxidized in the mitochondria through OXPHOS.

The pyruvate produced is then further oxidized through OXPHOS in the mitochondria. Reducing equivalents are first extracted in the tricarboxylic acid (TCA) cycle (Fig. 1.2) and are then oxidized in the electron transport chain (ETC) of the inner mitochondrial membrane (Fig 1.3). This latter step transfers electrons from NADH to the final acceptor oxygen. This highly exergonic reaction is coupled to proton pumping reactions from mitochondrial matrix towards intermembrane space. This produces an electrochemical potential ($\Delta\psi_m$) which is then used by the complex V to add an inorganic phosphate to adenosine diphosphate (ADP), producing the highly energetic ATP molecule. ATP can then be converted into phosphocreatine (PCr) through the action of mitochondrial creatine kinase (CKMt). As phosphocreatine has a higher chemical potential than ATP, this process is controlled through kinetics rather than

thermodynamics, i.e. driven by the high concentration of ATP in the matrix. This transfer of high energy phosphate allows to shuttle ATP out of the mitochondria and store energy into a second compound. The buffering properties of PCr ensure that a constant level of ATP is maintained in the cytoplasm. OXPHOS generates between 30 and 36 molecules of ATP from conversion of one molecule of glucose. This outstanding efficiency is compensated by the relatively slow dynamics of OXPHOS compared to glycolysis. The rapid ATP production rate of glycolysis requires cytoplasmic levels of NAD^+ to be maintained to avoid autoinhibition. As a result, the NADH produced is generally recycled by converting pyruvate to lactate or by transferring NADH into mitochondria through malate-aspartate shuttle. (Tymoczko et al., 2013)

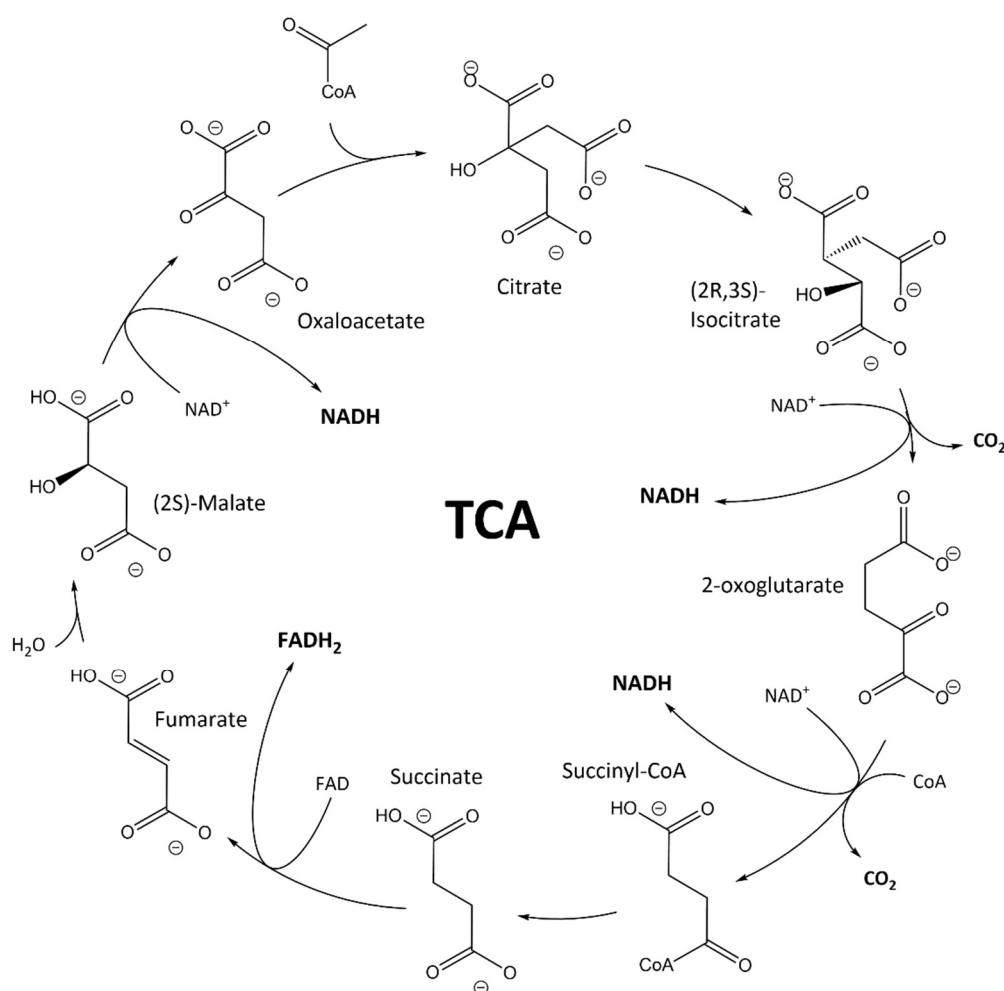


Figure 1. 2 : Tricarboxylic acid (TCA) cycle

The TCA cycle produces a large amount of reducing equivalents from the acetyl-CoA arising from either pyruvate or fatty acids. The carbons of acetyl-CoA are fully oxidized into CO_2 , while high energy electrons are stored into NADH and FADH_2 for further energetic conversion in the electron transport chain (ETC).

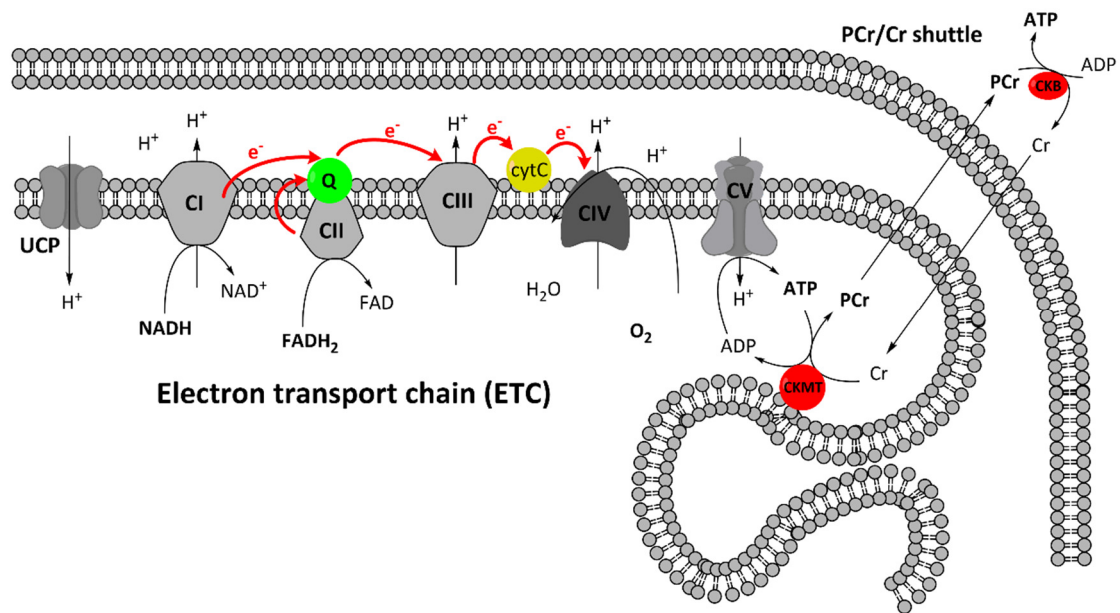


Figure 1. 3 : Electron transport chain and mitochondrial ATP synthesis

The high energy electrons contained in NADH and FADH₂ are transferred between several mitochondrial complexes (C_I → C_{IV}) that pump protons from the mitochondrial matrix to the inter-membrane space. The gradient of proton generated by this process is then used by the ATP-synthase (C_V) to generate ATP. Electrons transit between the complexes is thermodynamically favored and is triggered by their gradual decrease in energy from complexes I to IV, transiting from a “highest occupied molecular orbital” (HOMO) to a “lowest occupied molecular orbital” (LUMO), until reaching the final acceptor O₂. The oxidation of NADH results in production in water, but often generates reactive oxygen species (ROS) as a side product. Finally, the ATP produced is transferred out of the mitochondria through the PCr/Cr shuttle, which provides a mean to store high energy phosphates.

1.2.2 Brain function and metabolism

The brain has high energetic needs and requires an efficient metabolic machinery, due to its central role in processing neurotransmission information. This particularity can be illustrated by the high levels of oxygen consumption (~20% of body total O₂ utilization at rest), while the organ represents only 2% of body weight (Erecińska and Silver, 1989). The Na⁺/K⁺ ATPase, as a key enzyme restoring membrane potential, provides a potential basis for understanding the high energy consumption of neurons (Rolfe and Brown, 1997; Sokoloff, 1981). After each action potential, the plasma membrane needs to be brought back to resting potential quickly, which requires a highly ATP-demanding ion pumping. While action potentials and post-synaptic effects of glutamate have been considered to account for ~80% of total brain energy consumption (Attwell and Laughlin, 2001), it is now thought that, in cerebral cortex, most signaling energy (50%) is used on postsynaptic glutamate receptors, 21% is used on action potentials only, while 20% is used on resting potentials, 5% on presynaptic transmitter release, and 4% on transmitter recycling (Howarth et al., 2012). Nevertheless, given its central

biological function and energy-dependency, the brain is capable of metabolic adaptation (McIlwain, 1970). For instance, ketone bodies can replace glucose during starvation and diabetic ketosis (Achanta and Rae, 2017).

In the last decades, it has become clear that brain metabolism is compartmentalized. The finding that two distinct TCA cycles exist in the brain (Van Den Berg et al., 1969) has given new scopes to understanding neuroenergetics. In addition to neurons, glial cells have been identified as a key component of brain metabolism. Astrocytes, which were thought to have a solely structural function (glia being derived from the Greek work *gliok* meaning “glue”), appeared to be fundamental as trophic support for surrounding neurons. For instance, several metabolic substrates have been shown to be released by astrocytes with the potential to fuel neuronal metabolism (Dringen et al., 1993; Larrabee, 1983, 1992; Selak et al., 1985; Tsacopoulos et al., 1988). Astrocytes contain high levels of glycogen and their end-feets are in tight contact with blood vasculature. In particular, release of lactate from glycogen breakdown from astrocytes has been shown to be important for synaptic plasticity (Suzuki et al., 2011) as part of the astrocyte-neuron lactate shuttle (ANLS) (Pellerin and Magistretti, 1994). Astrocytes play thus a central role in coupling metabolic demands to neuronal activity through neurovascular coupling (Roy and Sherrington, 1890).

Astrocytes have been thought to outnumber neurons by approximately 1.5-fold for a long time (Pelvig et al., 2008), however, recent evidence suggest a comparable (1:1) abundance (von Bartheld et al., 2016). Nevertheless, their contribution to total brain energy consumption is significant and now well established. The fate of glutamate uptake by astrocytes is widely accepted to be part of the glutamate/GABA-glutamine cycle, in which glutamate is rapidly converted to glutamine by the glia-specific glutamine synthetase (Bak et al., 2006; Benjamin and Quastel, 1972; van den Berg and Garfinkel, 1971; Ottersen et al., 1992). Several other inter-cellular fluxes have been proposed like the alanine-lactate shuttle, ketone body shuttle, glycerol-phosphate shuttle or glutathione shuttle (Bolaños, 2016; Guzmán and Blázquez, 2001; McKenna et al., 2006; Zwingmann et al., 2000). While some mechanisms still need further investigations, it is clear that astrocytes have emerged as a fundamental component of brain function and homeostasis, which goes beyond the simple structural support (Nedergaard et al., 2003; Volterra and Meldolesi, 2005; Weber and Barros, 2015).

GABAergic neurons also possess metabolic interactions with astrocytes. GABA released in the synaptic cleft is taken up in part by astrocytes, which recycle it through the GABA-shunt (Walls et al., 2015). This process transforms GABA into succinate, which re-enters the TCA cycle. The contribution of this shunt to the total TCA flux has been estimated at 8% of glucose metabolism (Patel et al., 1970). Due to the lower GABAergic neuron abundance in the brain, inhibitory neurotransmission is thought to contribute generally less to glucose metabolism (Howarth et al., 2012). GABAergic energetic contribution might however be dependent on the neuronal type, the brain region or the network activity status. Typically, Fast-spiking parvalbumin-positive interneurons, which are particularly activated during gamma-oscillations in the hippocampus, are known to be very energy consuming and mitochondria-rich (Kann et al., 2014).

Much remains to be discovered and understood regarding biochemical interactions between the different types of cells and how the “metabolic ecosystem” is organized in the brain. Brain metabolic interactions are complex and depend on several factors like the cell type or local environment. A summary of principal metabolic interactions at the tripartite synapse is proposed in figure 1.4. The mysteries of brain metabolism are far from being unraveled and the development of new imaging technologies is prone to help solving important questions in the field.

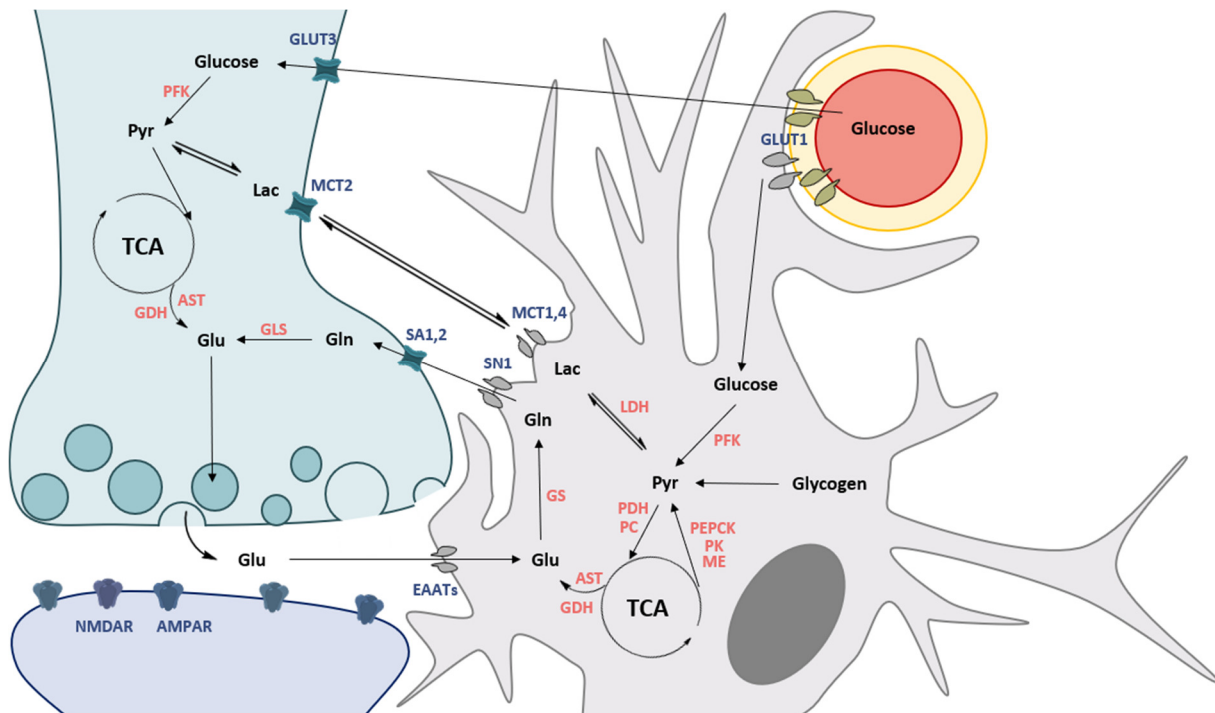


Figure 1. 4 : The tripartite synapse and its metabolic interactions

Astrocytes are in close contact with neuronal synapses and blood vessels. Glucose enters the brain parenchyma through glucose transporters (GLUT1) and is then taken up by the different cells for glycolysis. Several enzymes convert glucose in pyruvate but the rate limiting enzyme phosphofructokinase (PFK) is the key regulator of glycolysis. Astrocytes have the particularity to contain a set of anaplerotic enzymes like pyruvate carboxylase (PC), phosphoenol pyruvate carboxykinase (PEPCK), pyruvate kinase (PK) and malic enzyme (ME) which are able to replenish the pools of TCA cycle intermediates. Glutamate is synthesized in neurons from oxoglutarate through the action of glutamate dehydrogenase (GDH) or from transamination reactions typically through the action of aspartate aminotransferase (AST). Glutamate stored in synaptic vesicles in excitatory neurons is released in the synaptic cleft for binding to its target NMDA and AMPA receptors on the postsynaptic site. Glutamate is quickly cleared up by astrocytes which take up glutamate in a Na^+/K^+ APTase-dependent process. Transit of glutamate through the excitatory amino acid transporters (EAATs) occurs with a concomitant inflow of Na^+ and outflow of K^+ , which are counterbalanced by the astrocytic Na^+/K^+ APTase (not shown). Glutamate is then rapidly converted to glutamine by glutamine synthetase (GS) and is shuttled back to neurons for replenishing glutamate pool through the action of glutaminase (GLS). These exchanges of neurotransmitter glutamate between neurons and glia are called the glutamine/glutamate cycle. A similar cycle has been observed for GABA, which is recycled by astrocytes and inhibitory neurons through the GABA shunt (not shown). Finally, it has been shown that lactate can transit from one cell to the other for fueling the TCA cycle of the more oxidative cells.

Several imaging techniques have provided valuable information of brain metabolism *in vivo*.

The initial autoradiographic measurements using radio-labelled deoxyglucose has resulted in the now widely applied positron emission tomography (PET) imaging technique (Sokoloff, 1981). Changes in blood susceptibility during brain activation, as a result of changes in blood flow, blood volume and oxygen consumption, have given a basis for detecting metabolic activity through the BOLD (brain-oxygen level dependent) response in functional magnetic resonance imaging (fMRI). Finally, magnetic resonance spectroscopy (MRS) has provided a plethora of tools to investigate metabolic organization. While ^1H -MRS has been limited to

static measurements, that is quantifying total metabolic concentrations, ^{13}C -MRS has led to significant improvements in our understanding of metabolic interactions between the different brain cells (Gruetter et al., 2001; Lanz et al., 2014a; Mason et al., 1992; Morris and Bachelard, 2003). Major MRS techniques that have been used to study brain metabolic alteration in mood disorders are discussed in chapter 1.3.6.

1.2.3 Metabolic dysfunctions in mood disorders

Several peripheral and brain metabolic dysfunctions have been associated with mood disorders. Obesity, dyslipidemia, hypertension, hyperglycemia or insulin resistance are all parts of the so-called “metabolic syndrome”, which shows high comorbidity with mood disorders (Marazziti et al., 2014). The mechanisms and the causality relationship between peripheral metabolic alterations and dysfunction of the central mood regulation are still unknown. Glycolytic and mitochondrial energy productions are hard to distinguish given their high interdependence. These two energy systems normally work in parallel and regulate each other, so that dysfunction of mitochondria will be for instance compensated by an increase in glycolysis (glycolytic switch). In the brain, the significant reliance on glucose as energy substrate renders the mitochondria particularly sensitive to an impairment in glycolysis under normal blood glucose conditions. However, mitochondria can oxidize ketone bodies from the blood if the glucose metabolism impairment is more systemic. Interactions between central and peripheral metabolism are complex and multifactorial. The following paragraphs will thus focus on central metabolic alterations that have been associated with mood disorders, with an emphasis on glycolytic and oxidative metabolism.

1.2.3.1 *Glycolytic dysfunctions*

Glycolysis and lactate production have been shown to play a significant role in brain plasticity and memory formation (Shannon et al., 2016; Suzuki et al., 2011). However, high levels of glycolysis can reflect an impairment of mitochondrial oxidative capacity. For instance, high level of lactate have been observed in the cerebrospinal fluid of bipolar and depressed patients suggesting the appearance of a glycolytic switch (Bradley et al., 2016; Regenold et al., 2009). Lower levels of glycolysis itself have however been reported as well, with typically reduced blood flow and glucose metabolism as measured with PET (reviewed in (Videbech, 2000)). For instance, lower glucose metabolism together with a reduction of gray matter

volume has been identified in subgenual prefrontal cortex of unipolar and bipolar depressed patients (Drevets et al., 1997). The cerebral metabolic rate of glucose was shown to increase from depressed to manic bipolar patients, suggesting a relationship to the mood state (Baxter, 1985). An inverted metabolic activity was observed between the subgenual prefrontal and right prefrontal cortices during depression and normal sadness, suggesting that an opposite response might exist between limbic and cortical areas (Mayberg et al., 1999). Ketter et al. have reported a pattern of reduced anterior glucose metabolism in depressed bipolar patients together with an increase in limbic subcortical areas (ventral striatum, thalamus, amygdala), suggesting a limbic-cortical dysregulation (Ketter et al., 2001). While most of the studies are consistent with an overall reduced prefrontal metabolism (hypofrontality), some opposite results have been observed (Buchsbaum et al., 1986).

The origin of this abnormal glycolytic activity has been mainly attributed to differences in brain activity; an imbalance between limbic and cortical function leads to an opposite metabolic activation. Whether the impaired metabolic rate of glucose is the consequence of an altered neuronal/network activity or whether it is its cause remains to be determined. Recent studies have pointed towards a link between depression and glucose homeostasis, in particular through insulin resistance (Lyra e Silva et al., 2019). For instance, high levels of insulin resistance has been observed among depressive patients with childhood trauma (Nasca et al., 2019). Impairments in the ability to take up glucose from the blood could thus provide an interesting mechanism to explain the reduced glycolytic function of the affected brain areas. The brain is sensitive to insulin and contains insulin-dependent glucose transporter GLUT4 (Vannucci et al., 1998). Furthermore, blood insulin has been shown to have antidepressant-like effect in rodents (Mueller et al., 2018).

Glycolytic function is essential for mitochondrial well-being and vice-versa. Interaction between these two energetic processes is thus fundamental for normal brain functioning. For instance, Regenold et al. (Regenold et al., 2012) found lower levels of glycolytic rate-limiting enzyme HK1 attachment to the mitochondria outer membrane in post-mortem parietal cortex of mood disorder patients. This suggests an impaired linking of the cytosolic glycolysis to mitochondrial OXPHOS.

1.2.3.2 Mitochondrial dysfunctions

Given the difficulty in separating oxidative from glycolytic dysfunction *in vivo*, most of the molecular analyses of mitochondrial function have been performed on peripheral cells of patients or post-mortem. Extracted lymphocytes from the blood of BPD patients showed a lower expression level of ETC gene under glucose deprivation condition, suggesting an altered molecular adaptation to energetic stress (Naydenov et al., 2007). Another study revealed that fibroblast and lymphocyte as well as postmortem PFC cells from BPD patients show altered cellular distribution and morphology compared to age-matched controls (Cataldo et al., 2010). However, no activity of the ETC and energy production difference was observed in peripheral cells (Cataldo et al., 2010; Gubert et al., 2013). The intracellular calcium signaling response of platelets from BPD patients was increased and stabilized with antidepressant (Yamawaki et al., 1998).

Postmortem studies revealed several brain-specific implications of mitochondria in BPD. Proteomic and gene arrays analysis of BPD patients post-mortem showed reduction of many energy-related mitochondrial proteins and gene expression in PFC (Iwamoto et al., 2005; Pennington et al., 2008; Sun et al., 2006) and in hippocampus (Konradi et al., 2004). MacDonald, et al. (MacDonald et al., 2006) also reported a lower expression level of both creatine kinases (CKB and CKMt) in hippocampus and PFC of BPD patients. Finally, PFC complex I activity was found to be reduced in post-mortem samples of BPD patients (Andreazza et al., 2010). More recently, hippocampal dentate gyrus-like neurons derived from induced pluripotent stem-cells (iPSC) of patients with bipolar disorder were used to find mitochondrial alterations including a reduced size and increased membrane potential, leading to higher neuronal excitability (Mertens et al., 2015).

Animal models of BPD based on amphetamine-induced mania show lower levels of TCA cycle enzymes, creatine kinase and ETC components in the rodent brain (Corrêa et al., 2007; Feier et al., 2013; Rezin et al., 2014; Streck et al., 2008; Valvassori et al., 2010). Ouabain-induced animal models of mania show reduced creatine kinase activity in PFC and hippocampus as well (de Freitas et al., 2011). Furthermore, mood disorder-like phenotype with similar treatment response to bipolar disorder was observed in a mouse model expressing a mutated neuron-specific mtDNA polymerase (POLG) (Kasahara et al., 2016).

The two gold standard mood stabilizers used for bipolar treatment, lithium and valproate, have shown to affect significantly mitochondrial function and health. The first studies were performed *ex vivo* on extracted liver or brain mitochondria. Valproate has an inhibitory effect on OXPHOS ATP synthesis (Haas et al., 1981; Ponchaut et al., 1992; Silva et al., 1997), while lithium shows a protective and anti-apoptotic action (Shalbuyeva et al., 2007). Their effect has also been studied on animal models. Ouabain-induced drop in BDNF was restored (Jornada et al., 2010) or protection against meth-amphetamine-induced mitochondrial damage was increased (Bachmann et al., 2009) after treatment. Mice exposed to lithium had a high amount of up-regulated mitochondrial genes (Toker and Agam, 2014; Toker et al., 2014). A protective effect against mitochondrial toxicity by lithium and valproate was observed in rat neuronal cultures by stimulating glutathione metabolism (Cui et al., 2007) and increasing the anti-apoptotic response (Bcl-2/Bax) (Chen and Chuang, 1999). Lithium restored normal Ca^{2+} homeostasis in B-lymphoblast cell lines from bipolar patients (Wasserman et al., 2004) and increased the enzymatic OXPHOS activity of postmortem human cortex homogenates (Maurer et al., 2009).

Given the initial finding that antidepressant used for depression target the monoaminergic system, fewer attention has been directed towards neuroenergetic alterations (Cohen-Woods et al., 2013). Even though no “mitochondrial hypothesis” has been developed for MDD, several pieces of evidence suggest that oxidative metabolism might be impaired. As for BPD, a strong comorbidity exists between mitochondriopathies and MDD (Suomalainen et al., 1992). A few reports have also highlighted the importance of maternal transmission towards the development of depression, suggesting mtDNA-related genetic factors (Boles et al., 2005). A link between depression and the mtDNA copy number in leukocytes of old women was observed as well.

Reduced cellular ATP production rate of muscle biopsies (Gardner et al., 2003) as well as reduced respiratory rates in platelets and peripheral mononuclear cells (Hroudova et al., 2013; Karabatsiakos et al., 2014) suggest that mitochondrial dysfunctions are present and could be detected in peripheral tissues. Gene expression studies, however, failed in revealing mitochondria-related alteration in the mRNA profile (Aston et al., 2004; Iwamoto et al., 2005; Sibille et al., 2004; Tochigi et al., 2008).

Neuronal and synaptic plasticity has been largely implicated in the pathophysiology of depression and mitochondria play a central role in this process (Mattson et al., 2008). Brain derived neurotrophic factor (BDNF) is a key component of mood disorders, and brain plasticity disorders in general, as it induces growth and synapse strengthening through signaling via its receptor TrkB (Shimizu et al., 2003). Given the energetic need for every cellular trophic mechanism, it is not surprising that mitochondrial function is coupled to these signaling processes (Vaynman et al., 2006). Some studies even suggested a direct action of BDNF on the mitochondrial function, by stimulating brain mitochondrial respiratory control (Markham et al., 2004, 2012, 2014).

Inflammatory process have been associated with depression as well, where depressed patients show higher peripheral levels of pro-inflammatory cytokines (Dowlati et al., 2010; Liu et al., 2012; Maes, 2011). It is however still unclear whether inflammation is really a cause or a consequence of depression (Raison and Miller, 2011). Psychological stress is a well-documented cause of depressive behavior, and its histological consequences, such as neuronal excitotoxicity and ROS production in the brain, could make the link between mitochondrial dysfunction, inflammatory process and subsequent depression (Tobe, 2013). Chronic and acute stress are both known to differentially affect the immune system (Sorrells and Sapolsky, 2007; Sorrells et al., 2009; Steptoe et al., 2007) and have been proposed to be modulated by mitochondrial function (Picard et al., 2015). The allostatic load induced by any stressor, physiological, cellular or psychological, can only be overcome with an efficient and controlled production of energy. Mitochondria strength and efficiency are therefore very likely to be fundamental parameters for resilience to stress (Picard et al., 2018). Excessive stimulation of mitochondrial energy production can lead to ROS/RNS over-production and cell damage (Bhat et al., 2015). Excitotoxicity induced by a hyper-active/stressed brain network can induce cell and mitochondrial damage as well (Mehta et al., 2013). Furthermore, ROS production by mitochondria is a major step in the inflammatory activation of microglial cells (Park et al., 2015).

Studies on animal models of depression have also pointed towards mitochondrial implications in depression. Depressive-like behavior was observed in a genetic mouse model containing mtDNA mutations in the paraventricular thalamus (Kasahara et al., 2016). Replacing the homologous mouse DNA sequence with a pathogenic sequence from *CREB1* promoter

associated with MDD resulted in overexpression of a set of genes including components of mitochondrial OXPHOS machinery in mouse (Zubenko et al., 2014). Hippocampal reduction in mitochondrial number and size was also reported in a genetic rat model of depression (Chen et al., 2013). Stressing rodents chronically is another way of inducing a depressive-like phenotype. Restraint stress in rats has shown to induce a reduction in mitochondrial energy-related proteins (van Zyl et al., 2016). Chronic stress has shown to induce damages in mitochondrial ultrastructure as well as inhibited respiration rate in PFC, hippocampus and hypothalamus of mice (Gong et al., 2011). Chronic stress also inhibited mitochondrial respiratory chain (Rezin et al., 2008) and Na^+/K^+ ATPase (Gamero et al., 2003) while it increased mitochondrial ROS production (Lucca et al., 2009) in rats. This effect might not be limited to mammals as similar stress-induced dysfunctions have been observed in zebra fish (Chakravarty et al., 2013).

Many studies have reported an inhibitory effect of antidepressant on mitochondrial OXPHOS function when administered to isolated mitochondria from rat liver, heart, brain, pig brain, but also in CHO cells, rat primary hepatocytes and human HL-60 cells (Abdel-Razaq et al., 2011; Curti et al., 1999; Hroudova and Fisar, 2010; Li et al., 2012b; Souza et al., 1994; Weinbach et al., 1986; Xia et al., 1999). However, when administered to animals directly, studies reported an increase in mitochondrial function of rat liver and brain, in agreement with mood stabilizer role in improving mitochondrial function and metabolic resilience (Agostinho et al., 2011; Katyare and Rajan, 1988, 1995; Scaini et al., 2010).

Altogether, several findings support the mitochondrial and energetic dysregulation hypothesis of mood disorders first proposed by Kato et al. (Kato and Kato, 2000) and open the possibility for new treatments using mitochondrial modulators (Nierenberg et al., 2013). It is not clear whether these metabolic alterations are the cause or the consequence of the abnormal mood state and much need to be discovered in the relationship between mood and neuroenergetics.

1.3 Magnetic resonance spectroscopy to study brain metabolism *in vivo*

1.3.1 Basics of nuclear magnetic resonance (NMR)

Magnetic resonance spectroscopy (MRS) is a non-invasive imaging technique based on the detection of nuclear spins “resonating” when subjected to external magnetic fields. The basis of the signal arises from interactions between the magnetic component (B_1) of an electromagnetic (EM) wave in the range of radiofrequency (RF) and the magnetic moment of nuclei, when placed in an external magnetic field (B_0). Several nuclei of atoms possess a spin angular momentum, which is quantized in several components depending on the nuclear spin quantum number I . Most atoms investigated with MRS possess a quantum number $I = \frac{1}{2}$ leading to two vector components of momentum. Due to the positive charge of the atom, each of these components generate a magnetic moment μ with two opposite projections on a given axis. These two orientations, denoted as α and β , are degenerate in the absence of an external magnetic field, i.e. they have the same energy. When these vectors are exposed to an external magnetic field B_0 , the component aligned with the field (say) α has a lower energy than the antiparallel component β (Fig 1.5).

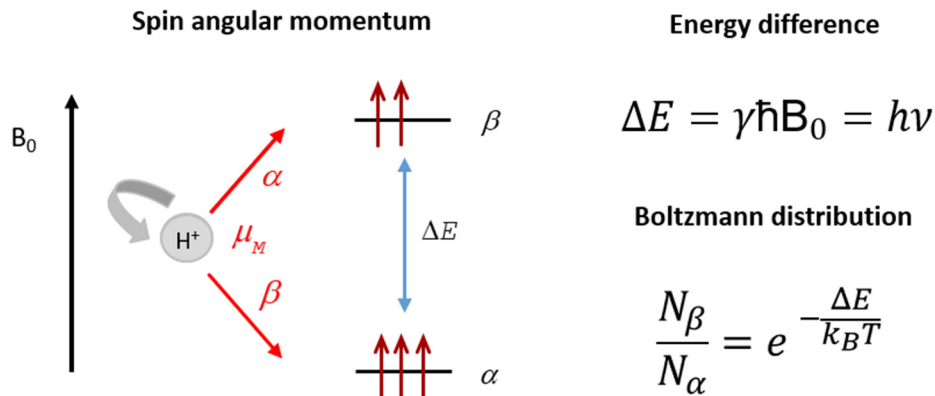


Figure 1. 5 : Effect of an external magnetic field B_0 on magnetic moments of nuclei with $I=1/2$

When placed in a magnetic field B_0 , the two vector components α and β of the nucleus magnetic moment have an energy difference, which is proportional to the applied field B_0 , the gyromagnetic ratio γ and Planck's constant ($\hbar = h/2\pi$). The Larmor frequency ν at which nucleus will “resonance” depends on this energy difference. The relative population of the two energy states is described by the Boltzmann distribution, where T is the temperature and k_B , the Boltzmann constant.

The energy difference between these two states will depend on the magnetic field B_0 and the gyromagnetic ratio γ , an intrinsic constant of each nucleus. The energy difference leads to a population difference between the two states described by the Boltzmann distribution. This difference in population leads to a net macroscopic magnetization M aligned with the magnetic field B_0 (Fig 1.6).

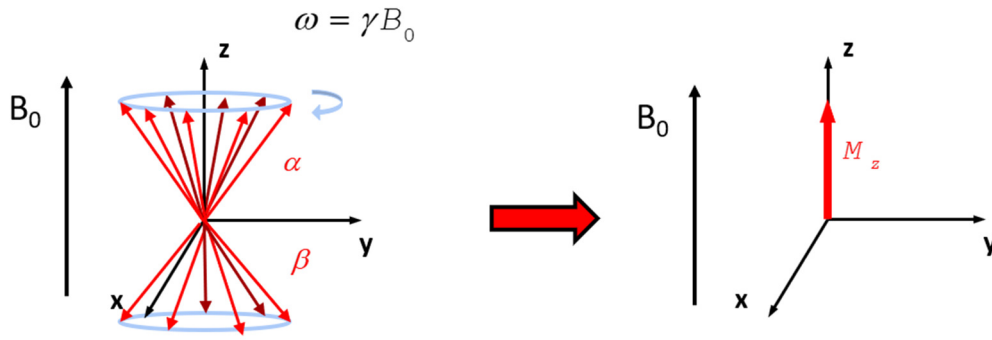


Figure 1. 6 : The population difference between α and β creates a net magnetization M along B_0

All the individual magnetic moments in a sample are randomly distributed around B_0 (say z axis), oscillating at their Larmor frequency ($\omega=2\pi\nu$). Due to the small increase in population of the state α , the net magnetization M is aligned with B_0 .

The origin of NMR signal can be described with a vector model for a basic understanding of magnetization dynamics. By applying an additional magnetic field B_1 provided by a radiofrequency EM wave in the transverse plane, the magnetization is flipped and can subsequently induce a current in a receiver coil (Fig 1.7).

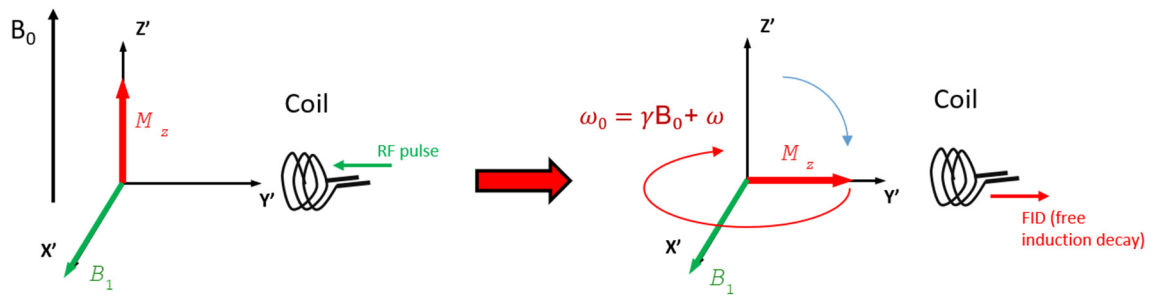


Figure 1. 7 : Signal detection with a solenoid RF coil

The magnetic field B_1 generated by a RF pulse flips the magnetization M_z in the transverse plane. M will rotate in the xy plane at the Larmor frequency and induce a current in the receiver coil in the form of a free induction decay (FID). By considering a reference frame (x', y', z') rotating with frequency γB_0 , the magnetization M will rotate in the $x'y'$ plane at frequency ω , if the Larmor frequency of M is $\omega_0 = \gamma B_0 + \omega$.

The electric current induced by M in the coil is typically an oscillating function of time, which is converted to a function of frequency by using a Fourier transform (Fig 1.8), leading to the typical spectra acquired in a MRS experiment. Because the frequency is dependent on the magnetic field, spectra are reported in chemical shift units (δ), i.e. in parts per millions (ppm) from a reference frequency: $\delta = 10^6 \cdot (\nu_x - \nu_{ref}) / \nu_{ref}$.

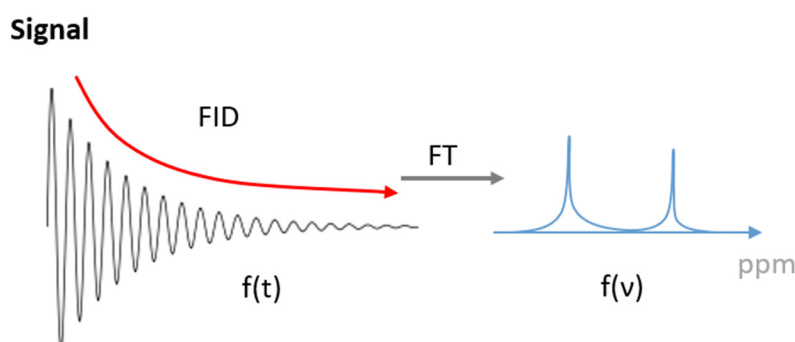


Figure 1. 8 : NMR signal acquisition and transformation

The free induction decay (FID) acquired is an oscillating function of time $f(t)$ which is transformed in a function of frequency $f(v)$ upon mathematical conversion using a Fourier transform. The peaks observed in the frequency domain correspond to the different resonating spins.

Unlike many other spectroscopic techniques, the population difference between α and β is not affected by the EM wave, only its orientation. Nevertheless, several relaxation processes exist, which lead to the loss of signal over time as can be seen from the exponentially decaying shape of the FID. The longitudinal relaxation corresponds to the recovery of M along the z axis and is described by the relaxation time T_1 . As a consequence, sufficient time (repetition time TR) is required between several acquisitions to allow the M_z to be fully relaxed. Typically, for a pulse acquired experiment with a flip angle of 90° , a delay of $\sim 5 \cdot T_1$ is preferred for an absolute quantification of a metabolite ($2 \cdot T_1$ for a flip angle of 30°). Another relaxation occurs in the transverse (xy) plane due to phase coherence loss induced by field inhomogeneities. This magnetization decay is described by the time constant T_2^* , which includes the contribution of T_2 , the intrinsic relaxation time and T_2' , which is the contribution of the local field inhomogeneity.

Molecules containing the observed nucleus can be distinguished given their slight difference in chemical shifts (δ), reflecting the molecular structural arrangement and electronic distribution. In other words, every molecule will be distinguishable within a tissue of interest given its specific chemical shift pattern. Since the intensity of the detected signal is proportional to the amount of spins, quantification of the observed molecules is possible. *In vivo* ^1H -MRS spectra are typically referenced to an internal reference or based on the water signal (Barker et al., 1993; Williams et al., 1988). The internal reference preferentially used in brain ^1H -MRS is creatine, as this molecule gives an isolated high-intensity singlet peak, which is fixed to an arbitrary (assumed constant) concentration (generally around 8mM). However, depending on the study, creatine levels might change between groups or subject and

approximating it to a fixed value could lead to non-negligible errors. The gold standard quantification method references the metabolite peaks to the water signal, assuming a water tissue content of generally 80% of pure water concentration (55,51M). However, the appropriate quantification methods should be motivated and adapted to the study's limitations and needs. (de Graaf, 2007; Hore, 1995; Hore et al., 2000)

1.3.2 Basics of localization for MRS

The basis underlying *in vivo* detection of nuclear magnetic resonance (NMR) is the ability to localize the signal acquired, typically relevant for the study of a given organ or one of its substructures. From a terminology point of view, *in vivo* NMR is generally referred to as magnetic resonance spectroscopy (MRS). Locating the origin of the signal in a tissue is achieved by using a gradient of magnetic field B_0 in the x,y and z dimensions. As a result, the resonance frequency has a space dependency, which allows the localized excitation of spins from a volume of interest (VOI). Spins surrounding the VOI are either not excited or dephased. (Lei et al., 2014)

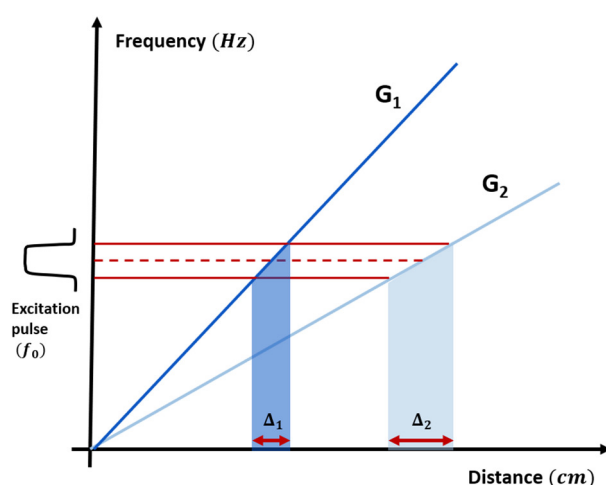


Figure 1. 9 : Principle of localization in MRS

The application of a RF pulse with a given bandwidth centered at frequency f_0 can select different slices along one axis by changing the gradient field strength from G_1 to G_2 . Similarly, changing the excitation frequency on a given gradient provides another mean to obtain spatial information. Following this scheme, the spatial resolution of localized MRS (Δ) depends on the strength of the magnetic field gradient G .

1.3.3 ^1H -MRS

^1H -MRS is generally the most commonly used MRS technique given the high signal provided by the proton (^1H) compared to other nuclei ($\gamma=42.6\text{MHz/T}$, natural abundance=99.98%). Water being the most abundant proton-containing molecule, this technique requires

suppressing the water signal to reveal all the other concentrated metabolites. ^1H -MRS in the brain can be used to detect up to 19 metabolites (depending on the magnetic field strength), which gives information on the neurochemical profile (Duarte et al., 2012; Mlynárik et al., 2008). Magnetic field strength is an important component for the quality and spectral resolution of the data, the number of metabolites quantifiable thus varies depending on the scanner. This number was shown to go up to 10 individual metabolites at 3 Tesla (Bednařík et al., 2015), 14 metabolites at 7 Tesla (Gambarota et al., 2009) and up to 19 in animal scanners at 9.4 and 14.1 Tesla (Mlynárik et al., 2012). For low magnetic field strength, detection of low concentration metabolites sometimes require some special edited sequences. Following table summarizes all the measurable metabolites visible in rodents and humans with average concentrations referred to as the neurochemical profile (Duarte et al., 2012).

Metabolite	Mouse	Rat	Human
Alanine (Ala)	0.9 – 1.2	0.4 – 0.6	0.3
Aspartate (Asp)	1.8 – 2.3	1.9 – 2.6	2.1 – 3.1
Phosphorylcholine (PCho)	0.5 – 0.6	0.4 – 0.5	-
Creatine (Cr)	3.9 – 4.5	2.7 – 3.8	3.2 – 5.8
Phosphocreatine (PCr)	3.6 – 4.3	3.8 – 5.2	2.2 – 4.5
γ -aminobutyric acid (GABA)	1.7 – 2.0	1.1 – 1.4	1.3 – 2.5
Glutamate (Glu)	10.3 – 11.2	10.3 – 12.9	8.9 – 12.8
Glutamine (Gln)	3.6 – 3.9	3.5 – 4.3	1.6 – 2.2
Glutathione (GSH)	1.2 – 1.4	0.7 – 1.2	1.1 – 1.4
Glycine (Gly)	0.9 – 1.5	0.6 – 0.9	1.2
Myo-inositol (Ins)	4.4 – 4.8	3.8 – 4.5	4.9 – 5.7
Lactate (Lac)	1.6 – 2.1	0.4 – 1.6	0.5 – 0.7
N-acetyl-aspartate (NAA)	8.7 – 9.7	8.6 – 10.5	11.0 – 13.5
Scyllo-inositol (scyllo)	<0.2	0.1 – 0.2	0.3 – 0.4
Taurine (Tau)	8.9 – 11.0	5.0 – 6.9	1.3 – 3.3
Ascorbate (Asc)	1.2 – 2.1	1.0 – 1.6	1.4
Glucose (Glc)	1.6 – 2.1	2.2 – 4.1	1.4 – 2.24
N-acetylaspartylglutamate (NAAG)	0.6 – 0.9	0.3 – 0.7	1.0–1.1
Glycerophosphorylcholine (GPC)	0.5 – 0.8	0.1 – 0.2	-
Phosphorylethanolamine (PE)	1.7 – 1.9	1.8 – 2.1	1.6 – 2.8
β -hydroxybutyrate (BHB)	-	0.5 – 1.3	-
GPC+PCho (CCC)	1.0 – 1.2	0.5 – 0.8	0.9 – 1.1

Figure 1. 10 : The neurochemical profile measurable with ^1H -MRS

List of visible metabolites in cortex of mouse, rat and human. Adapted from Duarte et al. (2012). Concentrations are given in mM.

The main advantage of ^1H -MRS resides in its high sensitivity and thus short time of acquisition, which is particularly relevant for clinical use or for study of very small volumes like rodent brains. Even though MRS has often been limited to research applications, it is gaining in importance as a clinical tool (Oz et al., 2014). ^1H -MRS however only provides information on the total pool of metabolites with no or little functional information. For instance, a reduction of a metabolite concentration cannot be easily explained. A decrease in biosynthesis or an increase in degradation can lead to the same observed drop. ^1H -MRS has thus mainly been used to identify potential biomarkers related to disease or treatment.

Several metabolites observed in ^1H -MRS are tightly linked to brain energetic function. Lactate and glucose are probably the most understandable and reliable markers as their concentration strongly depend on the energetic state of the tissue. The balance between glycolysis and OXPHOS directly influences the lactate accumulation or degradation. For instance, an accumulation of extracellular lactate can occur during a so-called Warburg effect, i.e. when a glycolysis exceeds the stoichiometric production of pyruvate for mitochondrial oxidation. For instance, lactate quantification with MRS has been widely used to study mitochondrial dysfunction (Cross et al., 1993; José da Rocha et al., 2008; Takahashi et al., 1999).

N-acetyl aspartate (NAA) is a high-concentrated metabolite present primarily in neurons. It has thus often been considered as a neuronal marker. Some studies suggest that NAA could also be a good mitochondrial marker as it is primarily synthesized by mitochondrial aspartate N-acetyl transferase (Ariyannur et al., 2008; Patel and Clark, 1979) proportionally to the OXPHOS status (Bates et al., 1996). Changes in NAA have thus been observed as reflecting mitochondrial impairment in studies of mitochondrial disorders (Bianchi et al., 2003; Lin et al., 2003; Takahashi et al., 1999) and brain trauma (Marmarou et al., 2005).

Glutathione (GSH) and ascorbate (Asc), also known as vitamin C, are the two main antioxidant molecules in the brain. Localization of GSH is generally considered to be more astrocytic, while ascorbate is more neuronal (Terpstra and Gruetter, 2004). Given their importance in dealing with ROS and the redox status, these two molecules are good markers of mitochondrial health. A drop of brain antioxidant content can thus be linked to mitochondrial dysfunction and excitotoxicity (Emir et al., 2011; Qiu et al., 2007).

Taurine and inositol are two osmolytes in the brain, which could potentially relate to mitochondrial function. Both taurine and inositol are increased in animal model of Huntington's disease, with known mitochondrial dysfunction (Browne and Beal, 2004). Taurine was found to have antioxidant and cytoprotective functions, which makes it an important parameter of mitochondrial health (Hemanth Kumar et al., 2012). Several lines of evidence indicated the importance of inositol in mitochondrial health. This idea mainly arises from the link between the altered levels of inositol metabolism in BPD and the mitochondrial dysfunction hypothesis (Deranieh and Greenberg, 2009; Stork and Renshaw, 2005; Toker and Agam, 2014; Toker et al., 2014).

Finally, creatine (Cr) and its phosphorylated analog phosphocreatine (PCr) play a key role in neuroenergetic function. ATP phosphorylates creatine via creatine kinase (CK) in the mitochondria producing PCr, which serves as a reservoir of ATP. The produced PCr is rapidly transferred out of the mitochondrial membranes in a process known as the PCr/Cr shuttle, allowing ATP to be released faster in the cytoplasm and reducing formation of ROS (Bessman and Carpenter, 1985; Wallimann et al., 2011). Changes in PCr/Cr ratio have been observed for instance in the striatum of the R6/2 and Q111 models of Huntington's disease, with known mitochondrial dysfunctions (Tkac et al., 2012; Zacharoff et al., 2012). It is however not straightforward to resolve the creatine and phosphocreatine peaks in an MRS spectrum, as their chemical shifts are very close (Cr: $\delta = 3.03\text{ppm}$, 3.93ppm / PCr: $\delta = 3.03\text{ppm}$, 3.91ppm). Reliability depends on the spectra quality and resolution to avoid quantification errors (Wermter et al., 2017). Typically, separation of these two peaks is generally not considered reliable in human studies, i.e. at $B_0 < 9.4\text{T}$ or when a difference between the two resonances at 3.9 ppm is not clearly visible in the spectrum.

1.3.4 ^{31}P -MRS

^{31}P -MRS is widely used due to the relatively high NMR sensitivity of phosphorous-31 atoms (^{31}P) ($\gamma=17.2\text{ MHz/T}$) and high natural abundance (100%). As cellular energy metabolism is processed through biochemical reactions involving phosphate groups, ^{31}P -MRS is the technique of choice for studying brain energy metabolism. Phosphocreatine, ATP, ADP, inorganic phosphate (P_i), but also NADH, NADPH and phosphomono- (PME) and phosphodiester (PDE) can be detected. PCr, ATP (α, β and γ) and P_i resonances can be

identified easily with good spectral resolution, while other phosphorus-containing metabolites often require high spectra quality, normally provided by strong magnetic fields or big volumes of interest (Arias-Mendoza and Brown, 2004; Lu et al., 2014). Another useful tool in ^{31}P -MRS is the measurement of the creatine kinase activity by magnetization transfer experiments (Befroy et al., 2012; Brindle et al., 1989; Ren et al., 2015). By measuring the exchange kinetics between ATP and P_i or PCr, this technique gives functional information regarding mitochondrial ATP production. Measurement of pH and Mg^{2+} concentration based on ^{31}P -MRS chemical shifts provides information about potential lactic acidosis (Pettegrew et al., 1988; Taylor et al., 1991). At high magnetic field, the ability to measure the NADH/NAD $^{+}$ ratio *in vivo* gives insight into the redox status and mitochondrial function (Lu et al., 2016a). ^{31}P -MRS has been extensively used to study cellular energetics in muscle (From and Ugurbil, 2011; Kemp and Brindle, 2012; Kemp et al., 2015; Layec et al., 2010) and has been used in many studies on mitochondrial dysfunctions/disorders as well (Boumezbeur et al., 2010a; Kasparová et al., 2005; Lodi et al., 1997).

1.3.5 ^{13}C -MRS

^{13}C -MRS is probably the most promising technique to investigate neuroenergetic function *in vivo* despite some technical challenges to overcome. Carbon-13 (^{13}C) is a difficult nucleus to study given its low gyromagnetic ratio ($\gamma=10.7$ MHz/T) and low natural abundance (1.1%). Upon infusion of a ^{13}C -labeled substrate, labeling of the different metabolic pools at specific positions of the molecular backbone allows to follow metabolism kinetically (Badar-Goffer et al., 1992; de Graaf et al., 2011; Lizarbe et al., 2018a). To overcome the low sensitivity of ^{13}C direct detection, the use of indirect ^{13}C MRS (^1H -[^{13}C]-MRS) is possible to take advantage of the higher proton signal by “sacrificing” spectral resolution. This method, typically referred to as proton-observed/carbon-edited (POCE) MRS uses an editing pulse in the ^{13}C -channel, in order to invert the signal of protons specifically bound to ^{13}C . By subtracting the inverted signal (with editing applied) to the total ^1H spectrum (without any editing applied), one can measure specifically the signal of metabolites bound to ^{13}C , providing a means of measuring ^{13}C “indirectly”. Another way to improve sensitivity works through hyperpolarizing the labeled substrate to make it more detectable (Bastiaansen et al., 2015; Park et al., 2013). Hyperpolarization methods however do not allow a reliable metabolic flux analysis as the parameters leading to fast and inhomogeneous depolarization of ^{13}C -labelled carbons are

hard to estimate. Different substrates have been used with different labeling positions like glucose (Sonny et al., 2017; Xin et al., 2015), lactate (Duarte et al., 2015) or acetate (Lanz et al., 2014a) providing information on different metabolic routes. Inevitably, labelling from these substrates will end up entering the TCA cycle and incorporate into glutamate and aspartate, which are in constant exchange with it through transaminase activity. As a result, ^{13}C -MRS has been proven to study the TCA cycle in a cell-specific way to reach comprehensive understanding of mitochondrial activity in the brain (Duarte and Gruetter, 2013; Sonny et al., 2016a).

Mathematical modelling of brain metabolism provides a mean to quantify metabolic fluxes associated with a ^{13}C -containing tracer. The labelled atom will enter the different metabolic pools and incorporate in the carbon backbone of molecules. The metabolic system can be described with mass balance equations, representing the concentration variation of a given substance P, and with labelling equations, reflecting the variation in labelling of that same substance P* (Fig 1.11). Typically, upon ^{13}C -MRS experiment, product labelling curves are measured and fitted with a mathematical model, which describes the metabolic pathways and distinguishes eventually the different cellular compartments involved.

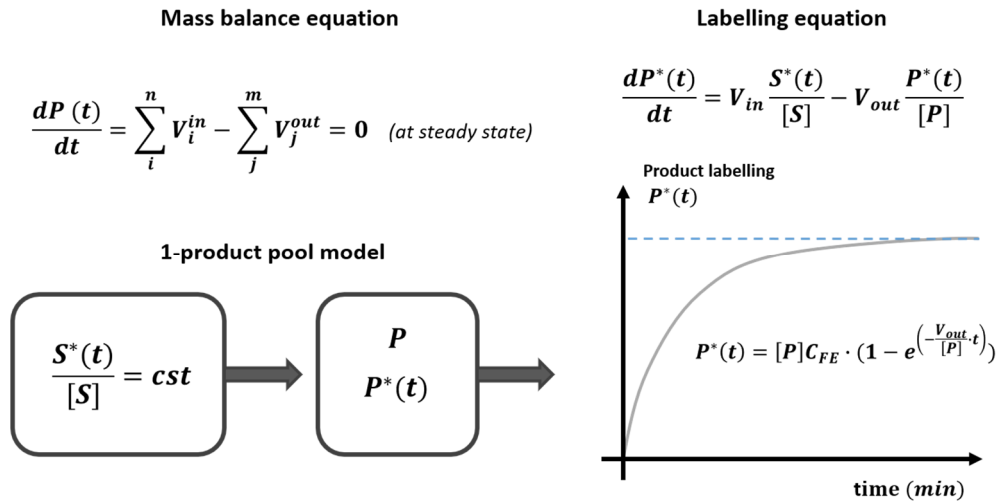


Figure 1. 11 : Metabolic flux analysis based on ^{13}C -MRS

^{13}C -MRS enables investigating brain metabolism through incorporation of labeled atom from a given substrate S into several products P. Mathematical modelling is based on the idea that the accumulation of a compound P is the difference between the amount produced (from an influx V_{in}) and the amount degraded/consumed (from an efflux V_{out}). Biological systems are generally considered to be at steady state, i.e. no net accumulation of P occurs and thus its variation over time is equal to 0. Considering a 1-product model with one labelled substrate S^* leading to the synthesis of one product P, the variation of labelling of P ($= dP^*(t)/dt$) can be described by the fractional enrichment of S ($= S^*(t)/[S]$) times the influx, minus the fractional enrichment of P ($= P^*(t)/[P]$) times the efflux (see "labelling equation"). This equation can be solved by assuming steady state ($V_{in} = V_{out}$) and assuming the

substrate fractional enrichment to be constant (see “product labelling”). This is typically the case when the substrate labelling represents a step function.

This fitting procedure can be performed using a Levenberg-Marquardt algorithm, where the free parameters of the regression are the metabolic fluxes. These flux estimations are optimized using a least-square regression method, minimizing the sum of squared differences between the experimental curves and the labelling curves representing the model. Test reliability of the fitted parameter is achieved by using a Monte-Carlo simulation analysis testing the reliability of the flux estimates. This numerical approach is based on the generation and fitting of artificial noisy data, typically repeated over a couple of hundreds of times, to create a distribution of the estimated parameter value.

1.3.6 Magnetic resonance spectroscopy (MRS) as a tool to study brain energy metabolism dysfunction associated with mood disorder

MRS has been extensively used for investigating pathophysiology of mood disorder. Due to its non-invasiveness and applicability in clinical settings, MRS has provided a large amount of *in vivo* data. However, the lack of consistencies in the results, due to the large variability of diseases and the difficulty of classification on a biological basis, have challenged the understanding of the pathophysiology and etiology of mood disorders.

Magnetic resonance imaging (MRI), generally acquired simultaneously to MRS, has provided volumetric information of patient’s brain. These studies have for instance revealed volumetric alterations of prefrontal and cingulate cortices (Bora et al., 2010; Konarski et al., 2008). The brain is an inhomogeneous organ, and specific regions are very likely to be affected differently. MRI provides thus a good way of precisely localizing the structures affected. As this technique does not give much metabolic information, spectroscopy has become a key player in investigating the underlying biological basis of mood disorders. The finding of altered neurotransmitter levels in prefrontal cortices of mood disorder patients has for instance led to a well-known theory of pathophysiology of mood disorders: the glutamatergic hypothesis published by Sanacora et al. (Sanacora et al., 2012). However, in the following paragraphs, we will mainly focus on the studies, which have pointed towards neuroenergetic dysfunctions.

¹H-MRS studies have revealed alterations in the metabolic profile of bipolar patients convincingly suggesting mitochondrial alterations (Stork and Renshaw, 2005). Dager et al.

(Dager et al., 2004) first reported an increase in lactate in grey matter of BPD patients, suggesting a glycolytic shift in the brain. This increase in lactate has also been observed in MDD and chronic fatigue syndrome (Bradley et al., 2016; Murrough et al., 2010). Other studies found altered choline containing compound (CCC) levels in anterior cingulate (Galińska-Skok et al., 2016). Lower levels of total creatine in DLPFC (Frey et al., 2007) have also been observed, however appears to be more a feature related to schizophrenia, which involves mitochondrial dysfunctions as well (Öngür et al., 2009). Changes in myo-inositol have also been reported related to the effect of lithium treatment (Davanzo et al., 2001).

³¹P-MRS provided an important amount of information on the energetic dysfunction of mood disorders and resulted in the first formulation by Kato et al. in the 90s of the “mitochondrial hypothesis” of mood disorders. Levels of PCr were found to be reduced in the frontal lobe of patients with BPD in the depressed state (Kato et al., 1991, 1992). This result seemed to be dependent on the mood state of the patient, where lower and higher levels were found in depressed and manic states respectively, as compared to the euthymic state (Kato et al., 1995). Increase in PCr was observed in the frontal lobe of unmedicated BPD adolescents compared to medicated and healthy controls (Shi et al., 2012). Other studies revealed a drop in intracellular pH (calculated from the difference in chemical shift of PCr and Pi) in BPD in line with the hypothesis of a glycolytic shift (Hamakawa et al., 2004; Kato et al., 1998). Membrane metabolism has been linked to mitochondria as synthesis and recycling is a high-energy consuming process (Purdon and Rapoport, 1998). Alteration of phospholipid metabolism has been observed, where a higher phosphodiester to monoester ratio was found in frontal lobe of BPD (Deicken et al., 1995). Changes in this ratio are generally thought to reflect difference in the cell membrane turnover, where phosphodiester (mainly glycerophosphorylcholine and glycerophosphorylethanolamine) are the degradation products and monoesters (mainly phosphocholine and phosphoethanolamine) are precursors of phospholipids. Results have also pointed towards a mood state-dependent change in this ratio (Kato et al., 1993). Lithium is a well-known inositol-monophosphatase (IMP) inhibitor leading to a drop of inositol and inositol-monophosphate accumulation (component of the PME signal in ³¹P-MRS) in the brain upon medication. This mechanism has been suggested as the link between inositol and PME changes in BPD (Stork and Renshaw, 2005). Fewer studies in MDD have been reported with as persuasive results as ³¹P-MRS in BPD patients. Nevertheless, reduced levels of ATP in the basal

ganglia (Moore et al., 1997) and altered PCr and P_i in the gray matter (Harper et al., 2017) of depressed patients have been observed.

¹³C-MRS studies have mainly been limited to animal models, where the mitochondrial metabolism has been investigated upon administration of treatments (Chowdhury et al., 2008, 2012) or upon chronic stress (Veeraiah et al., 2014). Most of the studies have however been limited to *ex vivo* ¹³C-NMR measurements. Abdallah et al. (Abdallah et al., 2014), have been able to perform ¹³C-MRS in patients *in vivo*, revealing a 26% reduced mitochondrial energy production in occipital cortex of depressed patients compared to healthy subjects.

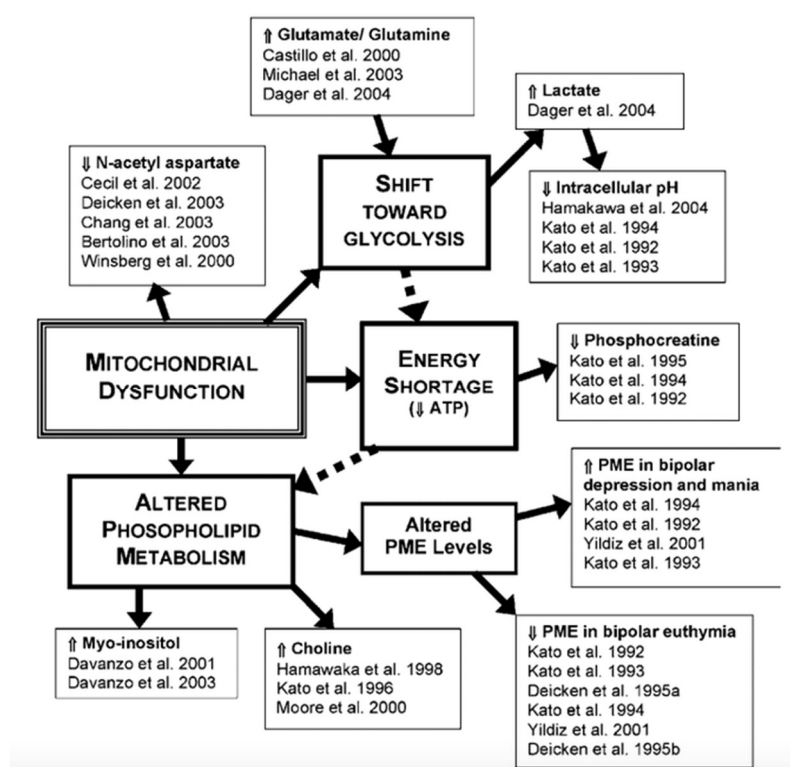


Figure 1. 12 : Summary of mitochondrial dysfunction in BPD from Stork & Renshaw (2005)

1.4 Aim of the thesis

Mood disorders are the leading cause of disability worldwide. This reflects the lack of understanding in the underlying pathophysiology and etiology of these complex and multifactorial diseases. Many patients are treatment resistant due to the difficulty in selecting a drug targeting an unknown biological function. Currently, the classification of mood disorders is based on subjective signs and symptoms rather than objective biological measurements. Furthermore, several (sometimes opposite) parameters are pooled into a common class of disorder. For instance, patients can be diagnosed with MDD when having opposite symptoms like showing psychomotor retardation or not, insomnia or hypersomnia, body weight loss or gain, etc. MRS can provide priceless *in vivo* information on brain metabolism and has been successfully applied to understand abnormalities in patients with mood disorders. However, the high discrepancies and inconsistent findings have challenged the use and clinical relevance of MRS for psychiatric disorders. The major problem certainly arises from the fact that MRS has repeatedly been applied in order to match the existing, rather vague, classification of mood disorders.

This thesis aimed at using another approach to investigate metabolic impairments associated with mood disorders. Instead of identifying the metabolic substrate associated with a given mood disorder category, we have investigated molecular and neurophysiological mechanisms, and their associated brain metabolic consequences visible with MRS, leading to impaired mood-related behavior in mice. We have focused on two animal models of mood disorder showing depressive-like behavior due to either a genetic or an environmental cause. The goal of this thesis was to identify potential MRS biomarkers and understand the associated molecular/pathophysiological mechanism from which they arise, in order to select a targeted treatment.

Chapter 2

Technical developments

Contributions to the work:

My contribution to this chapter consisted in the design of the study, acquisition of MRS data, metabolic flux analysis of metabolic data and statistical analysis. The result interpretation and manuscript writing have been realized by myself as well. All the PET measurements were performed by Dr. Carole Poitry-Yamate and analyzed by Dr. Bernard Lanz. The ^{13}C - ^1H coil design and construction were done in collaboration with Mr. Guillaume Donati and Mr. Yves Pilloud. Setting up the ^1H - ^{13}C -MRS acquisition protocol and associated calibrations was done with the help of Dr. Blanca Lizarbe and Dr. Hongxia Lei. The surgery for each *in vivo* ^1H - ^{13}C -MRS measurement was performed by the Vet-team.

This Chapter was partially adapted from:

Cherix A, Donati G, Lizarbe B, Lanz B, Poitry-Yamate C, Lei H and Gruetter R: Excitatory/inhibitory neuronal metabolic balance in mouse hippocampus upon infusion of [U- $^{13}\text{C}_6$]Glucose, JCBFM, *in revision*.

Abstract

This chapter describes the technical developments that have been made for an improved assessment of metabolic fluxes using *in vivo* indirect carbon-13 (^{13}C) magnetic resonance spectroscopy (^1H - ^{13}C]-MRS). This optimized ^{13}C -MRS protocol was subsequently applied in the study described in chapter 3. ^{13}C -MRS is a powerful technique for measuring metabolism kinetically and determine the directionality of chemical reactions. However, due to the low sensitivity of ^{13}C , *in vivo* acquisitions are challenging, and technical limitations undermine the measurement in small volumes. This is particularly problematic for the measurement of mouse brain and even worse for cerebral substructures such as the hippocampus. Here we propose an optimized protocol for simultaneously assessing excitatory and inhibitory neuronal metabolism in mouse hippocampus *in vivo* by applying ^{18}F FDG-PET and ^1H - ^{13}C]-MRS at 14.1T upon infusion of uniformly ^{13}C -labelled glucose ($[\text{U-}^{13}\text{C}_6]\text{Glc}$). Improving the spectral fitting by taking into account variable decoupling efficiencies of $[\text{U-}^{13}\text{C}_6]\text{Glc}$ and refining the compartmentalized model by including two γ -aminobutyric acid (GABA) pools, allowed us to evaluate the relative contributions of glutamatergic and GABAergic metabolism to total hippocampal neuroenergetics. Our results provide new strategies and tools for bringing forward the developments and applications of ^{13}C -MRS in specific brain regions of small animals.

2.1 Introduction

Mice are gold-standard models for studying brain metabolic dysfunctions associated with genetic or environmental factors. Several *in vivo* techniques based on magnetic resonance spectroscopy (MRS) and imaging (MRI) have proven to accurately quantify metabolism underlying brain function in mice (Lai et al., 2018a; Lizarbe et al., 2018b; Nabuurs et al., 2008). Carbon-13 MRS stands out as it allows a dynamic assessment of metabolic fluxes *in vivo* upon administration of a ^{13}C -labelled substrate (Duarte et al., 2011; Lanz et al., 2013). However, ^{13}C -MRS in mice remains a challenge due to the relative insensitivity of the technique particularly prejudiced by the small brain size of these animals (Lai et al., 2017).

Assessment of relative excitatory and inhibitory metabolic function has stirred up a great deal of interest in the field of psychiatric neurosciences (Krystal et al., 2002; Veeraiah et al., 2014). For instance, investigating inhibitory neuron metabolism is motivated by the idea that GABAergic neurons might use up to one third of glutamatergic neuron's signaling energy (Howarth et al., 2012). While several rodent studies have been able to distinguish glial and neuronal contributions from total metabolic activity (Lai et al., 2018b; Lanz et al., 2014a; Sonnay et al., 2018), only few studies have separated glutamatergic and GABAergic metabolism. GABAergic flux analysis has generally been limited to *ex vivo* experiments (Patel et al., 2005), qualitative *in vivo* assessment of [3- ^{13}C]-GABA formation upon ^{13}C -labelled substrate infusion (Deelchand et al., 2009; de Graaf et al., 2003; Pfeuffer et al., 1999). Quantitative assessment have generally been achieved after artificially increasing GABA levels (de Graaf et al., 2006; Manor et al., 1996) or upon infusion of several substrate (Tiwari et al., 2013).

Direct ^{13}C detection provides the best spectral resolution leading to good separation between metabolite resonances (Beckmann et al., 1991; Gruetter et al., 1994), but the low resulting signal-to-noise (SNR) makes GABA detection rather difficult. Indirect methods like ^1H -[^{13}C]-MRS provide better SNR but high level of overlap of GABA with neighboring resonances have challenged the assessment of GABA labelling as well (Rothman et al., 1985, 1992). MRS at ultra-high field can thus alleviate some of the technical limitations and increase spatial resolution together with signal quality (Mlynárik et al., 2008). Studies at 9.4, 11.7 or 14T have led to significant improvement in the detection of GABA resonances (Duarte and Gruetter, 2013; van Eijdsden et al., 2010; Yang et al., 2005). However, to date, experiments on mice using

^1H - ^{13}C -MRS upon ^{13}C -glucose infusion have given limited insight into the relative GABAergic contribution to brain metabolism (Lizarbe et al., 2018c, 2018b; Xin et al., 2015).

A thorough description of brain energetics requires the simultaneous analysis of blood parameters in the course of the experiment, which is particularly difficult given the small blood volume of mice. Ideally, blood sampling can be performed only at the beginning and end of the experiment, provided that the analyzed parameters remain stable over time. Previous ^1H - ^{13}C -MRS studies have bypassed blood analyses by using brain lactate as an input function, which was justified by the difficulty in reliably fitting brain glucose labelling (Lizarbe et al., 2018c, 2018b; Xin et al., 2015). Typically, these experiments are performed using 1-, 1,6- or U- (uniformly) ^{13}C -labelled glucose. Infusion of [1,6- ^{13}C]Glc provides twice as much signal as [1- ^{13}C]Glc, but both glucose lead to rather challenging glucose quantification in a ^1H - ^{13}C -MRS spectrum. While C1 (α and β) positions of glucose are almost undetectable with current excitation bandwidths, C2 overlaps strongly with GlxC2 resonances. [U- ^{13}C]Glc can potentially lead to an accurate fit given the several dependent resonances that can be fitted together. Nevertheless, ^1H - ^{13}C -MRS requires high ^{13}C -decoupling power, which cannot always provide a sufficient bandwidth for decoupling [U- ^{13}C]Glc resonances homogeneously, thus leading to inaccurate glucose fitting and quantification.

In this study, we have made significant improvements of the fitting approach for determining brain glucose input function and assessing GABA metabolism using ^1H - ^{13}C -MRS upon [U- $^{13}\text{C}_6$]Glc infusion. By combining ^{18}F FDG-PET and different ^{13}C modelling approaches, we provide a critical assessment of the feasibility of combined energetic and neurotransmission metabolic activity in mouse hippocampus. Our results provide a new understanding of relative metabolic contributions of excitatory and inhibitory neurons and a protocol for comparative animal studies in neuroscience research

2.2 Material and methods

2.2.1 Animals

All experiments were performed with the approval of the Cantonal Veterinary Authorities (Vaud, Switzerland). C57BL6/J mice were bred in house and weaned at the age of 21 days. Males from the same progeny were housed together in standard Plexiglass filter-top cages in

a controlled facility with temperature set at 23 ± 1 °C and humidity at 40%. Animals were housed in a normal 12h daylight cycle and had *ad libitum* access to water and standard rodent chow diet.

2.2.2 Surgery and animal preparation

Male mice (N=8) at the age of 6 weeks (18.1 ± 0.7 g) were fasted overnight (12h) and isolated in a new cage on the evening prior to the scan. Anesthesia was induced with isoflurane at 3% in a mixture of air/O₂ (1:1), after what animals were maintained in a range of 1-2% isoflurane for the surgery and the scan. Blood glucose concentration was measured using a Breeze-2 meter (Bayer AG, Leverkusen, Germany) before (6.9 ± 0.3 mM) and after (7.7 ± 1 mM) the surgery. The surgery consisted in placing a catheter in the femoral vein of the left leg for infusion of a 20% (v/v) [U-¹³C₆] glucose solution during the scan (Sigma Aldrich, St Louis, MO). The cannulated animals were placed after the surgery in a horizontal holder with the head fixed with help of a nose cone and two ear bars. During the scan, animals were monitored for body temperature (rectal probe and circulating water bath) and respiration (small animal monitor system: SA Instruments Inc., New York, NY, USA) to keep stable physiological parameters (temperature at 36.5 ± 0.4 °C and breathing rate between 70 – 100 rpm). After a first 5-min bolus of glucose (3.2 mL/kg of 99% enriched ¹³C glucose) the infusion was maintained at a constant rate (10 mL/kg/h of 70% enriched [U-¹³C₆]-glucose) over the whole infusion time (up to 4 hours). At the end of the experiment, blood glucose and lactate levels were quantified using a GM7 analyzer (Analox Instruments Ltd, Stourbridge, UK).

2.2.3 ¹H-[¹³C]-MRS of mouse hippocampus

Animals (N=8) were scanned in a horizontal 14.1T/26 cm Varian magnet (Agilent Inc., USA) with a homemade ¹H-¹³C surface coil. A set of fast-spin echo (FSE) images were acquired (TE_{eff}=40ms, TR= 2000ms, average=1, slices = 15, thickness = 0.6 mm, data matrix = 128x128, FOV = 20x20 mm²) for localizing the volume of interest (VOI). The VOI (2x5.5x1.5mm³) was placed to include both dorsal hippocampi after what field homogeneity was optimized using FAST(EST)MAP to reach a typical water linewidth of 20 ± 1 Hz in that voxel, based on the full width at half maximum (FWHM) (Gruetter and Tkáč, 2000). ¹H-[¹³C]-MRS spectra were acquired using the full intensity SPECIAL-BISEP sequence (TE=2.8ms, TR=4000ms, averages =

8) as previously described (Lizarbe et al., 2018b; Lizarbe et al., 2018c; Xin et al., 2009). SPECIAL-BISEP is a proton-observed/carbon-edited (POCE) sequence based on the addition of a carbon editing section (B1-insensitive spectral editing pulse; BISEP), typically used with adiabatic pulse, to a standard SPECIAL sequence used in localized ^1H -MRS. The editing pulse (180° in the C-channel) produces the inversion of the phase of the protons selectively bound to ^{13}C . Proton frequency offset of the inversion pulse was set at the resonance of glutamate C4 (2.34 ppm), while carbon frequency offset for the decoupling and inversion pulses were set at 45 ppm, to ensure a maximal coverage of glucose resonances. The powers of the respective pulses were previously calibrated with a phantom containing an aqueous solution of $[2\text{-}^{13}\text{C}]$ acetate (Sigma Aldrich, St. Louis, MO) in a voxel with similar properties (distance and size) as the *in vivo* hippocampus. These calibrations resulted in a bandwidth for the inversion pulse of 14 kHz (90 ppm at 14.1T) for the carbon channel. The bandwidth of the ^{13}C decoupling pulse was limited to 10 kHz (65 ppm at 14.1T) due to power restrictions. Decoupling consisted in a hyperbolic secant HS8 adiabatic full-passage (Tannüs and Garwood, 1996) together with a MLEV-4 cycle and five-step phase supercycle (Fujiwara et al., 1993) applied during the entire acquisition period (145 ms). The proton and inverted spectra (editing ON and OFF) were obtained using an interleaved acquisition and were subtracted in the post processing steps (Fig 2.1). Each proton spectrum was first subtracted with its associated edited counterpart to obtain the final edited spectrum containing only ^{13}C -bound ^1H resonances. The 16 averages of each block were then frequency corrected and summed for quantification with LCModel. Total proton spectra were quantified using a standard basis set including simulated mouse brain metabolite: glucose (Glc), lactate (Lac), alanine (Ala), creatine (Cr), phosphocreatine (PCr), ascorbate (Asc), glutathione (GSH), N-acetyl-aspartate (NAA), N-acetylaspartyl-glutamate (NAAG), myo-inositol (myo-Ins), scyllo-inositol (scyllo-Ins), Glutamate (Glu), glutamine (Gln), γ -aminobutyric acid (GABA), aspartate (Asp), taurine (Tau), glycerophosphorylcholine (GPC), choline (Cho), phosphocholine (PCho), phosphoethanolamine (PE), as well as macromolecules (mac) (Kunz et al., 2010). The basis set of the edited spectra was adapted for $[\text{U-}^{13}\text{C}_6]\text{Glc}$ infusion metabolism. Mainly this basis set included following resonances: LacC3, LacC2, AlaC2+C3 (Ala), GluC4, GluC3, GluC2, GlnC4, GlnC3, GlnC2, AspC3, AspC2, GABAC4, GABAC3, GABAC2 and phantom based spectra of glucose.

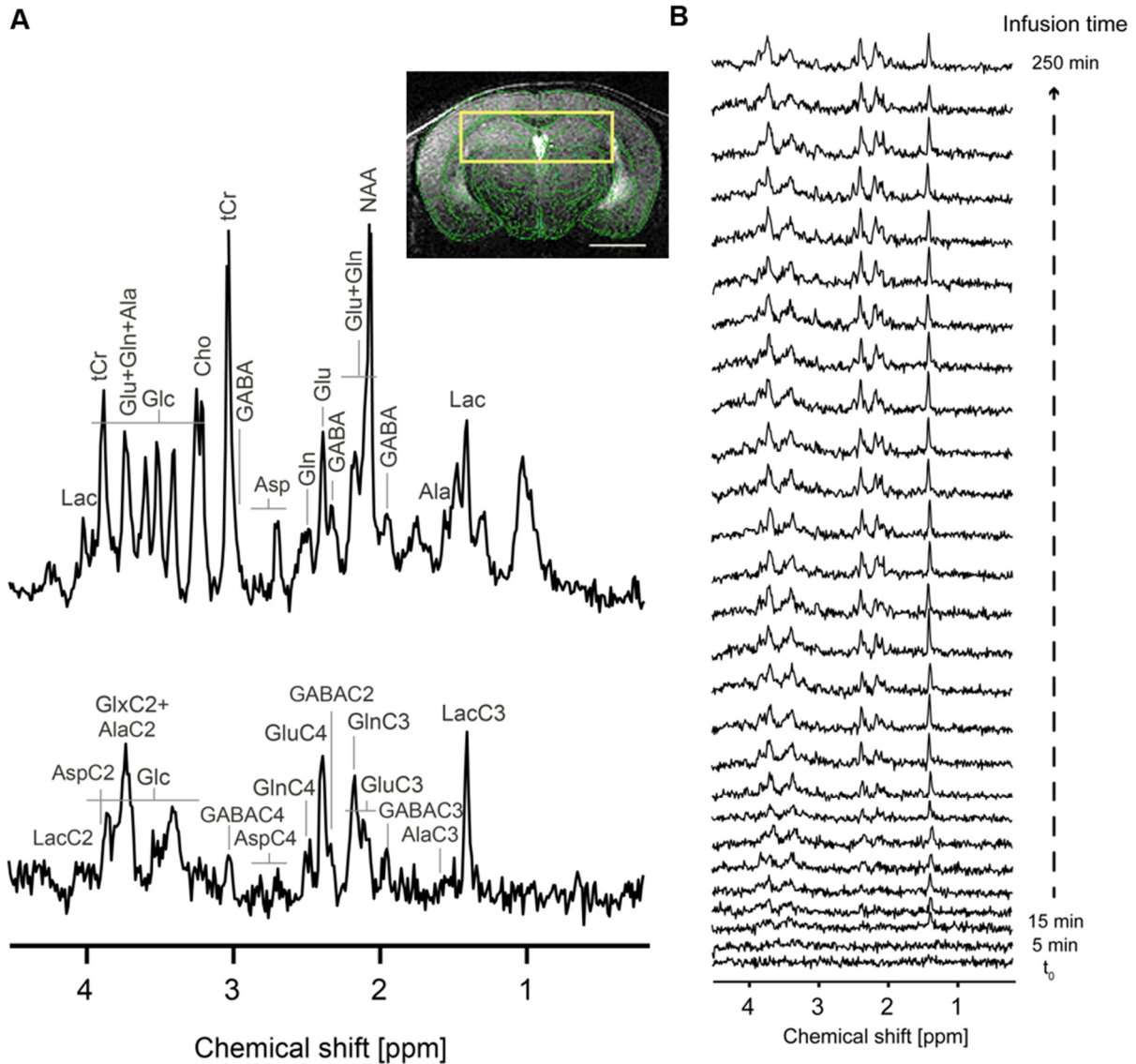


Figure 2. 1 : ^1H - ^{13}C -MRS in mouse dorsal hippocampus

A. Typical voxel position used for ^1H - ^{13}C -MRS with associated typical non-edited (top) and edited (bottom) spectra acquired after 3 hours of $[\text{U-}^{13}\text{C}_6]\text{glucose}$ infusion. Labelling of relevant metabolites are indicated: Lactate (Lac), glutamate (Glu), glutamine (Gln), alanine (Ala), γ -aminobutyric acid (GABA) and aspartate (Asp). In the edited spectrum, the carbon position number coupled with the observed proton resonance is indicated for each metabolite. **B.** Typical timeline of the edited spectra over the course of $[\text{U-}^{13}\text{C}_6]\text{glucose}$ infusion with a time resolution of 10min.

Glucose ^{13}C resonances are highly deshielded compared to the other resonances leading eventually to reduced decoupling efficiency during the acquisition. To overcome this problem, three different components were added in the edited basis set reflecting the resonances of the poorly decoupled glucose (Fig 2.3). These three component were acquired in an aqueous solution of $[\text{U-}^{13}\text{C}_6]\text{Glc}$ during full decoupling of resonances C2-6 (dec), full coupling (coup) and partial decoupling (part). The latter was set to the situation where glucose resonances are centered in the slope of the decoupling bandwidth (as depicted in Fig 2.2).

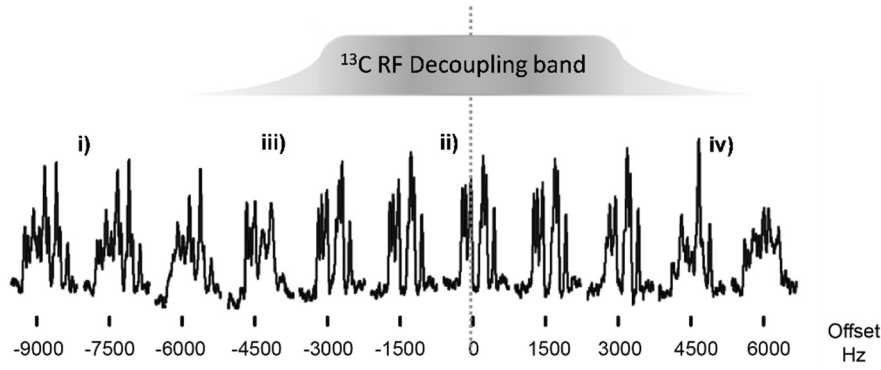


Figure 2. 2 : Glucose spectrum dependency on the decoupling efficiency

Example of $[U-^{13}C_6]$ glucose resonance dependence with decoupling efficiency in a 1H -MRS spectrum. The shape of glucose signal varies with the frequency offset of the 1H - ^{13}C decoupling pulse bandwidth. **i)** fully coupled glucose, **ii)** fully decoupled glucose, **iii)** partially decoupled glucose in the ascending slope of the decoupling pulse and **iv)** partially decoupled glucose in the descending slope of the decoupling pulse.

These three components provided a means to assess the relative efficiency of the decoupling *in vivo* calculated as follows: % Coupling = $(Glc_{coup}/\Sigma Glc_x) \cdot 1 + (Glc_{part}/\Sigma Glc_x) \cdot 0.5$; where $\Sigma Glc_x = Glc_{coup} + Glc_{part} + Glc_{dec}$, i.e. the sum of the individual spectra of glucose quantified with the modified basis set (See Fig 2.3B) Finally, the three glucose components were summed to determine the total amount of ^{13}C -labelled brain glucose. The non-edited spectra were quantified with LCModel (Provencher, 2001) using the water signal as internal reference assuming 80% brain water content. Fitting quality was assessed with the Cramér-Rao lower bounds errors (CRLB) (Cavassila et al., 2001) using a cut-off of 50%, over which quantification was assumed to be unreliable. Correlation of the different peak intensities were reported as given by the LCModel. Isotopic fractional enrichment (FE) was calculated for each metabolite by dividing the labelled atom signal over the metabolite concentration as described previously (Xin et al., 2010). Finally, the FE curves were multiplied by the metabolite concentration to obtain the metabolic ^{13}C -enrichment curves, which were then averaged for all the animals and used for the metabolic modelling.

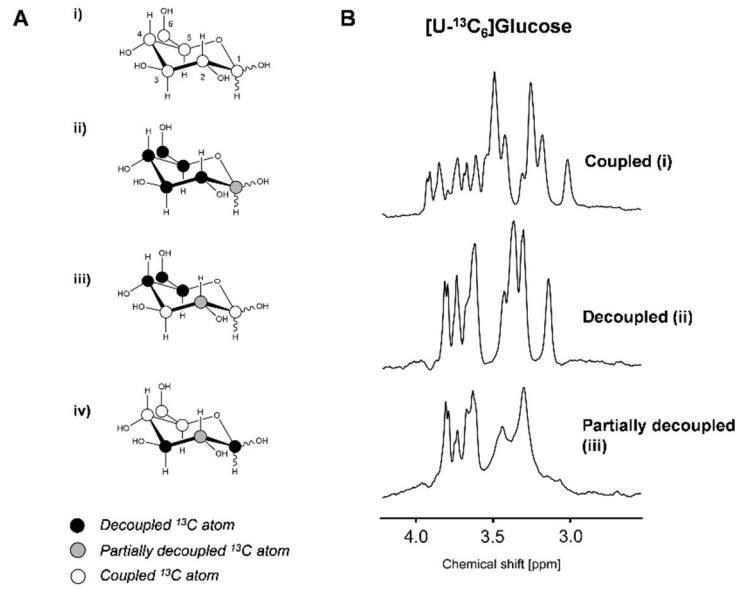


Figure 2. 3 : (^1H - ^{13}C)-Coupled glucose resonances

A. $[\text{U-}^{13}\text{C}_6]\text{glucose}$ carbon positions associated with the observed coupling in Fig 2.2. **B.** Glucose resonances used in the basis set to fit the edited spectra. **i)** fully coupled glucose, **ii)** fully decoupled glucose, **iii)** partially decoupled glucose in the ascending slope of the decoupling pulse and **iv)** partially decoupled glucose in the descending slope of the decoupling pulse.

2.2.4 Modelling of hippocampal metabolic fluxes

Hippocampal metabolism was investigated by comparing mainly two different models of brain energy metabolism considering cell-specific utilization of glucose. A simple one-compartment model was tested including GABA metabolism comparable to a previous study (Lizarbe et al., 2018c) and compared with a novel model referred to as pseudo 3-compartment model herein. ^{13}C enrichment curves were fitted to each model using MATLAB (Version 8.2, The MathWorks, Inc., Natick, MA) in order to estimate the metabolic fluxes. Fluxes were estimated using a standard built-in ordinary differential equation solver together with a modified Levenberg-Marquardt nonlinear weighted regression method. A weighting based on the relative CRLB of each ^{13}C metabolite resonance was used for each labelling curve in the regression cost function. Precision of the metabolic fluxes was determined with 300 Monte Carlo simulations of the curves providing a flux uncertainty (Lanz et al., 2013). The simple model was used to fit only Glc, LacC3, GluC4, GluC3, GlnC4, GlnC3, AspC3 and GABAC2 enrichment curves while the pseudo 3-compartment model used these resonances added to GluC2, GlnC2, GABAC3 and GABAC4. Because spectral resolution in ^1H - ^{13}C -MRS does not allow a reliable separation between GluC2 and GlnC2, only the sum (GlxC2) was used and assumed to have a relative

enrichment which is equal to that of the GluC3 and GlnC3. For instance, GluC2 was calculated as follows: $\text{GluC2} = \text{GluC3} \times (\text{GlxC2}/\text{GlxC3})$. This is only relevant because of the properties of uniformly labelled glucose, which does not produce differential labelling between C2 and C3 positions due to pyruvate carboxylase (PC) activity. Glucose fractional enrichment curve was used as an input function for both models and was fitted to an inverse exponential function $(a \cdot t + b) \cdot (1 - \exp(-c \cdot t))$. Fluxes determined from the simple model included the cerebral metabolic rate of glucose (CMR_g), a dilution flux from blood lactate ($V_{\text{dil}}^{\text{in}}$ and $V_{\text{dil}}^{\text{out}}$), the tricarboxylic acid cycle flux (V_{TCA}), transmittochondrial flux (V_x), neurotransmission rate (V_{NT}), a dilution flux from acetyl carriers like blood acetate or ketone bodies (V_{dil}^g) and a flux representing GABAergic metabolism (V_{GABA}).

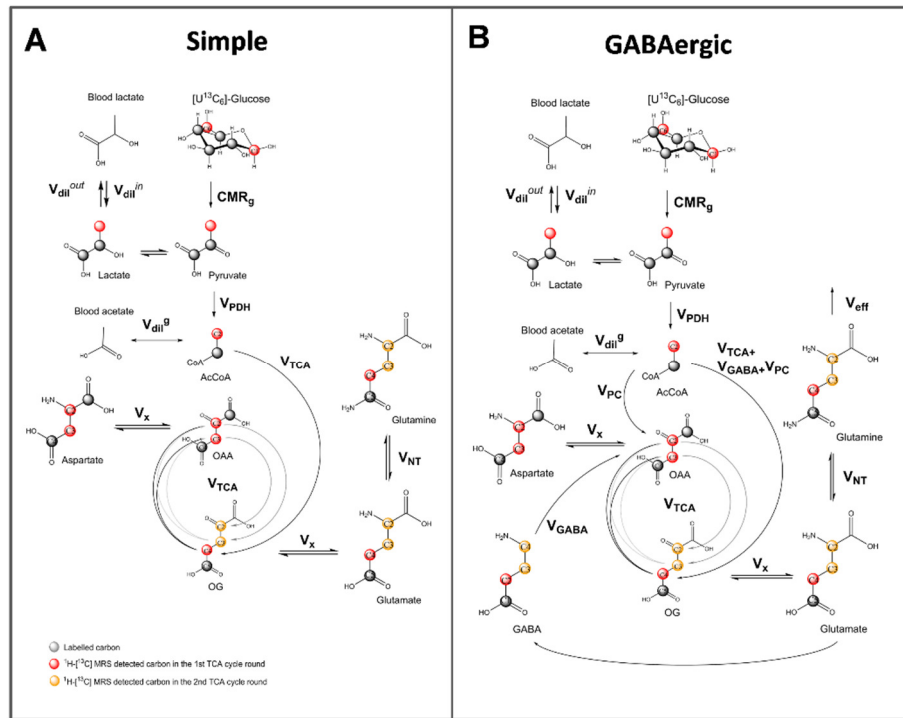


Figure 2. 4 : 1-compartment models of brain metabolism

A. Simple model used for the 1-compartment modelling including: the cerebral metabolic rate of glucose (CMR_g), pyruvate dehydrogenase activity (V_{PDH}), tricarboxylic acid cycle (V_{TCA}), a dilution flux from blood lactate ($V_{\text{dil}}^{\text{in}}$ and $V_{\text{dil}}^{\text{out}}$) and from blood acetate (V_{dil}^g), a transmittochondrial flux (V_x) and a neurotransmission flux (V_{NT}). **B.** GABAergic version of the 1-compartment model including the same fluxes as the simple version, but with addition of pyruvate carboxylase flux (V_{PC}), a Gln efflux (V_{eff}) and GABA flux (V_{GABA}).

The pseudo 3-compartment model was designed to resemble more the reality of brain cell-specific metabolism and particularly the differences between glutamatergic (excitatory) and GABAergic (inhibitory) neurons. This model was adapted from the 3-compartment model described in Duarte et al. in 2013 and simplified to match the limited amount of data available. Because uniformly-labelled glucose does not allow obtaining information about glial-specific

metabolism due to the absence of differential labelling produced by the PC, all glial fluxes were fixed to known values from the literature. Mainly, the pyruvate carboxylation flux (V_{PC}) was set to $0.04 \mu\text{mol/l/min}$ (Lai et al., 2018b; Lizarbe et al., 2018c), glial tricarboxylic acid cycle was set to $V_g = 0.16 \mu\text{mol/l/min}$ (Lai et al., 2018b) and V_x^g was set be equal to V_g . The other fluxes determined were CMR_g , V_{dil}^{in} , glutamatergic fluxes V_{PDH}^e , V_x^e , V_{NT}^e , GABAergic fluxes V_{PDH}^i , V_x^i , V_{NT}^i , glutamate decarboxylase activity (V_{GAD}), as well as two exchange fluxes V_{ex}^g and V_{ex}^i reflecting the presence of two Gln pools in glia as well as two GABA pools in inhibitory neurons respectively. The presence of a second glial pool in astrocytes was reported previously to provide a better mean to fit data in a 3-compartment model (Duarte and Gruetter, 2013). Here we propose a similar approach for GABAergic neurons that is closer to the biochemical reality underlying the function of the two GAD isoforms, one being more cytoplasmic (GAD67) and the other being neurotransmission-related (GAD65) (Martin and Rinvall, 1993). GAD activities are very heterogeneous and highly regulated, however, for simplification purpose, relative GABA pools were set to relative GAD concentrations in the mouse hippocampus, i.e. a 1:1 relation for both isoforms (Sheikh et al., 1999). More details of the equations describing the mathematical models used are given in the Appendix (2.5) of this chapter.

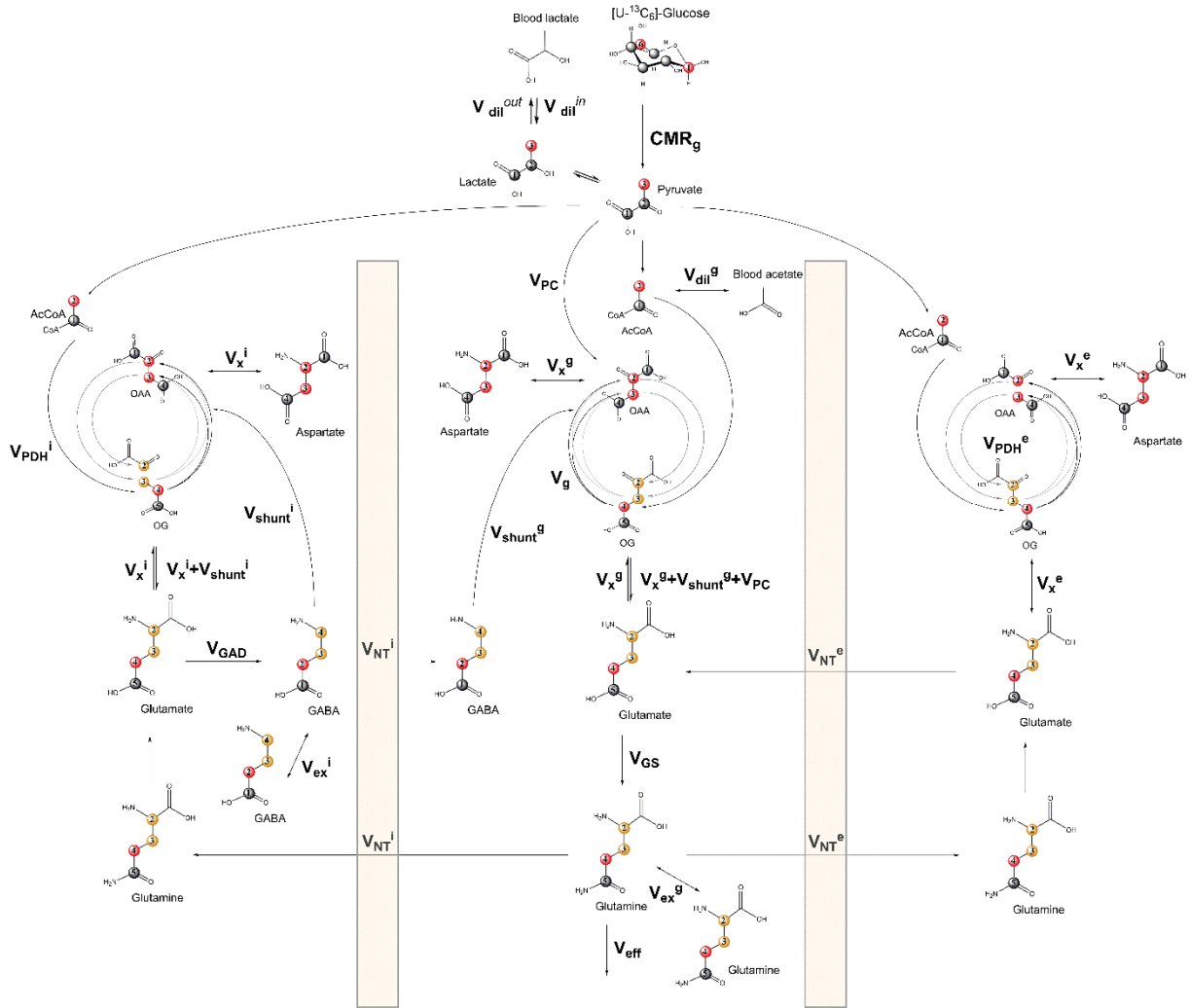


Figure 2.5 : Pseudo 3-compartment model of brain glucose metabolism

Pseudo 3-compartment model used to fit the ^{13}C enrichment curves. Fluxes are separated into glutamatergic (g), GABAergic (i) and glial (e) compartments. Cerebral metabolic rate of glucose (CMR_g), pyruvate dehydrogenase activity (V_{PDH}), glial tricarboxylic acid cycle (V_g), a dilution flux from blood lactate ($V_{\text{dil}}^{\text{in}}$ and $V_{\text{dil}}^{\text{out}}$) and from blood acetate (V_{dil}^g), a transmittochondrial flux (V_x), a neurotransmission flux (V_{NT}), pyruvate carboxylase flux (V_{PC}), a Gln efflux (V_{eff}), glutamine synthetase activity (V_{GS}), glutamate decarboxylase activity (V_{GAD}), GABA TCA shunt (V_{shunt}) and two exchange fluxes between two Gln of two GABA pools (V_{ex}). Gray atoms: labelled carbon; Red atoms: labelled carbons in the 1st TCA cycle round; Orange atoms: labelled carbons in the 2nd TCA cycle round.

2.2.5 Blood FE measurements

The animal blood values of enrichment in glucose, lactate and acetate were measured in a subgroup of 3 animals that underwent surgery and $[\text{U-}^{13}\text{C}_6]\text{Glc}$ infusion without any scan. Retro-orbital blood collection was performed at three different time points (20, 60 and 180 min after glucose infusion start) with lithium/heparin Microvette collection tube (Sarstedt AG, Nümbrecht, Germany). Blood was then centrifuged for 2 minutes at room temperature (6'000 rpm) to extract the plasma that was then frozen on liquid nitrogen. Blood metabolites were subsequently extracted using a chloroform/methanol extraction protocol followed by

lyophilization (Folch et al., 1957). Metabolites were then resuspended in deuterium oxide containing 0.1 mM DSS (4,4-dimethyl-4-silapentane-1-sulfonic acid) as internal reference. High resolution ^1H -NMR (HR-NMR) was performed on the samples with a DRX-600 spectrometer (Bruker BioSpin, Fällanden, Switzerland) using a pulse acquired ^1H sequence (flip angle= 30° , pulse delay= 5s, acquisition time= 2.7s, number of acquisitions= 160). Fractional enrichment was calculated based on the resonances of β -glucose H6, lactate H3 and acetate H3, which split in the presence of a ^{13}C atom on which they are bound. The coupled resonances were identified based on the coupling constant (Glucose $J_{\text{C-H}}(\beta\text{-H1})$: 169Hz, Lactate $J_{\text{C-H}}(\text{H3})$: 131Hz, Acetate $J_{\text{C-H}}(\text{H3})$: 130Hz), the sum of coupled (^1H - ^{13}C) and uncoupled (^1H - ^{12}C) resonances were integrated, normalized and calculated into the corresponding FE.

2.2.6 ^{18}F FDG-PET

Quantitative, *in vivo*, measurement of cerebral glucose uptake in mice was performed with positron emission tomography (PET) as previously described in detail (Lanz et al., 2014b). Briefly, catheter insertion of the tail vein was performed under isoflurane anesthesia, allowing for substrate administration, and blood sampling to establish initial and final glycemia. Mice were prone positioned on the scanner bed to accommodate continued delivery of isoflurane via a nose mask, and positioned with the field of view centered on the thoracic region, allowing the inferior vena cava and brain to be imaged simultaneously. List mode acquisitions (see below) were acquired and initiated with i.v. injection of ^{18}F -fluorodeoxyglucose (^{18}F FDG) (~50 MBq) through the tail vein catheter within the first 10 s of the PET scan, followed by 50–200 μL of saline chase solution. Imaging was performed using an avalanche photodiode, dedicated small animal micro-PET scanner (LabPET4; Gamma Medica, Sherbrook, Canada). During the entire 50 min scanning period, mice were maintained under 1% (vol/vol) isoflurane anesthesia in oxygen using a face mask with constant monitoring of temperature and breathing rate. For image reconstruction, list mode data were sorted for the determination of the (1) standardized uptake value (SUV), defined as (mean ROI activity [kBq/cm^3])/(injected dose [kBq]/body weight [g]); and (2) CMR_g . In the first case, list mode data were sorted into 1 min time frames, of which the last 20 minutes of the 50 min scan were used to estimate intracellular ^{18}F FDG-6-phosphate accumulation at steady-state. In the second case, to properly characterize the input function, list mode data of the vena cava and brain was sorted into the following number of frames (F) and frame duration (s) : 24F, 5s ; 6F, 30s ; 5F, 2min ; 7F, 5min.

Post-processing of images were performed using PMOD 2.95 software (PMOD Technologies Ltd). For the determination of SUV, regions of interest, e.g. hippocampus were manually drawn over 3 successive axial slices. Mathematical modeling of hippocampal glucose metabolism was performed as previously described (Lanz et al., 2014b) using the activity density (Bq/cm^3) corrected for the decay at the initial scan time. Briefly, glucose kinetic parameters were obtained from a Sokoloff model description of FDG metabolism with 4 parameters pools using the activity measured in the vena cava as the input function and the tissue activity from the hippocampus (including 3% partial blood volume). The blood glucose concentration (C_p) was the value obtained from the tail vein at the end of the PET experiment and the lumped constant (LC) was fixed to 0.6. The adjusted metabolic parameters were: the transport constants between blood and hippocampus (k_1 and k_2), phosphorylation constants (k_3 and k_4) and CMR_g (calculated as $(C_p/\text{LC}) \cdot k_1 \cdot k_3 / (k_2 + k_3)$).

2.2.7 Statistical analysis

All values are given as mean \pm SEM unless stated otherwise. All statistical tests were performed using GraphPad Prism (GraphPad software, San Diego, CA, USA) using an alpha factor of $p < 0.05$.

2.3 Results

2.3.1 ^1H - ^{13}C -MRS of mouse dorsal hippocampus at 14 Tesla

Blood glucose concentration was 7.7 ± 1.2 mM before the scan and 20.8 ± 1.4 after the glucose infusion. Blood lactate level post-infusion was also measured and was 7.9 ± 0.9 mM. During the 230 min scanning time, respiration rate was maintained at 78 ± 5 bpm and body temperature at 36.2 ± 0.3 °C. Spectra were acquired in block of 16×8 averages (128 scans) leading to a time resolution of 10 min (9min 48s) for every metabolite. The signal-to-noise ratio (SNR) of the non-edited spectra was 21 ± 1 , while for the edited spectra it was 6.2 ± 0.5 over the whole infusion time course (5 ± 2 in the first half of the protocol, 8 ± 1 in the second). The linewidth of the non-edited spectra was 17 ± 2 Hz as calculated by the LCModel. Hippocampal lactate levels were also relatively stable (2.5 ± 0.4 mM) with an increase of only 0.2 mM from the initial value at the end of the infusion. Other concentrations obtained from

non-edited spectra and used for the modelling were Glu: 6.4 ± 0.3 mM, Gln: 2.6 ± 0.2 mM, Asp: 1.0 ± 0.1 mM, and GABA: 1.7 ± 0.2 mM.

2.3.2 Spectral fitting

The inclusion of glucose spectral patterns with three different decoupled efficiencies in the basis set (Fig 2.3) improved the quantification of glucose and GABAC4, i.e. with reduced average CRLB of Glc = $3.4 \pm 0.7\%$ (from $5.1 \pm 3.7\%$) and GABAC4 = $18 \pm 4\%$ (from $110 \pm 318\%$). Average CRLBs for the other resonances were largely not affected, i.e.: LacC3 = $5 \pm 1\%$, GluC4 = $3.1 \pm 0.4\%$, GluC3 = $6.8 \pm 1.5\%$, GluC2+GlnC2 = $20 \pm 11\%$, GlnC4 = $8 \pm 1\%$, GlnC3 = $12 \pm 2\%$, AspC3 = $28 \pm 6\%$, GABAC2 = $26 \pm 7\%$ and GABAC3 = $21 \pm 5\%$. The correlation matrix resulting from the different resonance fitting by LCModel indicated that GluC3 and GlnC3 were relatively less correlated than usual ($R = -0.73$), while GluC2 and GlnC2 were highly dependent ($R = -0.85$) (Fig 2.6). As a result, the two GluC3 and GlnC3 resonances were used separately in the modelling while their respective C2 counterparts were kept as a sum (GlxC2).

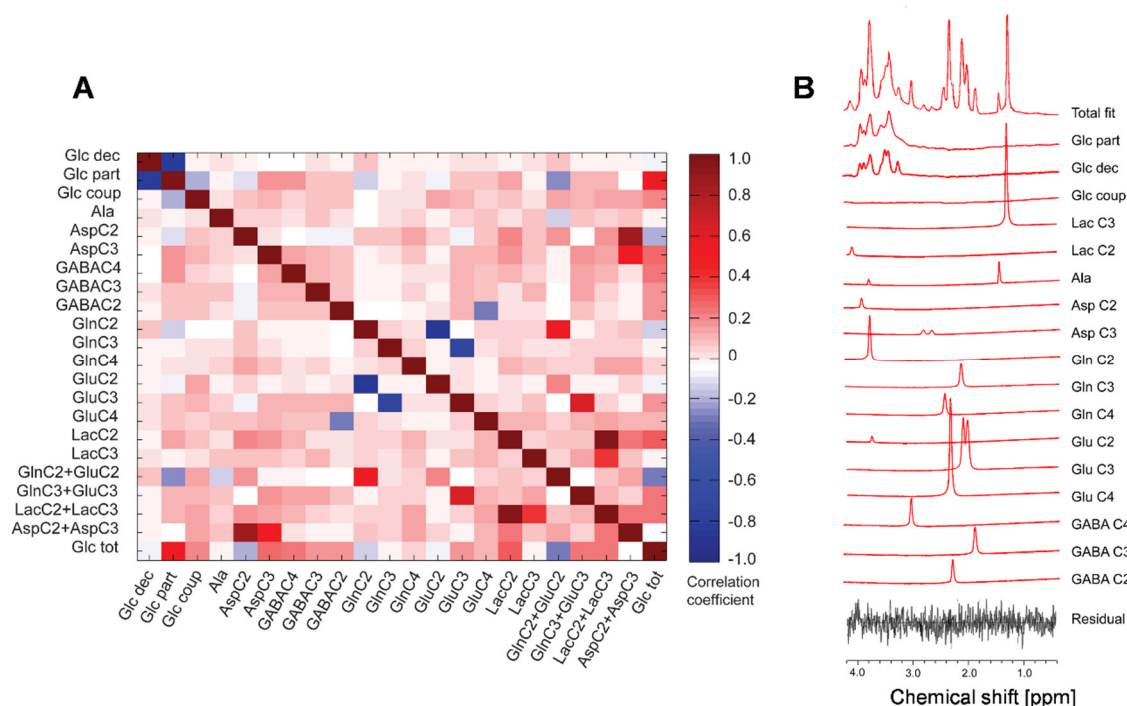


Figure 2. 6 : Fitting improvements with a basis set corrected for glucose ^1H - ^{13}C coupling

A. Example of edited spectrum fitting with LCModel using a basis set corrected for glucose coupling. **B.** correlation coefficients between the different fitted components of the basis set after LCModel analysis in edited spectra.

Addition of the coupled and decoupled spectra of glucose into the basis set revealed that decoupling efficiency was not homogeneous throughout the infusion protocol (Fig 2.7A). The

use of this basis set corrected for glucose improved significantly the fitting of GABAC4 while it didn't affect significantly GlxC2 (Fig 2.7B). The relative improvement in the fitting (%CRLB difference) correlated with the percentage of coupling in the spectra for Glc and GABAC4 but not for GlxC2 (Fig 2.7C).

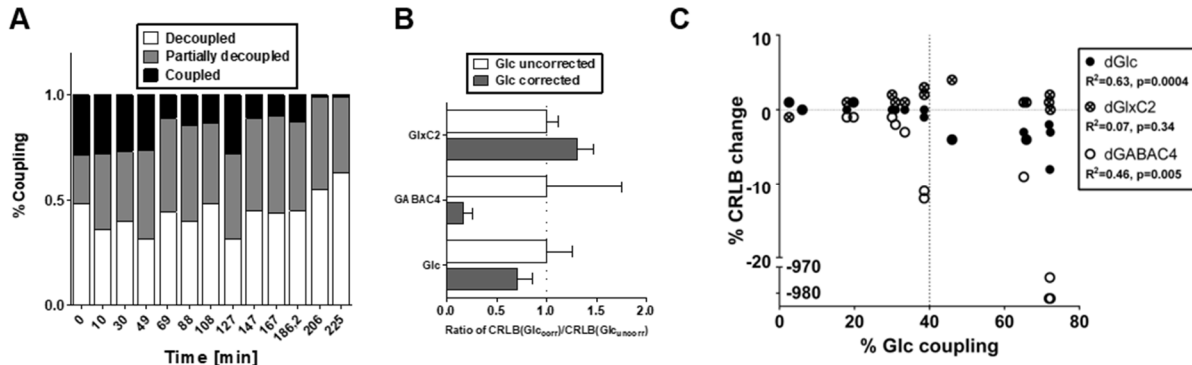


Figure 2. 7 : Quantification improvements with a basis set corrected for glucose ^1H - ^{13}C coupling

A. Averaged decoupling efficiency during ^1H - ^{13}C -MRS experiment estimated from spectra fitting. **B.** Relative Cramer-Rao Lower Band (CRLB) value using an uncorrected or corrected basis set for glucose decoupling. **C.** Relation between CRLB improvement and the estimated decoupling efficiency.

2.3.3 Quantification of metabolic labelling

The resulting fractional enrichments (FE) obtained from the *in vivo* data showed a satisfactory pattern, with Glc being a near step function reaching a plateau at 0.64 ± 0.03 (Fig 2.8A). The FE obtained for blood Glc, Lac and acetate indicate that the plateau of blood Lac FE (~ 0.5) was lower than brain Lac FE (0.60 ± 0.01) with a slower labelling slope (Fig 2.8B). GluC4 and GlnC4 ^{13}C concentrations reached a plateau after 150 min at 3.36 ± 0.07 mM and 1.20 ± 0.04 mM respectively. GluC3, GlnC3 and GlxC2 reached a steady state around 180 min at concentrations of 3.53 ± 0.04 mM, 1.29 ± 0.03 mM and 4.18 ± 0.17 mM respectively. Surprisingly, all the GABA labelling curves showed a rapid labelling pattern reaching a stable concentration around 150 min for GABAC2 and 180 min for GABAC3 and 4. The labelling concentration at steady state were 0.63 ± 0.03 mM for GABAC2, 0.66 ± 0.02 mM for GABAC3 and 0.58 ± 0.03 mM for GABAC4 and not statistically significant from each other. Finally, AspC3 showed the highest variability in the labelling but reached a plateau around 150 min at 0.57 ± 0.13 mM.

The accumulation curves of ^{18}F FDG during the PET experiments (Fig 2.8C) were reproducible and modeling of glycolytic flux led to a cerebral metabolic rate of $\text{CMR}_g = 0.61 \pm 0.02$

$\mu\text{mol/g/min}$. The other ^{18}F FDG rate constants obtained were as follows: $k_1 = 0.39 \pm 0.08 \text{ min}^{-1}$, $k_2 = 0.57 \pm 0.11 \text{ min}^{-1}$, $k_3 = 0.06 \pm 0.02 \text{ min}^{-1}$, $k_4 = 0.04 \pm 0.02 \text{ min}^{-1}$.

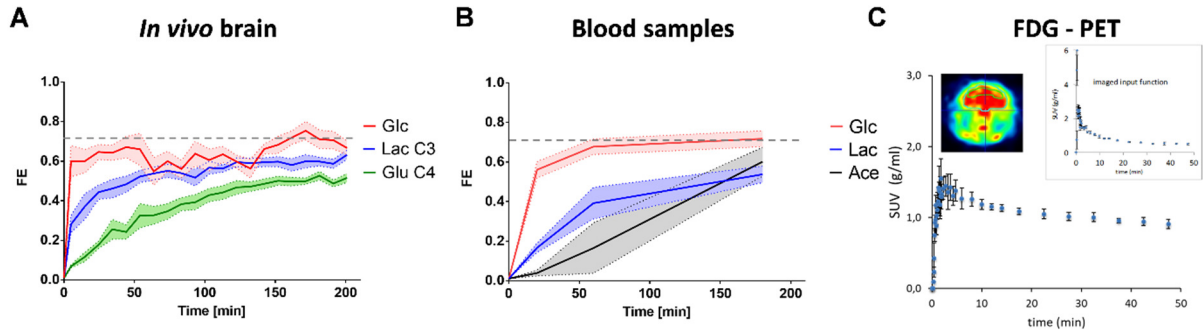


Figure 2. 8 : Glucose kinetics in brain and plasma

A. Averaged fractional enrichment (FE) of brain glucose, lactate C3 and glutamate C4 during the *in vivo* MRS experiment. **B.** Blood plasma FE measured during $[\text{U-}^{13}\text{C}_6]\text{glucose}$ infusion (N=3). **C.** Glucose standard uptake value in hippocampus and cava vein input function (upper right) measured by ^{18}F FDG-PET (N=3).

2.3.4 Mathematical modelling of hippocampal metabolism

2.3.4.1 1-compartment model

Several variants of 1-compartment models were tested (Fig 2.4). The simplest version ("simple") of the 1-compartment model was achieved using only the LacC3, GluC4, GluC3, GlnC4, GlnC3 and AspC3 labelling. This model generated a good fit of the data (Fig 2.10), however correlations were relatively high for several fluxes ($R > 0.7$) indicating low precision in the flux estimation (Fig 2.9). Nevertheless, fluxes values were in good agreement with the literature (Table 2.1) with a TCA cycle of $V_{\text{TCA}} = 1.03 \pm 0.23 \mu\text{mol/g/min}$, lactate dilution flux $V_{\text{dil}}^{\text{in}} = 0.50 \pm 0.30 \mu\text{mol/g/min}$, a transimitchondrial flux of $V_{\text{x}} = 0.14 \pm 0.01 \mu\text{mol/g/min}$, neurotransmission rate $V_{\text{NT}} = 0.066 \pm 0.001 \mu\text{mol/g/min}$ and a glial dilution flux $V_{\text{dil}}^{\text{gl}} = 0.001 \pm 0.12 \mu\text{mol/g/min}$. The glycolytic rate CMR_{g} was found to be $0.35 \pm 0.05 \mu\text{mol/g/min}$, which is significantly lower than the value measured by PET, i.e. $0.61 \pm 0.02 \mu\text{mol/g/min}$.

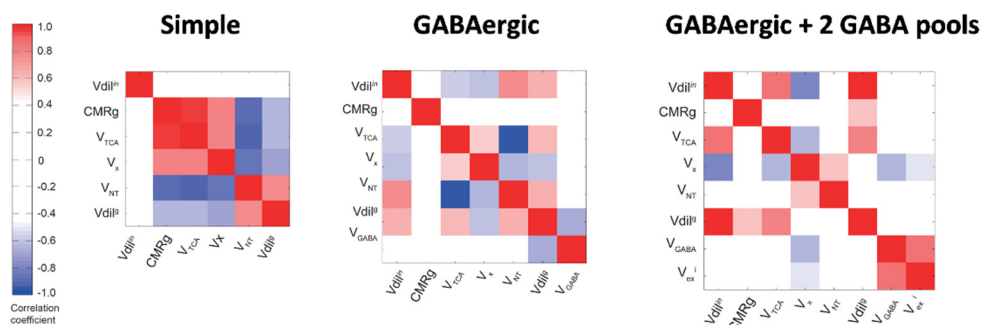


Figure 2. 9 : 1-compartment metabolic fluxes correlations

Correlation matrices obtained from the metabolic flux analysis using a simple or GABAergic model. The correlations obtained by adding an extra GABA pool to the GABAergic model is also shown.

A more complex model was used to consider GABAergic metabolism in the hippocampus. This model has been adapted from (Lizarbe et al., 2018c) in order to take into account the fluxes upstream of lactate. As this model requires the addition of a pyruvate carboxylase flux V_{PC} , which cannot be determined using uniformly labelled glucose, we fixed this flux to 0.04 $\mu\text{mol/g/min}$ as reported previously in the literature for mouse brain (Lai et al., 2018b; Lizarbe et al., 2018c). The addition of GABAC2 turnover curves led to significantly lower correlations between fluxes (Fig 2.9). However, this model failed to fit the GABAC2 data indicating that the obtained flux estimates are not representative of the *in vivo* measurements (Fig 2.10).

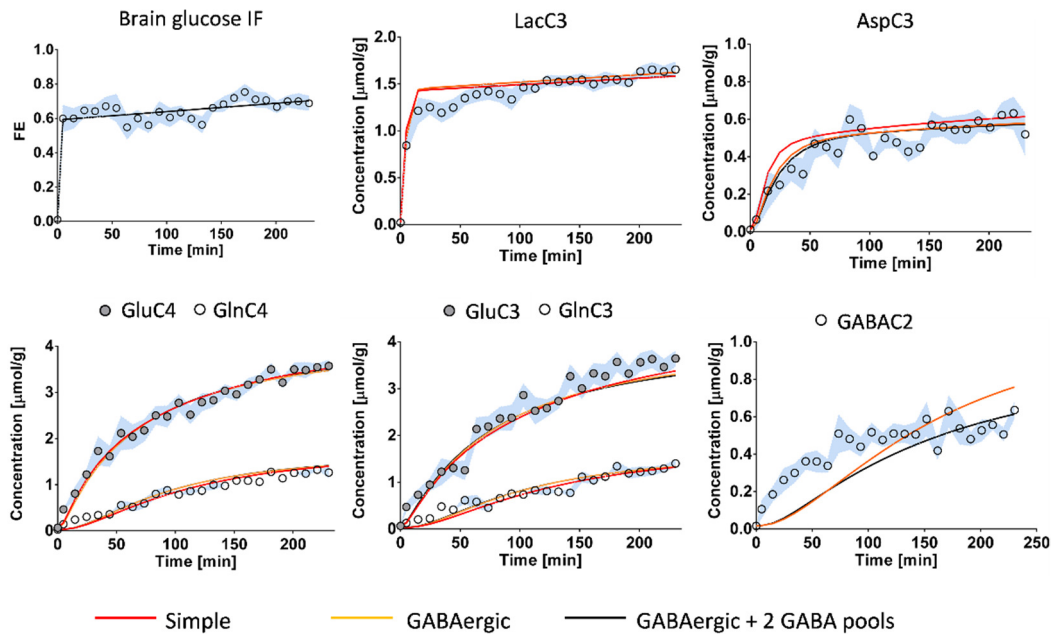


Figure 2. 10 : Fitting comparison between the different 1-compartment models

Fitting results of the 3 different 1-compartment models used. Simple model (red), GABAergic model (orange) and 2-GABA pool GABAergic model (black). ^{13}C enrichment data is shown as the mean for all animals \pm SD.

The addition of a second GABAergic pool was considered with only slight improvement in the fitting. Finally, fixing CMR_g to 0.35 $\mu\text{mol/g/min}$ increased precision in the estimates but did not improve the fitting of the GABA. Altogether, these results suggest, that a “simple GABAergic” model is not representative of the biological reality measured in the dorsal hippocampus of mice, which requires a more complete model to model excitatory/inhibitory balance.

1-compartment model							
Current study Mouse / isoflurane					Lizarbe et al. 2018 Mouse / isoflurane	Xin et al. 2015 Mouse / isoflurane	Lai et al. 2017 Mouse / isoflurane
R^2	0.966	0.982	0.976	0.979	$^1\text{H}[^{13}\text{C}]\text{MRS}/$ $1,6[^{13}\text{C}_2]\text{Glc}$	$^1\text{H}[^{13}\text{C}]\text{MRS}/$ [U- $^{13}\text{C}_6]\text{Glc}$	$^{13}\text{CMRS}/$ [1,6- $^{13}\text{C}_2]\text{Glc}$
GABA pools	0	1	2	2	1	0	0
VPC fixed	0	+	+	+	-	0	-
CMRg fixed	-	-	-	+	Lactate IF	Lactate IF	+
$V_{\text{dil}}^{\text{in}}$	0.50±0.30	0.35±0.16	0.50±0.26	0.80±0.37	-	-	-
CMR _g	0.35±0.05	0.31±0.04	0.32±0.06	0.35	-	-	0.4
V_{TCA}	1.03±0.23	0.93±0.13	1.06±0.22	1.31±0.24	0.83±0.05	1.05±0.04	0.16±0.03 (V_g) + 0.56±0.03 ($V_{\text{TCA}}^{\text{gl}}$)
V_x	0.14±0.01	0.07±0.01	0.05±0.01	0.05±0.01	0.68±0.21	0.48±0.02	0.18±0.02
V_{NT}	0.066±0.001	0.04±0.01	0.04±0.01	0.04±0.01	0.41±0.07	0.20±0.02	0.084±0.008
$V_{\text{dil}}^{\text{g}}$	0.001±0.12	0.002±0.03	0.09±0.36	0.02±0.16	0.06±0.01	-	0.23±0.05
V_{GABA}	-	0.018±0.002	0.0001±0.011	0.021±0.006	0.13±0.01	-	-
V_{PC}	-	0.04	0.04	0.04	0.04±0.01	-	0.041±0.003
V_{ex}^{i}	-	-	0.008±0.002	0.005±0.002	-	-	-

Table 2. 1 : Comparison between flux estimation with different 1-compartment models and relevant literature

Cerebral metabolic rate of glucose (CMR_g), pyruvate dehydrogenase activity (V_{PDH}), tricarboxylic acid cycle (V_{TCA}), a dilution flux from blood lactate ($V_{\text{dil}}^{\text{in}}$ and $V_{\text{dil}}^{\text{out}}$) and from blood acetate ($V_{\text{dil}}^{\text{g}}$), a transmemitochondrial flux (V_x) and a neurotransmission flux (V_{NT}). (B) GABAergic version of the 1-compartment model including the same fluxes as the simple version, but with addition of pyruvate carboxylase flux (V_{PC}), and GABA flux (V_{GABA}). Superscripts represents excitatory (^e), inhibitory (ⁱ) and glial (^g) compartments.

2.3.4.2 Pseudo 3-compartment model

With the goal of defining a model that would fit the measurements, we investigated the feasibility of a 3-compartment model including excitatory and inhibitory neuron, but also glial, metabolism (Fig 2.5). As this model leads to more parameters to include, additional considerations had to be made. First, GlxC2 was added in the fitting process and separated into GlnC2 and GluC2 assuming a similar ratio as for GlxC3 (see methods for more details). GABAC3 and GABAC4 were included as well. Because [U- $^{13}\text{C}_6$]Glc does not allow to assess reliably glial metabolism, all the glial parameters were fixed with known values from the literature. Mainly, V_{PC} was fixed at 0.04 $\mu\text{mol/g/min}$, glial TCA cycle V_g was fixed at 0.25 $\mu\text{mol/g/min}$ and glial transmemitochondrial flux was set equal to V_g . The effect of constraining these values on the other estimated parameters was tested and a $\pm 100\%$ difference in the fixed parameter led to only $\pm 25\%$ difference in flux estimation (Fig 2.11).

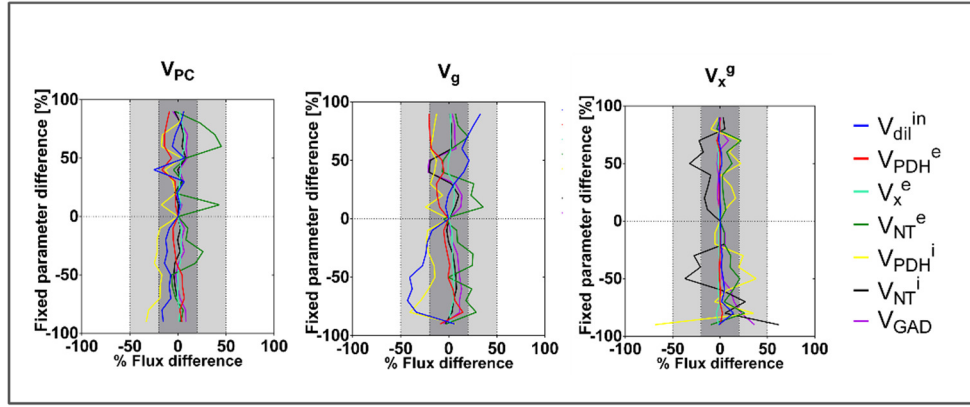


Figure 2. 11 : Validation of fixed parameters from pseudo 3-compartment model

Dependency of the flux estimations with the values chosen for the fixed glial parameters.

Several variants of the model were tested: the addition of a second Gln pool led to significant improvement in the GlnC4 and GlnC3 fit as had been shown by Duarte et al. in 2013. Fixing CMR_g to $0.35 \mu\text{mol/g/min}$ did not improve significantly the correlations or the fitting but affected the values of V_{dil}^{in} and V_{PDH}^e . Finally, the best fit was obtained by including a second pool of GABA in exchange with the neurotransmission-related GABA through the flux V_{ex}^i . This dilution of GABA labelling results in a slower slope of the enrichment curve of all the GABA fitting curves corresponding to the reality of the data. This model, including two Gln pools, two GABA pools and with fixed CMR_g gave the best results in terms of curve fitting ($R^2 = 0.984$), the lowest correlations (only V_{dil}^{in} and V_{PDH}^e were above 0.8, with $R = 0.93$) and resulted in coherent results: The blood lactate influx $V_{dil}^{in} = 0.50 \pm 0.21 \mu\text{mol/g/min}$, excitatory neuron pyruvate dehydrogenase activity $V_{PDH}^e = 0.64 \pm 0.13 \mu\text{mol/g/min}$, excitatory neuron transmittochondrial flux $V_x^e = 0.063 \pm 0.006 \mu\text{mol/g/min}$, excitatory neurotransmission rate $V_{NT}^e = 0.012 \pm 0.009 \mu\text{mol/g/min}$, inhibitory neuron pyruvate dehydrogenase activity $V_{PDH}^i = 0.07 \pm 0.06 \mu\text{mol/g/min}$, inhibitory neurotransmission flux $V_{NT}^i = 0.001 \pm 0.01 \mu\text{mol/g/min}$, glutamate decarboxylase activity $V_{GAD} = 0.10 \pm 0.05 \mu\text{mol/g/min}$, Gln exchange rate $V_{ex}^g = 0.016 \pm 0.007 \mu\text{mol/g/min}$ and GABA exchange rate $V_{ex}^i = 0.001 \pm 0.001 \mu\text{mol/g/min}$, while the inhibitory neuron transmittochondrial flux V_x^i and the glial dilution factor V_{dil}^g were both equal to zero. These estimated fluxes were used to calculate the remaining fluxes of the model including GABAergic TCA cycle rate $V_{TCA}^i = 0.17 \pm 0.04 \mu\text{mol/g/min}$, glial TCA cycle rate $V_{TCA}^g = 0.20 \pm 0.001 \mu\text{mol/g/min}$, glutamine synthetase activity $V_{GS} = 0.05 \pm 0.01 \mu\text{mol/g/min}$, GABA shunt rate $V_{shunt}^i (= V_{shunt}^g) = 0.09 \pm 0.06 \mu\text{mol/g/min}$, lactate blood efflux $V_{dil}^{out} = 0.16 \pm 0.07 \mu\text{mol/g/min}$ and the total TCA cycle or the oxidative cerebral metabolic rate of glucose $CMR_g(ox) = 0.52 \pm 0.07 \mu\text{mol/g/min}$.

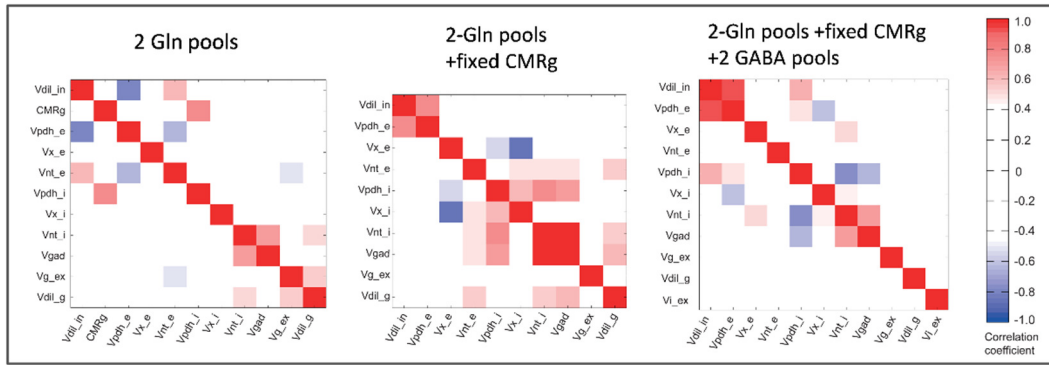


Figure 2.12 : Pseudo 3-compartment metabolic fluxes correlations

Correlation matrices obtained from the metabolic flux analysis using 3 different pseudo 3-compartment models. Cerebral metabolic rate of glucose (CMR_g), pyruvate dehydrogenase activity (V_{PDH}), a dilution flux from blood lactate (V_{dil}^{in} and V_{dil}^{out}) and from blood acetate (V_{dil}^e), a transmembrane flux (V_x), a neurotransmission flux (V_{NT}), Glutamate decarboxylase activity (V_{GAD}), two exchange fluxes between two glial Gln pools or two GABA pools (V_{ex}^g and V_{ex}^i).

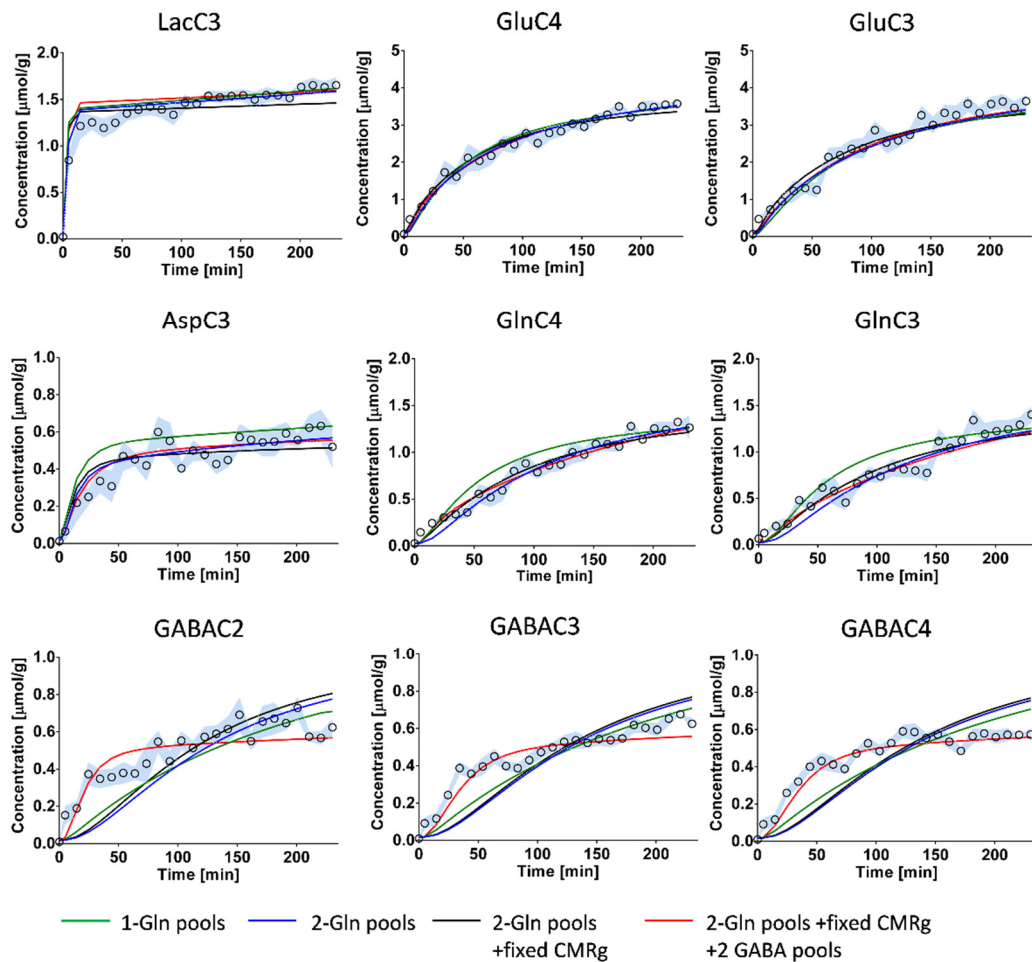


Figure 2.13 : Fitting comparison between the different 3-compartment models

Fitting results of 4 different pseudo 3-compartment models used. Model using one Gln pool (green), two Gln pools (blue), two Gln pools and a fixed CMR_g (black) or two Gln pools, fixed CMR_g and two GABAergic pools (red). ^{13}C enrichment data is shown as the mean for all animals \pm SD.

Pseudo 3-compartment model								
	Current study Mouse / isoflurane						Duarte et al. 2013 Rat / α -chloralose	
R^2	0.979	0.977	0.976	0.977	0.978	0.984	0.972	0.976
Gln pools	1	1	1	2	2	2	13	2
GABA pools	1	1	2	1	1	2	1	1
CMRg fixed	-	+	+	-	+	+	+	+
V_{dil}^{in}	0.0±0.20	0.55±0.29	0.49±0.25	0.0±0.10	0.44±0.23	0.50±0.21	-	-
CMR _g	0.73±0.34	0.35	0.35	0.67±0.27	0.35	0.35	0.52	0.52
V_{PDH}^e	1.1±0.7	0.69±0.17	0.64±0.15	1.02±0.55	0.68±0.11	0.64±0.13	0.36±0.01	0.33±0.01
V_x^e	0.067±0.007	0.075±0.007	0.067±0.0057	0.084±0.007	0.085±0.009	0.063±0.006	0.41±0.02	0.39±0.02
V_{NT}^e	0.0±0.005	0.0±0.01	0.0±0.01	0.003±0.007	0.01±0.01	0.012±0.009	0.16±0.01	0.18±0.01
V_{PDH}^i	0.14±0.14	0.11±0.04	0.06±0.05	0.05±0.13	0.01±0.05	0.07±0.06	0.024±0.005	0.017±0.005
V_x^i	0.3±10	0.0±0.0	0±0.0	0±0.0	0±0.0	0±0.0	0.0067±0.0038	0.0068±0.0034
V_{NT}^i	0.0007±0.003	0.001±0.003	0.0007±0.001	0.07±0.03	0.07±0.02	0.001±0.001	0.044±0.002	0.053±0.003
V_{GAD}	0.009±0.002	0.02±0.02	0.06±0.02	0.06±0.02	0.06±0.01	0.10±0.05	0.098±0.003	0.11±0.01
V_{dil}^g	0.09±0.10	0.06±0.06	0.07±0.06	0.33±0.13	0.26±0.09	0±0.0	1.1±0.1	0.76±0.07
V_{ex}^g	-	-	-	0.03±0.01	0.02±0.02	0.016±0.007	-	0.060±0.008
V_{ex}^i	-	-	0.0005±0.0005	-	-	0.0011±0.0010	-	-

Table 2. 2 : Comparison between flux estimation with different pseudo 3-compartment models and relevant literature

Cerebral metabolic rate of glucose (CMR_g), pyruvate dehydrogenase activity (V_{PDH}), a dilution flux from blood lactate (V_{dil}^{in} and V_{dil}^{out}) and from blood acetate (V_{dil}^e), a transmittochondrial flux (V_x), a neurotransmission flux (V_{NT}), Glutamate decarboxylase activity (V_{GAD}), two exchange fluxes between two glial Gln pools or two GABA pools (V_{ex}^e and V_{ex}^i).

2.4 Discussion

This study shows for the first time that a metabolic flux analysis of mouse hippocampal glucose metabolism is feasible in mouse brain *in vivo* using 1H - $[^{13}C]$ -MRS and ^{18}F FDG-PET to distinguish glutamatergic and GABAergic neuron activity. By optimizing the spectra fitting process and improving the mathematical modelling approach, we have been able to assess metabolic fluxes in hippocampal excitatory and inhibitory neurons. This work provides new tools to assess brain metabolic dysfunctions leading to excitatory/inhibitory imbalance typically relevant for genetically engineered mice models.

2.4.1 Optimization of glucose fitting improves data quality for $[U-^{13}C_6]Glc$ infusion

Power restrictions due to ^{13}C -decoupling is a key limiting factor for the realization of an optimal 1H - $[^{13}C]$ -MRS experiment using $[U-^{13}C_6]Glc$ infusion. However, an adjusted post-processing protocol can sometimes overcome the hardware limitations. This idea was

explored by improving the spectra fitting for metabolite quantification. Here we propose the addition of two additional glucose spectra in the basis set of the carbon-edited spectra to correct for incomplete decoupling of glucose. The C1-3 resonances of glucose in the carbon spectrum are generally difficult to excite with a decoupling bandwidth that targets the other main metabolite resonances. Typically, LacC3 is a critical component to decouple and represents the lowest observable chemical shift in the shielded part of the spectrum. By using a set of ^1H - ^{13}C decoupled, coupled and partially-decoupled $[\text{U-}^{13}\text{C}_6]\text{Glc}$ spectra to fit our data, we have been able to significantly improve the quantification of glucose itself but also GABAC4. The ability to have a reliable access to labelled brain glucose during the infusion protocol made it possible to use it as an input function for the mathematical modelling. This is a significant improvement as lactate input function has been generally preferred in indirect ^{13}C detection experiments (Lizarbe et al., 2018c; Xin et al., 2015) and gives insights into glucose metabolism upstream of the mitochondria. The exclusion of glucose in the modelling has been generally due to poor fitting, while $[\text{U-}^{13}\text{C}_6]\text{Glc}$ generates a lot of coupled resonances, $[\text{1,6-}^{13}\text{C}]\text{Glc}$ produces only one singlet correlating excessively with the overlapping GlxC2 peak. The use of LacC3 enrichment curves as input function instead of glucose can lead to other issues. Lactate is produced very quickly upon glucose infusion; however, enrichment curves not always resembles an optimal step-function. Consequently, glucose infusion rates are often manually adjusted and increased over the first minutes of the protocol to ensure a rapid lactate labelling. Glucose infusion is normally performed using a hyperglycemic clamp, to reduce dilution of glucose labelling from liver gluconeogenesis (Henry et al., 2006). This protocol is based on the idea that glucose brain entry is not dependent on blood glucose concentration (Duckrow and Bryan, 1987). Nevertheless, severe hyperglycemia is likely to have some physiological consequence related to long term alteration of insulin levels (DeFronzo et al., 1979). While we did not have access to the plasma glucose levels over the time of infusion, due to the animal's small blood volume, it appears that blood glucose levels after the experiment were in perfect agreement with the 20mM target calculated for the infusion rate.

2.4.2 Modelling of brain excitatory/inhibitory metabolic balance

Subsequently, with the additional information obtained from improved fitting of ^1H - ^{13}C -MRS spectra, i.e. Glc and GABAC4, mathematical modeling of hippocampal metabolic fluxes was

extended to target compartmentalization of excitatory and inhibitory neurons. The method used here can be seen as either a “bottom-up” or a “top-down” approach to test different model. Here, a bottom-up approach would suggest a simple model, where only the most reliable data are fitted to ensure a correct mathematical description of the system; On the other hand, a top-down approach would suggest the use of a complex model with more unknowns to determine, but closer to the biological reality. While most of the models did not describe our data correctly (imprecise fitting), we report two models which led to a good fit, mild correlations and flux values within a realistic range. The first model is a simple 1-compartment version of brain metabolism, which does not include GABA; the second model is a more complex pseudo 3-compartment description, including excitatory and inhibitory neurons.

We have been unable to fit our data with a GABAergic 1-compartment model as proposed in Lizarbe et al. When taking a closer look at the GABA enrichment curves, it appears that our data do not resemble a sigmoid function as seen in other studies (van Eijsden et al., 2010; Lizarbe et al., 2018c). Rather, the curves had a steep slope and reached a steady-state quickly as seen in Duarte et al. 2013 and Xin et al. in 2015. The first points are a critical part for the modelling and can often be overestimated by LCMODEL due to low SNR. To make sure this wasn't the case, we quantified GABA by reducing two-fold the time resolution (20min) and found no significant difference in the curve shape. The simple GABAergic model may have failed to describe our data most probably because it does not well include the glial GABA recycling, due to the glutamate-dependence of the V_{GABA} flux rather than glutamine (in the 3-compartment model), which is primarily glial. Another interesting observation is the similar time course of GABAC2 compared to C3 and C4, observed as well by Xin et al. in 2015. Due to its direct relation with GluC4, and closeness to the TCA cycle, GABAC2 is normally labelled faster than the other carbon positions. This difference in labelling is probably reduced due to the higher amount of labelling provided by $[\text{U-}^{13}\text{C}_6]\text{Glc}$ upon pyruvate carboxylation leading to higher GABAC3 levels than with $[1,6\text{-}^{13}\text{C}]\text{Glc}$. Furthermore, due to their low SNR and high level of overlap, GABA resonances lead to some imprecision in their quantification. GABAC2 overlaps with GluC4, as can be seen with their correlation, leading to higher errors of the enrichment curve. GABAC3 and GABAC4 give more accurate results but might be overestimated due to presence of overlapping NAAC6 and NAAC3 resonances which were not

considered in the fitting process, due to their low labelling rate and impossibility to be distinguished with LCMoel (Choi and Gruetter, 2004). This similar labelling of all GABA carbons might also be a specificity of the hippocampus and, in general, dependent on the local GABA neuron populations.

A significant difference was observed in the glycolytic rate CMR_g obtained from ^{18}F FDG-PET ($0.61 \pm 0.02 \mu\text{mol/g/min}$) as compared to the 1H - ^{13}C -MRS results with one-compartment model ($0.35 \pm 0.05 \mu\text{mol/g/min}$). When CMR_g was not fixed, the pseudo 3-compartment model reached a more comparable value ($0.73 \pm 0.34 \mu\text{mol/g/min}$) but with higher error. It is unclear whether this gap arises from the difference in glucose infusion protocol (euglycemia for PET and hyperglycemic clamp for 1H - ^{13}C -MRS) or the modelling approach. Nevertheless, if a ^{18}F FDG-PET measurement of CMR_g is available, fixing this value in the modelling provides a better mathematical analysis by reducing the number of unknowns.

Our flux analysis is in good agreement with available literature but reveals some important points. The transmitochondrial flux of excitatory neurons was rather small compared to several studies (Mason et al., 1995; Sibson et al., 1998) but similar to *in vivo* mouse data reported recently (Lai et al., 2018b). This flux was found to be zero in the GABAergic neurons, which is in good agreement with Duarte et al. 2013. While the latter reported a neurotransmission rate of $0.16 \pm 0.01 \mu\text{mol/g/min}$ for excitatory neurons (V_{NT}^e) and $0.044 \pm 0.002 \mu\text{mol/g/min}$ for inhibitory neurons (V_{NT}^i), we found much smaller values ($V_{NT}^e = 0.012 \pm 0.009 \mu\text{mol/g/min}$, $V_{NT}^i = 0.001 \pm 0.001 \mu\text{mol/g/min}$). A possible explanation is the use of isoflurane which was preferred to alpha-chloralose in this study. Isoflurane has been shown to induce hyperpolarization of hippocampal pyramidal (excitatory) cells (Berg-Johnsen and Langmoen, 1990). GABAergic contribution to neuronal total TCA was slightly higher (~7%) than previously reported by Duarte et al. (~5%) but still below the ~18% reported by Hyder et al. (Hyder et al., 2006). Another important observation is the higher $CMR_g(ox)$ ($=V_{TCA}/2$) relative to CMR_g compared to other studies (Duarte and Gruetter, 2013; Lai et al., 2018b). This difference might arise from the way lactate dynamics have been simulated here. The net brain lactate influx from blood ($V_{dil}^{in} - V_{dil}^{out}$) is generally set to be dependent on the estimated $CMR_g(ox)$ and the fixed CMR_g , while we relate this difference to the relative blood/brain lactate concentrations as well as blood FE (for more details see Appendix) (Boumezbeur et al., 2010b). Generally, a net efflux of lactate is observed upon glucose consumption from the

brain, in other words $CMR_g > CMR_g(ox)$ (Patel et al., 2004). We observed that hyperglycemic condition generates high levels of peripheral lactate at the end of the procedure resulting in a Lac_{brain}/Lac_{blood} ratio of ~ 0.32 . As lactate flux directionality is generally driven by the concentration gradient, it is likely to see a net accumulation of lactate from the blood to the brain. This effect is probably strengthened by isoflurane which has known effects on permeabilization of the blood brain barrier (BBB) (Acharya et al., 2015). Mice have high levels of blood and brain lactate compared to rats and humans. As such, the determination of these blood parameters is fundamental for an accurate assessment of brain energetic fluxes in mouse.

Further improvements of 1H - ^{13}C -MRS protocol after $[U-^{13}C_6]Glc$ infusion will allow clarifying some remaining questions. Isoflurane is generally a gold standard volatile anesthetic used for mice MRS rendering the whole acquisition pipeline less challenging in practice. However, it might have a stronger effect on brain activity than other anesthetics. The relatively low V_{NT} measured is in line with reduced isoelectricity induced by deep anesthesia (Choi et al., 2002). Working towards a simplified glucose infusion and MRS protocol will make the use of lighter (and generally more invasive) anesthetics more applicable. Optimizing the quantification protocol of blood metabolite concentration and labelling during the scan will also lead to more precision in the modelling. This could help reduce the number of parameters or values that had to be approximated. For instance, fixing blood lactate FE to a constant value had an effect on the fitting of brain $LacC3$ by overestimating the slope of the enrichment curve (Fig 2.10 and 2.13). Furthermore, increasing the complexity of the mathematical model allowed a better fitting of the data but led to several flux estimations to be equal to zero. As the addition of these parameters might appear useless, we think that they could provide freedom for the model to find specific metabolic differences in comparative animal studies. No mathematical model can pretend to be perfect and approximations have always to be made. It is however important that the prior knowledge is motivated by biological evidences and *a priori* knowledge, which is relevant for the animal model to be studied.

In conclusion, quantification of 1H - ^{13}C -labelled metabolites at 14T during $[U-^{13}C_6]Glc$ infusion can be improved. With a joint ^{18}FDG -PET measurement and additional blood labeling analysis, a metabolic flux analysis distinguishing GABAergic and glutamatergic neuronal metabolism was possible using a 3-compartment model with fixed glial parameters. Taken together, our

results provide new tools typically applicable in comparative studies of mouse brain with glutamatergic/GABAergic metabolic imbalance.

2.5 Appendix

2.5.1 Supplementary information

The mathematical description of the model was adapted from previously published models (Duarte and Gruetter, 2013; Lizarbe et al., 2018c). Main differences arise from the utilization of uniformly labelled glucose and the use of brain glucose as input function, which was the main improvement described in this study. We propose two different models which are suitable for modelling of brain metabolism upon infusion of [U-¹³C₆] glucose. Both models assume the metabolic pools sizes to be constant over the time of the infusion and were obtained from the real-time concentrations quantified from the neurochemical profile.

1-Compartment Model

Mass-balance equations and isotope balance equations reflect the model presented in figure 2.5 under metabolic steady state condition. The assumptions which have been made throughout the model are described below.

Mass balance

The net amount of pyruvate oxidized by the pyruvate dehydrogenase (PDH) corresponds to the pyruvate synthesis from glycolysis, also known as the cerebral metabolic rate of glucose (CMR_g) added to the net brain lactate influx ($V_{dil}^{in} - V_{dil}^{out}$).

$$V_{PDH} = 2 \cdot CMR_g + V_{dil}^{in} - V_{dil}^{out} = V_{TCA}$$

Blood lactate relation

A difference in glucose consumption from glycolysis (CMR_g) and oxidation ($CMR_g(ox)$) in the mitochondria is a well-established mechanism which occurs during rest but mainly during neuronal activation. For instance, Patel et al. found that the ratio of CMR_g over $CMR_g(ox)$ was around 1.5:1 after bicuculline-induced intense neuronal activity compared to a 1:1 ratio in controls (Patel et al., 2004). The resulting lactate accumulation is generally thought to be released in the blood or used internally for non-oxidative purpose. Due to the use of isoflurane anesthesia leading to possibly low neuronal activity and associated lactate dynamics, we did not assume any direct relationship between CMR_g and $CMR_g(ox)$. Rather, we propose a lactate dynamic based on plasma values, and driven by a concentration gradient. We assumed a linear relation of brain lactate (Lac_{brain}) with plasma lactate levels (Lac_{blood}) as described in (Boumezbeur et al., 2010c), which allowed us to predict the relation between lactate influx and efflux from the brain. Lac_{brain} was determined as the averaged concentration in the hippocampal voxel over the time of infusion and Lac_{blood} was set at the plasma value obtained after the scan.

$$V_{dil}^{out} = V_{dil}^{in} \frac{Lac_{brain}}{Lac_{blood}}$$

Blood lactate and acetate values

Because labelling of blood metabolites occurs through utilization of glucose outside of the brain, we included the contribution of plasma lactate and acetate ^{13}C -labelling contribution. In a separate experiment with animals infused with $[\text{U-}^{13}\text{C}_6]\text{glucose}$ outside of the scanner, we analyzed the relative labelling of glucose, lactate and acetate by performing a 3 time-point blood sampling (Fig 4B). Result indicated a relative steady-state of lactate of 0.5 with a slower kinetic that in the brain. Acetate labelling occurred much slowly and did not reach a steady state in our experimental time-frame. As a result, we approximated blood lactate FE to 0.5 and acetate FE to 0.3 and set them as constant over time (as reported for rats in Duarte et al 2011).

$$\frac{\text{Lac}_3(t)_{\text{Blood}}}{\text{Lac}_{\text{Blood}}} = 0.5 \quad \frac{\text{Acetate}_2(t)_{\text{Blood}}}{\text{Acetate}_{\text{Blood}}} = 0.3$$

Lactate-pyruvate fast exchange

Pyruvate FE can be considered equal to Lactate FE in the brain due to fast exchange occurring with PDH activity (Leong et al., 1981; Xu et al., 2007).

$$\frac{\text{Pyr}_3(t)}{\text{Pyr}} = \frac{\text{Lac}_3(t)}{\text{Lac}}$$

Uniformly labelling of glucose considerations

The use of uniformly labelled glucose allows a set of possible assumptions and simplifications in the model. The absence of a differential labelling arising from pyruvate carboxylation in glial cells typically observed with $[1,6\text{-}^{13}\text{C}]\text{glucose}$ leads to a similar enrichment profile of several C2 and C3 positions of TCA cycle intermediates and thus metabolites in direct exchange with it. Typically, $\text{OAA}_3(t)=\text{OAA}_2(t)$, $\text{OG}_3(t)=\text{OG}_2(t)$, $\text{Asp}_3(t)=\text{Asp}_2(t)$, $\text{Glu}_3(t)=\text{Glu}_2(t)$ and $\text{Gln}_3(t)=\text{Gln}_2(t)$.

$$\frac{\text{Asp}_3(t)}{\text{Asp}} = \frac{\text{Asp}_2(t)}{\text{Asp}} \leftrightarrow \frac{\text{OAA}_3(t)}{\text{OAA}} = \frac{\text{OAA}_2(t)}{\text{OAA}}$$

Set of differential equations (Simple model)

The set of differential equations used in the 1-compartment model is shown below. The small intermediates (OAA, OG and AcCoA) pool sizes were all approximated at $0.1 \mu\text{mol/g}$. The mathematical model used the brain glucose fractional enrichment as input function (IF). The estimated fluxes were: The cerebral metabolic rate of glucose (CMR_g), a dilution flux from plasma lactate ($V_{\text{dil}}^{\text{in}}$), the tricarboxylic acid cycle flux ($V_{\text{TCA}} = 2 \cdot \text{CMR}_g(\text{ox})$), the neurotransmission or Gln/Glu cycle flux (V_{NT}), and a dilution factor arising from mitochondrial oxidation of ketone bodies, fatty acids or acetate (V_{dil}^g).

$$\text{Glu C4:} \quad \frac{d\text{Glu}_4}{dt} = V_x \cdot \frac{\text{OG}_4(t)}{\text{OG}} + V_{\text{NT}} \cdot \frac{\text{Gln}_4(t)}{\text{Gln}} - (V_x + V_{\text{NT}}) \cdot \frac{\text{Glu}_4(t)}{\text{Glu}}$$

$$\text{Glu C3:} \quad \frac{d\text{Glu}_3}{dt} = V_x \cdot \frac{\text{OG}_3(t)}{\text{OG}} + V_{\text{NT}} \cdot \frac{\text{Gln}_3(t)}{\text{Gln}} - (V_x + V_{\text{NT}}) \cdot \frac{\text{Glu}_3(t)}{\text{Glu}}$$

$$\text{Gln C4:} \quad \frac{d\text{Gln}_4}{dt} = V_{\text{NT}} \cdot \frac{\text{Glu}_4(t)}{\text{Glu}} - V_{\text{NT}} \cdot \frac{\text{Gln}_4(t)}{\text{Gln}}$$

$$\text{Gln C3:} \quad \frac{d\text{Gln}_3}{dt} = V_{\text{NT}} \cdot \frac{\text{Glu}_3(t)}{\text{Glu}} - V_{\text{NT}} \cdot \frac{\text{Gln}_3(t)}{\text{Gln}}$$

$$\text{Asp C3:} \quad \frac{dAsp_3}{dt} = V_x \cdot \frac{OAA_3(t)}{OAA} - V_x \cdot \frac{Asp_3(t)}{Asp}$$

$$\text{Asp C2:} \quad \frac{dAsp_2}{dt} = V_x \cdot \frac{OAA_2(t)}{OAA} - V_x \cdot \frac{Asp_2(t)}{Asp}$$

$$\text{OG C4:} \quad \frac{dOG_4}{dt} = V_{TCA} \cdot \frac{AcCoA_2(t)}{AcCoA} + V_x \cdot \frac{Glu_4(t)}{Glu} - (V_x + V_{TCA}) \cdot \frac{OG_4(t)}{OG}$$

$$\text{OG C3:} \quad \frac{dOG_3}{dt} = V_{TCA} \cdot \frac{OAA_2(t)}{OAA} + V_x \cdot \frac{Glu_3(t)}{Glu} - (V_x + V_{TCA}) \cdot \frac{OG_3(t)}{OG}$$

$$\text{OAA C3:} \quad \frac{dOAA_3}{dt} = \frac{1}{2} \cdot V_{TCA} \cdot \frac{OG_4(t)}{OG} + \frac{1}{2} \cdot V_{TCA} \cdot \frac{OG_3(t)}{OG} + V_x \cdot \frac{Asp_3(t)}{Asp} - (V_x + V_{TCA}) \cdot \frac{OAA_3(t)}{OAA}$$

$$\text{OAA C2:} \quad \frac{dOAA_2}{dt} = \frac{1}{2} \cdot V_{TCA} \cdot \frac{OG_4(t)}{OG} + \frac{1}{2} \cdot V_{TCA} \cdot \frac{OG_3(t)}{OG} + V_x \cdot \frac{Asp_2(t)}{Asp} - (V_x + V_{TCA}) \cdot \frac{OAA_2(t)}{OAA}$$

$$\text{Lac C3:} \quad \frac{dLac_3}{dt} = 2 \cdot CMR_g \cdot IF + V_{in} \cdot \frac{Lac_3(t)_{Blood}}{Lac_{Blood}} - (V_{PDH} + V_{out}) \cdot \frac{Lac_3(t)}{Lac}$$

$$\text{AcCoA C2:} \quad \frac{dAcCoA_2}{dt} = V_{PDH} \cdot \frac{Pyr_3(t)}{Pyr} + V_{dil}^g \cdot \frac{Acetate_2(t)_{Blood}}{Acetate_{Blood}} - (V_{TCA} + V_{dil}^g) \cdot \frac{AcCoA_2(t)}{AcCoA}$$

Set of differential equations (GABAergic model)

The set of differential equations for the GABAergic model was similar to the simple 1-compartment model with a few exceptions. The contribution of pyruvate carboxylation was included and fixed to values obtained from the literature in mouse brain (Lai et al., 2018b; Lizarbe et al., 2018c), $V_{pc}=0.04 \mu\text{mol/g/min}$. To compensate for this net anabolic input, a glutamine efflux (V_{eff}) was added and set equal to (V_{pc}). Finally, GABA metabolism was included by the addition of a V_{GABA} flux coming directly from decarboxylation of glutamate.

$$\text{Glu C4:} \quad \frac{dGlu_4}{dt} = (V_x + V_{GABA} + V_{eff}) \cdot \frac{OG_4(t)}{OG} + V_{NT} \cdot \frac{Gln_4(t)}{Gln} - (V_x + V_{NT} + V_{GABA} + V_{eff}) \cdot \frac{Glu_4(t)}{Glu}$$

$$\text{Glu C3:} \quad \frac{dGlu_3}{dt} = (V_x + V_{GABA} + V_{eff}) \cdot \frac{OG_3(t)}{OG} + V_{NT} \cdot \frac{Gln_3(t)}{Gln} - (V_x + V_{NT} + V_{GABA} + V_{eff}) \cdot \frac{Glu_3(t)}{Glu}$$

$$\text{Gln C4:} \quad \frac{dGln_4}{dt} = (V_{NT} + V_{eff}) \cdot \frac{Glu_4(t)}{Glu} - (V_{NT} + V_{eff}) \cdot \frac{Gln_4(t)}{Gln}$$

$$\text{Gln C3:} \quad \frac{dGln_3}{dt} = (V_{NT} + V_{eff}) \cdot \frac{Glu_3(t)}{Glu} - (V_{NT} + V_{eff}) \cdot \frac{Gln_3(t)}{Gln}$$

$$\text{Asp C3:} \quad \frac{dAsp_3}{dt} = V_x \cdot \frac{OAA_3(t)}{OAA} - V_x \cdot \frac{Asp_3(t)}{Asp}$$

$$\text{Asp C2:} \quad \frac{dAsp_2}{dt} = V_x \cdot \frac{OAA_2(t)}{OAA} - V_x \cdot \frac{Asp_2(t)}{Asp}$$

$$\text{OG C4:} \quad \frac{dOG_4}{dt} = (V_{TCA} + V_{GABA} + V_{pc}) \cdot \frac{AcCoA_2(t)}{AcCoA} + V_x \cdot \frac{Glu_4(t)}{Glu} - (V_x + V_{TCA} + V_{GABA} + V_{pc}) \cdot \frac{OG_4(t)}{OG}$$

$$\text{OG C3:} \quad \frac{dOG_3}{dt} = (V_{TCA} + V_{GABA} + V_{pc}) \cdot \frac{OAA_2(t)}{OAA} + V_x \cdot \frac{Glu_3(t)}{Glu} - (V_x + V_{TCA} + V_{GABA} + V_{pc}) \cdot \frac{OG_3(t)}{OG}$$

$$\text{OAA C3:} \quad \frac{dOAA_3}{dt} = V_{pc} \cdot \frac{Pyr_3(t)}{Pyr} + \frac{1}{2} \cdot V_{TCA} \cdot \frac{OG_4(t)}{OG} + \frac{1}{2} \cdot V_{TCA} \cdot \frac{OG_3(t)}{OG} + V_x \cdot \frac{Asp_3(t)}{Asp} - (V_x + V_{TCA} + V_{GABA} + V_{pc}) \cdot \frac{OAA_3(t)}{OAA}$$

OAA C2:
$$\frac{dOAA_2}{dt} = V_{pc} \cdot \frac{Pyr_3(t)}{Pyr} + \frac{1}{2} \cdot V_{TCA} \cdot \frac{OG_4(t)}{OG} + \frac{1}{2} \cdot V_{TCA} \cdot \frac{OG_3(t)}{OG} + V_x \cdot \frac{Asp_2(t)}{Asp} - (V_x + V_{TCA} + V_{GABA} + V_{pc}) \cdot \frac{OAA_2(t)}{OAA}$$

Lac C3:
$$\frac{dLac_3}{dt} = 2 \cdot CMR_{Glc} \cdot IF + V_{in} \cdot \frac{Lac_3(t)_{Blood}}{Lac_{Blood}} - (V_{PDH} + V_{out}) \cdot \frac{Lac_3(t)}{Lac}$$

AcCoA C2:
$$\frac{dAcCoA_2}{dt} = V_{PDH} \cdot \frac{Pyr_3(t)}{Pyr} + V_{dil}^g \cdot \frac{Acetate_2(t)_{Blood}}{Acetate_{Blood}} - (V_{TCA} + V_{GABA} + V_{pc} + V_{dil}^g) \cdot \frac{AcCoA_2(t)}{AcCoA}$$

GABA C2:
$$\frac{dGABA_2}{dt} = V_{GABA} \cdot \frac{Glu_4(t)}{Glu} - V_{GABA} \cdot \frac{GABA_2(t)}{GABA}$$

GABA C3:
$$\frac{dGABA_3}{dt} = V_{GABA} \cdot \frac{Glu_3(t)}{Glu} - V_{GABA} \cdot \frac{GABA_3(t)}{GABA}$$

GABA C4:
$$\frac{dGABA_4}{dt} = V_{GABA} \cdot \frac{Glu_2(t)}{Glu} - V_{GABA} \cdot \frac{GABA_4(t)}{GABA}$$

Pseudo 3-Compartment Model

Brain metabolism is highly compartmentalized (Gruetter et al., 2001) and therefore ideally requires a distinction between the different cellular compartments present in the brain for an accurate mathematical modelling. Typically, brain compartments are generally segregated into neuronal and astrocytic metabolism. Excitatory neurons release neurotransmitter glutamate in the synaptic cleft, which is taken up by astrocytes and recycled back. This process is known as the Glu-Gln cycle, or neurotransmission rate, as it is based on the astroglial ability to rapidly convert the glutamate taken up into glutamine via the enzyme glutamine synthetase (GS) and shuttle it back into neurons. This cycle exists for GABA in inhibitory neurons as well, with the main difference that GABA is recycled via the GABA shunt. This pathway consists in the transformation of GABA into succinate through the action of GABA transaminase and is re-incorporated into the TCA cycle. GABA has been shown to be also taken up by inhibitory neurons in which the GABA shunt can also take place. Another specificity of glial metabolism is the anabolic reactions taking place through the action of pyruvate carboxylase (PC), which converts pyruvate into oxaloacetate, which feeds the TCA cycle. This reaction is central for the distinction between neurons and astrocyte metabolism. The $[3-^{13}\text{C}]$ pyruvate formed from $[1,6-^{13}\text{C}]$ glucose produces a specific ^{13}C -labelling dilution on position C2 of the glutamate and glutamine measured upon exchange with TCA cycle intermediates. This dilution effect is not produced with $[\text{U}-^{13}\text{C}_6]$ glucose rendering the assessment of glial metabolism impossible. Therefore, we have fixed all the glial parameters based on values from the literature. The model proposed here is an extended version of the aforementioned 1-compartment model, with several additions adapted from Duarte et al in 2013.

Uniformly labelling of glucose considerations

As for the 1-compartment model description, a major simplification was made to reduce the number of equations to be used. Mainly, labelling of AspC3 was set equal to AspC2, GluC3 set equal to GluC2 and GlnC3 set equal to GlnC2.

$$\frac{Asp_3(t)}{Asp} = \frac{Asp_2(t)}{Asp} \quad \frac{OAA_3(t)}{OAA} = \frac{OAA_2(t)}{OAA}$$

As an attempt to improve the amount of available data to gain precision in the modelling, we also included a separation of GluC2 and GlnC2. As we were not able to separate these two resonances in the fitting process but only had access to GlxC2, we extracted the relative concentrations based on the measured GlnC3 and GluC3 results. This correction process is only possible due to the absence of ^{13}C -dilution from arising from PC activity:

$$\frac{Glu_3(t)}{GlxC_3(t)} = \frac{Glu_2(t)}{GlxC_2(t)} \quad \frac{Gln_3(t)}{GlxC_3(t)} = \frac{Gln_2(t)}{GlxC_2(t)}$$

Pool sizes

The relative metabolic pool sizes of the small TCA intermediates were all fixed at $0.1 \mu\text{mol/g}$ and similar for three compartments: glia (g), excitatory neurons (e) and inhibitory neurons (i).

$$AcCoA^g = OG^e = OG^i = OG^g = OAA^e = OAA^i = OAA^g = 0.1$$

The other cell-specific metabolic pool sizes were the same as in Duarte et al in 2013.

80% of all glutamate is in excitatory neurons, the rest is distributed equally

$$Glu^e = 0.8 \cdot (Glu^e + Glu^i + Glu^g)$$

$$Glu^i = 0.1 \cdot (Glu^e + Glu^i + Glu^g)$$

$$Glu^g = 0.1 \cdot (Glu^e + Glu^i + Glu^g)$$

80% of all aspartate is in excitatory neurons, the rest is distributed equally

$$Asp^e = 0.8 \cdot (Asp^e + Asp^i + Asp^g)$$

$$Asp^i = 0.1 \cdot (Asp^e + Asp^i + Asp^g)$$

$$Asp^g = 0.1 \cdot (Asp^e + Asp^i + Asp^g)$$

80% of all glutamine is glial, the rest is distributed equally

$$Gln^g = 0.8 \cdot (Gln^e + Gln^i + Gln^g)$$

$$Gln^i = 0.1 \cdot (Gln^e + Gln^i + Gln^g)$$

$$Gln^e = 0.1 \cdot (Gln^e + Gln^i + Gln^g)$$

90% of all GABA is in inhibitory neurons, the rest is in glial cells only

$$GABA^i = 0.9 \cdot (GABA^i + GABA^g)$$

$$GABA^g = 0.1 \cdot (GABA^i + GABA^g)$$

Lactate dynamics

As for the 1-compartment model, the following relationship was used for blood lactate dynamics.

$$V_{dil}^{out} = V_{dil}^{in} \frac{Lac_{brain}}{Lac_{blood}} \quad \frac{Lac_3(t)_{Blood}}{Lac_{Blood}} = 0.5 \quad \frac{Acetate_2(t)_{Blood}}{Acetate_{Blood}} = 0.3 \quad \frac{Pyr_3(t)}{Pyr} = \frac{Lac_3(t)}{Lac}$$

Mass balance

The amount of glucose oxidized entering the TCA cycle is defined as the cerebral metabolic rate of glucose $CMR_g(ox)$. A factor 2 is added to consider that 1 mol of glucose leads to 2 moles of pyruvate.

$$2 \cdot CMR_g(ox) = 2 \cdot CMR_g + V_{dil}^{in} - V_{dil}^{out}$$

The different cellular contributions to the total TCA cycle activity were similar as described in Duarte 2013. TCA cycle activity of excitatory neurons is based mainly on PDH activity, while an extra contribution of GABA shunt is added in inhibitory neurons. Similarly, glial TCA cycle includes a contribution from glial GABA shunt (V_{shunt}) together with together with the extra amount of oxaloacetate produced from pyruvate carboxylation which must be oxidized to maintain anaplerosis (V_{PC}).

$$V_{TCA}^e = V_{PDH}^e$$

$$V_{TCA}^i = V_{PDH}^i + V_{shunt}^i$$

$$V_{TCA}^g = V_g + V_{PC} + V_{shunt}^g$$

The total rate of glucose oxidation entering the TCA cycle at steady state is then equal to the sum of the cell-specific TCA components and the proportion of glucose used for pyruvate carboxylation.

$$CMR_{Glc(ox)} = V_{TCA}^e + V_{TCA}^i + V_{TCA}^g + V_{PC}$$

GABA recycling V_{shunt} in inhibitory neurons equals the rate of GABA synthesis from glutamate decarboxylation (V_{GAD}) minus the amount which is taken up by astrocytes (V_{NT}^i).

$$V_{shunt}^i = V_{GAD} - V_{NT}^i$$

All the GABA entering glial compartment is considered to be recycled through the glial GABA shunt.

$$V_{shunt}^g = V_{NT}^i$$

The net synthesis of glutamine in astrocytes corresponds to the amount of glutamate taken up from excitatory neurotransmission summed with the anaplerosis induced by the amount of oxaloacetate produced from GABA recycling and PC activity

$$V_{GS} = V_{NT}^e + V_{shunt}^g + V_{PC} = V_{NT}^e + V_{NT}^i + V_{efflux}$$

Fixed parameters

Pyruvate carboxylase activity (V_{PC}), glial TCA cycle (V_g) and glial transmitochondrial flux (V_x^g) were fixed to known values from the literature (Lai et al., 2018a).

Astrocyte metabolism

$$V_{PC} = 0.04 \text{ } \mu\text{mol/g/min}$$

$$V_g = 0.16 \text{ } \mu\text{mol/g/min}$$

$$V_x^g = V_g$$

Mainly, pyruvate carboxylation flux was set to $V_{pc} = 0.04 \text{ } \mu\text{mol/g/min}$ and equal to a net efflux of glutamine from the brain (V_{eff}). Glial $V_g = 0.16 \text{ } \mu\text{mol/g/min}$ and $V_x = V_g$.

Set of differential equations

Mass-balance equations and isotope balance equations reflect the model presented in figure 2.5 under metabolic steady state condition.

$$\text{Lac C3: } \frac{dLac_3}{dt} = 2 \cdot CMR_{Glc} \cdot IF + V_{in} \cdot \frac{Lac_3(t)_{Blood}}{Lac_{Blood}} - (V_{TCA} + V_{out}) \frac{Lac_3(t)}{Lac}$$

Excitatory Neuron

$$\text{Glu C4:} \quad \frac{dGlu_4^e}{dt} = V_x^e \cdot \frac{OG_4^e(t)}{OG^e} + V_{NT}^e \cdot \frac{Gln_4^e(t)}{Gln^e} - (V_x^e + V_{NT}^e) \cdot \frac{Glu_4^e(t)}{Glu^e}$$

$$\text{Glu C3:} \quad \frac{dGlu_3^e}{dt} = V_x^e \cdot \frac{OG_3^e(t)}{OG^e} + V_{NT}^e \cdot \frac{Gln_3^e(t)}{Gln^e} - (V_x^e + V_{NT}^e) \cdot \frac{Glu_3^e(t)}{Glu^e}$$

$$\text{Glu C2:} \quad \frac{dGlu_2^e}{dt} = V_x^e \cdot \frac{OG_2^e(t)}{OG^e} + V_{NT}^e \cdot \frac{Gln_2^e(t)}{Gln^e} - (V_x^e + V_{NT}^e) \cdot \frac{Glu_2^e(t)}{Glu^e}$$

$$\text{Gln C4:} \quad \frac{dGln_4^e}{dt} = V_{NT}^e \cdot \frac{Gln_4^g(t)}{Glu^e} - V_{NT}^e \cdot \frac{Gln_4^e(t)}{Gln^e}$$

$$\text{Gln C3:} \quad \frac{dGln_3^e}{dt} = V_{NT}^e \cdot \frac{Gln_3^g(t)}{Glu^e} - V_{NT}^e \cdot \frac{Gln_3^e(t)}{Gln^e}$$

$$\text{Gln C2:} \quad \frac{dGln_2^e}{dt} = V_{NT}^e \cdot \frac{Gln_2^g(t)}{Glu^e} - V_{NT}^e \cdot \frac{Gln_2^e(t)}{Gln^e}$$

$$\text{Asp C3:} \quad \frac{dAsp_3^e}{dt} = V_x \cdot \frac{OAA_3^e(t)}{OAA^e} - V_x \cdot \frac{Asp_3^e(t)}{Asp^e}$$

$$\text{Asp C2:} \quad \frac{dAsp_2^e}{dt} = V_x \cdot \frac{OAA_2^e(t)}{OAA^e} - V_x \cdot \frac{Asp_2^e(t)}{Asp^e}$$

$$\text{OG C4:} \quad \frac{dOG_4^e}{dt} = V_{PDH}^e \cdot \frac{Pyr_3(t)}{Pyr} + V_x^e \cdot \frac{Glu_4^e(t)}{Glu^e} - (V_x^e + V_{PDH}^e) \cdot \frac{OG_4^e(t)}{OG^e}$$

$$\text{OG C3:} \quad \frac{dOG_3^e}{dt} = V_{PDH}^e \cdot \frac{OAA_2^e(t)}{OAA^e} + V_x^e \cdot \frac{Glu_3^e(t)}{Glu^e} - (V_x^e + V_{PDH}^e) \cdot \frac{OG_3^e(t)}{OG^e}$$

$$\text{OG C2:} \quad \frac{dOG_2^e}{dt} = V_{PDH}^e \cdot \frac{OAA_3^e(t)}{OAA^e} + V_x^e \cdot \frac{Glu_2^e(t)}{Glu^e} - (V_x^e + V_{PDH}^e) \cdot \frac{OG_2^e(t)}{OG^e}$$

$$\text{OAA C3:} \quad \frac{dOAA_3^e}{dt} = \frac{1}{2} \cdot V_{PDH}^e \cdot \frac{OG_4^e(t)}{OG^e} + \frac{1}{2} \cdot V_{PDH}^e \cdot \frac{OG_3^e(t)}{OG^e} + V_x^e \cdot \frac{Asp_3^e(t)}{Asp^e} - (V_x^e + V_{PDH}^e) \cdot \frac{OAA_3^e(t)}{OAA^e}$$

$$\text{OAA C2:} \quad \frac{dOAA_2^e}{dt} = \frac{1}{2} \cdot V_{PDH}^e \cdot \frac{OG_4^e(t)}{OG^e} + \frac{1}{2} \cdot V_{TCA}^e \cdot \frac{OG_3^3(t)}{OG^3} + V_x^e \cdot \frac{Asp_2^e(t)}{Asp^e} - (V_x^e + V_{PDH}^e) \cdot \frac{OAA_2^e(t)}{OAA^e}$$

Inhibitory Neuron

$$\text{Glu C4:} \quad \frac{dGlu_4^i}{dt} = (V_x^i + V_{shunt}^i) \cdot \frac{OG_4^i(t)}{OG^i} + V_{NT}^i \cdot \frac{Gln_4^i(t)}{Gln^i} - (V_x^i + V_{GAD}) \cdot \frac{Glu_4^i(t)}{Glu^i}$$

$$\text{Glu C3:} \quad \frac{dGlu_3^i}{dt} = (V_x^i + V_{shunt}^i) \cdot \frac{OG_3^i(t)}{OG^i} + V_{NT}^i \cdot \frac{Gln_3^i(t)}{Gln^i} - (V_x^i + V_{GAD}) \cdot \frac{Glu_3^i(t)}{Glu^i}$$

$$\text{Glu C2:} \quad \frac{dGlu_2^i}{dt} = (V_x^i + V_{shunt}^i) \cdot \frac{OG_2^i(t)}{OG^i} + V_{NT}^i \cdot \frac{Gln_2^i(t)}{Gln^i} - (V_x^i + V_{GAD}) \cdot \frac{Glu_2^i(t)}{Glu^i}$$

$$\text{Gln C4:} \quad \frac{dGln_4^i}{dt} = V_{NT}^i \cdot \frac{Gln_4^g(t)}{Glu^i} - V_{NT}^i \cdot \frac{Gln_4^i(t)}{Gln^i}$$

$$\text{Gln C3:} \quad \frac{dGln_3^i}{dt} = V_{NT}^i \cdot \frac{Gln_3^g(t)}{Glu^i} - V_{NT}^i \cdot \frac{Gln_3^i(t)}{Gln^i}$$

$$\text{Gln C2:} \quad \frac{dGln_2^i}{dt} = V_{NT}^i \cdot \frac{Gln_2^g(t)}{Glu^e} - V_{NT}^i \cdot \frac{Gln_2^i(t)}{Gln^e}$$

$$\text{Asp C3:} \quad \frac{dAsp_3^i}{dt} = V_x \cdot \frac{OAA_3^i(t)}{OAA^i} - V_x \cdot \frac{Asp_3^i(t)}{Asp^i}$$

$$\text{Asp C2:} \quad \frac{dAsp_2^i}{dt} = V_x \cdot \frac{OAA_2^i(t)}{OAA^i} - V_x \cdot \frac{Asp_2^i(t)}{Asp^i}$$

$$\text{OG C4:} \quad \frac{dOG_4^i}{dt} = (V_{PDH}^i + V_{shunt}^i) \cdot \frac{Pyr_3(t)}{Pyr} + V_x^i \cdot \frac{Glu_4^i(t)}{Glu^i} - (V_x^i + V_{PDH}^i + V_{shunt}^i) \cdot \frac{OG_4^i(t)}{OG^i}$$

$$\text{OG C3:} \quad \frac{dOG_3^i}{dt} = (V_{PDH}^i + V_{shunt}^i) \cdot \frac{OAA_2^i(t)}{OAA^i} + V_x^i \cdot \frac{Glu_3^i(t)}{Glu^i} - (V_x^i + V_{PDH}^i + V_{shunt}^i) \cdot \frac{OG_3^i(t)}{OG^i}$$

$$\text{OG C2:} \quad \frac{dOG_2^i}{dt} = (V_{PDH}^i + V_{shunt}^i) \cdot \frac{OAA_3^i(t)}{OAA^i} + V_x^i \cdot \frac{Glu_2^i(t)}{Glu^i} - (V_x^i + V_{PDH}^i + V_{shunt}^i) \cdot \frac{OG_2^i(t)}{OG^e}$$

$$\text{OAA C3:} \quad \frac{dOAA_3^i}{dt} = \frac{1}{2} \cdot V_{PDH}^i \cdot \frac{OG_4^i(t)}{OG^i} + \frac{1}{2} \cdot V_{PDH}^i \cdot \frac{OG_3^e(t)}{OG^e} + \frac{1}{2} \cdot V_{shunt}^i \cdot \frac{GABA_2^i(t)}{GABA^i} + \frac{1}{2} \cdot V_{shunt}^i \cdot \frac{GABA_3^i(t)}{GABA^i} + V_x^i \cdot \frac{Asp_3^i(t)}{Asp^i} - (V_x^i + V_{PDH}^i + V_{shunt}^i) \cdot \frac{OAA_3^i(t)}{OAA^i}$$

$$\text{OAA C2:} \quad \frac{dOAA_2^i}{dt} = \frac{1}{2} \cdot V_{PDH}^i \cdot \frac{OG_4^i(t)}{OG^i} + \frac{1}{2} \cdot V_{PDH}^i \cdot \frac{OG_3^e(t)}{OG^e} + \frac{1}{2} \cdot V_{shunt}^i \cdot \frac{GABA_2^i(t)}{GABA^i} + \frac{1}{2} \cdot V_{shunt}^i \cdot \frac{GABA_3^i(t)}{GABA^i} + V_x^i \cdot \frac{Asp_2^i(t)}{Asp^i} - (V_x^i + V_{PDH}^i + V_{shunt}^i) \cdot \frac{OAA_2^i(t)}{OAA^i}$$

$$\text{GABA C2:} \quad \frac{dGABA_2^i}{dt} = V_{GAD} \cdot \frac{Glu_4^i(t)}{Glu^i} - (V_{NT}^i + V_{shunt}^i) \cdot \frac{GABA_2^i(t)}{GABA^i}$$

$$\text{GABA C3:} \quad \frac{dGABA_3^i}{dt} = V_{GAD} \cdot \frac{Glu_3^i(t)}{Glu^i} - (V_{NT}^i + V_{shunt}^i) \cdot \frac{GABA_3^i(t)}{GABA^i}$$

$$\text{GABA C4:} \quad \frac{dGABA_4^i}{dt} = V_{GAD} \cdot \frac{Glu_2^i(t)}{Glu^i} - (V_{NT}^i + V_{shunt}^i) \cdot \frac{GABA_4^i(t)}{GABA^i}$$

Glial compartment

$$\text{AcCoA C2:} \quad \frac{dAcCoA_2^g}{dt} = (V_g + V_{shunt}^g + V_{PC}) \cdot \frac{Pyr_3(t)}{Pyr} + V_{dil}^g \cdot \frac{Acetate_2(t)_{Blood}}{Acetate_{Blood}} - (V_g + V_{shunt}^g + V_{PC} + V_{dil}^g) \cdot \frac{AcCoA_2^g(t)}{AcCoA^g}$$

$$\text{Glu C4:} \quad \frac{dGlu_4^g}{dt} = (V_x^g + V_{shunt}^g + V_{PC}) \cdot \frac{OG_4^g(t)}{OG^g} + V_{NT}^e \cdot \frac{Glu_4^e(t)}{Glu^e} - (V_{GS} + V_x^g) \cdot \frac{Glu_4^g(t)}{Glu^g}$$

$$\text{Glu C3:} \quad \frac{dGlu_3^g}{dt} = (V_x^g + V_{shunt}^g + V_{PC}) \cdot \frac{OG_3^g(t)}{OG^g} + V_{NT}^e \cdot \frac{Glu_3^e(t)}{Glu^e} - (V_{GS} + V_x^g) \cdot \frac{Glu_3^g(t)}{Glu^g}$$

$$\text{Glu C2:} \quad \frac{dGlu_2^g}{dt} = (V_x^g + V_{shunt}^g + V_{PC}) \cdot \frac{OG_2^g(t)}{OG^g} + V_{NT}^e \cdot \frac{Glu_2^e(t)}{Glu^e} - (V_{GS} + V_x^g) \cdot \frac{Glu_2^g(t)}{Glu^g}$$

$$\text{Gln C4:} \quad \frac{dGln_4^g}{dt} = V_{GS} \cdot \frac{Glu_4^g(t)}{Glu^g} - (V_{NT}^i + V_{NT}^e + V_{eff}) - \frac{Gln_4^g(t)}{Gln^g}$$

$$\text{Gln C3:} \quad \frac{dGln_3^g}{dt} = V_{GS} \cdot \frac{Glu_3^g(t)}{Glu^g} - (V_{NT}^i + V_{NT}^e + V_{eff}) - \frac{Gln_3^g(t)}{Gln^g}$$

$$\text{Gln C2:} \quad \frac{dGln_2^g}{dt} = V_{GS} \cdot \frac{Glu_2^g(t)}{Glu^g} - (V_{NT}^i + V_{NT}^e + V_{eff}) - \frac{Gln_2^g(t)}{Gln^g}$$

$$\text{Asp C3:} \quad \frac{dAsp_3^g}{dt} = V_x^g \cdot \frac{OAA_3^g(t)}{OAA^g} - V_x^g \cdot \frac{Asp_3^g(t)}{Asp^g}$$

$$\text{Asp C2: } \frac{d\text{Asp}_2^g}{dt} = V_x^g \cdot \frac{\text{OAA}_2^g(t)}{\text{OAA}^g} - V_x^g \cdot \frac{\text{Asp}_2^g(t)}{\text{Asp}^g}$$

$$\text{OG C4: } \frac{d\text{OG}_4^g}{dt} = (V_x^g + V_{shunt}^g + V_{PC}) \cdot \frac{\text{Pyr}_3(t)}{\text{Pyr}} + V_x^g \cdot \frac{\text{Glu}_4^g(t)}{\text{Glu}^g} - (V_x^g + V_{shunt}^g + V_g + V_{PC}) \cdot \frac{\text{OG}_4^g(t)}{\text{OG}^g}$$

$$\text{OG C3: } \frac{d\text{OG}_3^g}{dt} = (V_x^g + V_{shunt}^g + V_{PC}) \cdot \frac{\text{OAA}_2^g(t)}{\text{OAA}^g} + V_x^g \cdot \frac{\text{Glu}_3^g(t)}{\text{Glu}^g} - (V_x^g + V_{shunt}^g + V_g + V_{PC}) \cdot \frac{\text{OG}_3^g(t)}{\text{OG}^g}$$

$$\text{OG C2: } \frac{d\text{OG}_2^g}{dt} = (V_x^g + V_{shunt}^g + V_{PC}) \cdot \frac{\text{OAA}_3^g(t)}{\text{OAA}^g} + V_x^g \cdot \frac{\text{Glu}_2^g(t)}{\text{Glu}^g} - (V_x^g + V_{shunt}^g + V_g + V_{PC}) \cdot \frac{\text{OG}_2^g(t)}{\text{OG}^g}$$

$$\text{OAA C3: } \frac{d\text{OAA}_3^g}{dt} = \frac{1}{2} \cdot V_g \cdot \frac{\text{OG}_4^g(t)}{\text{OG}^g} + \frac{1}{2} \cdot V_g \cdot \frac{\text{OG}_3^g(t)}{\text{OG}^g} + \frac{1}{2} \cdot V_{shunt}^g \cdot \frac{\text{GABA}_2^g(t)}{\text{GABA}^g} + \frac{1}{2} \cdot V_{shunt}^g \cdot \frac{\text{GABA}_3^g(t)}{\text{GABA}^g} + V_{PC} \cdot \frac{\text{Pyr}_3(t)}{\text{Pyr}} + V_x^g \cdot \frac{\text{Asp}_3^g(t)}{\text{Asp}^g} - (V_x^g + V_{shunt}^g + V_g + V_{PC}) \cdot \frac{\text{OAA}_3^g(t)}{\text{OAA}^g}$$

$$\text{OAA C2: } \frac{d\text{OAA}_2^g}{dt} = \frac{1}{2} \cdot V_g \cdot \frac{\text{OG}_4^g(t)}{\text{OG}^g} + \frac{1}{2} \cdot V_g \cdot \frac{\text{OG}_3^g(t)}{\text{OG}^g} + \frac{1}{2} \cdot V_{shunt}^g \cdot \frac{\text{GABA}_2^g(t)}{\text{GABA}^g} + \frac{1}{2} \cdot V_{shunt}^g \cdot \frac{\text{GABA}_3^g(t)}{\text{GABA}^g} + V_{PC} \cdot \frac{\text{Pyr}_2(t)}{\text{Pyr}} + V_x^g \cdot \frac{\text{Asp}_2^g(t)}{\text{Asp}^g} - (V_x^g + V_{shunt}^g + V_g + V_{PC}) \cdot \frac{\text{OAA}_2^g(t)}{\text{OAA}^g}$$

$$\text{GABA C2: } \frac{d\text{GABA}_2^g}{dt} = V_{NT}^i \cdot \frac{\text{GABA}_2^i(t)}{\text{GABA}^i} - V_{shunt}^g \cdot \frac{\text{GABA}_2^g(t)}{\text{GABA}^g}$$

$$\text{GABA C3: } \frac{d\text{GABA}_3^g}{dt} = V_{NT}^i \cdot \frac{\text{GABA}_3^i(t)}{\text{GABA}^i} - V_{shunt}^g \cdot \frac{\text{GABA}_3^g(t)}{\text{GABA}^g}$$

$$\text{GABA C4: } \frac{d\text{GABA}_4^g}{dt} = V_{NT}^i \cdot \frac{\text{GABA}_4^i(t)}{\text{GABA}^i} - V_{shunt}^g \cdot \frac{\text{GABA}_4^g(t)}{\text{GABA}^g}$$

Second glial glutamine pool

The addition of a second Gln pool was shown to better describe the metabolic enrichment curves obtained upon ^{13}C -glucose administration in rats (Duarte and Gruetter, 2013). The authors proposed the existence of a non-visible Gln pool based on the difference in concentration observed between *in vivo* glutamine concentration measured with ^1H -MRS and *in vitro* with ^1H -NMR. The size of this second pool was proposed to be around half the total Gln concentration and in exchange with glial Gln only. As such, we used two distinct glial Gln pools of 50% (Gln^{g2}) and 30% (Gln^{g1}) of total Gln concentration. The addition of this pool led to an improvement in $\text{GlnC3}(t)$ and $\text{GlnC4}(t)$ enrichment fitting.

$$\text{Gln pool 1: } \frac{d\text{Gln}^{g1}_x}{dt} = V_{GS} \cdot \frac{\text{Glu}^g_x(t)}{\text{Glu}^g} - (V_{NT}^i + V_{NT}^e + V_{eff} + V_{ex}^g) \cdot \frac{\text{Gln}^{g1}_x(t)}{\text{Gln}^{g1}} + V_{ex}^g \cdot \frac{\text{Gln}^{g2}_x(t)}{\text{Gln}^{g2}}$$

$$\text{Gln pool 2: } \frac{d\text{Gln}^{g2}_x}{dt} = V_{ex}^g \left(\frac{\text{Gln}^{g1}_x(t)}{\text{Gln}^{g1}} - \frac{\text{Gln}^{g2}_x(t)}{\text{Gln}^{g2}} \right)$$

Second inhibitory GABA pool

With a comparable hypothesis of having two distinct metabolic pools of Gln in glia, we decided to test the relevance of a second pool of GABA in inhibitory neurons. GABA is synthesized from glutamate decarboxylase (GAD) only in GABAergic neurons but by two different enzyme isoforms, and thus in two compartments (Martin and Rimvall, 1993). GAD67, encoded by the gene *GAD1*, is expressed mainly in the cytoplasm of neurons and contributes to the “metabolic” GABA in neurons. GAD65, encoded by the gene *GAD2*, is located at the synapses

and functionally regulated based on neurotransmission demand (Pinal and Tobin, 1998). Relative GAD65 content in mouse hippocampus has been shown to be around 50% of total GAD (Sheikh et al., 1999). Therefore, GABAergic GABA pools were divided in two.

GABA pool 1:

$$\text{GABA C2: } \frac{dGABA_2^{i1}}{dt} = V_{GAD} \cdot \frac{Glu_4^i(t)}{Glu^i} + V_{ex}^i \cdot \frac{GABA_2^{i2}(t)}{GABA^{i2}} - (V_{NT}^i + V_{shunt}^i + V_{ex}^i) \cdot \frac{GABA_2^{i1}(t)}{GABA^{i1}}$$

$$\text{GABA C3: } \frac{dGABA_3^{i1}}{dt} = V_{GAD} \cdot \frac{Glu_3^i(t)}{Glu^i} + V_{ex}^i \cdot \frac{GABA_3^{i2}(t)}{GABA^{i2}} - (V_{NT}^i + V_{shunt}^i + V_{ex}^i) \cdot \frac{GABA_3^{i1}(t)}{GABA^{i1}}$$

$$\text{GABA C4: } \frac{dGABA_4^{i1}}{dt} = V_{GAD} \cdot \frac{Glu_2^i(t)}{Glu^i} + V_{ex}^i \cdot \frac{GABA_4^{i2}(t)}{GABA^{i2}} - (V_{NT}^i + V_{shunt}^i + V_{ex}^i) \cdot \frac{GABA_4^{i1}(t)}{GABA^{i1}}$$

$$\text{GABA pool 2: } \frac{dGABA^{i2}_x}{dt} = V_{ex}^i \left(\frac{GABA^{i1}_x(t)}{GABA^{i1}} - \frac{GABA^{i2}_x(t)}{GABA^{i2}} \right)$$

Chapter 3

MRS in a genetic model of mood disorder

Contributions to the work:

My contribution to this chapter consisted in the design of the study, acquisition of the data (high resolution ^1H - and ^{31}P -NMR, *in vivo* ^1H - and ^1H - ^{13}C -MRS, gene expression measurements, genotyping, treatment and behavioral experiments) and data/statistical analysis. The result interpretation and manuscript writing have been realized by myself as well, in collaboration with the co-authors. All the PET measurements were performed by Dr. Carole Poitry-Yamate and analyzed by Dr. Bernard Lanz. The respirometry experiments on brain homogenates were performed by Mr. Jocelyn Grosse in Prof. Carmen Sandi's lab. The GC-MS analyses were done by Dr. Laure Menin at the ISIC LC-MS platform, after optimization of the sample extraction by myself. The high-resolution NMR experiments were performed by myself at the ISIC NMR-platform with technical support from Dr. Emilie Baudat and Dr. Aurélien Bornet. The surgery for each *in vivo* ^1H - ^{13}C -MRS measurement was performed by the Vet-team.

This Chapter was partially adapted from:

Cherix A, Poitry-Yamate C, Lanz B, Zanoletti, O, Grosse J, Sandi C, Gruetter R and Cardinaux J-R: Deletion of *Crtc1* leads to hippocampal neuroenergetic impairments associated with depressive-like behavior: a magnetic resonance spectroscopy study (*Manuscript in preparation*).

Abstract

Genetic susceptibility is an important parameter in understanding the development of mood disorder. The study described in this chapter aimed at identifying metabolic impairments associated with the deletion of a brain-specific gene (*Crtc1*: CREB Regulated Transcription Coactivator 1) with known effect on mouse depressive-like behavior. More specifically, the goal was to identify potential biomarkers and/or endophenotypes in *Crtc1* knock-out mice with ^1H -MRS, associate these markers with a molecular/physiological mechanism and evaluate the effect of a treatment targeting the identified dysfunction. We report that the deletion of *Crtc1* leads to severe impairments in the glycolytic activity of the hippocampus, which translates into reduces levels of lactate and phosphocreatine visible with MRS, both of which were related to the depressive-like behavior of the mice. This hippocampal dysfunction, possibly linked to a reduced insulin sensitivity, leads to a strong imbalance between neuronal neurotransmitter cycling and energy production from glucose, in both inhibitory and excitatory neurons. Furthermore, reduced hippocampal energy status appeared to strongly affect inhibitory neurons, as revealed by the reduced expression of parvalbumin, glutamate decarboxylase 65 (GAD65) together with a higher GABAergic turnover of GABA. Treating the mice with ebselen, a mitochondrial boost with insulin-sensitization properties, improved the behavior, the hippocampal metabolic MRS-profile and gene expression, confirming the mechanistic link between depression and neuroenergetics. Our results provide a clear link between a behavior and an MRS-neuroenergetic profile and identify a treatment to target the pathophysiological mechanism involved. This chapter brings together most of the work I produced for this thesis.

3.1 Introduction

Mood disorders are among the leading causes of disability worldwide (Friedrich, 2017; Mathers et al., 2008). The difficulty in defining appropriate treatments is linked to the fact that these complex, dynamic and multifactorial psychiatric diseases are poorly understood (Li et al., 2012a). The way these diseases are approached complicates the identification of therapeutic targets: diagnosis is currently based on subjective signs and symptoms, rather than on objective biological or chemical measurements. In practice, there is an urgency to establish reliable biomarkers and endophenotypes within a framework of personalized treatment approaches (Hasler and Northoff, 2011; Lenzenweger, 2013). Defining subclasses of patients with consistent pathophysiological criteria is an essential starting point to achieve this aim. Magnetic resonance spectroscopy (MRS) can overcome this hurdle to quickly, non-invasively and accurately quantify the concentration of several neurochemicals in brain structures thought to be causal in the pathophysiology of mood disorders. A plethora of studies have already tried to identify reliable biomarkers specific to a given brain region or mood disorder subtype (Chitty et al., 2013; Luykx et al., 2012; Yildiz-Yesiloglu and Ankerst, 2006). However, the high level of discrepancies between these studies reflects the biological heterogeneity among patients from a common diagnostic category. Furthermore, metabolites quantified with MRS are multi-factorial entities, which require a thorough contextual analysis and *a posteriori* knowledge to be considered as reliable biomarkers. For instance, an increase in a given metabolite quantified with MRS can arise from an elevated synthesis or a reduced degradation, both related to a different pathological condition.

Applying MRS to animal models provides an efficient mean to link specific biomarkers with their associated pathophysiological mechanism. A rodent model cannot depict the whole complexity of a human psychiatric disorder. Nevertheless, dysfunctions in specific brain circuitries of a mammal are likely to give rise to comparable biochemical alterations in other species. This is particularly true for the limbic system as this set of structures has evolved in a similar way between *mus musculus* and *homo sapiens*. Understanding the mechanistic origin of limbic neurochemical disturbances in rodents provides an outstanding mean of relating a biomarker to a given pathological behavior and opens possible therapeutic strategies for psychiatric disorders. Genetically modified mice are gold standard models to study the

function of a given gene and provide a tool to investigate potential MRS biomarkers related to that gene.

CREB Regulated Transcription Coactivator 1 (CRTC1) is a protein expressed primarily in the brain and is abundant in limbic areas. Through its enhancement of CREB transcriptional activity and because of its ability to sense both Ca^{2+} and cAMP second messengers in neurons, CRTC1 has emerged as a key regulator of brain functions (Saura and Cardinaux, 2017; Uchida and Shumyatsky, 2018). *Crtc1* has been implicated in synaptic plasticity and memory formation (Kovács et al., 2007; Nonaka et al., 2014; Sekeres et al., 2012) and participates in regulation of energy and mood balance (Altarejos et al., 2008; Rossetti et al., 2017). Furthermore, *Crtc1* has been implicated in neurodegenerative disorders like Alzheimer's or Huntington's diseases (Parra-Damas et al., 2017; Xue et al., 2015). Several studies have identified a relationship of *Crtc1* polymorphisms with psychiatric disorders, with focus on obesity parameters (Choong et al., 2013; Lu et al., 2016b; Quteineh et al., 2016) and stress (Alisch et al., 2017). The molecular mechanisms implicating CRTC1 in the response to chronic stress has been recently addressed and revealed a stress-induced increase in SIK2 expression leading to CRTC1 phosphorylation and sequestration in the cytoplasm, inhibiting its transcriptional activity (Jiang et al., 2018). Finally, *Crtc1* has been implicated in the depressive-like behavior of rodent (Breuillaud et al., 2012; Ni et al., 2019). The *Crtc1* KO mouse model has been shown to be a promising model to study the pathways and mechanisms associated with treatment resistant depression, in particular to fluoxetine (Breuillaud et al., 2012; Meylan et al., 2016b, 2016a).

By applying MRS in the *Crtc1*^{-/-} mouse model, we have identified potential biomarkers related to hippocampal neuroenergetics and implicated in animal's depressive-like behavior. We have identified that these markers arise from impaired glucose metabolism and subsequent mitochondrial allostatic load leading to altered inhibitory neuron activity. Treating the animals with ebselen, a neuroprotective molecule with mood stabilizing properties, has allowed us to successfully reverse the energetic impairments and restore the behavior.

3.2 Material and methods

3.2.1 Animals

Crtc1 knock-out (KO) mice and wild-type (WT) littermates were bred and genotyped as previously described (Breuillaud et al., 2012). Mice were housed in standard Plexiglass filter-top cages in a normal 12h day-light cycle environment at a temperature of 23 ± 1 °C and humidity of 40%. Animals had *ad libitum* access to standard rodent chow diet and water. Weaning of newborn was done at 21 days followed by group-housing until being isolated at 6 weeks to prevent injuries of cage mates induced by the aggressive *Crtc1* KO male mice (Breuillaud et al., 2012). All experiments were performed in compliance with the ARRIVE (AnimalResearch: Reporting *in vivo* Experiments) guidelines with the accordance of the Swiss Federal Veterinary Office's guidelines and were approved by the Cantonal Veterinary Service.

3.2.2 Experimental design

This study was conducted with three different designs including male *Crtc1* KO and WT mice. The first set of experiments was done in mice at the age of 6 weeks to investigate basal metabolic dysfunctions before the separation from their littermates. The second batch was performed longitudinally, from 6 weeks to 24 weeks. After the first measurement time point, i.e. at 6 weeks of age, animals were isolated until the end of the study in a mild enriched environment including a paper house and a wooden stick. The third set of experiments was conducted on animals of 6 weeks, which were isolated after the first scanning session and kept isolated until the end of the 3-week stress/treatment protocol.

3.2.3 *In vivo* ^1H -Magnetic Resonance Spectroscopy (^1H -MRS)

Localized *in vivo* ^1H -magnetic resonance spectroscopy (^1H -MRS) was performed in the dorsal hippocampus (DH) and cingulate prefrontal cortex (PFC) of *Crtc1* KO and WT mice. Animals were under isoflurane anesthesia (1.5% mixed with 1:1 air:oxygen mixture) and monitored during the scan for physiological parameters. Breathing rate was maintained between 70 – 100 rpm using a small animal monitor (SA Instruments Inc., New York, USA) and rectal temperature was kept at $36.5 \pm 0.4^\circ\text{C}$ using a rectal temperature probe together with a circulating heating water bath. Animals were scanned in a horizontal 14.1T/26 cm Varian magnet (Agilent Inc., USA) with a homemade transceiver ^1H surface coil in quadrature. A set of T_2 -weighed images was acquired using a fast spin echo (FSE) sequence (15x0.4mm slices, $TE_{\text{eff}}/TR = 50/2000\text{ms}$, averages 2) to localize the volume of interest (VOI). The voxels were

positioned to include either a single dorsal hippocampus ($1 \times 2 \times 1 \text{ mm}^3$) or the cingulate prefrontal cortex ($1.4 \times 1.6 \times 1.2 \text{ mm}^3$). In each voxel, the field homogeneity was adjusted using FAST(EST)MAP (Gruetter and Tkáč, 2000) to reach a typical water linewidth of $15 \pm 1 \text{ Hz}$ for DH and $14 \pm 1 \text{ Hz}$ for PFC. Proton spectra were acquired with a spin echo full intensity acquired localized (SPECIAL) sequence ($TE/TR=2.8/4000 \text{ ms}$) (Mlynárik et al., 2006) using VAPOR water suppression and outer volume suppression. Scans were acquired in blocks of 30 times 16 averages for DH and 8 averages for PFC. Post processing included frequency correction based on the creatine peak and summing of all the spectra before quantification with LCModel (Provencher, 2001). Water signal was used as internal reference and fitting quality was assessed using Cramer-Rao lower bounds errors (CRLB) for a typical rejection threshold of $\text{CRLB} \geq 50\%$ (Cavassila et al., 2001). MRI images acquired were used to quantify prefrontal cortex volume using a pattern-based morphometric approach. A surface in the shape of a kite was drawn on the coronal images with each corner situated between the major sulcus, the central lower part of the corpus callosum and the two cingulum bundles as reference points. The surface was quantified and averaged for each brain section.

3.2.4 *In vivo* indirect carbon-13 Magnetic Resonance Spectroscopy (^1H - ^{13}C -MRS)

Preparation of the animal was comparable to ^1H -MRS with the main differences that animals underwent femoral vein cannulation for the infusion of $[\text{U-}^{13}\text{C}_6]\text{glucose}$ and the coil included a ^{13}C channel (for more details, see Chapter 2). The VOI included the bilateral dorsal hippocampus ($2 \times 5.5 \times 1.5 \text{ mm}^3$) and led to a typical water linewidth of $20 \pm 1 \text{ Hz}$ after field homogeneity adjustment. ^1H - ^{13}C -MRS spectra were acquired using the full intensity SPECIAL-BISEP sequence ($TE=2.8 \text{ ms}$, $TR=4000 \text{ ms}$, averages = 8) as previously described (Lizarbe et al., 2018b; Lizarbe et al., 2018c; Xin et al., 2009). The proton and inverted spectra (editing ON and OFF) were obtained using an interleaved acquisition and were subtracted in the post processing steps. The non-edited (proton) spectra were quantified using a standard basis set, while the non-edited (subtracted) spectra were fitted to a homemade basis set including LacC3, LacC2, AlaC2+C3, GluC4, GluC3, GluC2, GlnC4, GlnC3, GlnC2, AspC3, AspC2, GABAC4, GABAC3, GABAC2 and phantom-based spectra of glucose. Enrichment curves of each metabolite carbon position were determined by multiplying the fractional enrichment (FE) with the concentration measured in real time. Mathematical modelling was performed using

a pseudo 3-compartment model of brain energy metabolism (see Chapter 2) including following fluxes: Blood lactate influx V_{dil}^{in} ; excitatory neuron pyruvate dehydrogenase (PDH) activity V_{PDH}^e ; excitatory neuron transmittochondrial flux V_x^e ; excitatory neurotransmission rate V_{NT}^e ; inhibitory neuron PDH activity V_{PDH}^i ; inhibitory neurotransmission rate V_{NT}^i ; glutamate decarboxylase activity V_{GAD} ; and Gln exchange rate V_{ex}^g ; GABAergic exchange rate V_{ex}^i ; inhibitory neuron transmittochondrial flux V_x^i ; and glial dilution factor V_{dil}^g . The other parameters were calculated from the estimated fluxes: inhibitory TCA cycle V_{TCA}^i ; glial TCA cycle rate V_{TCA}^g ; glutamine synthetase activity V_{GS} ; GABA shunt rate $V_{shunt}^i (=V_{shunt}^g)$; lactate blood efflux V_{dil}^{out} ; total TCA cycle or the oxidative cerebral metabolic rate of glucose $CMR_g(ox)$.

3.2.5 *In vivo* ^{18}F FDG-PET

Dynamic non-invasive ^{18}F FDG positron emission tomography (PET) was performed as described previously (Lanz et al., 2014b; Seyer et al., 2013) and reported in Chapter 2.

3.2.6 High resolution NMR Spectroscopy

Mice were sacrificed using a microwave fixation apparatus (Gerling Applied Engineering Inc., Modesto, CA, USA) at 4kW for 0.6s after intraperitoneal injection of a lethal dose of sodium pentobarbital (~50 μ l to reach a dose of 150mg/kg). Brain was extracted, dorsal hippocampus was removed, frozen on liquid nitrogen and stored at -80°C. Samples were then ground on mortar using liquid nitrogen, weighed and followed by a $CHCl_3$ /MeOH Folch-Pi extraction (Folch et al., 1957). Samples were stirred at 4°C in a 1:1:1 mixture of $CHCl_3$:MeOH:H₂O for 30 min after which the aqueous phase was collected and lyophilized. The resulting extracted metabolites were resuspended in 600 μ l deuterium oxide containing 0.1 μ M 4,4-dimethyl-4-silapentane-1-sulfonic acid (DSS) as internal reference. High resolution NMR was performed using a DRX-600 spectrometer (Bruker BioSpin, Fällanden, Switzerland). 1H -NMR spectra were acquired with 400 scans using a pulse-acquired sequence (flip angle 30° and 5s pulse delay). ^{31}P -NMR spectra were acquired on the same sample with 10'000 scans using a proton-decoupled pulse-acquired sequence (flip angle 90° and 5s pulse delay). Spectra were analyzed and quantified using the MestReNova software (Mestrelab Research, Santiago de Compostela, Spain). Spectra were phase and baseline corrected manually, after which peaks

were integrated and referenced to the DSS resonance and normalized to NAA. NAA concentration in dorsal hippocampus was assumed to be 7mM as measured *in vivo*. Following resonance (δ in ppm) were integrated in the ^1H spectrum: lactate δ 1.31 (1H, d), ATP δ 6.13 (1H, d), alanine δ 1.47 (3H, d), creatine δ 3.026 (3H, s), phosphocreatine δ 3.028 (3H, s), N-acetyl-aspartate δ 2.00 (1H, s), aspartate δ 2.80 (1H, dd) glutamate δ 2.33 (2H, m), GABA δ 2.28 (2H, t), glutamine δ 2.43 (2H, m), myo-inositol δ 3.52 (2H, dd), taurine δ 3.42 (2H, t) and α -glucose δ 5.22 (1H, d) as 36% of total glucose. The peak of water-soluble lipids at 1.28 ppm were quantified (peak height) and normalize to NAA as a potential neurogenesis marker. Following resonance were integrated in the ^{31}P spectrum after setting the PCr resonance to 0 ppm: NAD^+ δ -8.31 (2P, q), NADH δ -8.15 (2P, m), UDPGlc δ -9.83 (2P, m), Pi δ 3.8 (1P, m), GPC δ 3.07 (1P, s). Due to overlap between resonances, the NADH/ NAD^+ ratio was calculated as follows: the left part of the NAD^+ quadruplet ($X = 2 \cdot \text{NADH} + \text{NAD}^+ + \text{UDPGlc}$) was integrated as well as the right part of the quadruplet ($Y = \text{NAD}^+$) and the -9.83 ppm UDPGlc resonance ($Z = \text{UDPGlc}$). Then, NADH was obtained by subtracting Y and Z from X followed by a division by 2.

3.2.7 Gene expression analysis

Total RNA was extracted and purified from micropunches of DH using an RNAeasy Plus Minikit (Qiagen, Venlo, Netherland) according to the manufacturer's instructions. NanoDrop Lite (Thermo Scientific, Wilmington, DE, USA) was used for the UV spectrophotometric quantification of RNA concentrations and purity assessment. cDNAs were obtained by reverse transcription of the mRNA samples in 50 μl reaction using Taqman Reagents and random hexamers (Applied Biosystems, Foster City, CA, USA). Real-time quantitative PCR was subsequently performed with cDNA concentrations of 0.16ng/ μl on a 96-well plate with SYBR Green PCR Master Mix (Applied Biosystems). The reaction started with a 2min step at 50°C and 10min at 95°C, followed by 45 cycles of 15 s at 95°C and 1 min at 60°C. The relative gene expression was determined using the comparative $\Delta\Delta\text{Ct}$ method and normalized to β -actine and $\beta 2$ microglobulin ($\beta 2\text{M}$) as housekeeping genes. The primers were used at a concentration of 250 nM.

3.2.8 Mitochondrial DNA copy number and damage quantification

Total DNA was purified and extracted from micropunches of the brain structures using a DNeasy Blood and Tissue kit (Qiagen, Venlo, Netherlands) according to the manufacturer's instructions. DNA concentrations of 0.16ng/μl were used for real-time qPCR in 96-well plates using SYBR Green PCR Master Mix (Applied Biosystems). Reaction steps were similar to the cDNA amplification and relative gene expression was determined with the $\Delta\Delta C_t$ method by normalizing the amplified mtDNA gene (ND6) to the genomic DNA gene ($\beta 2M^*$). Mitochondrial damage was quantified in a similar way as described in (Acevedo-Torres et al., 2009). Polymerase chain reaction of long fragments provides a good mean to assess the relative level of damage on DNA, as typical ROS-induced AP-sites (abasic sites) will stop polymerase activity and block fragment amplification prematurely. In this method, long fragments of DNA and mtDNA are amplified and normalized to the amplification of a shorter fragment. Amplification of large fragments of mtDNA (10kb) and nDNA (6.9kb) were performed on a thermocycler using GoTaqMix (Promega Corporation, Madison, WI, USA) with an initial denaturation step of 45s at 94°C, followed by 40 cycles of denaturation for 15s at 94°C, and annealing/extension at 68°C for 12min. A final extension at 72°C for 10min was done at the completion of the profile. Small mtDNA (91bp) and nDNA were amplified with a similar initial denaturation for 45s at 94°C, followed by 32 cycles of denaturation for 94°C, and annealing/extension at 64°C for 45s at 72°C. The final extension was performed as well. The samples were loaded with ethidium bromide on a 0.7% agarose gel for the large fragment and 2% agarose gel for small fragment together with 1kb and 100bp benchmarks respectively. The gel was run at 85mV for ~1h in TBE buffer. The primers were used at a concentration of 250 nM.

3.2.9 Mitochondrial respirometry

Animals were sacrificed by rapid decapitation followed by dorsal hippocampus dissection. The tissue was weighed, placed in a petri dish on ice with 2ml of relaxing solution (2.8 mM Ca_2K_2EGTA , 7.2 mM K_2EGTA , 5.8 mM ATP, 6.6 mM $MgCl_2$, 20 mM taurine, 15 mM phosphocreatine, 20 mM imidazole, 0.5 mM dithiothreitol and 50 mM MES, pH = 7.1) until further preparation. Gentle homogenization was then performed in ice-cold respirometry medium (miR05: 0.5 mM EGTA, 3mM $MgCl_2$, 60 mM potassium lactobionate, 20mM taurine,

10mM KH_2PO_4 , 20 mM HEPED, 110 mM sucrose and 0.1 % (W/v) BSA, pH = 7.1) with an Eppendorf pestle. 2mg of tissue were then used for high resolution respirometry (Oroboros Oxygraph 2K, Oroboros Instruments, Innsbruck, Austria) to measure mitochondrial respiration rates at 37°C. The experimental protocol consists in several experimental steps which test the capacity of the different mitochondrial electron transport chain component by measuring O_2 flux in the sample. 1) the activity of complex I (CI) is measured by adding ADP (5mM) to a mixture of malate (2mM), pyruvate (10mM) and glutamate (20mM). 2) Succinate (10mM) is subsequently added to the medium to stimulate complex II and measure the capacity of both complexes (CI+CII). 3) the protonophore FCCP (carbonyl cyanide 4-(trifluoromethoxy)phenylhydrazone) is then used (successive titrations of 0.2 μM until reaching maximal respiration) to uncouple the respiration and provides information on the maximal capacity of the electron transport system (ETS). 4) Rotenone (0.1 μM) was then used to inhibit complex I and quantify the contribution of complex II in the uncoupled state (ETS CII). 5) Antimycin (2 μM) is added to inhibit complex III and block the ETS in order to assess the residual oxygen consumption (ROX) provided by oxidative reactions unrelated to mitochondrial respiration. Oxygen fluxes were normalized by the wet weight of tissue sample and corrected for ROX.

3.2.10 Open field test

Animals were placed in a white arena (50 x 50 x 40 m^3) illuminated with dimmed light (30 lx). After 30 minutes of habituation in the experiment room, mice were introduced in the center of the arena and were allowed to explore for 25 min. Analysis of the videos provided the mean distance travelled and velocity. Mice were tracked for 20min, after removing the habituation period of the 5 first minutes, using a tracking software (Ethovision 11.0 XT, Noldus, Information Technology). (Walsh and Cummins, 1976)

3.2.11 Porsolt forced swim test

Animals were introduced into a 5L capacity cylinder of 15 cm in diameter containing 23-25°C tap water in dimmed light (30 lx). The session was recorded for 6min from above and videos were analyzed using a tracking software (Ethovision). Immobility time was measured after discarding the first minute of swimming (Breuillaud et al., 2012).

3.2.12 Tail suspension test

Mice were suspended individually by the tail on a metal bar at a height of ~35 cm. A stripe of adhesive tape was attached to the mouse tail at ~2cm from the extremity to perform the suspension to the bar. Animals were videotaped from the side and immobility time was recorded manually for 5 min (Breuillaud et al., 2012). In the longitudinal study, an averaged behavioral despair was computed based on the immobility times from the FST and TST. In this case, the percent immobility time of both experiments was averaged.

3.2.13 Repeated open-space forced swim test

The repeated OSFST protocol was used as described previously (Breuillaud et al., 2012; Meylan et al., 2016a). Animals were introduced into a cage (45x28x20) filled up to ~13cm with 34-35°C tap water colored with milk. Mice underwent a 4 consecutive day swim (day -4 to -1) for 15minutes followed by repeated sessions of 3-4 days of interval for 3 weeks (Days 0, 4, 8, 11, 13, 17, 20) under treatment. Water was replaced every 2 mice had swum to keep water temperature constant. Animals were videotaped from above and immobility time was recorded manually.

3.2.14 Ebselen treatment

Animals were treated upon chronic administration of ebselen (Tokyo Chemical Industry, Tokyo, Japan) from day 0 of the end of the repeated OSFST protocol (Fig 4A). Mice received oral administration (gavage) of ebselen (10mg/kg) dissolved in 5% (w/v) carboxymethylcellulose (CMC ; Sigma Aldrich) 2 times a day (mornings and evenings) for 21 consecutive days. Vehicle group were administered the same volume of 5% CMC solution. The dose was adjusted to the body weight gain.

3.2.15 Gas chromatography-mass spectrometry ebselen quantification

Brains were collected after the treatment protocol, frozen on liquid nitrogen, weighed, and processed with a Folch-Pi $\text{CHCl}_3/\text{MeOH}$ method (Folch et al., 1957). At the beginning of the extraction process (total of 48h), samples were spiked with PDID (2-phenyl-2,3-dihydro-1H-Indole-1,3-dione) as internal standard for the GC-MS measurements. To do so, PDID was dissolved in CHCl_3 and a volume corresponding to 22 nmol/wet tissue was added. The

chloroform phase was then collected and evaporated under N₂ flow until further gas chromatography coupled to mass spectrometry (GC-MS) experiments. Samples were suspended in 50 µl CHCl₃, centrifuged 10 min at 10'000 rpm and 1 µl was injected in GC-MS. Detection was performed with a TSQ 8000 Evo Triple Quadrupole Mass Spectrometer interfaced with a Trace 1300 Series GC (Thermo Scientific, Bremen, Germany). Samples were centrifuged for 10min at 10'000 rpm prior to injection (1 µl) in a 0.25 mm x 30 m Zebron ZB-5ms column (Phenomenex, CA, USA) using the following program: initial temperature 100°C held for 1min, ramped to 150°C at 15°C/min, ramped to 250°C at 20°C/min and held at 250°C for 10 min. The transfer line and ion source temperatures were kept at 250°C and 200°C, respectively. Ionization was done by electron-impact (EI, 70 eV) in the selected ion monitoring (SIM) mode, in the m/z range of 179-223 for PDID (5-14min, 0.2s dwell-time) and 195-275 (14-22 min, 0.2s dwell-time) for ebselen. Data were processed using XCalibur software (Thermo Scientific). Stock solutions of ebselen and PDID were prepared at 10 mM in CHCl₃. Calibration curve of ebselen was done by serial dilution of the stock solution in CHCl₃ spiked with 1 µM of PDID to final ebselen concentrations of 10nM, 100nM, 500nM, 1µM, 5µM, 10µM and 50µM. Each standard was injected in triplicate and the limit of detection for ebselen was around 500 nM. The ratio of ebselen/PDID signal were obtained from integration of the chromatogram and referenced to the initial PDID/brain weight ratio calculated for each sample.

3.2.16 Statistics

Statistics were all performed with GraphPad Prism (GraphPad Software, San Diego, CA, USA). All values are given as mean ± SEM unless stated otherwise. P-values of $p < 0.05$ were considered statistically significant. Metabolite data from high resolution ¹H- and ³¹P-NMR were analyzed with a non-parametric Welch t-test. Gene expression and metabolic comparisons with two factors (genotype and treatment) were analyzed with 2-way analysis of variance (ANOVA) with Bonferroni post-hoc test when appropriate. Data from the OSFST behavioral measurements were analyzed with a 2-way ANOVA with repeated measures followed by a fisher LSD post-hoc test (Meylan et al., 2016a). Standard deviation of metabolic flux estimates was obtained from 300 Monte-Carlo simulations. Flux comparisons between KO and WT was performed with a permutation analysis with 2000 random permutations, followed by individual two-tailed Student t-tests (Sonnay et al., 2016b). All the other

comparisons between WT and KO animals were performed with Student t-test. No correction for multiple comparisons was performed unless stated otherwise, as the reproducibility of the statistical outcome was favored, typically by repeating the measure with another method, rather than solely statistical significance in a given test.

3.3 Results

3.3.1 Neurochemical profile of *Crtc1*^{-/-} mice reveals low levels of hippocampal energy metabolites

In vivo ¹H-MRS performed in the dorsal hippocampus (DH) and in the cingulate prefrontal cortex (PFC) of *Crtc1*^{-/-} mice and their WT littermates led to the reliable quantification of up to 20 individual metabolites (Fig 3.1A). Spectra quality was comparable for both groups with a signal-to-noise ratio (SNR) of 11.8±0.9 for WT vs. 13.4±1.3 for KO in DH, and 15.0±0.7 for WT vs. 15.7±1.0 for KO in DH. The profile of DH showed marked decrease in Glu/GABA, choline containing compounds (CCC; PCho and GPC) and glucose compared to PFC, while Asp, and Asc were higher. KO animals showed a significant reduction in energy metabolites lactate, alanine and PCr/Cr ratio in DH (Fig 3.1B). The situation was different in PFC where these metabolites were unchanged, however, Tau, Glu and GPC were significantly higher (Fig 3.1B, bottom). The metabolic changes in PFC were associated with a PFC volume increase (Fig 3.2) together with a shrinking of the ventricles (data not shown).

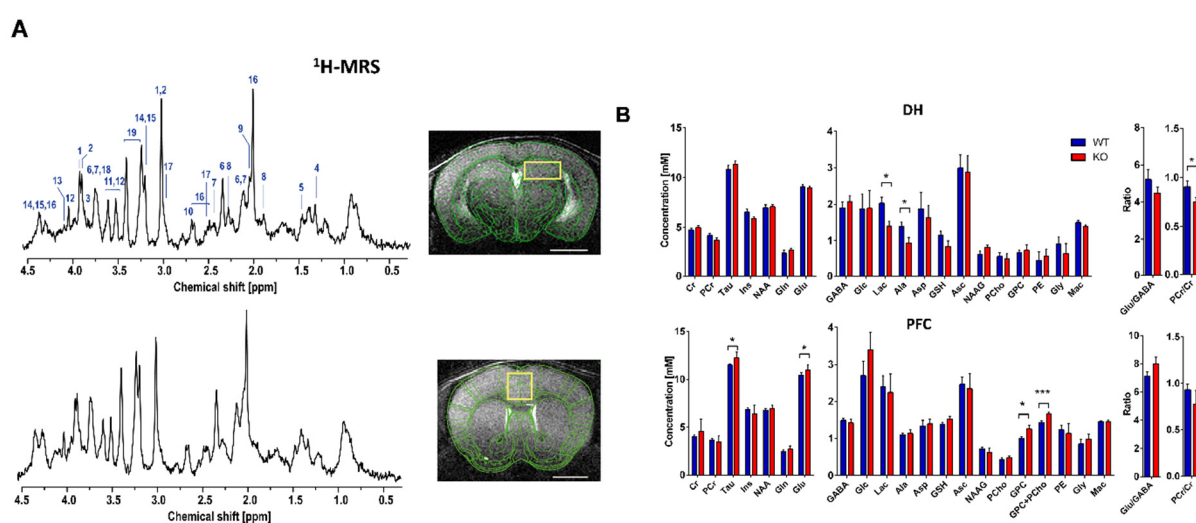


Figure 3. 1 : The neurochemical profile of *Crtc1*^{-/-} mice and WT littermates in DH and PFC *in vivo*
A. ¹H-MRS spectra acquired in the dorsal hippocampus (up) and cingulate prefrontal cortex (down) to assess the neurochemical profile *in vivo*. Typical images acquired for localization of the voxel of interest. Basis set included: 1. phosphocreatine (PCr), 2. creatine (Cr), 3. glucose (Glc), 4. lactate (Lac), 5. alanine (Ala), 6. glutamate (Glu), 7.

glutamine (Gln), 8. γ -aminobutyric acid (GABA), 9. N-acetylaspartyl-glutamate (NAAG), 10. aspartate (Asp), 11. glycine (Gly), 12. myo-inositol (Ins), 13. phosphoethanolamine (PE), 14. glycerophosphorylcholine (GPC), 15. phosphorylcholine (PCho), 16. N-acetyl-aspartate (NAA), 17. glutathione (GSH), 18. ascorbate (Asc), 19. taurine (Tau) as well as macromolecules (mac). Scale bar = 2mm. **B.** Neurochemical profile of the dorsal hippocampus (top) and prefrontal cortex (down) ($N_{WT}=10$, $N_{KO}=6$). All p values are from unpaired Student t-test, * $p<0.05$, ** $p<0.01$, *** $p<0.005$.

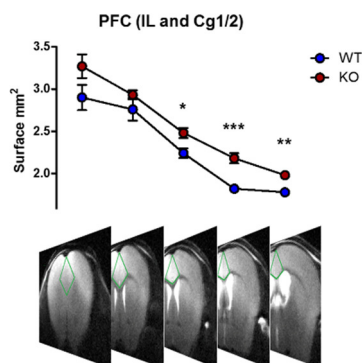


Figure 3. 2 : Morphometric analysis of mouse prefrontal cortex

Pattern-based analysis of prefrontal (infralimbic and cingulate cortices) volume at 6 weeks of age. All p values are from unpaired Student t-test, * $p<0.05$, ** $p<0.01$, *** $p<0.005$.

To confirm the hippocampal observations, we quantified the metabolic profile of DH with high resolution ^1H -NMR after metabolite extraction from microwave-fixed brains (Fig 3.3). PCr and the PCr/Cr ratio were found to be reduced in the KO animals as well, however, lactate and alanine did not appear to be different, which might be explained by the use of pentobarbital that was administered to the mice in that experiment rather than isoflurane used for the *in vivo* study. Myo-Inositol was reduced in the extracts while no difference was seen *in vivo*. No difference in ATP levels were observed. High resolution ^{31}P -NMR spectroscopy on the same samples revealed no change the NADH/NAD⁺ ratio but a significant rise in inorganic phosphate, in line with higher PCr hydrolysis (Fig 3.4).

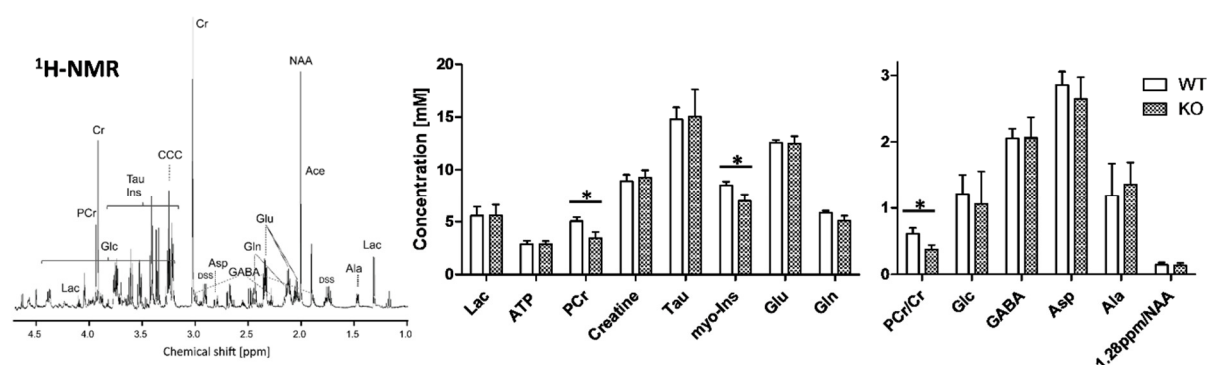


Figure 3. 3 : The ^1H -neurochemical profile of $Crtc1^{-/-}$ mice and WT littermates in DH metabolic extracts
 ^1H -NMR spectrum of hippocampal metabolic extracts (*left*) with quantifications (*right*) ($N_{WT}=10$, $N_{KO}=9$). All p values are from unpaired Student t-test, * $p<0.05$.

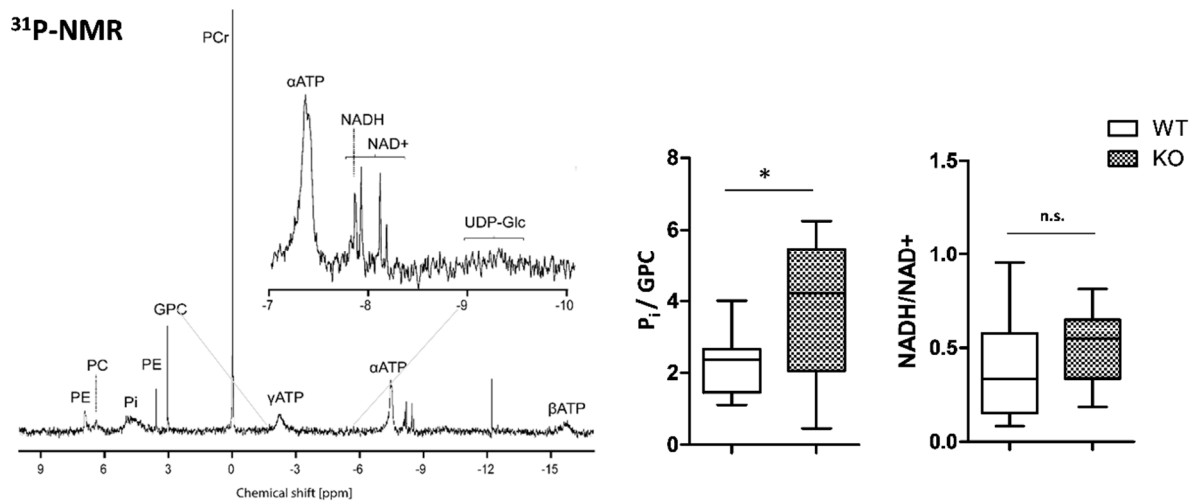


Figure 3. 4 : The ^{31}P -neurochemical profile of *Crtcl* $^{-/-}$ mice and WT littermates in DH metabolic extracts

^{31}P -NMR spectrum (*left*) of metabolic extracts from dorsal hippocampi with quantification (*right*) of inorganic phosphate (P_i) relative to GPC and the NADH/NAD $^{+}$ ratio ($N_{\text{WT}}=10$, $N_{\text{KO}}=9$). All p values are from non-parametric Welsch test, * $p<0.05$.

To test whether these energetic alterations arise from mitochondrial impairments, we investigated several mitochondrial parameters (Fig 3.5). Mitochondrial mass was comparable in all investigated brain regions based on relative mtDNA copy number measurements, besides a drop observed in the dentate gyrus (DG) part of the hippocampus (Fig 3.5A). Nevertheless, this drop was not confirmed at later age (12 weeks) and did not lead to a significant reduction in expression of mtDNA-encoded electron transport chain (ETC) components (Fig 3.5B) or ETC respiratory capacity (Fig 3.5C). Finally, expression levels of creatine kinases were higher (Fig 3.5D), while expression of GABA-synthesizing glutamate decarboxylases (GAD65 and 67) were reduced in the KO animals (Fig 3.5F). Together these results indicated that oxidative phosphorylation (OXPHOS) capacity of producing ATP was not altered and that the low levels of high-energy phosphates must have an origin upstream of mitochondria.

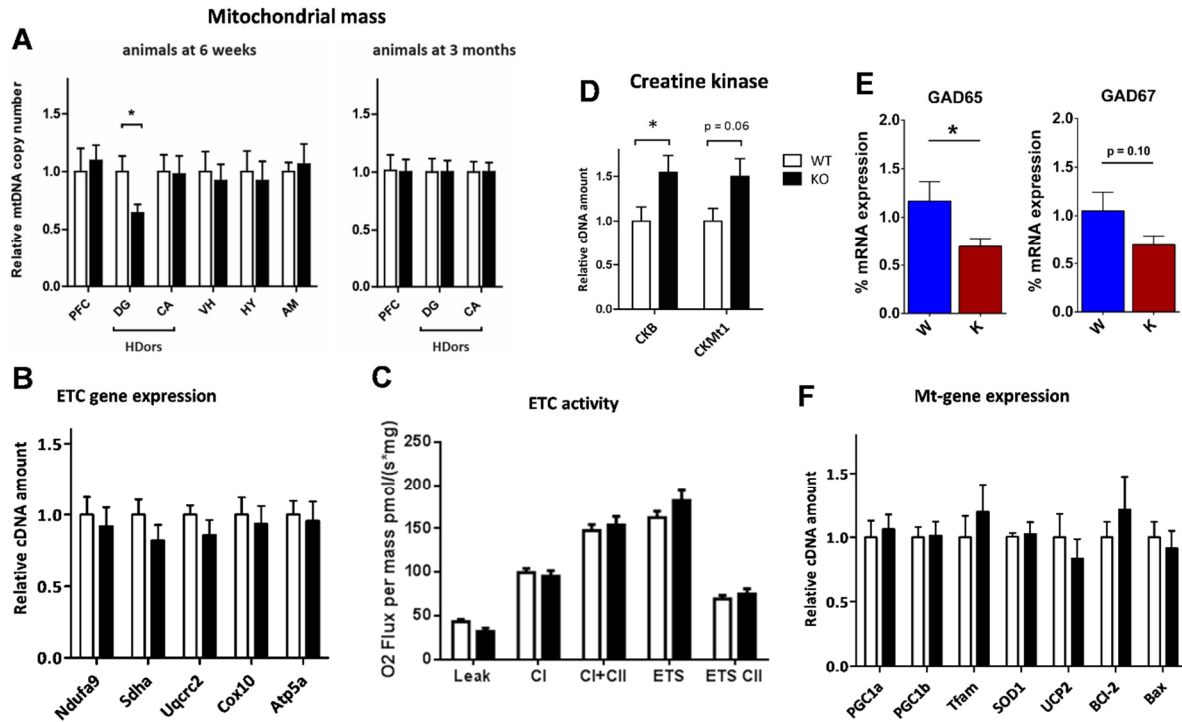


Figure 3. 5 : Gene expression analysis of *Crct1*^{-/-} mice and WT littermates at 6 weeks

A. Mitochondrial mass quantified in several brain regions of mice of 6 weeks and 3 months of age. Prefrontal cortex (PFC), Dentate gyrus part of the dorsal hippocampus (DG), Cornu Ammonis part of the dorsal hippocampus (CA), ventral hippocampus (VH), hypothalamus (HY) and amygdala (AM). **B.** Gene expression of components of the electron transport chain (ETC) ($N_{WT}=8$, $N_{KO}=8$). *Ndufa9* (Complex I), *Sdha* (Complex II), *Uqcrc2* (Complex III), *Cox10* (Complex IV), *Atp5a* (Complex V). **C.** Respirometric analysis of dorsal hippocampus. Complex 1 (CI), complex 2 (CII) and Electron transfer system (ETS) ($N_{WT}=8$, $N_{KO}=6$). **D.** Creatine kinase brain type (*CKB*) and mitochondrial isoform (*CKMT1*) expression. **E.** Glutamate decarboxylase expression (*GAD*) isoforms 65 and 67 ($N_{WT}=6$, $N_{KO}=6$). **F.** Gene expression of several mitochondria-related genes. Peroxisome proliferator-activated receptor gamma coactivator 1 (*PGC1a* and β), Mitochondrial transcription factor A (*Tfam*), Superoxide dismutase (*SOD1*), Uncoupler protein 2 (*UCP2*), B-cell lymphoma 2 (*BCL-2*), BCL-2 associated X (*Bax*) ($N_{WT}=8$, $N_{KO}=8$). All p values are from unpaired Student t-test, * $p<0.05$.

3.3.2 Hippocampal low energy metabolic profile is associated with impaired cerebral metabolic rate of glucose and GABA turnover in *Crct1*^{-/-} mice

In vivo ¹⁸FDG-PET experiments allowed us to further investigate the source of hippocampal energy dysfunctions. Brain extracts ¹⁸FDG from the blood, which leads to an intracellular accumulation of ¹⁸FDG-6P through the action of hexokinase. Accumulation curves of ¹⁸FDG showed a decrease in glucose entry and glucose phosphorylation in *Crct1*^{-/-} mice ($CMR_g = 0.49 \pm 0.03 \mu\text{mol/g/min}$) compared to their WT littermates ($CMR_g = 0.61 \pm 0.02 \mu\text{mol/g/min}$, * $p = 0.0045$, unpaired Student t-test; Fig 3.6A). The kinetics of ¹⁸FDG uptake and metabolism in *Crct1*^{-/-} mice was concomitant with development of hyperglycemia. Intergroup differences could not be attributed to differences in the amount of ¹⁸FDG entering the blood, body weight, nor to differences in the kinetics of the arterial input function. Subsequently, *in vivo* ¹H-[¹³C]-

MRS Allowed us to follow the fate of brain glucose and its incorporation in several brain metabolites during a 230 min long infusion of [U- $^{13}\text{C}_6$]Glc. Scanning the bilateral dorsal hippocampus allowed us to quantify 12 metabolite resonances (Fig 3.6B) with a 10 min time resolution and a comparable SNR between WT and KO (SNR(^1H): 21.4 ± 1.4 vs. 21.5 ± 0.8 ; SNR($^1\text{H}[^{13}\text{C}]$): 6.2 ± 0.5 vs. 5.6 ± 0.5 , for WT and KO respectively, mean \pm SEM). Fractional enrichment curves of glucose confirmed the lower glucose entry observed with PET in the KO animals but also revealed lower levels of lactate labelling (mainly due to the lower total lactate concentration) and higher GABA labelling in carbon positions 2,3 and 4 (Fig 3.7).

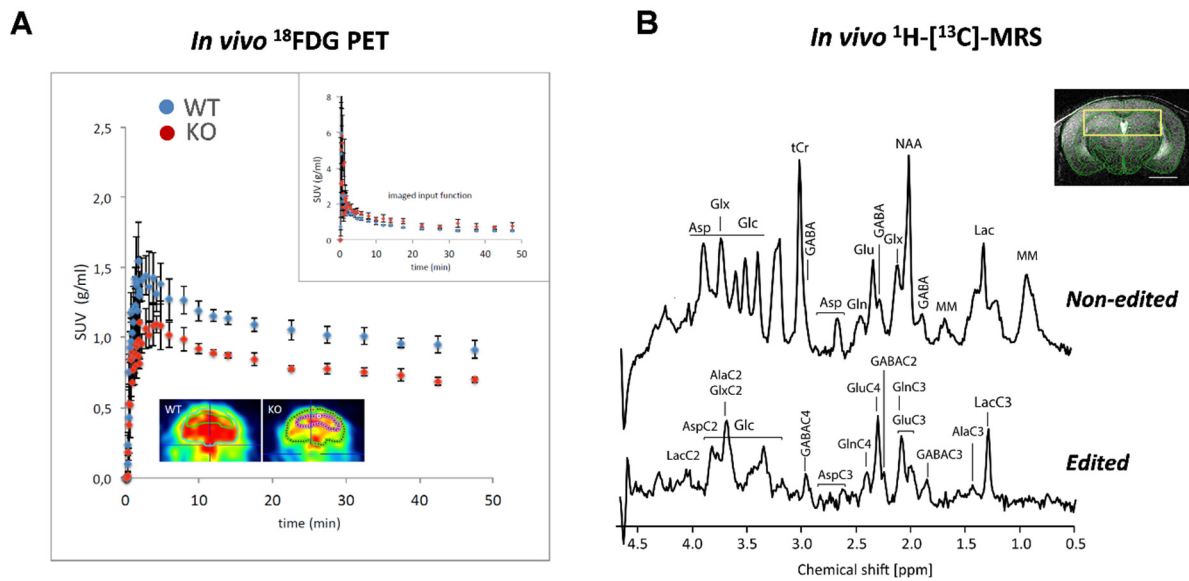


Figure 3. 6 : *in vivo* ^{18}F FDG-PET and ^1H - ^{13}C -MRS in *Crtcl* $^{-/-}$ mice and WT littermates at 6 weeks

A. *In vivo* ^{18}F FDG-PET indicates low glucose entry and ^{18}F FDG-P accumulation. Time course of the standard uptake value (SUV) is represented for WT (blue) and KO (red) for the region corresponding to dorsal hippocampus as represented on the color-coded image ($N_{\text{WT}}=3$, $N_{\text{KO}}=3$). Top-right: SUV of the vein cava used as input function for the PET modelling. **B.** ^1H - ^{13}C -MRS spectra acquired in the bilateral dorsal hippocampus. The non-edited spectrum (top) shows the total metabolic profile, while the edited spectrum identifies the fraction of metabolites which have incorporated ^{13}C .

Mathematical modelling of metabolic fluxes resulted in comparable values between the 1- and the pseudo 3-compartment model (Table 3.1). Results indicated that mitochondria suffer from the lack of pyruvate produced from glycolysis leading to reduced TCA cycle ($\text{CMR}_{\text{g(ox)}} = 0.85 \pm 0.06$ (WT) vs. 0.62 ± 0.06 (KO) $\mu\text{mol/g/min}$, **** $p < 0.0001$, Student t-test), while neurotransmitter cycling is increased (Fig 3.8). Among the GABAergic parameters, only the inhibitory TCA cycle was significantly reduced ($V_{\text{TCA}}^i = 0.35 \pm 0.05$ (WT) vs. 0.30 ± 0.02 (KO) $\mu\text{mol/g/min}$, * $p < 0.05$, Student t-test) and the exchange rate between the two GABA pools was increased in KO mice ($V_{\text{ex}}^i = 0.0006 \pm 0.0002$ (WT) vs. 0.0070 ± 0.0030 (KO) $\mu\text{mol/g/min}$, * $p < 0.05$, Student t-test). The latter flux was introduced as it allowed describing ^{13}C enrichment

data with an accurate fit by taking into account two distinct GABA pools generated by the two GAD isoforms and their respective role in inhibitory neuron metabolism. Together these results indicate that the absence of *Crtc1* leads to reduced glucose uptake and metabolism with concomitant increase in GABAergic function in DH.

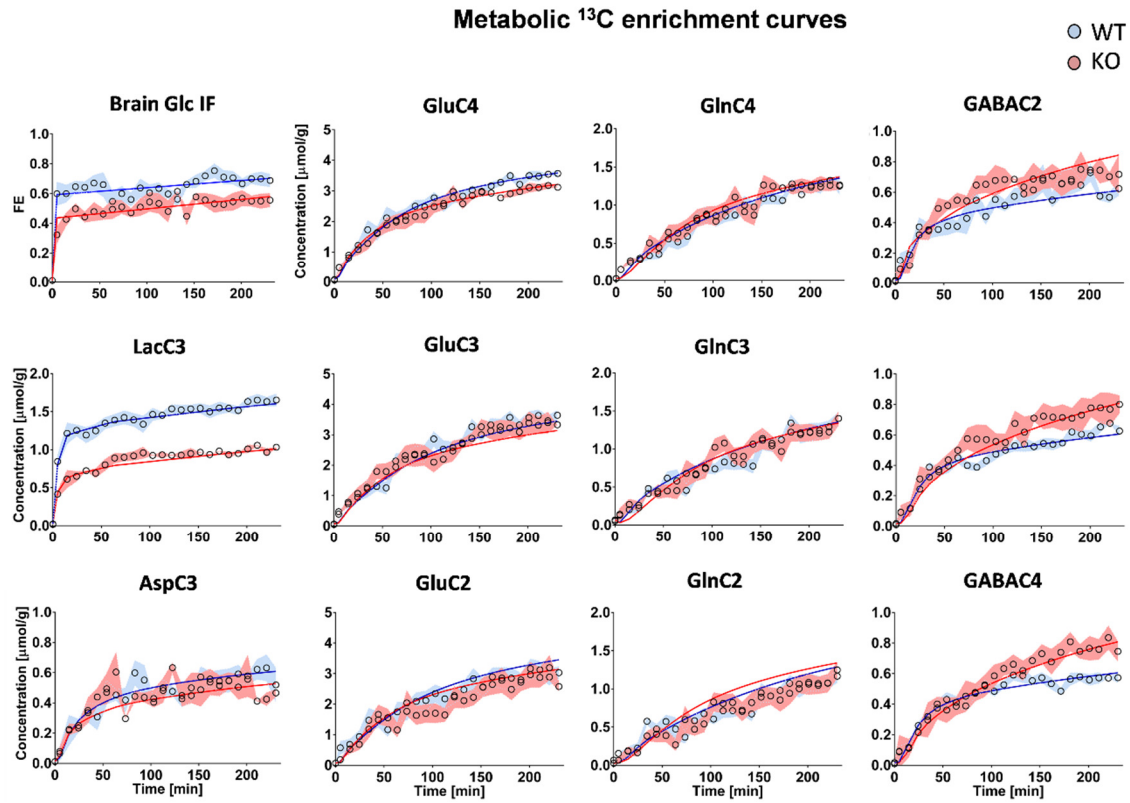


Figure 3. 7 : Fitting of a pseudo 3-compartment model of hippocampal glucose metabolism to the data measured with ^1H - ^{13}C -MRS in *Crtc1*^{-/-} mice and WT littermates

Time course of the labelling of each metabolite carbon positions detected in ^1H - ^{13}C -MRS. Data points represent the enrichment concentrations averaged over the whole group for WT (blue) and KO (red). Data is shown with the SD (colored shading) and the fitting curve from the metabolic flux analysis ($N_{\text{WT}}=8$, $N_{\text{KO}}=8$).

1-compartment model			Pseudo 3-compartment model					
	WT	KO		WT	KO			
$V_{\text{dil}}^{\text{in}}$	0.65±0.04	0.40±0.08****	$V_{\text{dil}}^{\text{in}}$	0.73±0.17	0.43±0.12**	V_{ex}^{g}	0.03±0.03	0.11±0.10
CMR_{g}	0.61	0.49*	CMR_{g}	0.61	0.49	V_{ex}^{i}	0.0006±0.0002	0.007±0.003*
V_{TCA}	1.71±0.03	0.77±0.07****	$V_{\text{PDH}}^{\text{e}}$	1.1±0.1	0.70±0.08****	Calculated fluxes		
V_{x}	0.46±0.17	0.22±0.09*	V_{x}^{e}	0.088±0.009	0.15±0.01	$V_{\text{TCA}}^{\text{i}}$	0.35±0.05	0.30±0.02*
V_{NT}	0.062±0.006	0.09±0.02**	V_{NT}^{e}	0.005±0.004	0.01±0.01	$V_{\text{TCA}}^{\text{g}}$	0.200±0.001	0.201±0.003
$V_{\text{dil}}^{\text{g}}$	0.56±0.01	0.10±0.03****	$V_{\text{PDH}}^{\text{i}}$	0.03±0.03	0±0.0	V_{GS}	0.046±0.005	0.05±0.01
Calculated flux			V_{x}^{i}	0±0.0	0±0.0	$\text{CMR}_{\text{g}}^{\text{(ox)}}$	0.85±0.06	0.62±0.06****
			V_{NT}^{i}	0.0006±0.0006	0.0016±0.0015	$V_{\text{shunt}}^{\text{i}}$	0.32±0.07	0.30±0.03
			V_{GAD}	0.32±0.06	0.30±0.08	$V_{\text{dil}}^{\text{out}}$	0.24±0.08	0.09±0.04****
$V_{\text{dil}}^{\text{out}}$	0.64±0.21	0.23±0.04***	$V_{\text{dil}}^{\text{g}}$	0±0.0	0±0.0	V_{x}^{g}	0.16	0.16

Table 3. 1 : Hippocampal metabolic fluxes obtained with a 1- or pseudo 3-compartment model of glucose metabolism in *Crtc1*^{-/-} mice and WT littermates

Estimated parameters from the 1-compartment model of brain energy metabolism: Blood lactate influx V_{dil}^{in} ; TCA cycle V_{TCA} ; transmittochondrial flux V_x ; neurotransmission flux V_{NT} ; glial dilution factor V_{dil}^g , and lactate blood efflux V_{dil}^{out} . Estimated parameters from the pseudo 3-compartment model of brain energy metabolism: Blood lactate influx V_{dil}^{in} ; excitatory neuron pyruvate dehydrogenase (PDH) activity V_{PDH}^e ; excitatory neuron transmittochondrial flux V_x^e ; excitatory neurotransmission rate V_{NT}^e ; inhibitory neuron PDH activity V_{PDH}^i ; inhibitory neurotransmission flux V_{NT}^i ; glutamate decarboxylase activity V_{GAD} ; and Gln exchange rate V_{ex}^g ; GABAergic exchange rate V_{ex}^i ; inhibitory neuron transmittochondrial flux V_x^i ; glial dilution factor V_{dil}^g . Parameters calculated from these metabolic fluxes: inhibitory TCA cycle V_{TCA}^i ; glial TCA cycle rate V_{TCA}^g ; glutamine synthetase activity V_{GS} ; GABA shunt rate $V_{shunt}^i (=V_{shunt}^g)$; lactate blood efflux V_{dil}^{out} ; total TCA cycle or the oxidative cerebral metabolic rate of glucose $CMR_g(ox)$. All the p values are from unpaired Student t-test, * $p < 0.05$, ** $p < 0.005$, *** $p < 0.0005$, **** $p < 0.0001$. Flux estimates are reported with the standard deviation generated by the MC simulation. All fluxes are given in $\mu\text{mol/g/min}$.

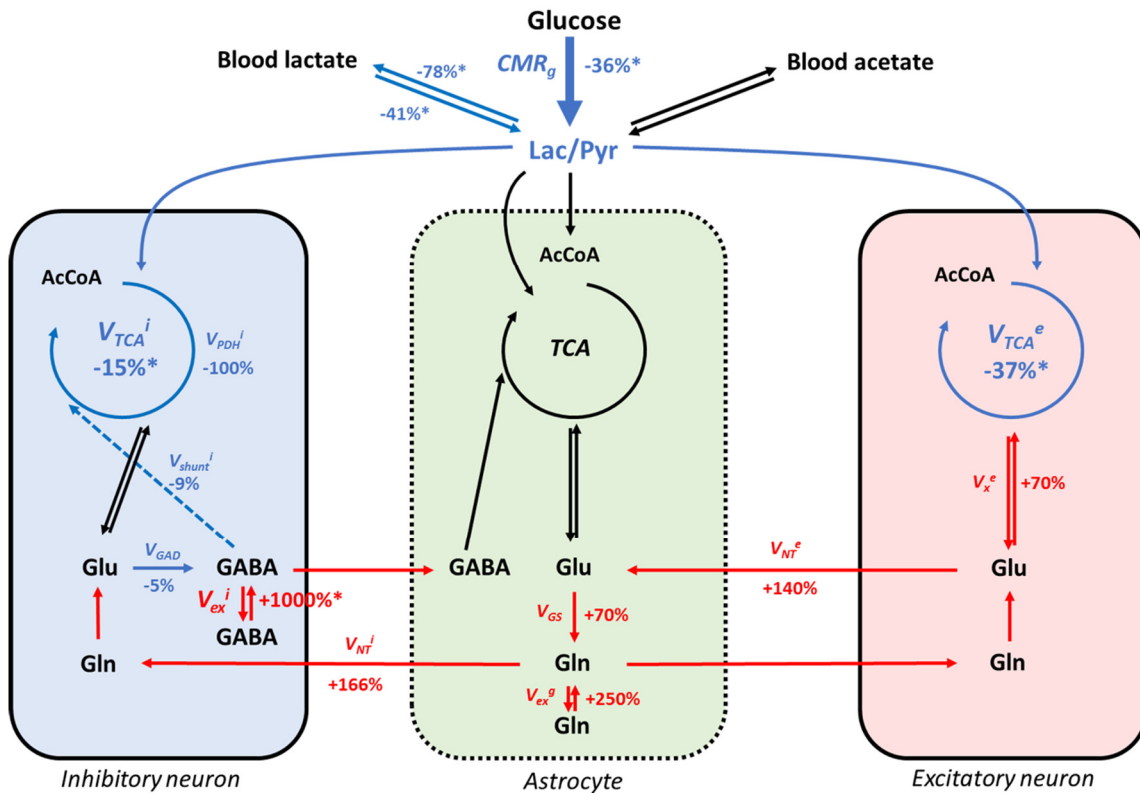


Figure 3.8 : Scheme of metabolic fluxes modeled with 3-compartment model in *Crct1*^{-/-} mice

Simplified representation of the 3-compartment model of brain glucose utilization, with fluxes found to be higher (red) and lower (blue) in KO animals compared to their WT littermates. Cerebral metabolic rate of glucose CMR_g ; excitatory neuron TCA cycle (V_{TCA}^e); inhibitory neuron TCA cycle (V_{TCA}^i); excitatory neuron transmittochondrial flux V_x^e ; excitatory neurotransmission rate V_{NT}^e ; inhibitory neurotransmission rate V_{NT}^i ; glutamate decarboxylase activity V_{GAD} ; and Gln exchange rate V_{ex}^g ; GABAergic exchange rate V_{ex}^i ; glutamine synthetase activity V_{GS} ; GABA shunt rate V_{shunt}^i . All statistically significant fluxes compared to the WT littermates are represented by an asterisk (*). All fluxes are given in $\mu\text{mol/g/min}$.

3.3.3 Hippocampal energetic and GABAergic profile correlate with the depressive-like behavior of *Crct1*^{-/-} mice

The relevance of the observed metabolic alterations in DH and PFC for animal's behavior was tested by following their evolution together with the depressive-like behavior upon animal

isolation (Fig 3.9A). Results indicated a clear correlation between hippocampal lactate levels and the depressive-like behavior (Fig 3.9B). At the age of 24 weeks (18 weeks of social isolation), KO animals showed significantly less depressive-like behavior as measured with the FST and TST. Overall, an inversion in the depressive-like behavior was observed between the two groups as a result of social isolation. A net difference in body weight appeared after a few weeks but did not impact the locomotor activity measured with the open field test (Fig 3.9D). The hippocampal energetic profile remarkably followed the behavioral evolution (Fig 3.9E). Hippocampus of WT animals at 24 weeks contained less lactate, PCr/Cr and Glu/GABA than before isolation and the opposite was observed for KO mice. Notably, the metabolic alterations observed in PFC did correlate or follow the behavior (Fig 3.9F). For instance, choline containing compounds were still higher in KO animals of 24 weeks compared to WT mice.

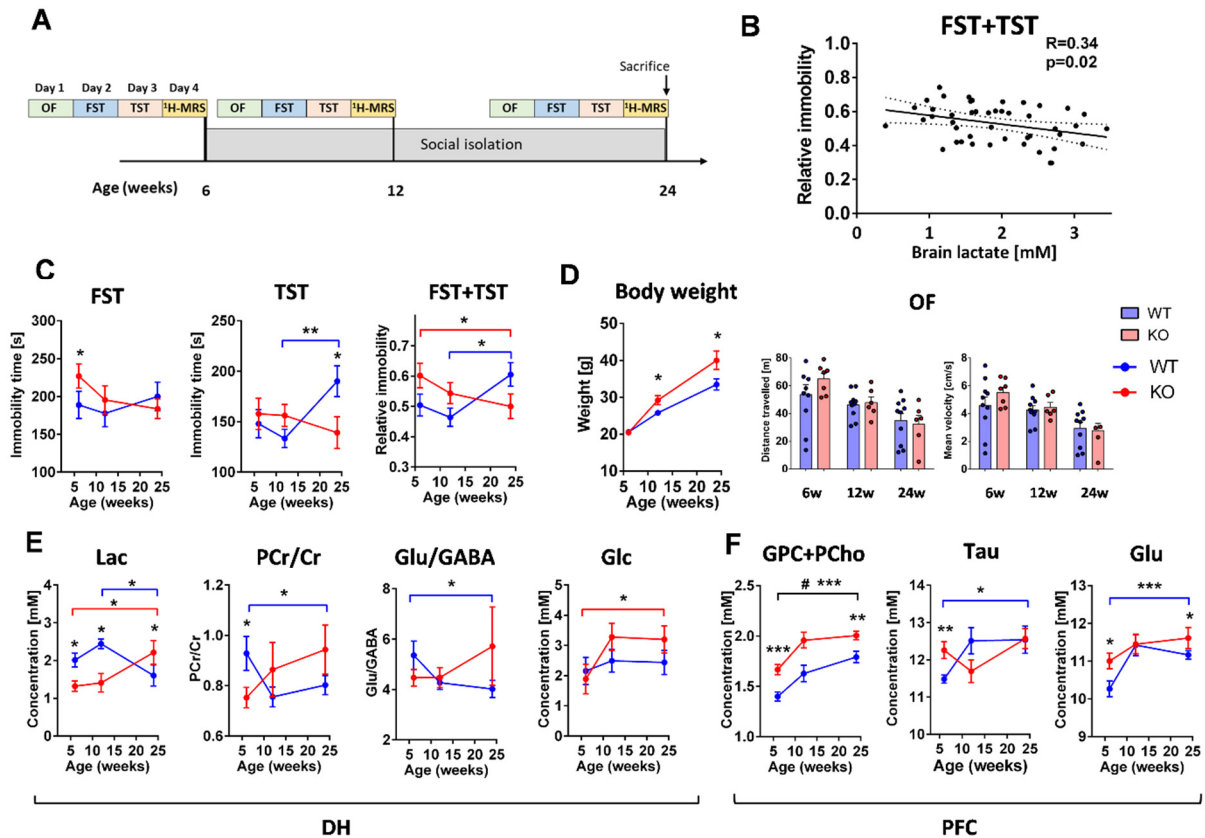


Figure 3. 9 : Hippocampal energetic and GABAergic MRS-profile correlates with the depressive-like behavior of *Crct1*^{-/-} mice.

A. Timeline of the longitudinal experiment. Locomotor activity was assessed on day 1 using an open field test (OF), followed by a forced swimming test (FST) on day 2, and a tail suspension test (TST) on day 3, before the ^1H -MRS session performed on day 4. Right after the first scan, at the age of 6 weeks, animals were isolated until the end of the study. The same set of behavioral tests was performed before the ^1H -MRS scan at the age of 12 weeks and 24 weeks. **B.** Hippocampal lactate levels correlated with the intensity of the depressive-like behavior. **C.** Longitudinal assessment of mice depressive-like behavior. **D.** Body weight and locomotor activity assessed with OF. **E.** Neurochemical profile of dorsal hippocampus (DH) measured with ^1H -MRS reveals an inversion of energy metabolite content. Lactate (Lac), phosphocreatine/creatine (PCr/Cr), glutamate/GABA ratio (Glu/GABA) and

glucose (Glc). **F.** Neurochemical profile of prefrontal cortex (PFC) measured with ^1H -MRS does not reveal an inversion in metabolite content for choline containing compounds (GPC+PCho), Taurine (Tau) and glutamate (Glu). All the p values are from unpaired or paired Student t-test, * $p < 0.05$, ** $p < 0.01$, *** $p < 0.005$, $N_{\text{WT}}=10$, $N_{\text{KO}}=6$.

Gene expression analysis of DH at the end of the longitudinal protocol revealed significant differences in energy metabolism related regulators, and showed an inverted trend compared to results at 6 weeks mentioned previously (Fig 3.10). KO animals showed higher expression levels of mitochondrial biogenesis factor PGC1 α but no difference in creatine kinases compared to control. This is a significant shift from the higher levels of creatine kinases with no difference of PGC1 α that were observed in KO animals at 6 weeks (Fig 3.5D and F). Furthermore, a consistent increase in GAD and parvalbumin expression was observed in KO mice, which confirms a link between energy metabolism and inhibitory function. Finally, GLUT4 was found to be reduced in KO animals while no difference was observed in other glycolysis-related genes (GLUT3, GLUT1, PFK1, PFK2, MCT1 and MCT2) suggesting that improvement of glycolytic function is not underlying the improved behavior of KO mice after 6 months of isolation. Rather, improved mitochondrial function appears to be beneficial. Together these results suggest that KO animals respond more positively to social isolation than WT littermates leading to a lower depressive-like behavior and increased energetic function.

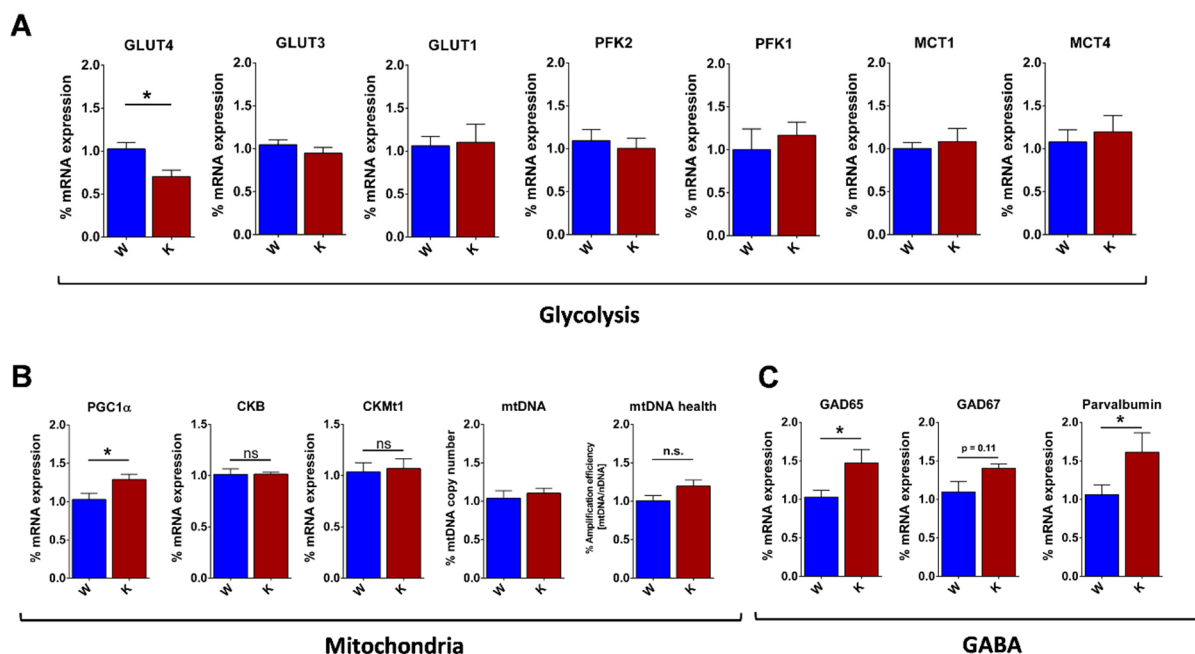


Figure 3. 10 : Hippocampal energetic and GABAergic gene expression relate to the depressive-like behavior of *Crtl*^{-/-} mice.

A-C. Hippocampal gene expression analysis at the age of 24 weeks indicates an inversion in glycolytic, mitochondrial and GABAergic gene expression. **A.** Glycolysis-related gene expression: Glucose transporter 4,3 and 1 (GLUT4,3 and 1), phosphofructokinase 1 and 2 (PFK1-2), monocarboxylate transporter 1 and 4 (MCT1 and 4). **B.** Mitochondria-related gene expression: Peroxisome proliferator-activated receptor gamma coactivator 1-

alpha (PGC1 α), Creatine kinase brain type (CKB) and mitochondrial isoform (CKMt1), relative mitochondrial DNA copy number (mtDNA) and relative mtDNA damage assessed by long fragment PCR (mtDNA health). **C.** GABA-related gene expression: Glutamate decarboxylase isoforms (GAD65 and 67) and parvalbumin. All the p values are from unpaired Student t-test, *p<0.05, N_{WT}=10, N_{KO}=6.

3.3.4 Hippocampal energetic and GABAergic profile is impaired by stress and can be restored with the mood stabilizer ebselen

With the working hypothesis that stress is likely to induce a depressive-like behavior in animals with lower energetic resilience in DH, we subjected the animals to a repeated open-space forced swim test (OSFST) protocol together with ¹H-MRS. After 4-consecutive days of swimming sessions and establishment of a stable depressive-like behavior, animals were treated with an oral dose of ebselen 2x a day for 3 weeks. As expected from previous studies, before the initiation of the treatment, KO animals showed a marked increase in immobility time compared to WT (Fig 3.11). Ebselen restored the behavior of KO animals to a level comparable to WT animals but had no or little effect on WT mice. Analysis of ebselen concentration in the brain using GC-MS after the treatment protocol indicated that ebselen crossed the blood-brain barrier as we were able to detect its presence in metabolic extracts (at 275 m/z). Concentrations were relatively variable but always lower than the brain concentrations typically observed after chronic Li⁺ treatment, i.e. in the millimolar range (Fig 3.11C). Ebselen, considered as a “safe-lithium mimetic” due to the similar molecular target, appears to be ~100x less concentrated in the brain, in line with its ~100x lower IC₅₀ (for IMPase activity) (Singh et al., 2013).

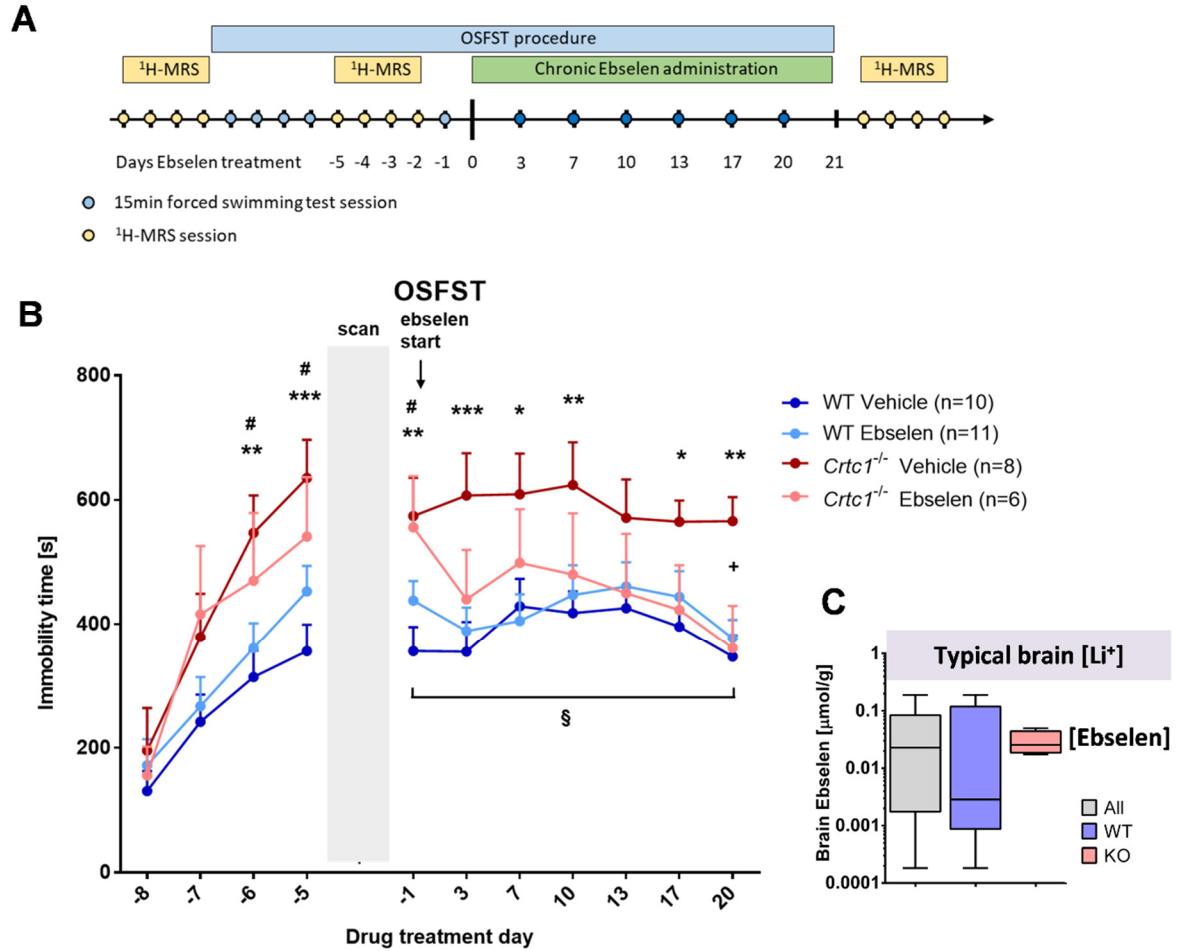


Figure 3. 11 : *Crtc1*^{-/-} mice depressive-like behavior is impaired by stress and can be restored with the mood stabilizer ebselen.

A. Timeline of the open-space forced swimming test (OSFST) and ebselen treatment experiment ($N_{WT(CTRL)}=9$, $N_{WT(EBS)}=8$, $N_{KO(CTRL)}=9$, $N_{KO(EBS)}=6$, mean±SEM). Animals were scanned once during the 4 days prior to the test followed by 4 consecutive daily sessions of swimming. A second scan was performed before the initiation of the treatment, after what animals were exposed to chronic forced swimming with concomitant administration of ebselen or carboxymethylcellulose (CMC) for 21 days. At the end of the experiment, a last session of scan was performed before sacrificing the animals for hippocampal gene expression analysis. **B.** Depressive-like behavior determined with the immobility time spent during the OSFST. A Two-way ANOVA for repeated measures indicated a strong genotype effect ($F_{1,10}=65.09$, $p<0.0001$) as well as an interaction ($F_{1,10}=41.84$, $p<0.0001$) and a treatment effect ($F_{1,10}=5.45$, $p=0.04$). Post hoc analysis with LSD Fisher test indicated that all the KO mice showed a significant increase in immobility after the first 4 days swimming session (** $p<0.01$, *** $p<0.005$ for VEH and # $p<0.05$ for EBS vs their respective WT group). Depressive-like behavior of KO VEH group remained significantly higher than WT over the 21 days of test (* $p<0.05$, ** $p<0.01$ and *** $p<0.005$ for VEH KO vs VEH WT). After the 21 days of OSFST, the depressive-like behavior of the treated KO animals was significantly reduced (* $p<0.05$ compared to KO VEH at day 20 and § $p<0.05$ compared to KO EBS at day 0). **C.** Brain ebselen concentration after the treatment was in the 0.01mM range as determined by GC-MS. Typical brain lithium concentration [Li⁺] range used for bipolar disorder is indicated as benchmark.

Gene expression analysis in DH at the end of the protocol (Fig 3.12) indicated an effect of treatment on the expression of PGC1 α and CKMt1 suggesting improved mitochondrial function. An effect on GLUT4 was also observed suggesting that glycolytic activity and/or

insulin sensitivity are also stimulated by ebselen. GABA-related gene expression was impaired by the stress protocol and normalized after ebselen treatment.

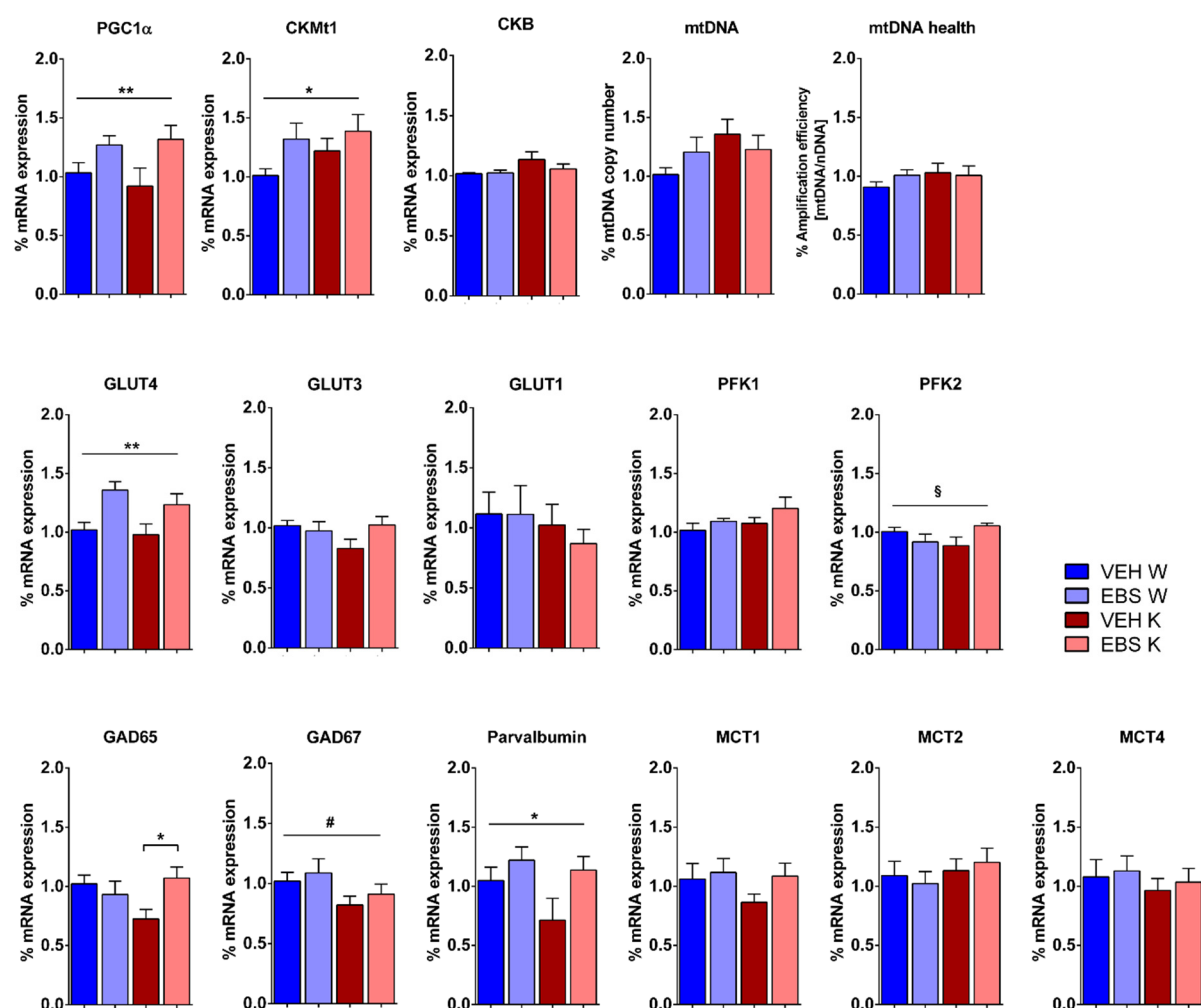


Figure 3. 12: Hippocampal energetic and GABAergic gene expression is impaired by stress and can be restored with the mood stabilizer ebselen.

GABA-related genes were differentially impaired by the stress and ebselen increased energy-related mRNA levels. Gene expression analysis reveals an effect of *Crtc1* on GAD67 ($F_{1,28}=4.39$, $*p<0.05$, two-way ANOVA), and GAD65 (Interaction: $F_{1,27}=5.53$, $*p<0.05$, two-way ANOVA; $*p<0.05$, Bonferroni's post-hoc test) mRNA content, together with an effect of treatment on PGC1 α ($F_{1,27}=13.28$, $**p<0.005$, two-way ANOVA), CKMT1 ($F_{1,27}=4.79$, $*p<0.05$, two-way ANOVA), GLUT4 ($F_{1,23}=8.22$, $**p<0.01$, two-way ANOVA) and parvalbumin ($F_{1,24}=4.28$, $*p<0.05$, two-way ANOVA). An interaction in PFK2 levels was also observed (Interaction: $F_{1,28}=4.87$, $*p<0.05$, two-way ANOVA).

The energetic profile measured with ^1H -MRS over the whole stress protocol (difference between day 21 and day -9) indicated that stress tend to reduce hippocampal PCr/Cr ratio while increasing lactate, suggesting an oxidative-to-glycolytic switch (Fig 3.13). This glycolytic switch correlated well with the worsening of the depressive-like behavior when comparing final stage with basal neurochemical profile (difference between day 21 and day -8). Similarly, the improvement of the behavior after treatment correlated well with an inversion of this

glycolytic switch, resulting in higher PCr/Cr ratio and lower lactate levels (difference between day 21 and day 0) (Fig 3.14).

In vivo ¹H-MRS – Stress effect

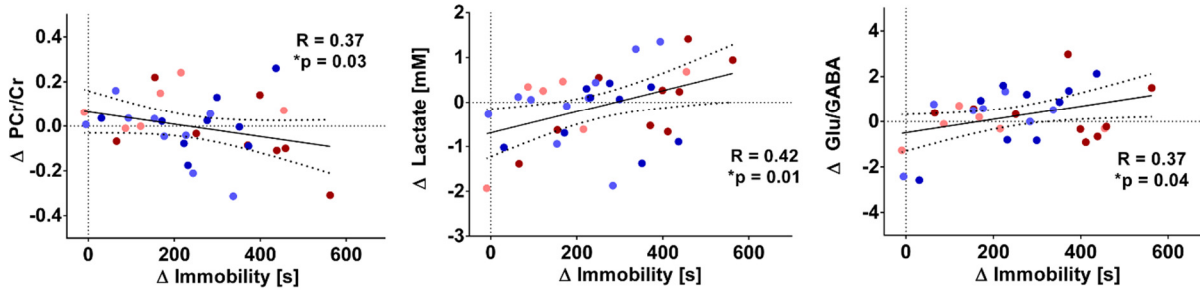


Figure 3.13 : Effect of chronic stress on the hippocampal MRS-profile

Effect of chronic stress exposure with OSFST on hippocampal energetic profile and depressive-like behavior (difference between day 21 and day -9). The difference in hippocampal PCr/Cr, Lac and Glu/GABA content correlated with the increase in depressive-like behavior between day -9 and post-OSFST (day 21). The dotted lines represent the 95% confidence interval of the linear regression line.

In vivo ¹H-MRS – Treatment effect

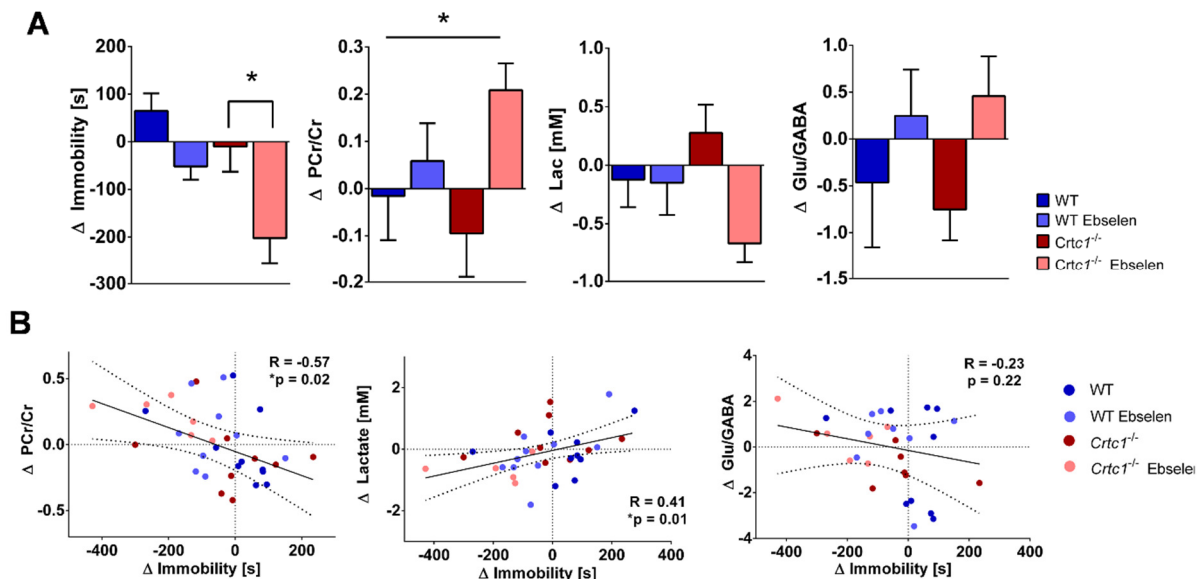


Figure 3.14 : Effect of ebselen on the hippocampal MRS-profile

Effect of ebselen treatment on hippocampal neurochemical profile (difference between day 21 and day 0). **A.** Ebselen treatment led to an increase in PCr/Cr ratio (Treatment effect: $F_{1,31}=4.41$, $*p<0.05$) and a drop in lactate (Treatment effect: $F_{1,31}=3.49$, $p=0.07$) together with a reduction of immobility (Treatment effect: $F_{1,31}=13.7$, $***p<0.001$; $Crtc1$ effect: $F_{1,31}=7.30$, $*p<0.05$, two-way ANOVA). **B.** The hippocampal increase in PCr/Cr ratio and drop in lactate correlated with the improvement of the depressive-like behavior. The dotted lines represent the 95% confidence interval of the linear regression line.

3.4 Discussion

In this study, we have identified a set of potential biological MRS markers in hippocampus and prefrontal cortex related to the deletion of *Crtc1*. We have identified a potential mechanism leading to the observed hippocampal energy impairments and related it to the animal's depressive-like behavior. Finally, we have been able to reverse the metabolic dysfunction and improve the depressive-like behavior by selecting an appropriate mood stabilizer targeting the identified mechanism.

3.4.1 Deletion of *Crtc1* induces neuroenergetic impairments in hippocampus

Deletion of *Crtc1* has been shown to induce an obesity and insulin resistance phenotype (Altarejos et al., 2008). Even though *Crtc1* KO mice do not show body weight differences at early adulthood (6 weeks of age), glucose entry in the brain is significantly reduced as revealed by our PET and ^1H - ^{13}C -MRS results. The reduced expression levels of GLUT4, the insulin-dependent glucose transporter, could provide a mechanistic link to explain the origin of hippocampal inability to efficiently absorb blood glucose. However, reduced GLUT4 levels were only observed after social isolation of KO mice, together with an improved behavior. Social isolation is a well-established stressor for mice due to the deprivation of social interaction (Ueno et al., 2017). Assuming isolation is a less stressful event for KO mice than sharing their litter, one could argue that the development of a depressive-like behavior depends on the exposure to stress and not only on the ability for glucose to enter the brain (seen as lower GLUT4 levels). Several lines of evidence suggest an association between insulin resistance and depression (Ali et al., 2006; Kan et al., 2013; Lyra e Silva et al., 2019). For instance, insulin and IGF-1 have been shown to induce an IGF-1 receptor dependent antidepressant-like effect in rats after intraventricular injection (Mueller et al., 2018). STZ induced diabetes provokes a depressive-like behavior in mice, which is reversed with insulin treatment (Gupta et al., 2014). PET studies showed reduced glucose metabolism and blood flow in frontal cortical areas of depressed patients (Videbech, 2000), suggesting that the link between depression and insulin resistance might indeed be the reduced glucose entry in the brain. On the other hand, Fu et al. reported an increased hippocampal activity concomitant with reduced anterior cingulate metabolism using ^{18}F FDG-PET together with resting state BOLD-fMRI in depressed patients (Fu et al., 2018). While the link between insulin resistance

and depression remains to be elucidated, our results indicate that *Crtc1* KO mice provide a good framework for finding mechanistic links between altered cerebral glucose metabolism and their effect on behavior.

The consequences of impaired glucose metabolism go beyond the reduction in lactate production. Our findings consistently reveal reduced hippocampal PCr levels together with increased inorganic phosphates; a sign that mitochondria are under pressure. High levels of ADP and P_i (mainly in the mitochondrial matrix) due to lower ATP-synthase activity are likely to explain the lower levels of PCr (mainly cytoplasmic). It is unclear whether increase in creatine kinase expression is related to the lack of ATP shuttling from the mitochondria to the cytoplasm as these enzymes usually operate close to equilibrium. Furthermore, phosphotransfer kinetics appear to be very complex and difficult to model into a simple 2-compartment (mitochondria-cytoplasm) chemical reaction. For instance, phosphotransfer networks, including several near-equilibrium phosphotransfer enzymes (like creatine kinases) aligned in chains in the mitochondria (Dzeja and Terzic, 2003). However, following this idea, increase in both CK enzymes might thus provide a mechanism to compensate for the “lack of diffusional flux” of high energy phosphates impaired by the low mitochondrial ATP production (and thus low mitochondrial ATP concentration) (Fig 3.15). As a result, homeostasis is maintained, as revealed by the constant ATP and NAD/NAD⁺ levels measured, but at a certain metabolic cost, i.e. an allostatic load. An allostatic load can be seen as an energy-costly response to a stressor in order to maintain homeostasis (see introduction) (McEwen, 1998). Mitochondrial dysfunctions have been observed in various diseases including metabolic disease, type II diabetes, cancer, neonatal fatalities and neurodegenerative disorders (Golpich et al., 2017). Physiological, structural and genetic alterations have been observed in psychiatric patients leading to the development of several mitochondrial hypotheses regarding disease pathophysiology. High comorbidity exists between genetic mitochondrial disorders and bipolar disorders (BPD) (Fattal et al., 2006). Increased levels of lactate in cerebrospinal fluid have been found in both BPD and schizophrenic patients, suggesting a glycolytic switch or reduced OXPHOS activity in the brain (Regenold et al., 2009), corroborated with findings highlighting reduced mitochondrial ETC activity brain postmortem and in platelets (Ben-Shachar et al., 1999; Maurer et al., 2009). Our results emphasize the dependence of oxidative metabolism on glycolysis and vice-versa. As a result, impaired

glucose homeostasis is likely to affect mitochondrial function, and cellular viability, especially under high energy demands.

3.4.2 Hippocampal energy impairments result in GABAergic dysfunction

As a response to overall hippocampal energy depletion, we observe a concomitant rise in GABA turnover and drop in GAD expression. Our metabolic flux analysis suggests a potential increase in GABA dynamics inside inhibitory neurons, typically related to altered GAD activity. GAD exists in two isoforms, which are differentially located inside inhibitory neurons. While GAD67 is more structural with relative constant activity, GAD65 is more prominent at synapses and its activity correlates with neuronal neurotransmission rate. GAD conformation switches from an Apo (inactive) to a Holo (active) form in response to reduction of high energy phosphate, i.e. increased inorganic phosphate or reduced PCr and ATP (Kass et al., 2014; Martin and Rinvall, 1993; Petroff, 2002). These GABAergic properties provide a protective mechanism to reduce neuronal electrical activity when energy demands exceed the metabolic capacities. As a result, the low level of PCr and Pi in KO mice would suggest a higher GAD65 activation in its Holo state, however, the lower expression levels of this enzyme, with possible lower levels of GAD65 protein as well, might explain why GAD activity measured *in vivo* was comparable in both groups. Nevertheless, GABA labelling upon [U-¹³C₆]Glc infusion is higher in KO mice which translated into a higher V_{ex}^i flux measured. Our model could not take into account two separate GAD metabolic pathways, and for simplification purpose, our model only considered one of the GABA pools to interact with the inhibitory TCA cycle. This inhibitory exchange flux could reflect the part of the neurotransmission GABA that is released into the synaptic cleft, but is not taken up by astrocytes (V_{NT}) nor recycled directly in the GABA neuron through the TCA cycle (V_{shunt}^i). Rather this increased V_{ex}^i might account for the part of the neurotransmission GABA that is taken up back into GABAergic neurons and reused without any metabolic transformation. Following this hypothesis, inhibitory neurotransmission activity would be ~14 times higher in KO mice, i.e. $(V_{NT}^i + V_{ex}^i) = 0.0086 \pm 0.0033 \mu\text{mol/g/min}$ for KO vs. $0.00063 \pm 0.00063 \mu\text{mol/g/min}$ for WT. Due to their high neurotransmission activity, GABAergic neurons, and in particular high energy-consuming parvalbumin neurons, might be suffering the most from reduced ATP production from glucose. While the relative conformation of both GAD enzymes could not be investigated, our results point towards an imbalance in their respective activities occurring as a result of metabolic distress. Several studies have reported

an effect of stress on GABAergic function, particularly during early life (Uchida et al., 2014). Several studies have reported lower levels of expression of GAD67 in PFC of BPD and SZ patients post mortem (Fung et al., 2010; Guidotti et al., 2000; Hashimoto et al., 2008; Steiner et al., 2016; Woo et al., 2004). The drop in GAD mRNA we observe in KO mice likely reflects a compensatory mechanism induced by the higher GABA turnover revealed by ^1H - ^{13}C -MRS. While the absolute concentration of GABA alone did not differ, an increase in Glu/GABA in hippocampus appeared to be associated with improved behavior in the longitudinal study, but not in the ebselen study.

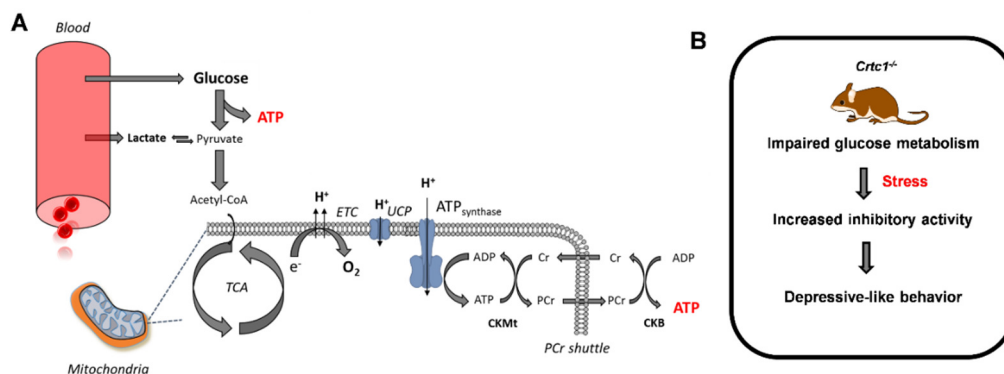


Figure 3. 15 : Proposed neuroenergetic mechanism of *Crct1*-related susceptibility

A. Deletion of *Crct1* leads to impaired hippocampal glucose entry and metabolism. As a result, less ATP is produced, and less lactate accumulates. This results in an allostatic load put on the mitochondria as revealed by the drop of PCr/Cr ratio. **B.** Exposing the susceptible/*Crct1*^{-/-} mice to an energy demanding stressor leads to the development of a depressive-like behavior.

3.4.3 Hippocampal vulnerability is challenged by the environment

Our results show that the removal of stressful environmental factors contributes to the improvement of *Crct1* KO mice brain metabolism and behavior. *Crct1* KO mice are very aggressive (Breuillaud et al., 2012) and social deprivation appears to lead to an opposite behavioral response compared to the social WT mice (Fig 3.9). Social isolation is known to induce anxiety and depressive-like behavior in rodents (Brenes et al., 2008; Brenes Sáenz et al., 2006; Wallace et al., 2009). Brain oxidative damage (Haj-Mirzaian et al., 2016), loss of hippocampal parvalbumin neurons (Ueno et al., 2017) or drop in PCr content (Burjanadze et al., 2016; Shao et al., 2015) have been reported as an outcome of social deprivation. Our results are in line with these observations pointing towards an environmental influence on the hippocampal metabolic profile. As a result, the impaired neuroenergetics of *Crct1* KO mice improved upon isolation, together with their depressive-like behavior. Interestingly, upon social isolation the rapid kinetics of PCr/Cr content contrasted with the delayed lactate

fluctuations. The idea that lactate drops only after prolonged stress explains why the short term OSFST did only reduce PCr/Cr. In other words, the ~18-week social isolation protocol might thus lead to a higher allostatic load than a ~3-week OSFST. The differential response to social deprivation in the two mice groups is corroborated by the inverted expression pattern of CK and GAD compared to basal condition. Higher levels of PGC1 α regardless of GLUT4 in KO mice after social isolation suggests that mitochondrial function plays a major role in restoring allostasis. This clear dependence between energetic status and depressive-like behavior led us to hypothesize that deletion of *Crtc1* is associated with a hippocampal susceptibility to stress due to impaired allostatic response (Fig 3.16A).

3.4.4 Ebsele protects the hippocampus by stimulating energy metabolism

Hippocampus is known to be a brain structure with high sensitivity to stress (McEwen, 2008; Sapolsky, 1986). Challenging the mice with a common repeated forced swimming stress provided a good mean of validating our model and test the efficacy of a treatment with known mitochondrial boosting properties. Ebsele is a selenium-based antioxidant compound with mood stabilizing effects. Its significant inhibitory properties on glycogen synthase kinase 3 β (GSK3 β) indicate a mechanism of action comparable to lithium, with much lower toxicity, making it a “safe lithium mimetic” (Singh et al., 2013). Lithium is known to be beneficial for mitochondrial function and health (Chen and Chuang, 1999; Maurer et al., 2009; Toker and Agam, 2014; Toker et al., 2014). Lithium has recently been shown to stimulate mitochondrial metabolism by increasing PGC1 α activity (Martin et al., 2018). We report a similar effect with a significant increase in PGC1 α expression as a result of ebsele treatment. This led in turn to improved mitochondrial function as indicated by higher CKMt1 and PCr/Cr levels but also improved glucose and GABA metabolism as revealed by the GLUT4 and GAD mRNA content. These results strengthen the causality relationship between hippocampal energetics and inhibitory activity, while strongly supporting the idea that mitochondrial function is a prerequisite for resilience to stress.

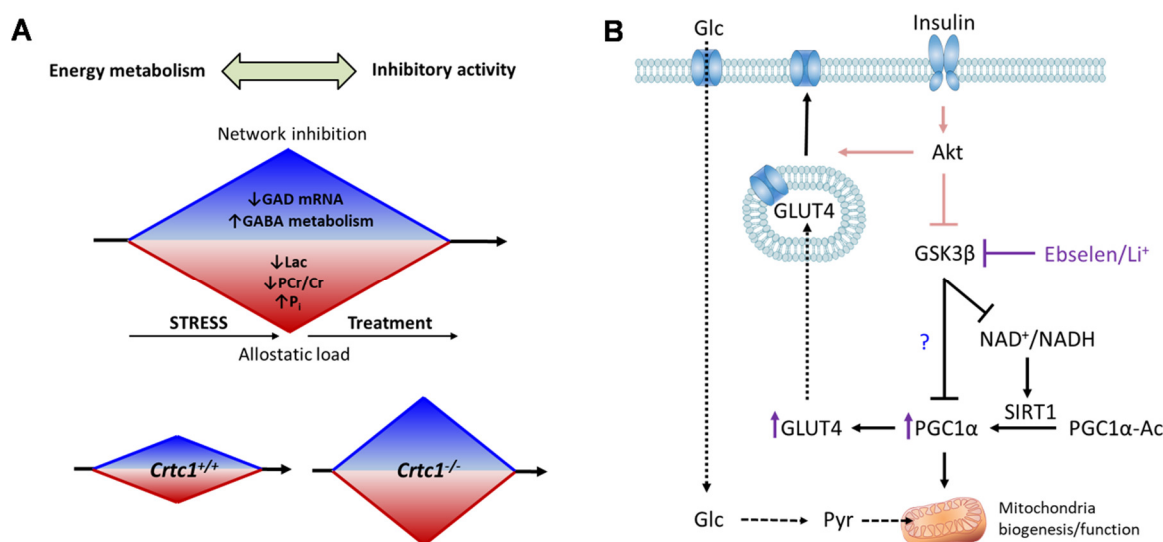


Figure 3. 16 : Relationship between hippocampal energetics and GABAergic function

A. Stress-induced energy drop leads to a concomitant rise in GABAergic metabolism as a mechanism to prevent excitotoxicity. Restoring hippocampal energetics with energy-stimulating drug improves both energy metabolic profile and GABAergic function. *Crtc1*^{-/-} mice are typically less resilient to a given stress, leading to higher energy depletion and network inhibition. **B.** Proposed molecular mechanism underlying ebselen metabolic improvement.

PGC1 α , often considered as the master mitochondrial biogenesis regulator, has been shown to be affected in BPD and depression (Geoffroy et al., 2016; Ryan et al., 2018). Its target, PPAR γ , has been related to several metabolic impairment including insulin resistance and obesity. PPAR γ agonists are well known insulin sensitizers with anti-inflammatory, antioxidant and pro-energetic properties (Watson et al., 2018). Stimulating PPAR γ has proven to have anti-depressant properties in animal models (Zhao et al., 2016) and patients (Kemp et al., 2014; Sepanjnia et al., 2012) leading to improved glucose metabolism (Lin et al., 2015). PGC1 α is inhibited through phosphorylation by GSK3 β (Anderson et al., 2008) and can enhance GLUT4 expression through stimulation of MEF2C transcription factor (Michael et al., 2001). Furthermore, CRTC2 has been shown to induce PGC1 α expression in muscle cells, suggesting that CRTC1, the brain homolog of CRTC2, could have the same properties (Rahnert et al., 2016). This led us to hypothesize that ebselen enhances mitochondrial energetics and glucose homeostasis through inhibition of GSK3 β and subsequent enhancement of PGC1 α function (Fig 3.16B).

3.4.5 Hippocampal energy metabolites as markers of depression

We found a clear correlation between hippocampal neuroenergetic dysfunctions and the depressive-like behavior of *Crtc1*^{-/-} mice, while prefrontal metabolic modifications were

unrelated. Hippocampus and cingulate cortex are highly interconnected and part of the Hippocampal-Diencephalic-Cingulate network, also known as circuit of Papez (Bubb et al., 2017). Interactions between the dorsal hippocampal and prefrontal area investigated here are complex and bidirectional. It is thus likely that the two distinct metabolic profile observed are somehow related to each other, but difficult to say whether one brain region causes the other's dysfunction. Nevertheless, the high cholinergic and glutamatergic content of PFC did not relate to the behavior and might thus reflect a more structural aspect rather than a biological substrate of the depressive-like phenotype. CRT1 has been implicated in the circadian clock function of the suprachiasmatic nucleus (Jagannath et al., 2013) and male *Crtc1*^{-/-} show increased spontaneous locomotor activity during the light phase (Rossetti et al., 2017). It would thus be hypothesized that the observed increase in choline containing compounds in PFC might reflect a higher cholinergic nerve terminals content and be associated with an altered acetylcholine function, one of the main systems involved in regulation of vigilance states. Several MRS studies have reported elevated CCC levels in the anterior cingulate cortex of patients with bipolar disorders (Cao et al., 2016; Galińska-Skok et al., 2018; Kubo et al., 2017; Soeiro-de-Souza et al., 2018) and prefrontal glutamate levels have been widely implicated in the field of mood disorders (Sanacora et al., 2012). We thus propose that prefrontal cortex and dorsal hippocampus are both linked in a common pathophysiological process leading to the KO mice behavioral dysfunctions, which could be seen as a "*Crtc1* susceptibility" (Fig 3.17A). While hippocampal MRS markers could serve as potential biomarkers of depression state, prefrontal MRS markers could provide useful information on susceptibility to develop depression.

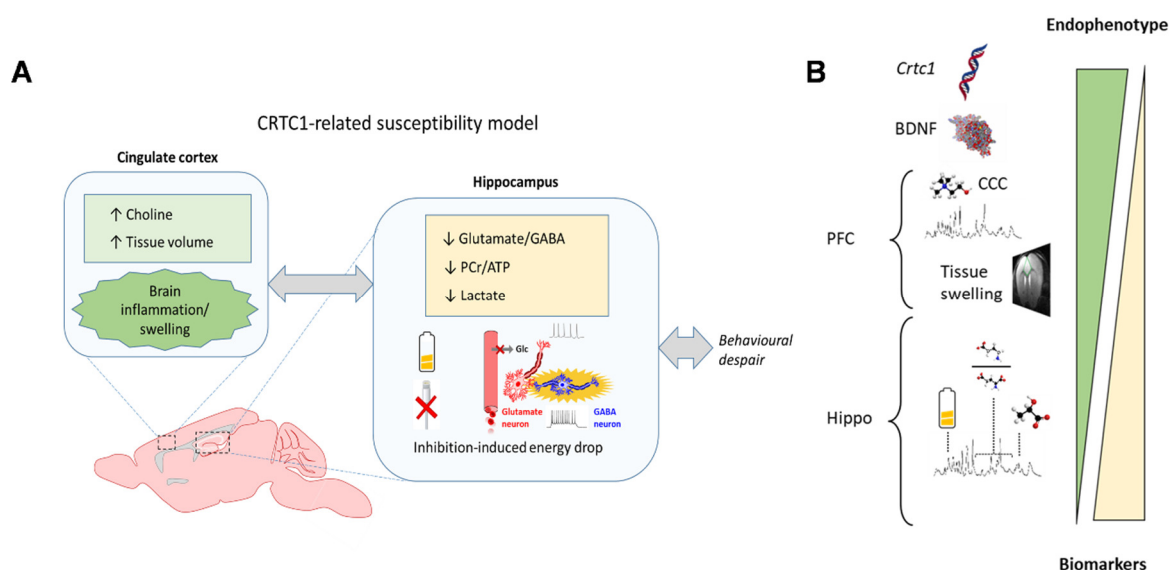


Figure 3. 17 : Summary of potential biomarkers related to *Crtc1*-susceptibility

A. CRCT1-related susceptibility model to development of depressive-like behavior and **B.** list of potential biomarkers and endophenotypes identified. Both PFC and DH seem to be implicated in *Crtc1*^{-/-} mice susceptibility to behavioral alterations. The observed PFC alterations in *Crtc1*^{-/-} mice seem to be “structural” and independent of the behavior, meaning they can be considered as potential endophenotypes (in green). The observed hippocampal alterations were dependent on the behavior, reflecting a neuroenergetic sensitivity with associated GABAergic overactivity, meaning they can be considered as potential biomarkers of mood disorder state (in yellow).

By applying MRS, we have identified potential clinically relevant biomarkers with their associated biological and environmental dependences, opening potential therapeutic strategies. While the neurochemical profile of PFC relates to potential endophenotypes, i.e. heritable biological features, the dorsal hippocampus reveals interesting potential biomarkers dependent on the behavior and treatment response (Fig 3.17B). Finally, we have furthered our understanding of CRTC1 function in the brain and how impaired neuronal trophic support can impact the normal neurochemical profile in mice.

Chapter 4

MRS in an environmental model of mood disorder

Contributions to the work:

This work was a close collaboration with the Laboratory for behavioral genetics (LGC) headed by Prof. Carmen Sandi at the EPFL and with Prof. Bruce McEwen from the Rockefeller University (New York). My contribution consisted in the acquisition of the MRS data, assembling the data of the whole study for statistical analysis (except the factor analysis). My work also consisted in the interpretation of the results and writing of the manuscript, together with the co-authors. All the behavioral experiments have been performed by Mr. Jocelyn Grosse and Mr. Thomas Larrieu from Prof. Sandi's lab. Treatment and body weight measurements were performed by Mr. Jocelyn Grosse. Factor analysis was performed by Dr. João Rodrigues and plasma sample analyses were performed by Ms. Olivia Zanoletti, both from Prof. Sandi's lab.

This Chapter was partially adapted from:

Larrieu T, **Cherix A**, Duque A, Rodrigues J, Lei H, Gruetter R, Sandi C (2017): Hierarchical Status Predicts Behavioral Vulnerability and Nucleus Accumbens Metabolic Profile Following Chronic Social Defeat Stress. *Curr. Biol.* 27: 2202–2210.e4.

and

Cherix A, Larrieu T, Grosse J, Rodrigues J, Zanoletti O, McEwen B, Nasca C, Gruetter R, and Sandi C: Metabolic signature in nucleus accumbens for antidepressant-like effects of acetyl-L-carnitine. *eLife*, *in revision*.

Abstract

Environmental factors, such as stress, can have a strong impact on the development of mood dysfunction, through their deleterious effects on brain integrity and function. Chronic exposure to stress can induce a depressive-like behavior on inbred mice, i.e. genetically identical. While some animals are resilient to chronic stress exposure, others respond negatively. The purpose of this study was the identification of social traits underlying this differential response, assess the metabolic alterations associated with it and select a treatment targeting the dysfunction. We report that social hierarchy is a susceptibility factor for naïve animals to developing depressive-like behavior after chronic stress exposure. The resulting behavioral dysfunctions were associated with neuroenergetic impairments in the nucleus accumbens of susceptible but not resilient mice, seen as a drop of phosphocreatine and taurine. Treating the susceptible mice with acetyl-L-carnitine, a mitochondria boosting supplement, prevented both the appearance of the depressive-like behavior and the drop of energy metabolites. In conclusion, we report that neuroenergetics in the nucleus accumbens are involved in the development of depressive-like behavior of mice that are susceptible to stress. Furthermore, we identified potential accumbal MRS-biomarkers and a treatment that targeted this dysfunction specifically.

4.1 Introduction

Major depressive disorders (MDD) is among the leading causes of disability worldwide, which reflects the current lack of understanding of its etiology and strengthens the need for identification of reliable biomarkers (Friedrich, 2017; Menke, 2018). Both genetic predispositions and environmental factors like stress are well accepted causes of a pathophysiological mechanism impacting normal mood state (Cohen-Woods et al., 2013; McEwen, 2006). Given the energetic needs required for a healthy stress response, it is not surprising to observe significant comorbidity between mood disorders and metabolic dysfunctions (Rasgon and McEwen, 2016). Insulin resistance and obesity are for instance commonly observed among patients with MDD (Nasca et al., 2019). Nevertheless, it remains unclear which factors provide resilience to stress in certain individuals and what are the underlying mechanisms (Larrieu and Sandi, 2018).

We have previously identified that the social hierarchy established in mice groups confers risk factors to developing a depressive-like behavior after chronic social defeat stress (CSDS) exposure (Larrieu et al., 2017). The induced behavioral alterations in dominant/susceptible mice were associated with a lower energy metabolism adaptation in the Nucleus Accumbens (NAc) than in the subordinate/resilient group. This opens new routes for mechanistic investigations and targeted treatment interventions. Acetyl-L-carnitine (LAC) has recently shown very promising potency to rapidly alleviate depressive symptoms while simultaneously improving brain energy function and metabolic fitness (Bigio et al., 2016; Lau et al., 2017). LAC and its deacetylated form L-carnitine (LC) are endogenous metabolites involved mainly in the transport and β -oxidation of lipids. Exchange of LC with LAC and other acylcarnitines through carnitine-acylcarnitine translocase (CACT) allows a bidirectional flow from cytoplasm into the inner mitochondrial matrix membrane for lipid oxidation. The ability of the LAC/LC system to transport acyl groups, via the exchange by the carnitine acetyl-transferase (CAT), seems to be a hallmark of its metabolic boosting effects. While acetyl groups carried by LAC can provide an interesting source of AcCoA for mitochondrial oxidation or protein acetylation, LC increases fatty acyl catabolism and can buffer extra AcCoA to prevent PDH (pyruvate dehydrogenase) substrate inhibition (Broderick, Tom L et al., 1992; Panchal et al., 2015; Smeland et al., 2012; Virmani et al., 1995). However, whether epigenetic and energetic factors mediate the antidepressant-like effect of LAC is still debated and requires further investigations.

Magnetic resonance spectroscopy (MRS) is the only non-invasive method that can provide information on brain metabolism *in vivo* (Duarte et al., 2012). MRS performed at 14 Tesla in the mouse brain can measure the concentration of up to 20 metabolites (Mlynárik et al., 2008). Besides the evident translational potential of such technique in identifying biomarkers, rodent MRI/MRS studies at ultra-high field bridge a potential pathological indicator and its associated molecular to physiological mechanisms. Finally, factor analysis of metabolic data measured by MRS provides an interesting means of assessing overall metabolic phenotypes between groups with in a metabolomics approach (Chung et al., 2015; Dunn et al., 2011).

Here, we investigated the effect of LAC supplementation as an attempt to protect dominant mice against stress-induced depressive-like behavior. By using *in vivo* ^1H -MRS we have identified key accumbal metabolites implicated in the response to LAC. Our results confirm an energy- and membrane metabolism process recovered by LAC and points towards potential astrocytic support. These metabolic restorations were associated with improvement of depressive-like behavior that are more likely to be energy-demanding.

4.2 Material and methods

4.2.1 Animals

All experiments were performed with the approval of the Cantonal Veterinary Authorities (Vaud, Switzerland) and carried out in accordance with the European Communities Council Directive of 24 November 1986 (86/609EEC). Six-week-old C57BL6/J mice were purchased from Charles River Laboratories and housed in groups of four per cage and allowed to acclimate to the animal facility for one week. Mice were weighed at arrival and monitored throughout the experiments. Cages consisted in standard Plexiglass filter-top cages in a temperature (23 ± 1 °C) and humidity (40%) controlled environment with normal 12h day-light cycle. Animals had *ad libitum* access to water and standard rodent chow diet.

4.2.2 Experimental design

This study was designed in two batches following a similar chronic restraint stress (CRS) protocol (as described later in figures 4.1A and 4.3A), with the main difference being that the second group of animals included a treated cohort. 1 week after arrival, mice were tested for

trait-anxiety using an elevated plus maze (EPM) and open field (OF). After four weeks of cohabitation in cages of four animals, a social confrontation tube test was used to assess the social rank of each individual (Larrieu et al., 2017). Dominant and subordinate mice were then subjected to a chronic restraint stress (CRS) protocol, 2 hours per day for 21 days. Depressive-like behavior with a non-energy and energy demanding component was tested using a social interaction (SI) test (at day 20 of CRS) and a forced swim test (FST) (at day 22), respectively. Finally, ^1H -NMR spectroscopy was performed at the end of the protocol followed by an immediate sacrifice of the animals and blood sampling. The second batch of animals included a treated group starting acetyl-L-carnitine (LAC) administration on day 15 of the CRS protocol.

4.2.3 Elevated Plus maze test

Animals were placed into a maze made from black PVC with a white floor. The system consisted of an elevated central platform ($5 \times 5 \text{ cm}^2$) at 65 cm from the ground, from which four opposing arms extended. Two of the arms were open ($30 \times 5 \text{ cm}^2$) and lit with 14-15 lx while the two others were closed ($30 \times 5 \times 14 \text{ cm}^3$) with reduced light intensity 3-4 lx. Animals were introduced in the maze facing the wall at the end of closed arms and left freely moving for 5 min. The mice were filmed from above the arena and tracked (Ethovision 11.0 XT, Noldus, Information Technology) to determine the time spent in open-arms, closed arms and the edges of the open arms (risk zones) as described previously (van der Kooij et al., 2015).

4.2.4 Open Field test

The OF consisted of a rectangular arena ($50 \times 50 \times 40 \text{ cm}^3$) that was illuminated with dimmed light (30 lx). Mice were introduced near the wall of the arena and allowed to explore for 10 min. Analysis was performed using a tracking software (Ethovision 11.0 XT, Noldus, Information Technology) by drawing a virtual zone ($15 \times 15 \text{ cm}^2$) in the center of the arena defined as the anxiogenic area. Several parameters were analyzed as described previously (van der Kooij et al., 2015) including the total distance travelled and the time spent in the different zones.

4.2.5 Social confrontation tube test

The test was reproduced as reported and described previously (Larrieu et al., 2017; Wang et al., 2011). Mice were housed together in groups of four during 7 weeks prior to the test to allow social hierarchy to be established in the cage. Mice were habituated to cross over a plastic tube (Plexiglas of 3 x 30 cm², diameter x length) for two consecutive days. Social ranks were then evaluated during 8 consecutive days as follows. Each mouse was first trained to go through the tube for one session prior to the test. Mice were subsequently guided by the tail on each side of the tube for a pairwise confrontation. Once the two mice were smoothly guided towards the middle of the tube, the tail was released, and the interaction time was recorded. The relative hierarchical rank can be determined by observing which of the two mice retreats, moving backwards to exit the tube, giving free way to the 'winner' of that specific trial. The four mice from the same cage were opposed with a round-robin design leading to 6 face-to-face trials. The tube was cleaned with 70% ethanol and dried between each session. An index of dominance was computed based on the percentage of winning time. Finally, the animals were ranked with an index from 1 to 4, where 1 corresponds to the highest in hierarchy, while 4 represents the lowest rank.

4.2.6 Chronic restraint stress

This protocol was adapted from (Lau et al., 2017; Nasca et al., 2015). Animals were introduced head first into a 50ml Falcon tube (11.5 cm in length; diameter of 3 cm) in which the cap was removed. Each restrain tube contained three 0.4 cm air holes to allow the air to reach the nose of the mouse. Paper was added at the other extremity to adjust the physical constraint to the mouse body size and allowing the tail to reach the open space. The mice were subjected to this restrained environment for two consecutive hours every day for a period of 21 days. Control mice were left undisturbed in their home cage and were body weighed each day for 21 days.

4.2.7 Porsolt forced swim test

Each animal was introduced into a cylinder of 15cm diameter and filled with 5L 25°C tap water. The level of water was sufficiently high to avoid any contact of the mouse with the bottom of the enclosure and low enough to avoid any possible escape. Animal's motion was tracked with

a camera positioned on top of the setup and recorded for 6 minutes. Immobility time was quantified using a scoring software (The Observer XT, Noldus, Information Technology).

4.2.8 Social interaction test

Each animal was introduced into a 40 x 40 x 30 cm white arena containing an unfamiliar old breeder CD1 male mouse (social target) restrained to one side of the box in a cylindrical drum with metallic bars. The test consisted in two specific events which were recorded from the top of the arena: The tested mouse was first allowed to move freely for 2.5 min in the arena when the target was not present (the arena contained only the drum). After this first habituation, the target was introduced in the drum at the interaction zone for a 2.5 min interaction session. A social avoidance score was assessed based on the following parameters, as described in (Larrieu et al., 2017): 1) The time spent in the interaction zone with the target present; 2) the time spent in the corners when the target was present; 3) the social interaction ratio defined as the time spent in the interaction zone when the target is present divided by the time spent in the interaction zone when the target is absent; and 4) corner zone ratio defined as the time spent in the corner zone when the target is present divided by the time spent in the corner zone when the target is absent.

4.2.9 Acetyl-L-carnitine treatment

Acetyl-L-carnitine hydrochloride (LAC) was purchased from (Sigma Aldrich). Mice received LAC in the drinking water at a concentration of 0.3 %. The treatment started at day 15 of the 21 day-CRS protocol. Vehicle and control groups received regular tap water available *ad libitum*.

4.2.10 ¹H-Magnetic Resonance Spectroscopy (¹H-MRS)

In vivo spectroscopy experiments were performed as previously described in the Nucleus Accumbens (NAc) of anesthetized mice (for further details see (Larrieu et al., 2017)). Animals were monitored for body temperature (rectal probe and circulating water bath) and respiration (small animal monitor system: SA Instruments Inc., New York, NY, USA) under 1.3-1.5% isoflurane anesthesia mixed with 50% air and 50% O₂. Physiological parameters were maintained at 36.5 ± 0.4°C and breathing rate ranged between 70 – 100 rpm. Animals were scanned in a horizontal 14.1T/26 cm Varian magnet (Agilent Inc., USA) with a homemade ¹H

surface coil. A set of Fast Spin Echo (FSE) images of the brain was acquired for localizing the Volume of Interest (VOI) of the ^1H -MRS scan. Acquisition was done using the spin echo full intensity acquired localized (SPECIAL) sequence (Mlynárik et al., 2006) in the VOI of $1.4 \times 4.1 \times 1.2 \text{ mm}^3$ (TE/TR = 2.8/4000ms) including the bilateral NAc after field homogeneity adjustment with FAST(EST)MAP (Gruetter and Tkáč, 2000). The resulting spectra (20 x 16 averages) were then frequency corrected, summed and quantified using LCModel (Provencher, 2001). Concentrations were referenced to the water signal and fitting quality assessed using Cramer-Rao lower bounds errors (CRLB) (Cavassila et al., 2001).

4.2.11 Blood metabolite measurements

Blood sampling were performed after the ^1H -MRS scan under isoflurane anesthesia. The head was decapitated, and blood was collected from the trunk in (Heparin/Li⁺ Microvette CB300 LH, Sarstedt) collection tubes. Samples were centrifugated at 4°C at 1'000g for 10 minutes leading to ~100uL plasma which was then frozen in liquid nitrogen and stored at -80°C.

4.2.12 Statistical analysis

All values are given as mean \pm SEM. Results from the social confrontation tube test were analyzed by a one-way analysis of variance (ANOVA), with social rank as fixed factor, followed by a Bonferroni post hoc test when appropriate. Results from elevated plus maze (EPM), openfield (OF) and blood values were analyzed using unpaired Student t-tests. Depressive-like behaviors (FST and SI) in the untreated batch were analyzed with a two-way ANOVA, using stress and social rank as fixed factors. Depressive-like behavior, plasma analysis and spectroscopy results in the treated batch were analyzed using one-way ANOVA. Cumulative weight gain was analyzed using a repeated measure two-way ANOVA with time and group as fixed factors. Analyses were followed by Bonferroni post hoc correction when appropriate. All statistical tests were performed with GraphPad Prism (GraphPad software, San Diego, CA, USA) using a critical probability of $p < 0.05$. Statistical analyses performed for each experiment are summarized in each figure legend with the chosen statistical test, sample size 'n' and P values, as well as degree of freedom and F values.

4.2.13 Factor analysis

Factor analysis was used as previously described (Larrieu et al., 2017) using IBM SPSS Statistics version 21 to allow statistical tests using the metabolite's latent variables as dependent variables in NAc. A linear combination is generated of the dependent variables in order to reduce the noise caused by the high amount of variables. Missing values were avoided by using mean value imputation before the computation of correlation matrices, to ensure positive definiteness. A total of three factors was chosen for the NAc after analyzing the scree plots, using principal axis factoring. This resulted in a total of variance explained of 52% without rotation and omitting coefficients below 0.4.

4.3 Results

4.3.1 CRS protocol reproduces the behavioral phenotype of CSDS in dominant animals

Behavioral assessment of naïve animals indicated higher basal trait-anxiety among dominant animals, in good agreement with our previously reported study. No reorganization of the animal hierarchy was observed during the whole confrontation tube test protocol indicating a rapid and robust establishment of social status during cohabitation period (Fig 4.1B). Rank assignment was in good agreement with the duration of the confrontation (Fig 4.1C) where the least time was spent in the tube when lowest rank animals (rank 4) were facing the highest rank (rank1) (time in the tube 1-2 vs 1-4, $p < 0.001$).

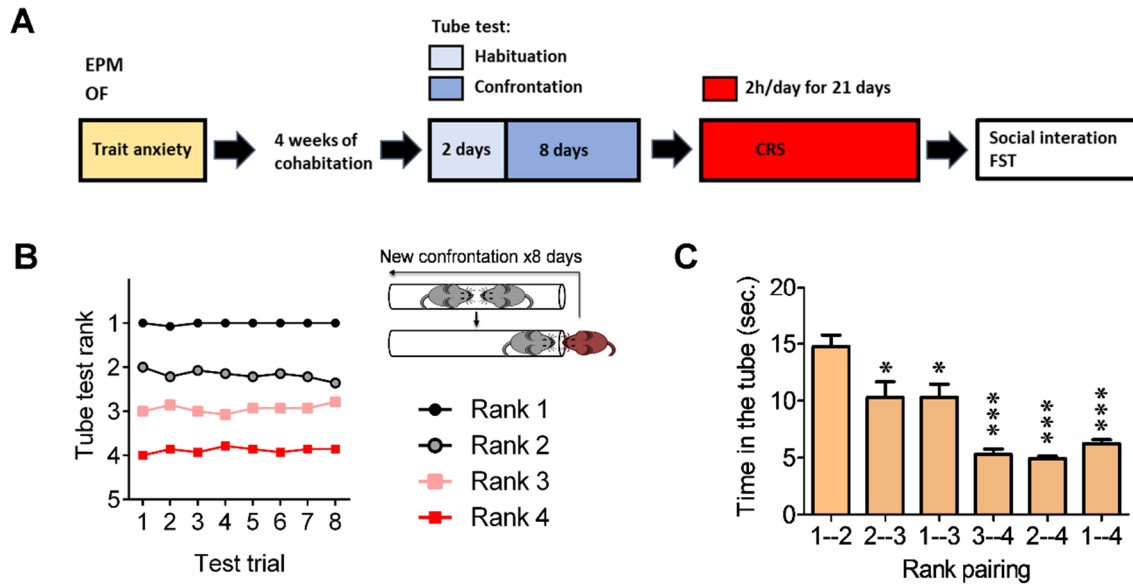


Figure 4. 1 : Determination of mouse hierarchical status

A. Experimental design of the restraint stress protocol. **B.** Summary of nine cages representing the tube test ranks and winning times as a function of tube test trials over the 6 days of test. **C.** Time spent in tube as a function of rank pairing ($F_{5,35}=18.19$, $p<0.0001$, one-way ANOVA; ** $p<0.01$, *** $p<0.001$, Bonferroni's test, $n=7$ per rank pairing). Data are displayed as Mean \pm SEM.

Dominant animals (rank 1 and 2) showed higher time spent in the open arms of the elevated plus maze (EPM) ($p=0.02$) as well as an increased latency to enter the anxiogenic central part of the open field (OF) arena ($p=0.049$). These results corroborate the idea that higher social status goes along with increased resource utilization and sustained vigilance state. Exposing the animals to a chronic restraint protocol induced a behavioral impairment that was comparable to the previously reported effect of chronic social defeat stress paradigm. Chronic exposure to a stressful physical restraint induced a depressive-like phenotype in the dominant but not subordinate mice. CRS induced social avoidance in the dominant animals compared to controls ($p=0.009$) and did not affect subordinate animals ($p>0.05$). No behavioral-despair phenotype was detected at this stage in dominant nor subordinate mice during the forced swimming session.

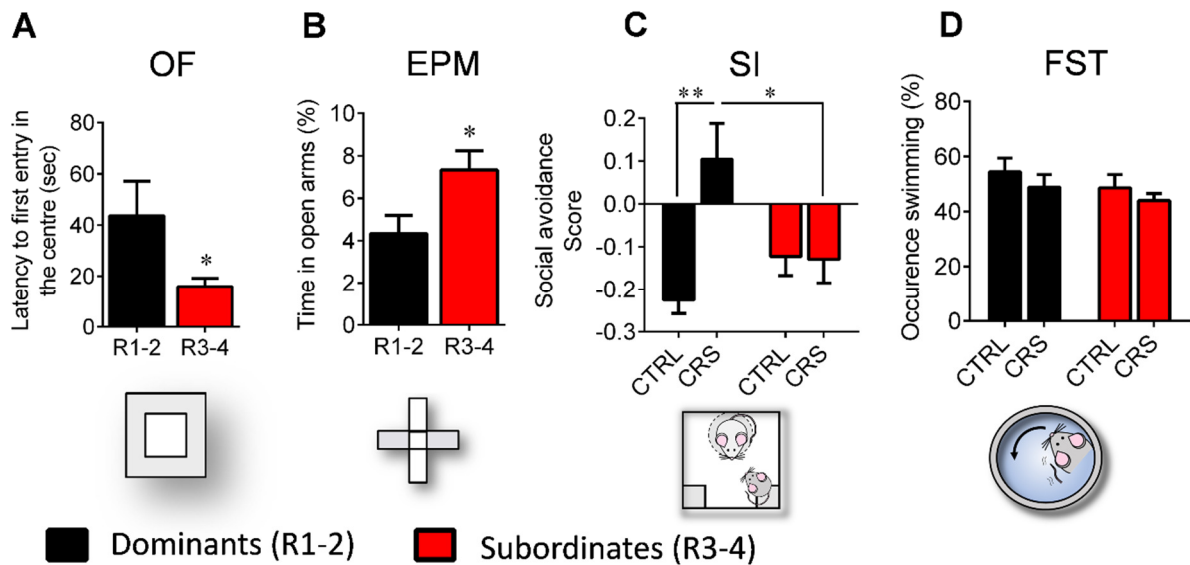


Figure 4. 2 : Dominant mice exhibit susceptible phenotype after 21 days of chronic restraint stress

A. Trait-anxiety measured based on the latency to first enter in the center of the open-field arena after segregation into dominant vs subordinate mice (* $p < 0.05$, unpaired t-test, two-tailed $n = 14$ per group). **B.** Trait-anxiety measured based on the time spent in the open arms of an elevated plus maze (* $p < 0.05$, unpaired t-test, two-tailed $n = 14$ per group). **C.** Social avoidance scores measured after chronic restraint stress protocol in dominant vs subordinate animals (Interaction: $F_{1,21}=7.75$, $P < 0.05$; stress effect: $F_{1,21}=1.18$, $P > 0.05$; rank effect: $F_{1,21}=7.15$, $P < 0.05$, two-way ANOVA; ** $p < 0.01$, Bonferroni's test, $n=6-7$ per group). **D.** Behavioral despair measured with a forced swim test between dominant and subordinate mice (Interaction: $F_{1,21}=0.01$, $P > 0.05$; stress effect: $F_{1,21}=1.42$, $P > 0.05$; rank effect: $F_{1,21}=1.53$, $P > 0.05$, two-way ANOVA; Bonferroni's test, $n=6-7$ per group). Data are displayed as Mean \pm SEM.

4.3.2 Treatment with LAC reverses the behavioral phenotype induced by stress in dominant mice

LAC, the acetylated form of carnitine has been proposed as a mean to treat several psychiatric and neurodegenerative disorders (Pettegrew et al., 1995; Wang et al., 2014) presenting underlying hypometabolic etiology. With the working hypothesis that dominant mice are under higher basal allostatic load and thus more susceptible to chronic stress, we tested whether chronic LAC treatment could counteract the induction of a depressive-like behavior by CRS. Furthermore, the prospect of finding potential molecular mechanisms of action and determining the factors that mediate LAC antidepressant-like effects have led us to analyze the *in vivo* metabolic profile of the NAc after stress. A second group of animals was thus exposed to the same CRS protocol with concomitant administration of LAC during the last 7 days of the stress period. CRS protocol induced a clear increase in immobility time measured with FST in dominant mice but not in the resilient subordinates ($p=0.02$). This increase in depressive-like behavior was not detectable in the treated group anymore. Interestingly, the social avoidance induced by the CRS protocol ($p=0.004$) did not get prevented by

administration of LAC. These results indicate that LAC prevents the stress-induced behavioral despair but not social avoidance.

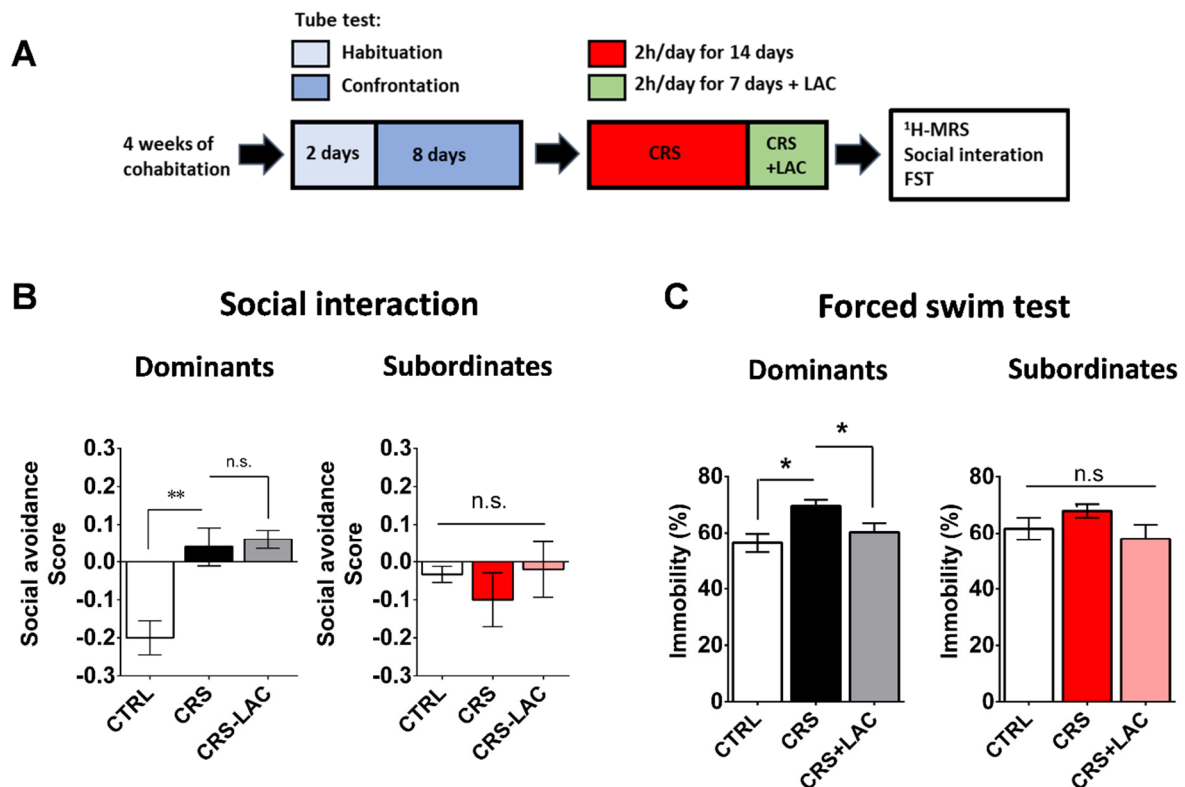


Figure 4.3 : Dominant mice respond to acetyl-L-carnitine treatment after chronic restraint stress

A. Experimental design of the restraint stress protocol and treatment procedure. **B.** Social avoidance scores measured after chronic restraint stress protocol in dominant ($F_{2,15}=12.08$, $P<0.01$, one-way ANOVA; ** $p<0.01$, Turkey's test, $n=6$ per group) and subordinate animals ($F_{2,15}=0.55$, $P>0.05$, one-way ANOVA; $n=6$ per group). **C.** Behavioral despair measured with a forced swim test between dominant ($F_{2,12}=5.31$, $P<0.05$, one-way ANOVA; * $p<0.05$, Bonferroni's test, $n=6$ per group) and subordinate mice ($F_{2,15}=1.62$, $P>0.05$, one-way ANOVA; $n=6$ per group). Data are displayed as Mean \pm SEM.

The body weight profile monitored during the whole stress duration indicates a similar physiological response in all animals. All animals exposed to CRS showed a clear net decrease in cumulative weight gain after only 3 days ($p<0.001$). Analysis of plasma triglycerides, glucose and insulin content revealed no significant difference in peripheral metabolism. Dominant mice tend to have higher plasma glucose levels in the control group compared to the stressed group ($p=0.06$).

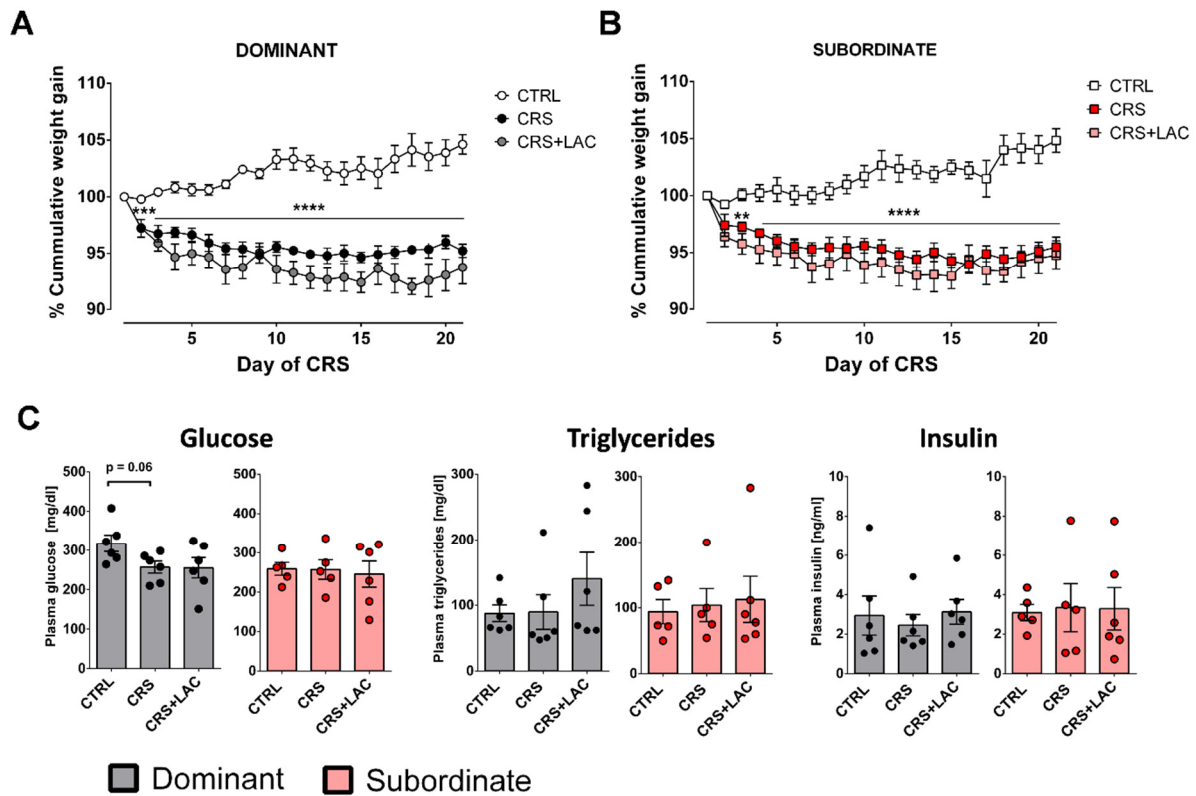


Figure 4.4 : Body metabolic effects of stress and LAC

A. Dominant mice show a reduction of cumulative weight gain during the restraint stress protocol (Interaction: $F_{40,20}=11.5$, $P<0.0001$; stress effect: $F_{2,10}=45.0$, $P<0.0001$, two-way ANOVA; *** $p<0.001$, **** $p<0.0001$, Bonferroni's test, $n=6$ per group). **B.** Subordinate mice show a reduction of cumulative weight gain during the restraint stress protocol (Interaction: $F_{40,20}=8.17$, $P<0.0001$; stress effect: $F_{2,10}=20.4$, $P<0.001$, two-way ANOVA; *** $p<0.001$, **** $p<0.0001$, Bonferroni's test, $n=6$ per group). **C.** Dominant mice show higher levels of blood glucose compared to the CRS group ($F_{2,15}=2.83$, $P=0.09$, one-way ANOVA; Mann-Whitney test, $n=5-6$ per group). Data are displayed as Mean \pm SEM.

Quantification of NAc metabolic profile using *in vivo* ^1H -MRS highlighted a biological basis that relates to the behavioral changes and treatment efficacy. With help of an unbiased multivariate factor analysis (FA) of the metabolic profile, we were able to identify 3 main factors that accounted for 31, 12% and 9% of total variance in the data from the NAc (not shown). Individual metabolite loadings above 0.4 included Taurine (Tau), myo-inositol (Ins), N-acetylaspartate (NAA), phosphocholine (PCho), aspartate (Asp), glutamate (Glu), γ -aminobutyric acid (GABA), phosphocreatine (PCr), creatine (Cr), glucose (Glc), glutathione (GSH) and ascorbate (Asc) for factor 1 (Fig 4.6A). Metabolites with loading above 0.4 for the two other components were glycerophosphorylcholine (GPC), PCho and Asc for factor 2, and glutamine (Gln) and lactate (Lac) for factor 3 (Fig 4.6B). The Factor 1 was able to discriminate for the stress and treatment response between dominant and subordinate mice (Fig 4.5B). These results indicate that stress had an effect on metabolites of factor 1 compared to the

control group ($p=0.002$) and that LAC had an effect on preventing this stress-induced difference ($p=0.04$).

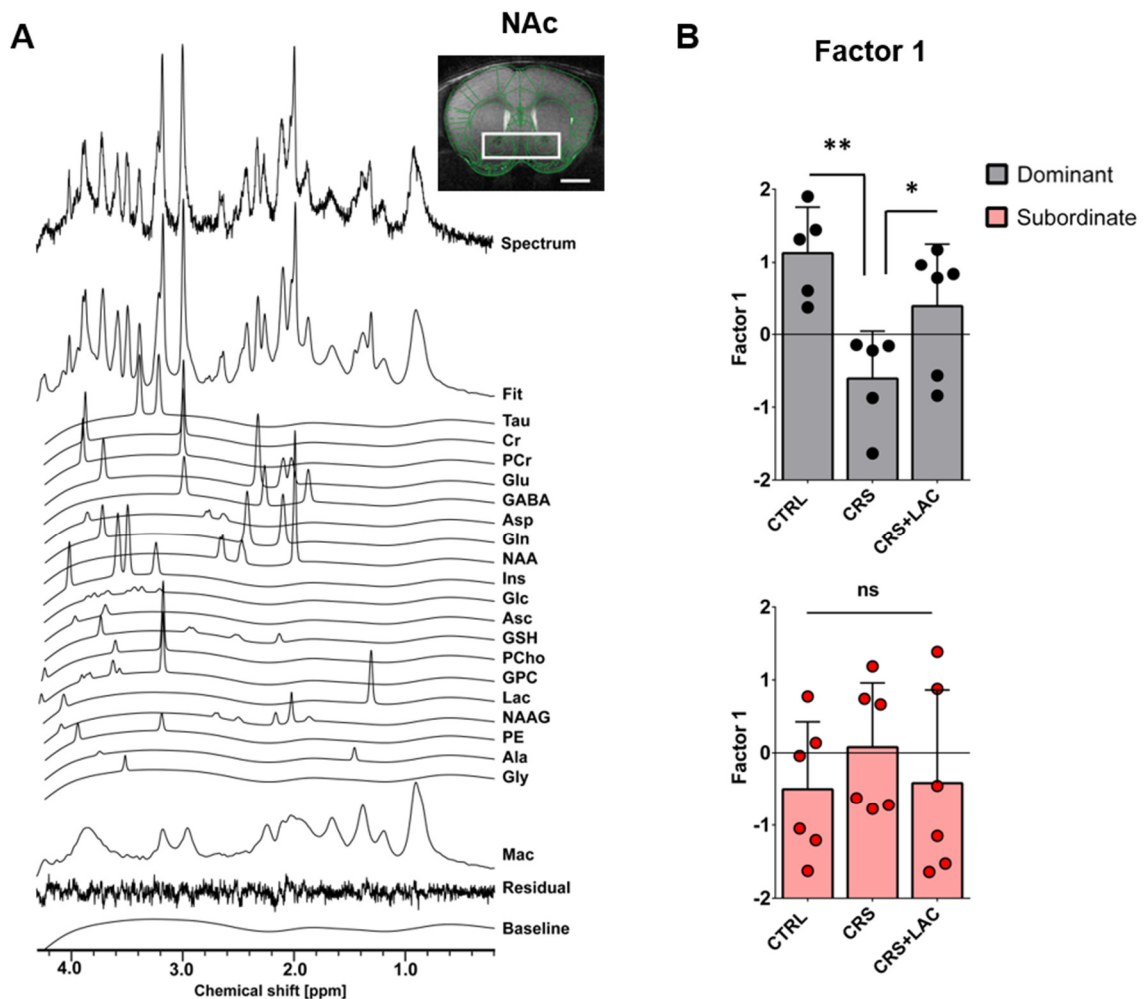


Figure 4.5 : Factor analysis identified one main factor that accounts for the variance in the metabolic profile of nucleus accumbens

A. Typical spectrum and neuroanatomical image of the NAc with respective voxel position in mouse brain. Spectrum is shown with a 1Hz exponential apodization. The fitted neurochemical profile was as follows: phosphocreatine (PCr), creatine (Cr), glucose (Glc), lactate (Lac), alanine (Ala), glutamate (Glu), glutamine (Gln) γ -aminobutyric acid (GABA), N-acetylaspartyl-glutamate (NAAG), aspartate (Asp), glycine (Gly), myo-inositol (Ins), phosphoethanolamine (PE), glycerophosphorylcholine (GPC), phosphorylcholine (PCho), N-acetyl-aspartate (NAA), glutathione (GSH), ascorbate (Asc), taurine (Tau) as well as macromolecules (Mac). **B.** Factor 1 represents a linear combination that summarizes neurochemical changes found in metabolites with strong (above 0.6: Tau, Ins, NAA, Glu, GABA and Cr) and moderate (0.4-0.6: PCho, Asp, PCr, Asc, GSH and Glc) contribution ($F_{2,13}=7.04$, $P<0.01$, one-way ANOVA; * $p<0.05$, ** $p<0.01$, unpaired t-test $n=6$ per group).

Among the metabolites loading in factor 1 the observed effect of stress was strongly carried by changes in Tau, Glu, PCr, NAA and PCho, while the effect of LAC was driven by Tau and PCho (Fig 4.6A and B). Among the metabolites loading in the factor 2 and 3, GPC/PCho ratio and Gln indicated a clear relation to stress with improvement after LAC treatment (Fig 4.6B). These

changes in accumbal PCho and GPG correlated well with plasma insulin ($R=0.57$ and $R=-0.59$) and glucose ($R=0.38$ and $R=-0.34$) levels (Fig 4.7) suggesting that peripheral metabolic regulation is involved.

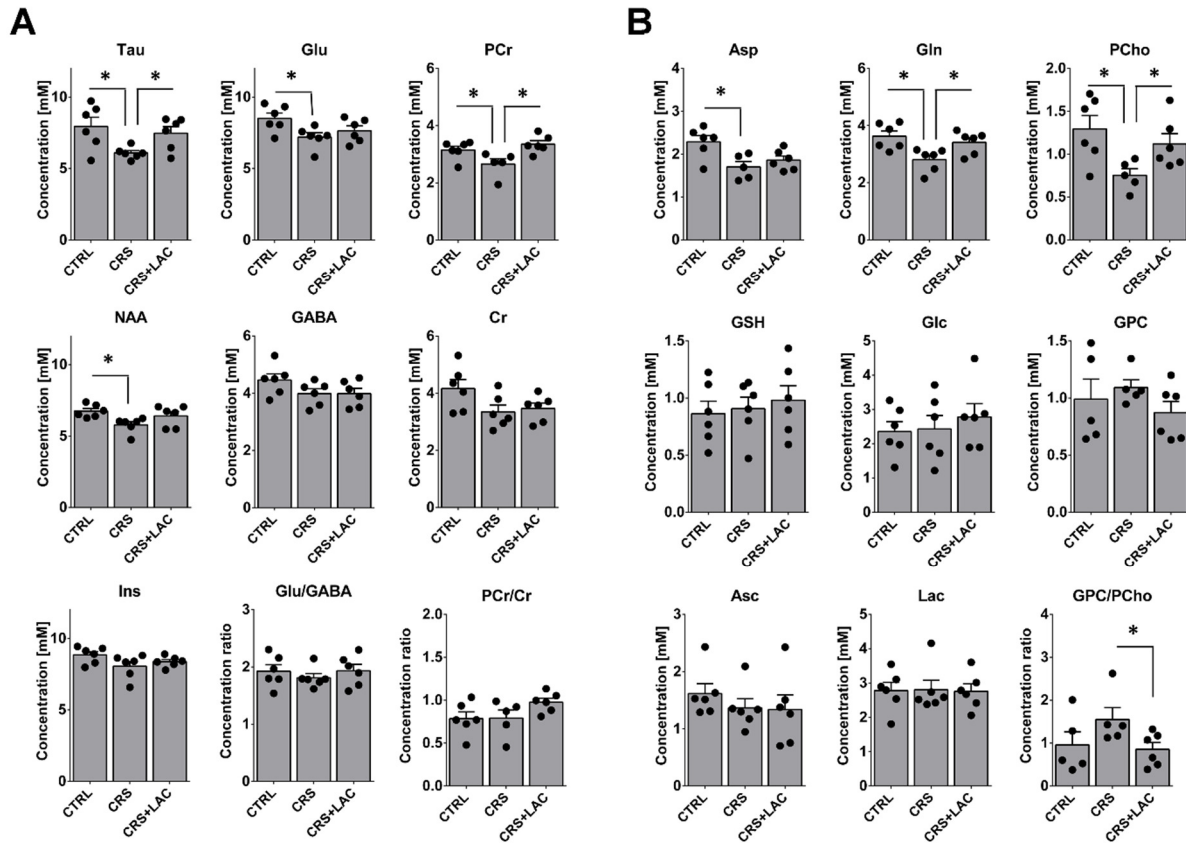


Figure 4.6 : Effect of LAC on the accumbal neurochemical profile of dominant mice after CRS

A. Metabolites from factor 1 with strong loading (above 0.6) included Tau, Glu, PCr, NAA, GABA, Cr and Ins. The ratio of Glu/GABA and PCr/Cr are shown as well. CRS induces a drop in Tau, Glu, PCho and NAA but only Tau and PCr are restored after LAC treatment. **B.** Metabolites with moderate loadings (0.4-0.6) from factor 1 and remaining metabolites from factor 2 and 3 included Asp, Gln, PCho, GSH, Glc, GPC, Asc and Lac. The ratio of GPC/PCho is also shown. CRS induces a drop in Asp, Gln and PCho but only Gln and PCho are restored after LAC treatment. The GPC/PCho ratio is also lowered after LAC administration. One-way ANOVA followed by LSD Fisher post-hoc test, * $p < 0.05$, $n=5-6$ per group

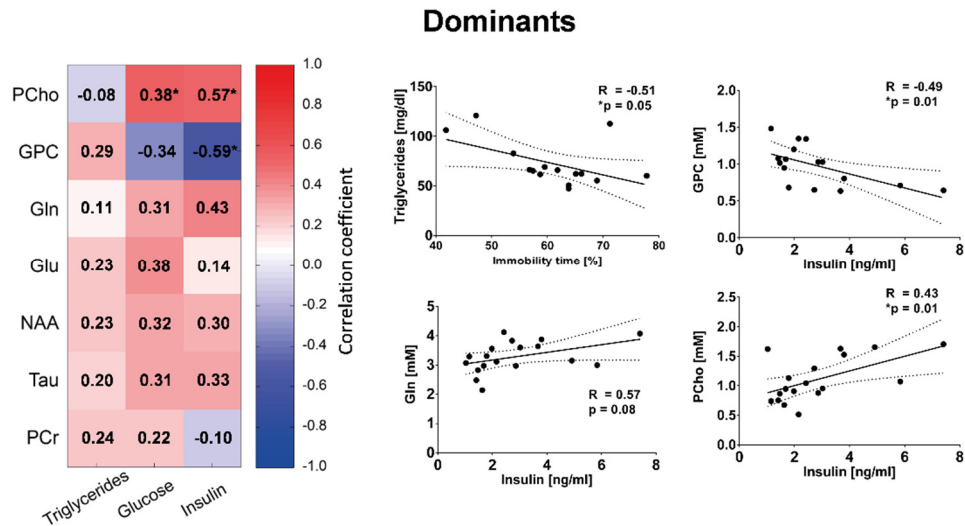


Figure 4. 7 : Associations between blood metabolites and neurochemistry in the nucleus accumbens. (Left) Correlation matrix between triglycerides, glucose and insulin in plasma and main metabolic targets of stress in the nucleus accumbens. Each cell includes the Pearson's correlation coefficient with the associated color scaling. (Right) Scatter plot of behavioral despair vs. plasma triglyceride and plasma insulin vs. glutamine, glycerophosphorylcholine or phosphorylcholine. * $p < 0.05$, $n = 16-18$ per group.

4.4 Discussion

In this study, we have investigated the effect of LAC on NAc metabolic profile in a mouse model of susceptibility to chronic stress. Our findings point towards metabolic candidates implicated in the resilience to stress, opening possible mechanistic pathways underlying the antidepressant-like effect of LAC.

4.4.1 Chronic LAC treatment produces antidepressant-like effect in dominant/susceptible animals subjected to CRS

Several lines of evidence suggest that LAC supplementation could be used to treat depression (Pettegrew et al., 2000; Wang et al., 2014). Recently, rodent studies have revealed that LAC antidepressant-like effect might arise from insulin resistance reversal (Bigio et al., 2016). High immobility time measured with the Porsolt forced swim test, which remains one of the most commonly used mean of assessing rodent depressive-like behavior, is known to be significantly reduced by LAC (Pulvirenti et al., 1990; Wang et al., 2015). Here, we report a similar effect in our group of treated dominant animals (Fig 4.2), confirming a behavioral response to the treatment. Social avoidance, which was impaired by stress did not get cancelled out upon LAC administration. A possible explanation could be that depressive-like

behaviors that are more fundamentally dependent on resources mobilization are more likely to be reversed by LAC's energy support. Restoring normal metabolic function is thus more prone to affect behavior in the context set by the FST - i.e. fighting against an unescapable situation – rather than in a social response. The cumulative weight loss induced by stress did not get recovered by the treatment, in line with a possible trophic support of LAC in the brain rather than the periphery. The susceptibility to stress was not associated with a clear systemic hyperinsulinemia or hyperlipidemia and stress did not exacerbate the existing hyperglycemia of control dominant mice (Fig 4.4). Rather, the intensity of behavioral despair in dominant mice was associated with lower plasma triglyceride levels. Of note, the relative similarity in cumulative weight gain data (however, not identical) in the CRS+LAC groups between dominant and subordinates (Fig 4.4A-B) might arise from the way the protocol is set: 2 dominant and 2 subordinate mice share the same cage. As a result, a systematic error occurring in the dominant data is likely to be observed in the subordinates of the same group as well.

4.4.2 Chronic restraint stress reproduces the depressive-like phenotype observed in chronic social defeat stress

We have previously reported that hierarchical status plays a significant role in the response to chronic social defeat stress (CSDS) in mice (Larrieu et al., 2017). In this paradigm, naïve animals are daily exposed to an aggressor and socially defeated, leading to a depressive-like phenotype at the end of the 10-day protocol. An increase in depressive-like behavior was observed post-CSDS in dominant C57BL/6 mice and proposed to arise from the greater loss of rank and resources compared to subordinates (Larrieu and Sandi, 2018). However, behavioral alterations observed after CSDS are typically measured in terms of social avoidance in a social interaction test, which exposes the stressed mouse to an unknown individual (Berton et al., 2006; Krishnan et al., 2007). The validity of such depressive-like assessment has thus been challenged and sometimes relegated merely to an adaptive response to aggression (Chaouloff, 2013; Henriques-Alves and Queiroz, 2016). The present study provides strong support against this idea, by giving evidence that another stressor devoid of social component like chronic restraint stress (CRS) can induce a similar phenotype in dominant mice (Fig 4.1). The dominant status was accompanied by a higher anxiety trait, in line with our previous study and significant evidences in the literature, which reported this characteristic in individuals at risk

for developing stress-related depressive-like behaviors (Castro et al., 2012; Miller et al., 2012; Sandi, 2008; Sandi and Richter-Levin, 2009).

4.4.3 LAC reverses stress-induced neuroenergetic- and membrane metabolism dysfunctions in NAc: potential astroglial mechanism

Several studies have assessed the effect of LAC on brain metabolic content: Magnetic resonance-based studies have reported changes in brain phospholipid metabolism, reduced glycolytic activity and increased mitochondrial function induced by LAC. ^{31}P - and ^1H -NMR analysis of rodent brain extracts have revealed a drop in lactate, increase in the PCr/Cr ratio and changes in choline containing phospholipid metabolites (Aureli et al., 1990, 2000). Similarly, changes in phosphomonoesters and PCr content were observed *in vivo* using ^{31}P -MRS (Pettegrew et al., 2002). Effects on lipid metabolism would be expected from carnitine given its ability to facilitate fatty acid transport through mitochondrial membranes, however, controlling choline phosphomono- and di-ester metabolism by providing brain with triethylamine supply would also be possible. The drop of lactate with concomitant rise in PCr/Cr ratio is likely to reflect the improved mitochondrial oxidative function, by either providing increased oxidizable fuel for mitochondria in the form of acetyl groups or by reducing substrate inhibition of pyruvate dehydrogenase (PDH) by buffering AcCoA. Several lines of evidence indicate that LAC action might also be strictly epigenetic, by providing and transporting acetyl moieties for protein acetylation. Smeland et al. (Smeland et al., 2012) have shown that LAC reduces $[3\text{-}^{13}\text{C}]\text{lactate}$ formation from $[1\text{-}^{13}\text{C}]\text{glucose}$ without interfering with its mitochondrial oxidation, resulting in increased overall PCr/Cr. Our results are in line with the idea of a restored mitochondrial function and support by LAC visible through the increase in PCr, but also taurine. Taurine is an antioxidant with neuroprotective properties, which is located in the mitochondrial matrix and particularly abundant in highly oxidative tissues (Hansen et al., 2006; Jamshidzadeh et al., 2017; Wang et al., 2016; Yang et al., 2013). PCho is increased along with a drop in the GPC/PCho ratio upon treatment with LAC. PCho serves as a precursor of phosphatidylcholine (PtdCho), one of the main brain phospholipid, while GPC is its degradation product (Morash et al., 1988). The GPC/PCho ratio is thus considered to reflect the membrane turnover, typically increased in the case of neurodegeneration or excitotoxicity (Kristián and Siesjö, 1998; Nitsch et al., 1992). Increase in GPC can only arise from increased phospholipase activity, which is frequent during excitotoxicity and has been

proposed to be a consequence of astrocyte activation (Ha et al., 2014; Klein, 2000). High levels of PCho and low levels of GPC correlating with plasma insulin and glucose levels brings a potential mechanistic link between a possible glial dysfunction in brain and a systemic energy regulation process. The role of astrocytes in the mechanism of action of LAC is corroborated by the clear improvement of Gln content in the treated group. Gln is mostly abundant in astrocytes (typically 80% of total concentration) due to their specific expression of glutamine synthetase (GS), which plays a key role in glutamate recycling at the synapse. Astrocytic function is fundamental in the resilience to stress and regulation of extrasynaptic glutamate homeostasis. For instance, LAC has shown effective control of astroglial cystine-glutamate exchanger (xCT), which is thought to improve mGlu2 function in hippocampus as a response to stress. A similar transcriptional response could be expected for glial GS, given its established responsiveness to glucocorticoids in stress (Carter et al., 2013; Rozovsky et al., 1995), and would underlie the observed Gln changes. Even though the acetyl moiety of LAC has been shown to be utilized for the build-up of metabolic neurotransmitters synthesized from the TCA cycle (Kuratsune et al., 2002), our treatment protocol was unable to restore stress-induced drop in Glu, NAA and Asp. This would suggest that the restoration in these metabolite levels by LAC might be secondary and part of a slower process. Another reason may be that the increased LAC availability in the mitochondria results in citrate production and export through mitochondrial transporter, which would lead to the subsequent drop of glutamate and aspartate as an anaplerotic consequence, i.e. maintaining TCA cycle intermediate levels constant. This mechanism could explain why no rise in Asp and Glu were observed following LAC treatment. A rise in cytoplasmic citrate would be an interesting mean of providing the nuclear source of AcCoA required for histone acetylation in a nuclear ATP-citrate lyase (ACLY) process (Arduini et al., 2016; Sutendra et al., 2014). Nevertheless, as NAA, Glu and Asp reflect mainly neuronal metabolism, we can hypothesize that astrocytes are primarily the first beneficiary of LAC supplementation. Astrocytes are indeed specifically shaped to uptake blood ketone bodies and acetate, and presumably acetyl-L-carnitine.

In conclusion, our study provides an *in vivo* basis for understanding antidepressant-like properties of LAC and its protective effects against chronic stress. Restoration of energy and lipid metabolism seems to be at the core of LAC effect in the nucleus accumbens possibly through an astrocytic mechanism.

Chapter 5

Study of metabolic remodeling during neurogenesis using MRS

Contributions to the work:

This chapter is the result of a collaborative work with the laboratory of Dr. Jean-Marc Matter at the University of Geneva. My contribution consisted in the design of the MRS protocol, acquisition and analysis of the NMR data. The interpretation of the data and manuscript writing have been done by myself as well, in collaboration with the co-authors. All the molecular and cellular analyses have been performed by Dr. Laurent Brodier. This includes the microscopic imaging experiments and gene expression analysis.

This Chapter was partially adapted from:

Cherix* A, Brodier* L, Poitry-Yamate C, Matter J-M and Gruetter R: The appearance of the Warburg effect in the developing avian eye characterized *in ovo*: how neurogenesis can remodel neuroenergetics. IOVS, *submitted*. *shared first authorship.

Abstract

Metabolic adaptation and remodeling are key aspects of resilience to stress that provide protection against the establishment of mood disorders. These mechanisms have been reported to be critical in processes that allow the brain to adapt to its environment, such as during neurogenesis. Given the evidence suggesting that adult neurogenesis is impaired in patients with mood disorder, there is strong interest in identifying metabolic pathways that characterize or stimulate the proliferation of progenitor and subsequent differentiation into newborn neurons. The following project aimed at identifying the metabolic processes occurring during embryonic neurogenesis and associated with the development of new neurons. With its well-established organization, the avian retina was investigated during embryogenesis using *in ovo* ^1H -MRS, providing metabolic information relevant to high-acuity vision organisms. In this study, we describe for the first time the appearance of a metabolic switch occurring in the chick retina, characterized by the transient appearance of a lactate peak together with glycolytic regulator expression. Comparing these result with the pigeon, whose neurogenesis is delayed by 3 days, allowed us to relate this switch to the maturation and axogenesis of retinal ganglion cells. Our findings provide new mechanisms and potential metabolic MRS-biomarkers that could be associated with neurogenesis in a context of mood disorders.

5.1 Introduction

There is growing evidence that alterations of brain energy metabolism is the source of several neurological disorders. A reason for this link is the high energetic needs of the brain generally considered to be around 20% of the whole body (Attwell and Laughlin, 2001; Rolfe and Brown, 1997), rendering this organ particularly sensitive towards energetic deprivation or allostatic load. The brain is thus prone to metabolic adaptation keeping a tight coupling between energy demands and energy supply for the highly consumptive neurons (McIlwain, 1970).

The brain uses several metabolites as oxidative energy substrate (Zielke et al., 2009), of which the predominance will depend on the physiological state. For instance, fasting and reduced glucose availability lead to increased ketone bodies utilization (Owen et al., 1967). Aerobic glycolysis observed during brain activity is another example of short-term neuronal adaptation to increased energetic needs. During this event, a mismatch between the amount of oxidized glucose and the glucose metabolized via glycolysis (or increased $CRM_g/CMR_g(ox)$ ratio) leads to an accumulation of cerebral lactate (Madsen et al., 1999). The exact role of lactate in brain neuroenergetics has been a central question over the past decades (Mason, 2017). From the hypothesis of ANLS (astrocyte-neuron lactate shuttle) (Magistretti and Pellerin, 1999), suggesting that a higher glycolytic rate in astrocytes drives lactate release and shuttle into neighboring neurons, to more recent in situ neuronal lactate production evidences (Díaz-García et al., 2017), the role of brain-born lactate has been intensively debated. Metabolic adaption occurs during development as well. The constant remodeling of an organism and evolving physiological organization require fine-tuned control on the time-dependent metabolic needs of every growing organ, which is true for the brain as well. The same is true for the brain during development, in which metabolic switches have been observed in several studies (Hellmann et al., 1982; Homem et al., 2014; Nehlig and Pereira de Vasconcelos, 1993; Ward Platt and Deshpande, 2005).

Retinal Ganglion Cells (RGCs) are among the most energy consuming neurons in the vertebrate brain (Wong-Riley, 2010). RGCs transmit retinal electrical activity through the optic tract from photoreceptor and interneurons to the brain. Their axons merge together forming the optic nerve at the level of the optic disk. As light has to cross the whole retina layer, including the RGCs, to reach the photoreceptors, RGC axons are generally not myelinated in the retinal nerve fiber layer to avoid interference with light by myelin. The consequence of low

myelination on long axons include higher energetic needs and increased sensitivity to metabolic stress (Morgan, 2004). RGCs are thus selectively impacted in several mitochondrial or metabolic diseases like inherited optic neuropathies or diabetic retinopathy leading to loss of vision (Kern and Barber, 2008; Yu-Wai-Man et al., 2011). Myelination can however occur partially in chick with onset at embryonic day E14 (Nakazawa et al., 1993; Rager, 1976). A reason for this particularity arises from the high level of development and efficiency of avian retina compared to other species, allowing sharp vision. Bird retina is closer to humans than any other experimentally studied mammal with higher number of RGC relative to the number of photoreceptors or the presence of high acuity spots named fovea. Nevertheless, interspecies disparities have been observed among chicks and pigeons arising from developmental differences. Although retinas grow at a similar pace in both species, cell differentiation and production of RGCs is delayed by ~3 days in pigeon (Rodrigues et al., 2016).

The idea that a different developmental onset of RGC production exists between chick and pigeon led us to investigate the existence of an associated difference in metabolic adaptation. ^1H -Magnetic Resonance Spectroscopy (^1H -MRS) is the technique of choice for studying metabolism *in vivo* without interfering with the subject's physiology. Several magnetic resonance studies have been conducted to investigate the structure of the eye (Fanea and Fagan, 2012; Smith et al., 1990), but only limited studies investigated its function and metabolism *in vivo* (Doganay et al., 2012; Duong, 2011; Ngumah et al., 2006; Peng et al., 2011). Most of the available data regarding retina metabolism has thus been obtained from *ex vivo* or *in vitro* techniques (Brown et al., 1977; Florian et al., 1996; Greiner et al., 2013; Li et al., 2011). Using a multi-modal approach of ^1H -MRS combined with molecular and biochemical analyses, we report the emergence of a developmental glycolytic switch linked to retinal neurogenesis. Our results suggest that one or more compartments lying around the vitreous play a crucial role in providing trophic support to the neighboring RGC neurons. We show that RGC axogenesis and their axonal accumulation of mitochondria that create the need to fuel mitochondrial oxidative metabolism coincide temporally with the disappearance of citrate and with a pH rise in the neighboring vitreous compartment. These changes appear to serve a metabolic signaling function in a cascade that involves PFK2 and PDK, leading to glycolysis activation in the retina. This results in the net accumulation of vitreous lactate, a recognized retinal energy source in chick embryo eyes (Zeevalk and Nicklas, 2000).

5.2 Material and methods

5.2.1 Animals

Chick embryos from White Leghorn strain (UNIGE Animal Resources Centre) were staged according to (Hamburger and Hamilton, 1992). Fertilized pigeon eggs were supplied by Philippe Delaunay (Pigeonneau de la Suisse Normande, Croisilles, France). Experimental procedures were carried out in accordance with Federal Swiss Veterinary Regulations. Bird eggs were hatched in a portable incubator keeping humidity and temperature (37°C) at optimal conditions for embryo development. Eggs were either scanned and placed back into incubator after the experiment or opened for retina/vitreous body dissection in DPBS medium (ThermoFisher) with removal of surrounding retinal pigmentary epithelium.

5.2.2 Reporter and expression plasmids

The Atoh7 reporter plasmids were described in (Skowronska-Krawczyk et al., 2009). The CMV-Mito:DsRed2 (pDsRed2-Mito) and CMV-Mito:GFP (pAcGFP1-Mito) plasmids were from Clontech. Atoh7-Mito:DsRed2 was designed using UGene software (Unipro). The GFP sequence was excised from Atoh7-GFP plasmid using Angel and KpnI restriction enzymes (New England BioLabs). The mito-DsRed2 sequence from the CMV-Mito:DsRed2 plasmid was amplified with PCR and extremities were digested with XmaI and KpnI restriction enzymes (New England BioLabs). Ligation was performed using Quick Ligation Kit (New England BioLabs).

5.2.3 Retina preparation

Eyes were removed and the RPE layer surrounding the retina was peeled with forceps. Stripped eyes were electroporated in electroporation cuvettes (BT 640, BTX) with the reporter plasmid CMV-GFP, Atoh7-RFP, or CMV-Mito:DsRed2 at 0.1 µg/ µl. Electroporation was performed in 100 µl using 5 pulses of 5 V and 50 ms, separated by 1 sec interval with BTX ECM830 electroporator. Electroporated retinas were cultured in DMEM (ThermoFisher) complemented with 10% Fetal Bovine Serum (ThermoFisher) and 1% Penicilin-Streptomycin (ThermoFisher) for 8h, 24h, or 48h at 37°C in an incubator with 5% CO₂. After 8h or 24h of tissue culture, electroporated retinas were washed with HBSS lacking Ca²⁺ and Mg²⁺

(ThermoFisher) and dissociated mechanically and enzymatically using Trypsin 0.05% (ThermoFisher) for 15-20 min at 37°C. Reaction was blocked by addition of 10% Fetal Bovine Serum (ThermoFisher).

5.2.4 Fluorescence Activated Cell Sorting

After dissociation, cells were pelleted and resuspended in DMEM (Amimed). Cells were sorted by FACS Aria II for GFP positive cells, or with FACS Astrios for GFP and red fluorescent protein (RFP) positive cells. Cells were pelleted and resuspended at 1-2 mio cells / ml. 100-200 µl was plated on a poly-dl-ornithine coated permanox chamber slide (Lab-Tek). Cells were left 30 min at 37°C and 5% CO₂ for adhesion, then were fixed with 4% paraformaldehyde for 20 min. Finally, after DPBS washing, DABCO was added and the slide was sealed with coverslip for imaging.

5.2.5 Confocal imaging

Dissociated cells were plated on permanox chamber slides (Lab-Tek) coated with poly-dl-ornithine (Sigma-Aldrich), left 30 min for adhesion in a 37°C 5% CO₂ incubator, and then fixed 20 min with 4% paraformaldehyde. Coverslips were sealed after addition of DABCO (Sigma-Aldrich) with 50% glycerol (Sigma-Aldrich) in DPBS (Thermo-Fisher). Imaging was done with Leica Sp5 Laser scanning Confocal microscope in photon counting mode using a Leica 20x multi-immersion objective (0.7 N.A.) in Leica type F-type immersion oil of refractive index 1.518. An Argon laser was used for 488 nm GFP excitation and DPSS561 for 561 nm RFP excitation. Optical sections of 1 µm were acquired with a 2-4x line accumulation. Confocal images were processed with ImageJ/Fiji softwares for counting.

5.2.6 Time-Lapse imaging

Electroporated E5 retinas were placed on a 35-mm glass bottom dish (Pelco, Wilco Wells) 24h later and incorporated in collagen prepared as described in (Chiodini et al., 2013). Retinas were flattened after removing the lens and vitreous body, allowing to follow axons growth in the horizontal plane. The dish was incubated at 37°C to allow collagen polymerization. Culture medium composed of DMEM without phenol red complemented with 10% fetal bovine serum and 1% Penicillin-Streptomycin was added on top of the collagen matrix. Retinas were imaged

using a Leica Widefield AF6000LX inverted microscope with a Leica 40x dry long-distance objective (0.55 N.A.) for up to 72 h in the Green and Red channel using Leica GFP and Rhodamine filter cubes. Stacks of images separated by 1 μm for a total of 40-60 microns were used with a time interval of 20 minutes, 2 minutes or 20 seconds. Data were saved as *.lif file.

5.2.7 *In vivo* proton Magnetic Resonance Spectroscopy (^1H -MRS)

5.2.7.1 *In vivo* measurement

Hen eggs (n=6) as well as pigeon eggs (n=6) were scanned at two embryonic stages (E6 and E8) in a horizontal 14.1T/26cm Varian magnet (Agilent Inc., USA). A similar setup was used as described in (Lindner et al., 2017) with the main difference that a receiver surface coil was preferred to volume coil in order to improve sensitivity for localized spectroscopy. Briefly, eggs were fixed on a holder and maintained at hatching temperature (37-37.5°C) during the scans using circulating water heating. A 17 mm transmit-receive ^1H quadrature surface coil fitting the shape of the egg was placed as close as possible to the chick embryo (i.e. on the top surface). T_2 -weighted fast spin-echo (FSE) images (Fig 5.1) were used for localization and proton spectra were acquired with the SPECIAL sequence (TE/TR=2.8/4000ms) with OVS and VAPOR water suppression (Duarte et al., 2012; Mlynárik et al., 2006). Shimming was performed using FAST(EST)MAP with the typical linewidth (FWHM) of water signal ranging between 5 and 10 Hz depending on the VOI size and position. The size of the volumes of interest were variable depending on the embryonic stage and the tissue as follows: vitreous body (Chicken E6: 4.5 μl ; E8: 20 μl / Pigeon E6: 1 μl ; E8: 16 μl) and full eye (Chicken E6: 60 μl ; E8: 160 μl / Pigeon E6: 18 μl ; E8: 80 μl). Scan time ranged between 20 minutes for the big voxels (full eye) and a couple of hours for the small ones (vitreous) to reach sufficient signal-to-noise ratio (SNR). Embryos start showing spontaneous muscular contraction leading to intense movements of the whole body at embryonic stage E8. Given the high motion-sensitivity of localized ^1H -MRS, embryos were scanned out of the egg at E8 by maintaining the organism alive in cold DPBS medium in a sealed bag. As the bird embryo's respiration is based on oxygen diffusion in the egg, this setup provided a valid mimetic of embryonic environment that allowed maintaining the embryo alive for the ~1h scan and prevented motion-induced artifacts. This scan out of the egg mentioned herein is thus referred to as "ex ovo" in

comparison to the E6 “in ovo” measurement. All the localized ^1H -MRS experiments (including *in ovo* and *ex ovo*) are mentioned as “in vivo” scans as the embryo was intact.

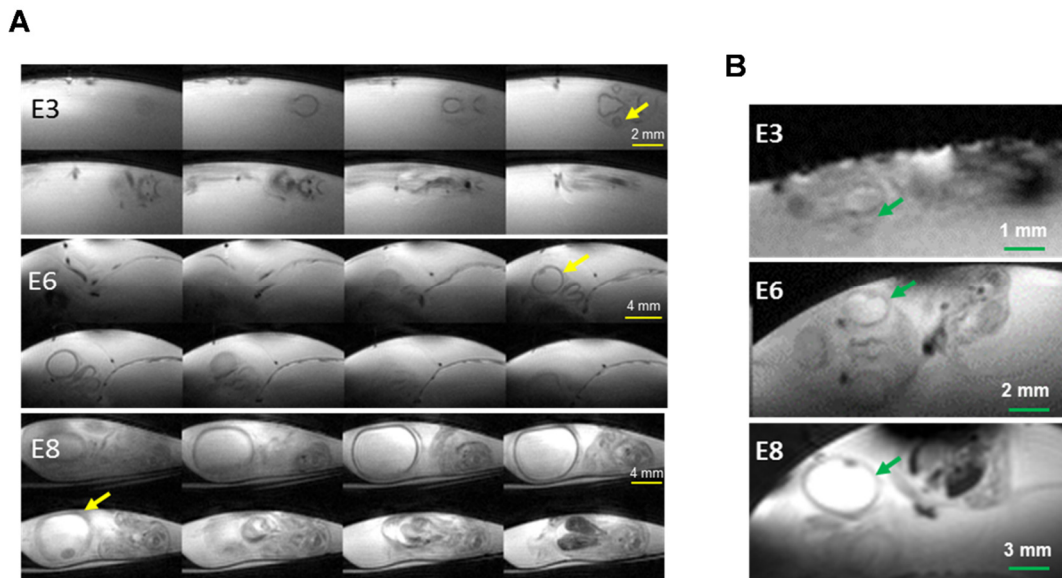


Figure 5. 1 : *In vivo* MRI images of the avian embryo.

A. Full set of T₂-weighted images of chick embryo *in vivo* at E3 and E6 as well as *ex vivo* at E8. **B.** T₂-weighted images of pigeon *in ovo* at E3, E6 and E8.

5.2.7.2 *In vivo* spectra quantification

^1H -MRS allowed measuring quantitatively metabolite concentrations in avian eyes, both *in ovo* and *ex ovo*. Spectra were corrected for B₀ drift and quantified using the jMRUI (v.5.2) Software package (Stefan et al., 2009). Metabolite spectra were quantified with QUEST routine of jMRUI using a simulated basis set including several metabolites as well as main lipid resonances. Water signal for each voxel were integrated using the Hankel Lanczos singular values decomposition (HLSVD) routine in JMRUI, normalized, as well as gain- and proton corrected. Absolute quantification of metabolite signal was performed using the water signal as an internal reference and with the assumption of its concentration to be 99% in the vitreous body and approximated as 80% in the full eye (Kokavec et al., 2016; Yadgary et al., 2010). *In vivo* ^1H -MRS allows measuring quantitatively and non-invasively metabolite concentration of metabolites above ~1mM. Upon quantification of the spectra, the Cramér-Rao lower bounds (CRLB) indicates the reliability of the fitting process.

5.2.7.3 *In vivo* pH measurement

Citrate chemical shift (δ) - pH dependence was measured in phantoms on the 14.1 Tesla scanner by dissolving 5mM citrate and lactate buffered at several pH ranging from 6.0 to 7.5. After scaling the spectra using lactate as internal reference, the center of the methylene resonances was measured and plotted against the pH. The pH was calculated by fitting the resulting data with a second order polynomial function ($\delta = 0.0159 \cdot \text{pH}^2 - 0.227 \cdot \text{pH} + 3.4$).

5.2.8 High resolution ^1H -NMR spectroscopy

5.2.8.1 *Metabolite extracts measurement*

Retina and vitreous bodies were dissected from embryos (chick E6 and E8; pigeon E6, E8 and E12) and frozen in liquid nitrogen. Retinal pigmented epithelium and lens were always carefully removed to avoid potential contamination. Tissue samples were ground on a mortar using liquid nitrogen, weighted, and metabolites were extracted using the methanol/chloroform Folch-Pi extraction technique (Folch et al., 1957). Briefly, 400 μl methanol was added on the powdered tissue, followed by subsequent addition of 400 μl milipore water and 400 μl chloroform. The mixture was left for 30 min at 4°C with stirring and centrifuged until phase separation (10 min at 400rpm and 4°C). The aqueous phase containing hydrophilic metabolites was then lyophilized and dissolved in 1ml deuterium oxide and 4,4-dimethyl-4-silapentane-1-sulfonic acid (DSS) as internal water-soluble reference at 0.1 μM . The lipophilic (chloroform) phase was evaporated on ice using a nitrogen flow and dissolved in 1ml deuterated chloroform with tetramethyl silane (TMS) as internal chloroform-soluble reference. Fully relaxed ^1H -NMR spectra (Fig 5.2) were acquired using a DRX-600 spectrometer (Bruker BioSpin, Fällanden, Switzerland). Each sample lead to a 520-spectra scan with a pulse-acquired sequence (30° pulse) using a pulse delay of 5s and an acquisition time of 2.7 s.

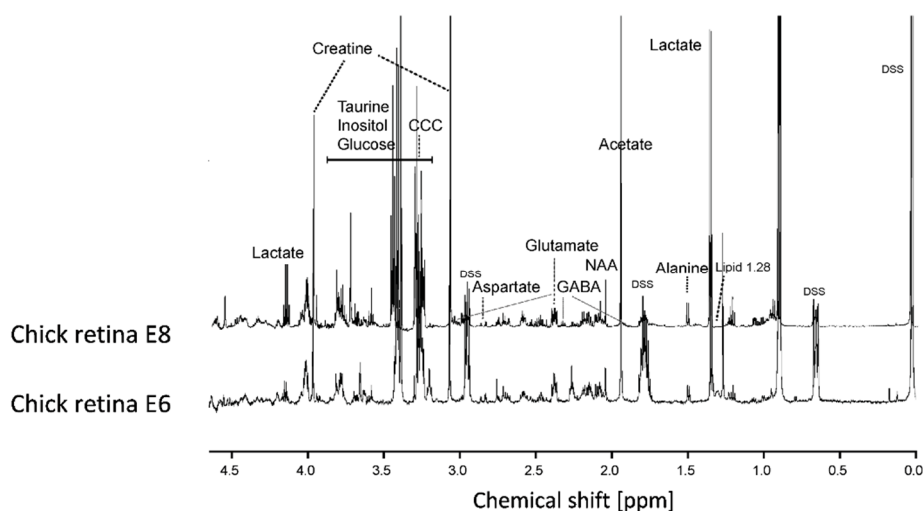


Figure 5. 2 : Typical spectra obtained from high-resolution ^1H -NMR at 600 MHz

5.2.8.2 Metabolite spectra quantification

Spectra were referenced to the internal reference (DSS or TMS), phase and baseline corrected manually using the MestReNova software. Selected metabolite peaks, with minimal adjacent resonances overlap, were integrated manually using MestReNova software. These peaks were proton corrected and normalized to the DSS methyl singlet at 0 ppm and referenced to the tissue sample mass in amount of metabolite extracted per mass of wet tissue [$\mu\text{mol/g}$]. Following resonances were considered: lactate δ 1.31 (1H, d), alanine δ 1.47 (3H, d), creatine δ 3.03 (3H, s), N-acetyl-aspartate δ 2.00 (1H, s), aspartate δ 2.80 (1H, dd) glutamate δ 2.33 (2H, m), GABA δ 2.28 (2H, t), glutamine δ 2.43 (2H, m), citrate δ 2.60 (2H, m), oxaloacetate δ 2.38 (2H, s), scyllo-inositol δ 3.33 (6H, s), myo-inositol δ 3.52 (2H, dd), taurine δ 3.42 (2H, t) and alpha glucose δ 5.22 (1H, d) as 36% of total glucose. Water-soluble lipid peak at 1.28 ppm was quantified by normalizing its height to the creatine (3.03 ppm) peak height. Lipid spectra were quantified using the methyl terminal peak of fatty acyl chains (CH_3) δ 0.91 (3H, t) as reference. Due to lipid shorter T_2 relaxation times leading to broader linewidths, the peak height rather than the integral was considered relevant for the selected measured resonances: Fatty acyl chain (CH_2) $_n$ δ 1.28 (2H, m), total cholesterol C18 δ 0.68 (3H, s), double unsaturated fatty acyl δ 2.80 (2H, m), phosphodiesteres 4.00 (2H, d), glyceryl backbone of triglycerides δ 4.15/4.29 (2H, m), glyceryl backbone of triglycerides δ 5.20 (1H, m) and mono unsaturated fatty acyl δ 5.30 (2H, m). Each peak height was measured and normalized to the 0.88 ppm peak after dividing the height by the number of protons.

5.2.9 RT-qPCR

RNA from FACS sorted cells or from whole retinas was extracted using TRIzol reagent (ThermoFisher) according to product manual in triplicate. Primers were designed using NCBI primer blast and Primer3 websites and sequence stored in UGene software. Primers were ordered from Microsynth. Primers were tested using RNA from total retina extracted with TRIzol. RNA quantification was done with spectrophotometer and Qubit 2.0 (ThermoFisher) and RNA quality was checked using BioAnalyzer (Agilent). RT was performed using Takara PrimeScript reverse transcriptase prior to qPCR.

5.2.10 mtDNA quantification by qPCR

DNA of FACS sorted cells or dissected retinas was extracted according to DNeasy Blood & Tissue DNA extraction kit (Qiagen). Primers were designed for targets on gDNA and mtDNA. qPCR was performed and gDNA used for normalization.

5.3 Results

5.3.1 Mitochondrial metabolism decreases during retinal development

In order to assess the overall oxidative metabolism in the retina, the retinal mitochondrial mass was assessed in the dissected retina by quantifying the relative mitochondrial DNA (mtDNA) copy number. Results indicate a constant drop in mtDNA in both chick and pigeon from E3 to E15 with the highest mitochondrial content at early stages of retina development (Fig 5.3A). This drop coincides well with a reduction of the master regulator of mitochondrial biogenesis PGC1 (peroxisome proliferator-activated receptor gamma coactivator 1) expression, with a stronger effect on the beta subunit rather than alpha (Fig 5.3B). Many other genes control and regulate the mitochondrial content and function, and as such, the expression of Nrf, TFAM, Ncor1 and Nix (Beckervordersandforth et al., 2017; Kiyama et al., 2018; Lima et al., 2018; Novak et al., 2010) have been investigated (Fig 5.3C). The drop in relative Nrf and TFAM mRNA content were consistent with lower mitochondrial biogenesis. The increase in Ncor1 also supports the idea that mitochondria biogenesis is repressed, while the steady levels of Nix is evidence against a mitophagy-related process. Retina were transfected with a CMV-GFP reporter together with an ubiquitous mitochondria-targeted

label (CMV-mitoDsRed2), whose accumulation in mitochondria has been shown to depend on mitochondrial membrane potential (Brodier, et al. 2019). Results indicated a drop of mitochondrial activity (Fig 5.3D), which in pigeon was delayed by ~3 days, suggesting that the temporal pattern of mitochondrial activity, unlike mitochondrial mass, is related to neurogenesis. Quantitative analysis of the relative mtDNA copy number in committed RGCs expressing Atoh7 at high level (Atoh7-RFP; Fig 5.3E), confirmed that the high content of mitochondria was comparable to that in early progenitors. This was corroborated by the high level of mitochondria activity in newborn RGCs identified with a Chrn3-GFP reporter (Brodier et al. 2019) (Fig 5.3F). Buono et al. have reported a similar drop in mitochondria in the inner part of the developing avian retina (Buono and Sheffield, 1991a). To investigate whether newly differentiated neurons are involved in the remodeling of mitochondrial content, we used confocal time-laps imaging of the retina at E6 expressing a mitochondrial-targeted fluorescent protein (CMV-MitoDsRed2) to get insight into their subcellular dynamics. Results show a high number of active mitochondria contained by RGC axons (Fig 5.3G), following the growth cone expansion (Fig 5.3H) with a significant anterograde directionality as revealed by kymograph analysis (Fig 5.3I and J). Our investigations confirm the previously reported developmental transformation of the avian retina into a glycolytic tissue, highlighting the migration of mitochondria during RGC axogenesis as possible mechanistic cause.

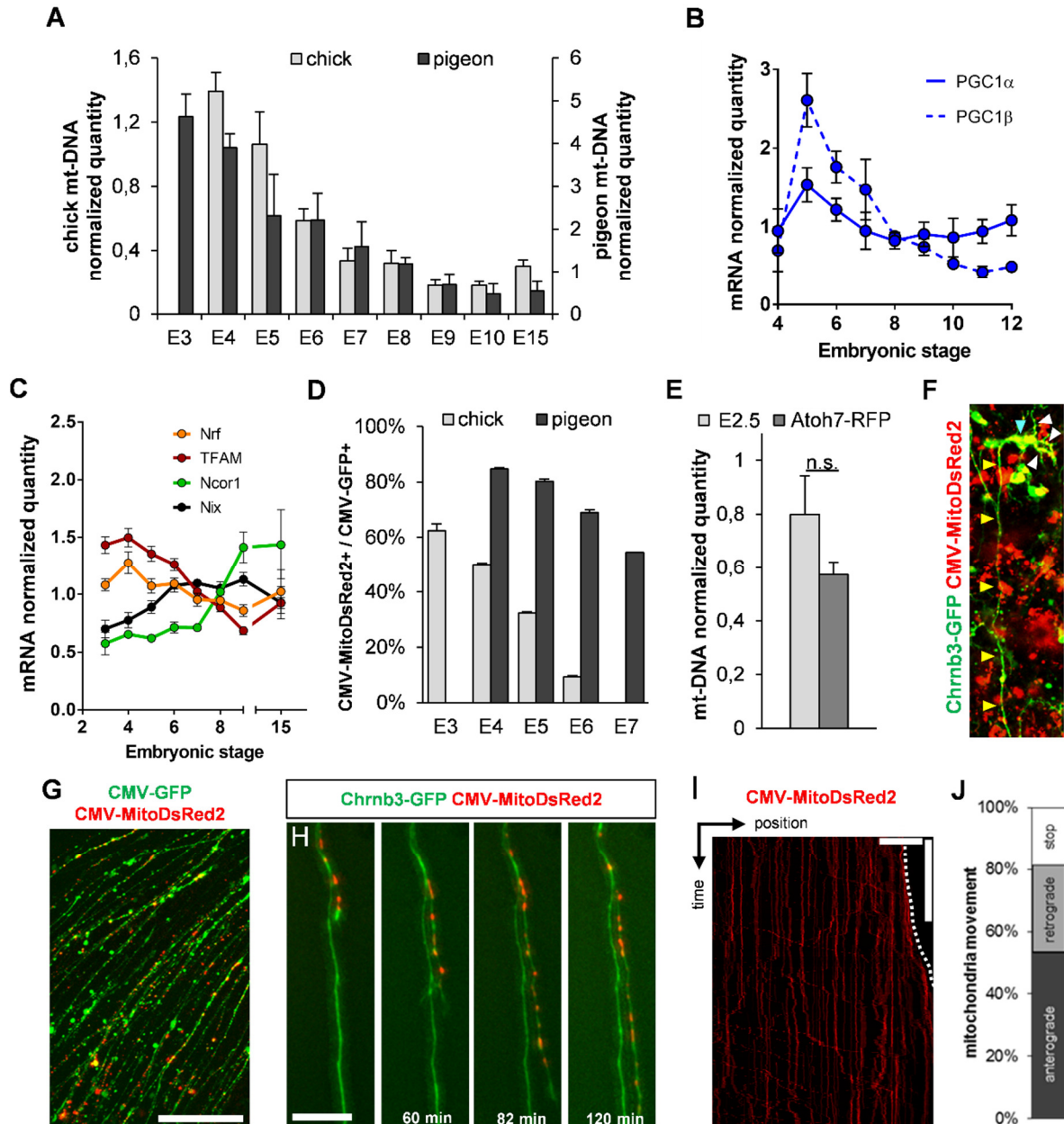


Figure 5.3 : Mitochondrial metabolism decreases as development proceeds in the avian retina

A. Ratio \pm SD of mt-DNA to g-DNA in whole retinas isolated from embryonic chick and pigeon. Data from biological triplicates with 4 targets (chick) or 2 targets on mt-DNA (pigeon). **B.** Relative mRNA expression of the master mitochondrial biogenesis factor Peroxisome proliferator-activated receptor gamma coactivator 1 (PGC1) in pigeon retina. **C.** Relative mRNA expression in chick retina from different target genes involved in mitochondrial biogenesis and autophagy. At each developmental stage, data are from three biological replicates including 3-10 retinas and presented as mean \pm SD. Nrf: Nuclear respiratory factor, TFAM: Mitochondrial transcription factor A, Ncor1: Nuclear receptor co-repressor 1, Nix: Nip3-like protein X. **D.** Proportions of cells that contain MitoDsRed2-labelled mitochondria during development of the chick and pigeon retinas, including 3-10 pooled retinas for each condition and processed as one biological replicate. All pairwise comparisons give $p < 0.001$ (Chi square test; Chick E3 $n = 370$ cells, E4 $n = 9754$, E5 $n = 8480$, E6 $n = 4109$; Pigeon E4 $n = 827$, E5 $n = 4861$, E6 $n = 3808$, E7 $n = 2516$). **E.** Whole E2.5 (HH18) chick retina and a chick committed and newborn RGCs identified with Atoh7-RFP and selected by FACS (unpaired t-test; $p = 0.134$; $n = 3$). **F-J.** E5 chick retinas were co-electroporated with CMV-GFP and CMV-MitoDsRed2 (G) or Chrb3-GFP and CMV-MitoDsRed2 (F, H, I, J) and observed 24 h later. **F.** The soma (cyan arrowhead), the dendrites (white arrowheads) and the axon (yellow arrowheads) of a single RGC by confocal imaging. **G.** Axons growing on the basal surface by confocal imaging. **H.** Stills from a time-lapse movie in the red

and green channels, showing growth cone progression and mitochondria dynamics. **I.** A kymograph of spatial position of mitochondria in a growing RGC axon. The vertical axis represents time at 30 seconds intervals. The dotted line indicates position of the growth cone. **J.** Proportion of mobile mitochondria moving in the anterograde or retrograde direction and stopped mitochondria from kymograph presented in **I.** Scale bars: 50 μm (F, I horizontal), 100 μm (G), 30 μm (H), and 1'800 seconds (I vertical).

5.3.2 Metabolic profile of the eye indicates energetic remodeling at onset of neurogenesis

To determine whether these mitochondrial reorganizations have an observable consequence on retina metabolism, we investigated the metabolic profile of the eye using *in vivo* ^1H -MRS. Chicken and pigeon eggs were scanned at two time points during development (E6 and E8) in a 14.1 Tesla MRI scanner. As ^1H -MRS requires sufficient tissue amount to record a decent signal, no earlier time points tested in embryonic age (E3) gave satisfactory SNR. The eyes were identified by imaging of the embryo with a clearly recognizable lens appearing dark on T_2 -weighted images due to its solid structure and low water content (Fig. 5.1). Due to its curved shape and small volume, the whole eye was chosen rather than the retina for better signal acquisition *in vivo*. The cubic VOI surrounded the whole eye and thus lead to non-negligible partial volume effects, i.e. inclusion of unwanted tissue in the VOI. As a result, the spectrum corresponds to the averaged signal of included tissues. The spectra were thus “contaminated” with lipid signal, rich in the extraembryonic fluid, as well as with vitreous body metabolites (Fig 5.4).

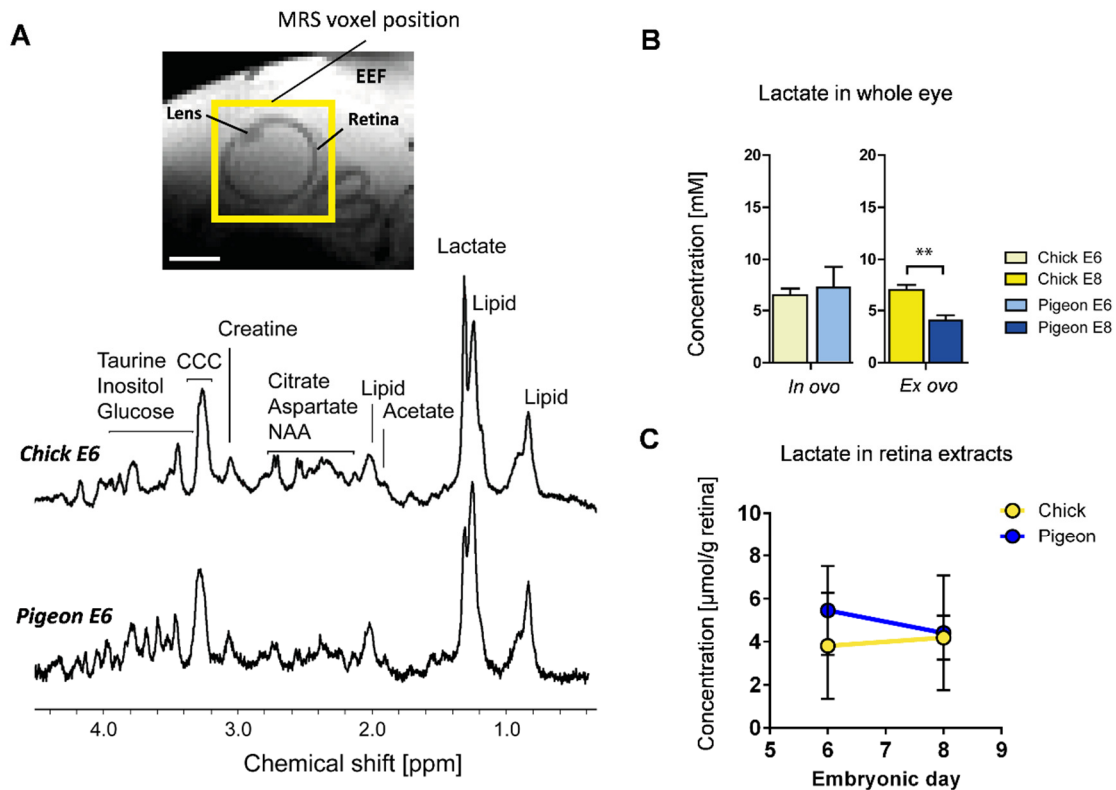


Figure 5.4 : Typical *in vivo* spectra of the whole avian eye and lactate quantification

A. Localized *in vivo* ^1H -MRS of avian embryo eye. (A, top) T_2 -weighted MRI image of a chick eye at embryonic stage E6 with the position of the volume of interest (VOI; yellow rectangle) for localized ^1H -MRS. Scale bar = 2mm. (A, bottom) *In vivo* spectra of the eye. **B.** Lactate quantification of the *in ovo* spectra at E6 and *ex ovo* spectra at E8 (mean \pm SEM, unpaired Student t-test, $**p < 0.005$, $n = 5-6$ per group). **C.** Lactate quantification of the high resolution ^1H -NMR spectra of the retina extracts (mean \pm SEM, unpaired Student t-test, $n = 6-8$ per group)

Quantification gave rise to relatively high CRLB and concentrations reported are thus mainly indicative (Fig 5.5). Lactate signal, however, lead to a good spectra fitting (CRLB mean \pm SEM: chick, $7.9 \pm 1.6\%$ (E6) and $21.8 \pm 8.5\%$ (E8); pigeon, $14.9 \pm 3.7\%$ (E6) and $21.1 \pm 8.1\%$ (E8)). Embryos at stage E8 had to be scanned *ex ovo*, i.e. maintained alive in a saline buffer-containing recipient, due to spontaneous muscular contraction compromising the scan *in ovo*. The difference in lactate content between the saline and the extraembryonic fluid included in the full eye VOI led us to perform comparisons only between species at a given embryonic stage. Metabolite quantifications indicated a significant increase in eye lactate content at E8 in the chick compared to the pigeon ($+72 \pm 20\%$, mean \pm SEM, $p = 0.004$; Fig 5.4B). In order to confirm a possible accumulation of lactate related to the retina, we analyzed the metabolic profile of the dissected retina using high resolution ^1H -NMR spectroscopy at the same embryonic stages. Lactate quantification indicated that lactate did not rise in the chick retina between E6 and E8 (Fig 5.4C) with no interspecies difference. Together these results suggest that delayed mitochondrial activity decline in pigeon has a metabolic consequence in the whole eye leading

to comparatively lower lactate content at E8. However, no difference in lactate concentration was detected in retina extracts suggesting that lactate is located in extra-retinal environment.

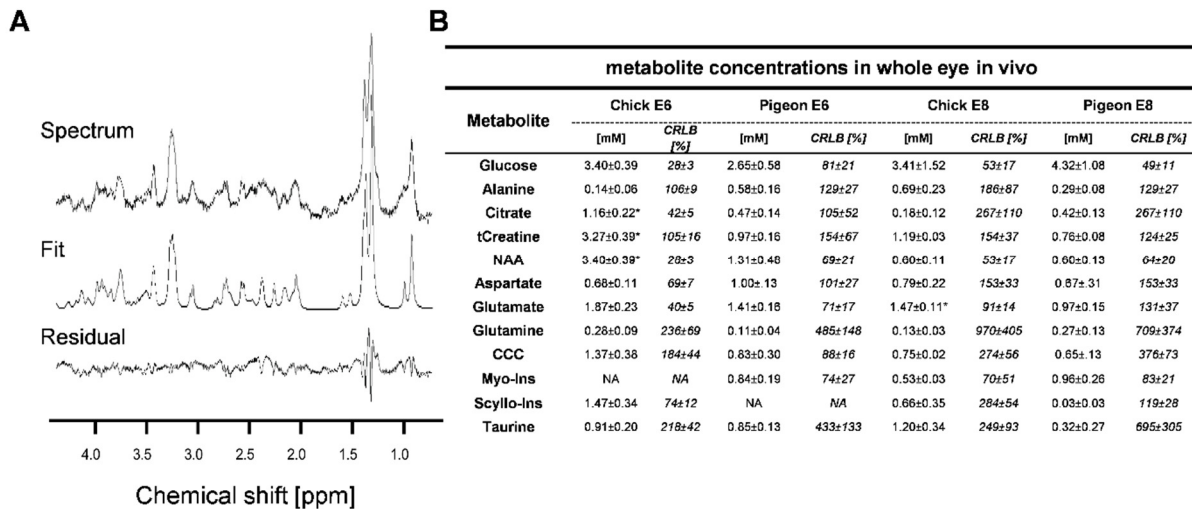


Figure 5.5 : Spectral fitting and quantification of remaining metabolites *in vivo*

A. Fit of the ^1H -MRS spectrum used for metabolite quantification of lactate in a spectrum of chick at embryonic stage E6. Typical basis set for the eye included alanine, aspartate, choline-containing compounds (phosphorylcholine, glycerophosphorylcholine and choline), citrate, creatine+phosphocreatine, glucose, glutamate, glutamine, lactate, myo-inositol, scyllo-inositol, N-acetylaspartate, taurine, as well as main lipid resonances. **B.** Table with quantifications of *in vivo* and *ex vivo* ^1H -MRS spectra (mean±SEM, unpaired Student t-test, * $p < 0.05$, $n = 6-8$ per group). NAA: N-acetyl aspartate, tCreatine: total creatine, CCC: choline containing compounds, Ins: inositol.

5.3.3 Lactate concentration increases in the vitreous body at onset of neurogenesis

The discrepancy between lactate content in the whole eye and the retina extracts suggested that lactate might accumulate in extracellular environment. We thus decided to analyze the vitreous body, given the strong prevalence of that tissue in our *in vivo* VOI (Fig 5.6A and B). The metabolic profile of the vitreous body consisted mainly in water-soluble energy-related metabolites like lactate, glucose, citrate but also oxaloacetate (OAA) and choline containing compounds (CCC; Fig 5.6C). Quantification of the spectra revealed a two-fold lactate increase in chick vitreous body (+106±30%, mean±SEM), while no apparent difference in pigeon embryos was observed (Fig 5.6D). This lactate accumulation was clearly visible on the acquired spectra and quantification lead to small fitting error (CRLB mean±SEM: chick, 6.6±1.8% (E6) and 1.7±0.1% (E8); pigeon, 14.9±7.0% (E6) and 9.1±3.3% (E8)).

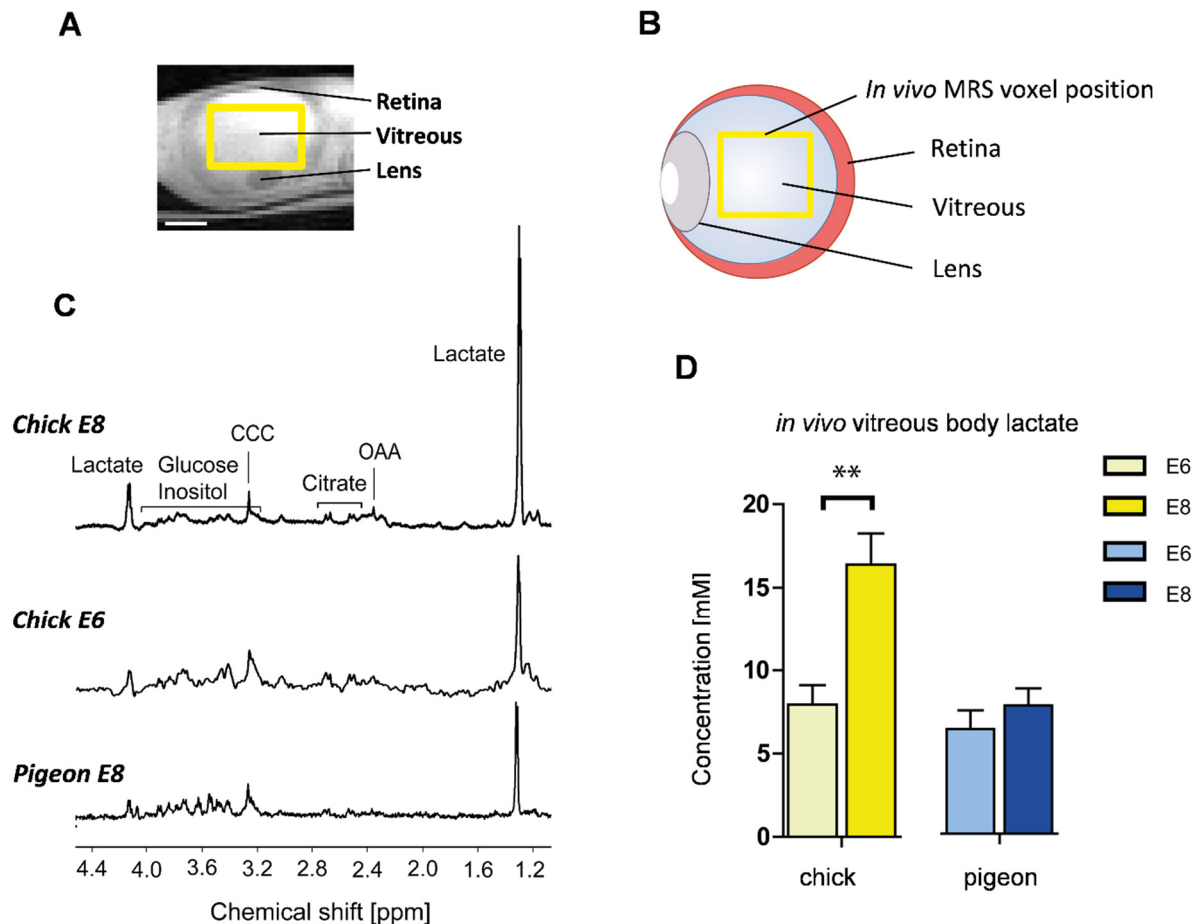


Figure 5.6 : Lactate concentration increases in the vitreous body at onset of neurogenesis

A. T₂-weighted MRI image of a chick eye at embryonic stage E8 with position of the volume-of-interest (VOI) (yellow rectangle) for *in vivo* ¹H-MRS. Scale bar = 2mm. **B.** Schematic representation of the voxel position. **C.** Localized *in vivo* ¹H-MRS spectra of the vitreous body of chick at E8 and E6 as well as in pigeon at E8. The sum of all the spectra per group is shown. CCC: choline containing compounds, OAA: oxaloacetate. **D.** Quantification of lactate in the *in vivo* spectra (mean±SEM; paired Student t-test; **p<0.005; n=5-6 per group).

To test reliability of this *in vivo* measurement, the result was confirmed by high resolution ¹H-NMR of metabolite extracts from dissected vitreous body (Fig 5.7A and B). A slight difference in absolute concentration between *in vivo* (in mM) and extract (in μmol/g) measurements was observed, which can be attributed to the different protocols and assumptions related to the quantification. Analysis of vitreous extracts revealed that pigeon show the same accumulation of lactate in the vitreous body at E12 (Fig 5.7B) in line with the delayed relative mitochondria drop. The accumulation of lactate as a glycolytic end-product in the vitreous body strongly suggests a developmentally-controlled appearance of the Warburg effect in the avian retina.

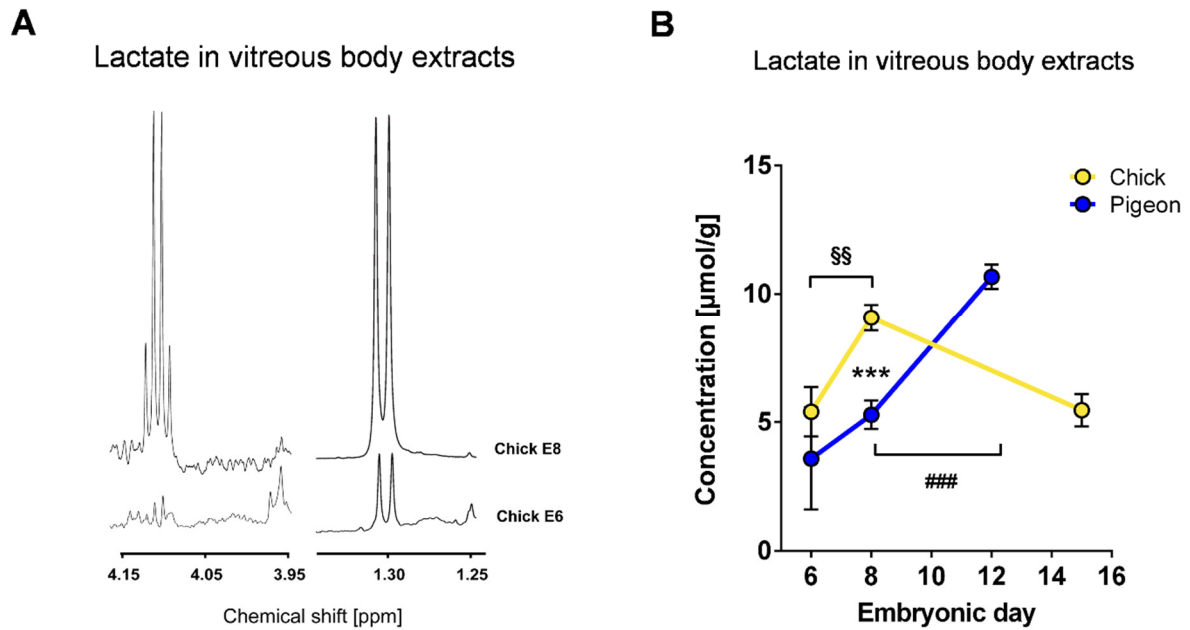


Figure 5.7 : High resolution ^1H -NMR of metabolic extracts confirm the rise of lactate in vitreous body.

A. Doublet and quadruplet resonances of lactate in *in vitro* ^1H -NMR spectra of vitreous body metabolite extracts from chick at i) E8 and i) E6. **B.** Quantification of the high resolution ^1H -NMR spectra of vitreous body extracts (mean \pm SEM; unpaired Student t-test; ** $p < 0.005$ *** $p < 0.0005$; Chick $n = 6-7$ per group; Pigeon $n = 4-7$ per group).

5.3.4 A decrease in vitreous citrate parallels lactate and pH increases as the retina undergoes a metabolic switch.

Vitreous body has been considered as an inert, shock-preventing tissue for a long time (Foulds, 1987). It is now clear that this fundamental component of the eye plays a major role in vision and can be implicated in several diseases (Bishop, 1996; De Smet et al., 2013). Nonetheless, the exact purpose of the vitreous body in development remains mostly unknown, which led us to further analyze its metabolic content. Citrate contains three carboxylic acids, and its four methylene proton chemical shifts are thus highly pH sensitive (Sultan Kedir et al., 2014). Based on the observation of this metabolite in the vitreous body (Fig 5.8A), we investigated whether a pH change was measurable *in vivo*. Using citrate as an internal probe (Fig 5.8B), we observed a difference of $+0.26 \pm 0.17$ pH units (mean \pm SEM, $p = 0.04$) between chick vitreous at E6 and at 8, which corresponds to a ~ 1.8 -fold drop in proton concentration (Fig 5.8C). Consistent with a delayed metabolic switch appearance, the pH of pigeon vitreous at E8 was in the same range as the chick at E6. Interestingly, this pH shift was accompanied by a significant 2-fold drop in citrate concentration itself ($-51 \pm 27\%$, mean \pm SEM, $p = 0.044$) in chick *in vivo* (Fig 5.8D). Interestingly, low ^1H concentration in the samples correlated with higher levels of lactate and lower levels of citrate (Fig 5.8E).

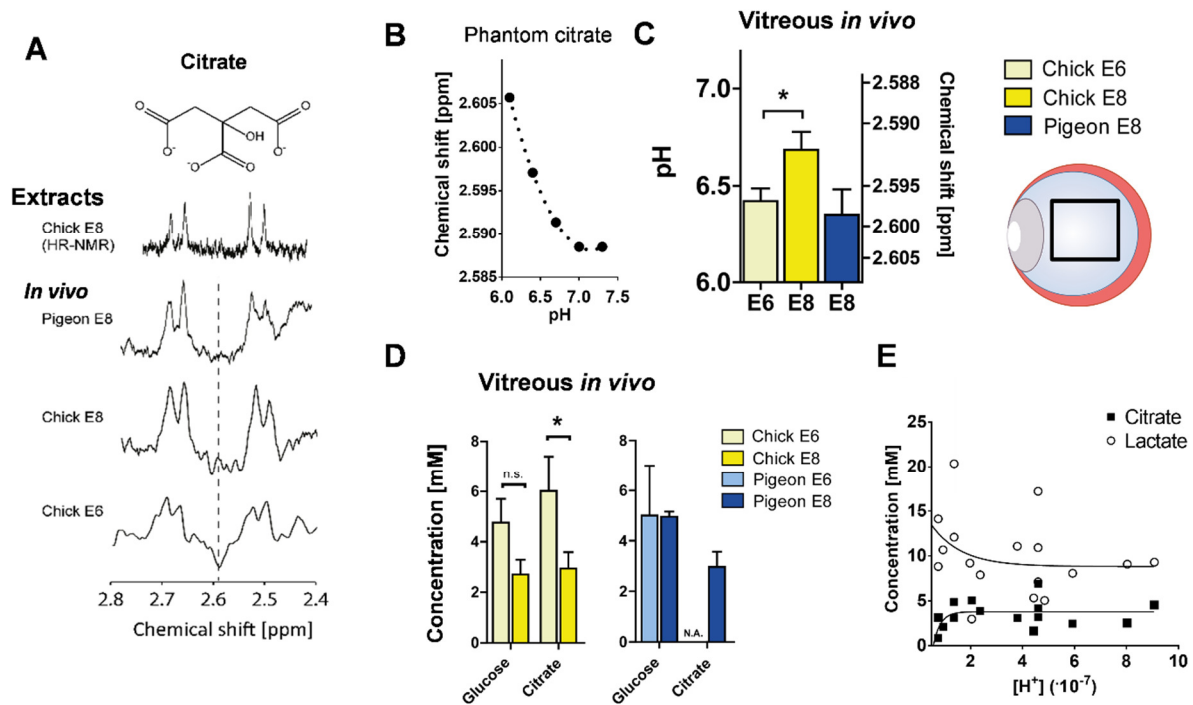


Figure 5. 8 : Vitreous body citrate drops along with lactate and pH increase at the appearance of the switch

A. The pH-dependent chemical shift of citrate at 2.60 ppm was identified in the vitreous body of bird embryo *in vivo* and confirmed *in vitro*. **B.** Citrate chemical shift pH-dependence around physiological value **C.** *in vivo* pH quantification in vitreous body. **D.** Quantification of *in vivo* ¹H-MRS spectra from chick and pigeon vitreous body (mean±SEM; paired Student t-test; **p<0.005; n=5-6 per group, N.A. refers to unquantifiable metabolites). **E.** Citrate and lactate relation to proton concentration.

Quantification of vitreous body metabolites other than lactate *in vivo* led to higher fitting errors (CRLB mean±SEM: Glucose, 32.4±4.3%; Citrate, 33.0±4.8%; Oxaloacetate, 70.5±7.7%) and therefore high resolution ¹H-NMR spectroscopy was used to confirm metabolic changes in dissected vitreous bodies (Fig 5.9). Quantification of these metabolic extracts in the ¹H-NMR spectra corroborated the drop of citrate (-77±32%, mean±SEM, p=0.012) in the chick vitreous body (Fig 5.9).

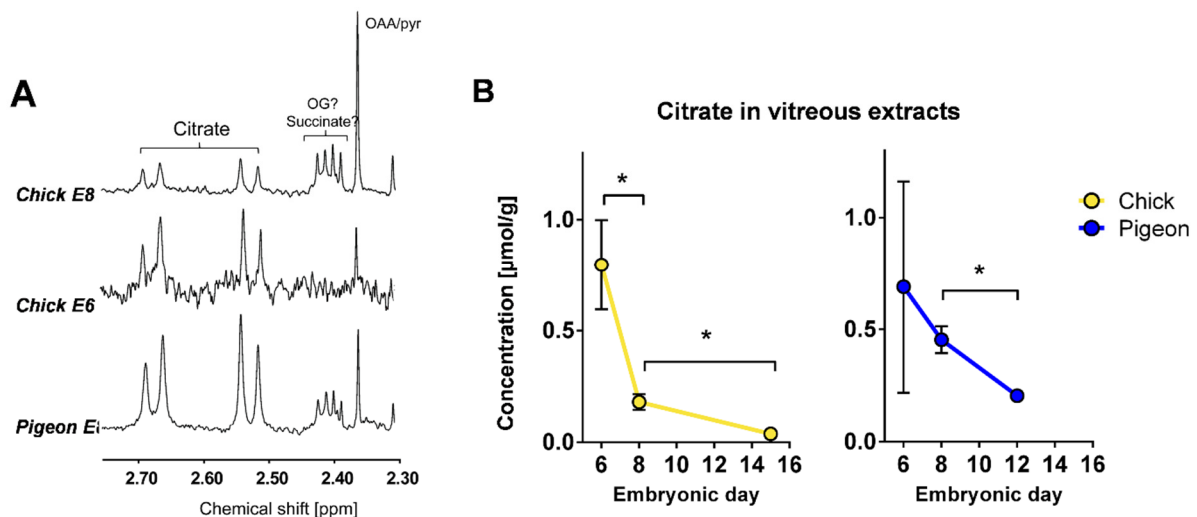


Figure 5.9 : High resolution ^1H -NMR of metabolic extracts confirm the drop of citrate in vitreous body

A. Typical *in vitro* ^1H -NMR spectra of extracted metabolites from vitreous of chick at E8, E6 and pigeon at E8 showing the citrate and neighboring resonances (OAA/pyr: oxaloacetate or pyruvate; OG: oxoglutarate). **B.** Quantification of citrate from *in vitro* ^1H -NMR spectra of the vitreous body of chick and pigeon (* $p<0.05$, unpaired Student t-test; $n=5-7$ per group).

Furthermore, a similar, if not stronger, citrate drop appeared in the pigeon 3 days later (Citrate: $-55\pm 17\%$, mean \pm SEM, $p=0.005$), strengthening the link between this metabolic remodeling and the delayed neurogenesis of the pigeon. Other metabolic changes were observed but not consistently similar between *in vivo* and extract quantifications like glucose (not shown). These discrepancies are likely to be due to the lower SNR in ^1H -MRS or resonance overlapping in high resolution ^1H -NMR leading to measurement imprecision. Noteworthy, scyllo-inositol was found to drop while myo-inositol increases slightly in both retina and vitreous of chick and pigeons between E6 and E8. Both are osmolytes which could be associated with regulation of the osmotic pressure of the growing eye.

RGCs lying at the retinal-vitreous interface, are likely to be the closest beneficiary of any vitreous trophic support. This idea is strengthened by the fact that RGC are the first neuronal cell type in the retina to undergo maturation, which peaks around E6. The strong synchronicity of citrate and lactate concentrations switching in the vitreous body at onset of the switch, led us to presume that RGC take advantage of this citrate reservoir for either lipid biosynthesis or oxidation in mitochondria.

5.3.5 Lipid synthesis does not account for the vitreous citrate decrease at the onset of RGC maturation.

Further analysis of high resolution ^1H -NMR spectra allowed to determine retina-specific metabolic changes (Fig 5.10). The 1.28 ppm resonance lipid peak of the aqueous phase of the chloroform/methanol metabolite extraction has been proposed as a marker of neural progenitor cells (NPCs) given the high amount of water-soluble lipid present in these proliferating cells (Manganas et al., 2007). Based on this assumption, the quantification of this peak relative to creatine, present in every cell, or NAA, considered a neuronal marker, gives an interesting mean to assess relative cell populations between the two animals. While a similar reduction in NPC relative to the total amount of cells appeared in both animals, pigeons had a ~2 fold higher amount of NPC/neuron ratio at E8 than chick based on this marker (Fig 5.10B).

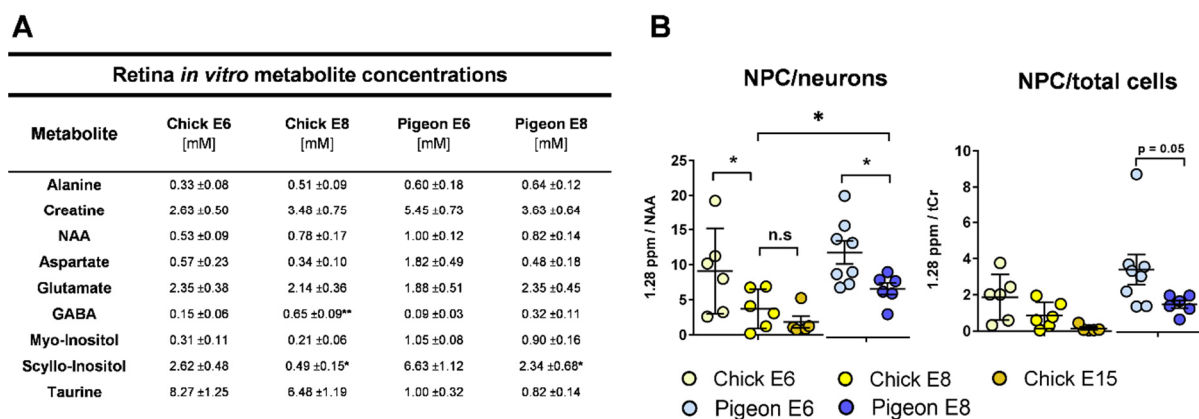


Figure 5. 10 : Quantification of remaining metabolites from the aqueous phase of retina extracts

A. Quantification of retina ^1H -NMR spectra (mean±SEM, n=6-8 per group). **B.** Quantification of the 1.28 ppm peak marker of neuronal progenitor cells (NPC). Resonance of hydrophilic lipid from the aqueous phase of metabolite extraction at 1.28 ppm corresponds to methylene resonances. Peak height was normalized to the signal of creatine (cellular marker) or NAA (neuronal marker) (mean±SEM, *p<0.05; unpaired Student t-test, n=6-8 per group).

Focus was mainly given to the chloroform phase of the extraction containing most of the lipids of the tissue. Citrate is a well-known substrate for lipid biosynthesis catalyzed by the ATP-citrate lyase enzyme (ACLY). To test whether the measured drop of citrate might be the result of an increase in lipid synthesis in the retina, we determined the relative lipid composition of the chloroform phase of retinal extracts with particular attention to steroid content, fatty acyl number and poly- or mono-unsaturations (Fig 5.11). Seven identifiable lipid resonances were quantified relative to the total amount of fatty acids (free fatty acids and fatty acyls: methyl peak at 0.88ppm).

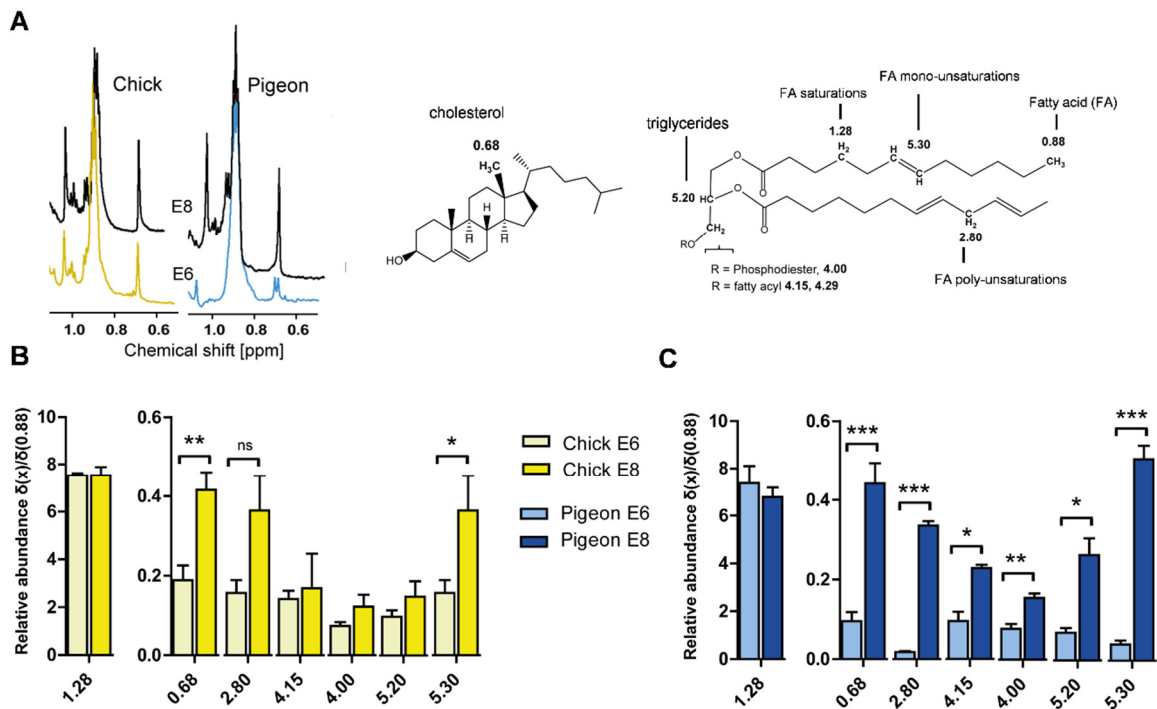


Figure 5. 11 : Lipidic profile of the retina is increased in chick and in pigeon during development.

A. Spectra of lipidic phase of retina metabolic extracts show marked cholesterol resonance increase in both chicken and pigeon. Assignment of cholesterol (A, center) and other lipid (A, right) resonances used for quantification. **B.** Quantification of lipid resonances from the ^1H -NMR spectra of lipidic phase from dissected retina of chick (mean \pm SEM, * p <0.05; unpaired Student t-test, n =6-8 per group). **C.** Quantification of lipid resonances from the ^1H -NMR spectra of lipidic phase from dissected retina of pigeon (mean \pm SEM, * p <0.05, ** p <0.005; *** p <0.0005; unpaired Student t-test, n =5-6 per group).

Results indicated no difference in relative fatty acyl chain length as indicated by the 1.28/0.88 [ppm/ppm] ratio. However, an increase in relative cholesterol content (0.68ppm) as well as relative mono- and polyunsaturated fatty acids (2.80ppm and 5.30ppm) was observed from E6 to E8 in both chicken and pigeon (Fig 5.11). Furthermore, only pigeons showed an increase in triglyceride (4.15ppm and 5.20ppm) and phospholipids (4.00ppm) content relative to total fatty acids. Together these results indicated that the citrate consumption is not likely to drive fatty acids or cholesterol synthesis: the observed lipid changes seem to be similar, if not more pronounced, in the pigeon compared to the chick, incompatible with the chick-specific citrate drop at this developmental stage.

5.3.6 Temporal modulation of glycolysis regulator expression in the retina suggests that the nature of the metabolic switch is glycolytic

Finally, we analyzed the expression of mRNA transcripts for several enzymes controlling the metabolic pathways of lactate and citrate metabolism using RT-qPCR in the isolated retina (Fig 5.12). Gene expression of the rate limiting glycolytic enzyme phosphofructokinase 1 (PFK1)

did not change during the metabolic switch window in pigeon (i.e. between E8 and E12) (Fig 5.12B). However, its allosteric activator, the enzyme phosphofructokinase 2 (PFK2), also called 6-phosphofructo-2-kinase/fructose-2,6-bisphosphatase (PFKFB), showed a ~4 fold increase in expression of the isoenzyme 3 at the end of the switch. Similarly, pyruvate dehydrogenase (PDH) mRNA levels were constant throughout the switch but its inhibitor, PDH kinase (PDK), was highly upregulated (Fig 5.12D). These results strongly indicate that the whole retina undergoes metabolic remodeling towards aerobic glycolysis, shutting down pyruvate utilization by the mitochondria while increasing its production from glucose. This reprogramming can only lead to a high lactate production by the lactate dehydrogenase (LDH) isoform A and export through monocarboxylate transporters (MCT) isoform 3 (Fig 5.12C). Citrate plasma membrane transporter (NaDC1), SLC13A2 isoform, dropped slightly during the switch, together with the drop of citrate. Furthermore, the enzyme ATP-citrate lyase (ACLY), synthesizing lipids from citrate showed low expression and no significant modification, in line with the utilization of citrate for oxidation rather than lipid biogenesis.

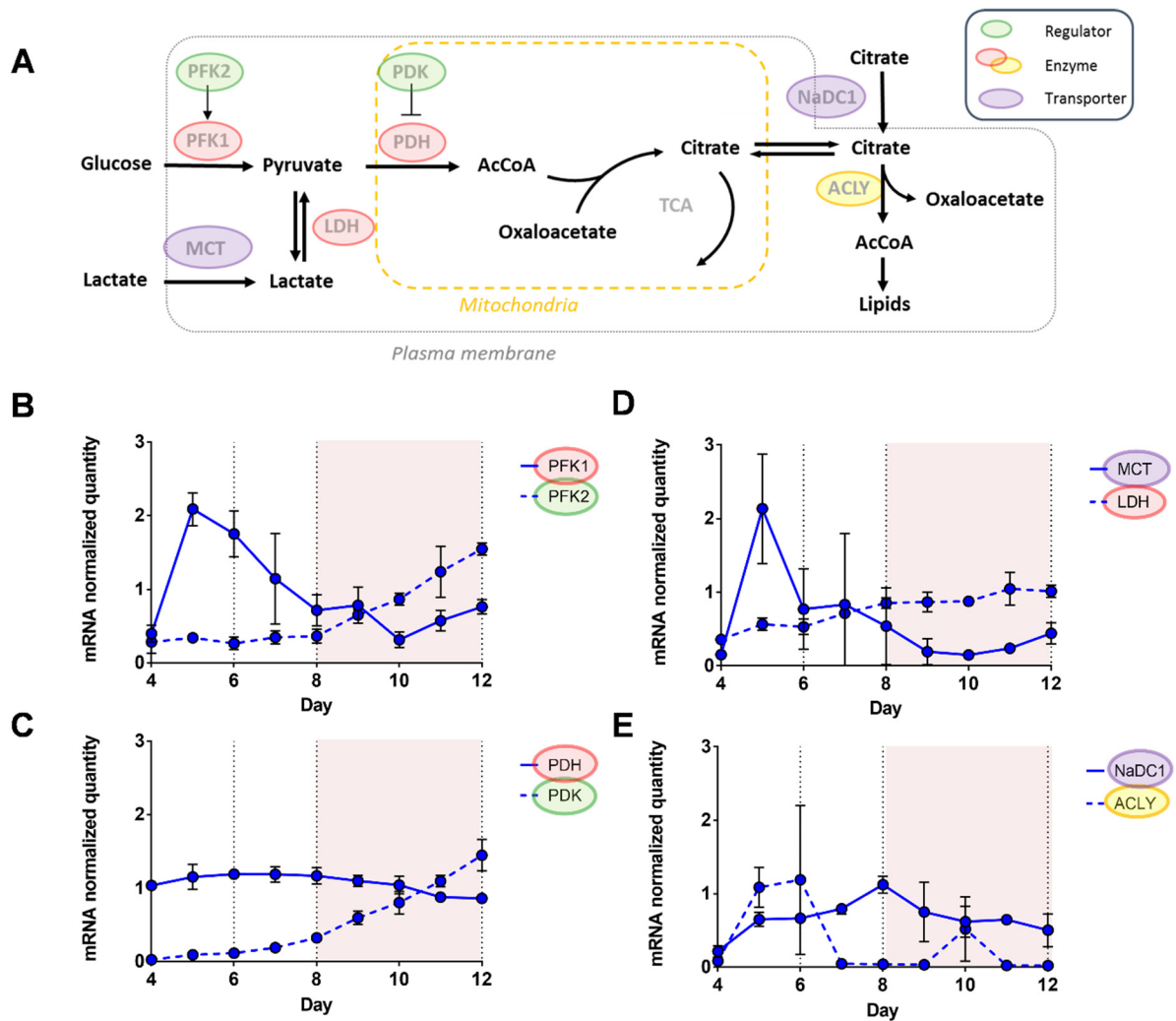


Figure 5. 12 : Increased glycolysis regulator expression in the retina correlates with appearance of the metabolic switch

A. Schematic representation of main metabolic pathways involved in the metabolic switch. PFK1/2: phosphofructokinase 1 or 2; PDH: pyruvate dehydrogenase; PDK pyruvate dehydrogenase kinase; LDH: lactate dehydrogenase; MCT: monocarboxylate transporter; ACLY: ATP-citrate lyase; NaDC1: Sodium citrate cotransporter. **(B-E)** Relative mRNA quantification in pigeon retina indicates a strong increase in PFK **(B)** and PDK **(G)** during the metabolic switch. At each developmental stage, data are from three biological replicates including 3-10 retinas and presented as mean \pm SD.

Finally, a delay of 3 days was again observed between the slopes of the time-dependent PFK2 expression levels of chick and pigeon, confirming the link of this metabolic switch with retina neurogenesis (Fig 5.13).

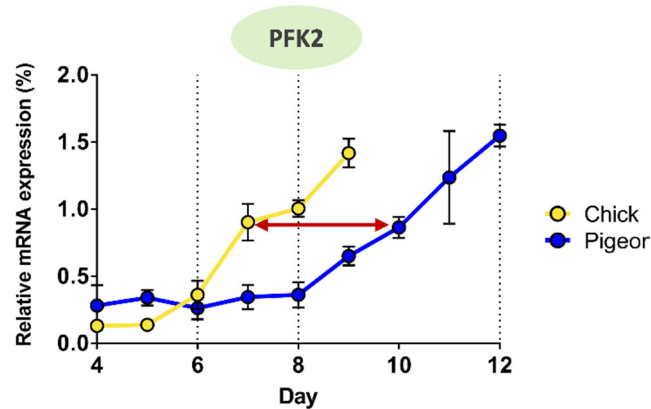


Figure 5. 13 : Expression of phosphofructokinase 2 (PFK2) increases in the developing retina with a three-day delay between chick and pigeon.

5.4 Discussion

For the first time, we have been able to identify and follow the appearance of the avian Warburg effect during retina development using *in vivo* ^1H -MRS. The beauty of ^1H -MRS lies in its non-invasiveness allowing studying the embryo in the egg without any disruption. This glycolytic switch leads to an imbalance between aerobic glycolysis and oxidative phosphorylation, which appears to be tightly related to neuronal differentiation in the avian retina.

5.4.1 Mitochondria characterization

We characterized mitochondria content and activity during avian retina development. Current knowledge suggests that proliferating cells rely mainly on glycolysis to produce their energy while upon differentiation they switch to oxidative phosphorylation for increased efficiency (Folmes et al., 2012). While the high content of active mitochondria found in uncommitted retinal progenitors does not exclude glycolytic activity, our results suggest higher oxidative capacity than previously anticipated in those cells.

In agreement with previous studies (Buono and Sheffield, 1991a, 1991b), we found that the number of mitochondria per cell gradually decreased between E3 and E10 in chick and pigeon retinas. Retinal progenitors have a fast cell cycle that lasts about 12h (Chiodini et al., 2013) and cytokinesis is a contributing factor to mitochondrial decrease. While cell number increases by about 100-fold between E4 and E8 (Rodrigues et al., 2016), we only observed a ~4-fold decrease of mt-DNA content during the same period, indicating that active mitochondria

production keeps pace with fast cell division. Together with the high expression of mitochondria biogenesis genes at early stages, this supports the idea that mitochondria play an important role in retinal progenitors. Conversely, we observe a gradual drop in mitochondrial biogenesis genes when progenitors differentiate, in line with the idea that post mitotic cells have lower mitochondrial requirements.

Interestingly, the drop of mitochondrial activity followed a different pattern that correlated with delayed cell differentiation in pigeon retina. This species-specific timing suggests metabolic remodeling associated with the onset of neurogenesis. Strikingly, as the majority of retinal cells display reduced mitochondria content and activity, RGCs whose genesis peaks at E6, manage to keep the high content of active mitochondria that characterize early retinal progenitors. The unique high oxidative activity of RGC probably reflects their particularly high metabolic requirements associated with their axogenesis.

5.4.2 Lactate accumulation is specific to the vitreous body

A rapid peak in lactate content appeared in the vitreous body, in which concentration doubles within a few days. This fast process suggests a developmentally programmed remodeling of energetics, which can be described as a metabolic “switch”.

Interestingly, comparison with the full eye and the retina specific metabolic profile revealed that this rise in lactate is limited to the vitreous body. Vitreous lactate accumulation matched delayed neurogenesis in the pigeon and correlated with the up-regulation of glycolysis genes in the retina of both species, strongly arguing in favor of the retinal origin of lactate. Cellular expression of PFK2 together with PDK provide an efficient way of blocking pyruvate entry in the mitochondria leading to significant lactate production and release. This phenomenon can be typically observed in cancer cells with high glycolytic activity (Atsumi et al., 2002). Contribution of other surrounding glycolytic tissues *in vivo* cannot be excluded as has been reported for the inner limiting membrane (Halfter et al., 1985) or the lens (Bassnett, 1990) during chick embryogenesis. However, since these tissues develop at the same rate in both species, they would not explain delayed lactate secretion in pigeon. Furthermore, mitochondrial decay in the lens has been shown to occur only from E8 in the chick (Bassnett and Beebe, 1992) and lactate measurements in the lens showed an accumulation from E8 only in the chick (data not shown).

How can lactate accumulate in the vitreous body against its concentration gradient? Lactate transport and release generally occur through monocarboxylate transporters (MCTs) with co-transport of H^+ (Becker et al., 2004). A 2-fold concentration difference between the retina and vitreous body can only be possible with an opposite concentration gradient of H^+ that are co-transported by MCTs. By assuming the system being in a chemical equilibrium between the two compartments, it becomes clear that for vitreous lactate to reach such levels, a 2-fold reduction in H^+ concentration must occur. Therefore, *in vivo* 1H -MRS citrate signal was used as an internal probe to assess the proton concentrations and revealed modifications of the vitreous pH. The observed decrease in proton concentration *in vivo* between E6 and E8 (-1.8-fold) supports the idea that pH is the driving force for lactate accumulation.

Active pumping could be implicated in removing H^+ from the vitreous. Early H^+ -ATPase expression has been observed in chick and implicated in the left-right patterning of the embryo (Adams, 2006; Levin et al., 2002; Narbaitz et al., 1995). Nevertheless, the directionality (release in the extracellular medium) of the proton flow would be difficult to conciliate with the observed extracellular (vitreous) pH rise. MCTs are also known to be co-expressed with HCO_3^-/Na^+ co-transporters which helps neutralizing acid upon lactate uptake (Becker et al., 2004); Again, these transporters provide a mean to stabilize intracellular pH upon extracellular lactate uptake and not release, incompatible with our model.

5.4.3 Citrate oxidation drives the glycolytic switch

Citrate is an important intermediate of the tricarboxylic acid (TCA) cycle in mitochondria, where its oxidation leads to a substantial part of cellular ATP production. The coincidence of citrate diminution with the simultaneous increase in lactate in the vitreous body, together with the 3-day delay between the two avian species, suggest that these events could be causally related. Dilution of preexisting vitreous metabolic pool upon eye growth is very unlikely as the eye grows at a similar pace in chick and pigeon (Rodrigues 2016). Moreover, the presence of NaDC1, which co-transport Na^+ with dicarboxylates like citrate at the plasma membrane, strengthens the idea that citrate could be taken up by retinal cells.

Active (MitoDsRed2-labelled) mitochondria are abundant in newborn RGCs where they are rapidly translocated in growing axons. Vitreous citrate would provide a source of carbon for the highly oxidative RGC axons. If citrate feeds the TCA cycle, the required maintenance of

anaplerosis would ultimately lead to release of OAA, malate or pyruvate from mitochondria, and possibly, into the extracellular space (Sonnewald, 2014). This process could be responsible for the increased OAA resonance observed in the vitreous given their synchronicity, but the exact metabolic pathway would require clarifications. Our vitreous pH measurements (pH=6.42) *in vivo* indicate that citrate at E6 is equally as abundant in its fully deprotonated state (Cit^{3-}) as it is in its dicarboxylate state (Cit^{2-}) ($\text{pK}_{a3}=6.40$). Due to the specificity of the NaDC1 transporter for the Cit^{2-} state, it follows that oxidation of citrate is a potential underlying cause of the vitreous pH rise driving lactate accumulation

It seems clear that the growth of RGC axons requires high amount of lipid production. However, the idea that citrate would serve primarily as a precursor for *de novo* lipid biosynthesis does not seem convincing. Eggs contain high amount of cholesterol and phosphatidylcholine (also called lecithin, from the greek word lekythos meaning “egg yolk”) and expression of several transport proteins from yolk sac coinciding with the studied chick development time points would rather suggest that lipid supply comes from embryonic storage (Bauer et al., 2013; Yadgary et al., 2010). In addition, a similar lipid profile change was observed in the retina of chick and pigeon between E6 and E8, before pigeon metabolic switch. This bears out the fact that citrate is not used for a sudden increase in lipid biosynthesis. Finally, the lipidogenic enzyme ATP-citrate lyase (ACLY) responsible for the cytoplasmic acetylCoA production from citrate was almost undetectable during the metabolic switch in favor of the idea that citrate is oxidized in the mitochondria rather than utilized for lipid synthesis.

Our results suggest that vitreous body appears to be a reservoir and buffer of energy metabolites providing trophic support to the adjoining neuronal cells in early development. Citrate oxidation and removal from the extracellular environment in turn provides the key initiation factor for a glycolytic switch in the retina.

5.4.4 Metabolic regulation and interactions at the retina level

The relatively high glucose concentration (~4mM) in the vitreous body suggests that oxygen from the choroid is more likely to be the key element to be spared for oxidative metabolism in RGCs. This is in line with our hypothesis that increased glycolysis in the non-RGC cells saves blood-born oxygen and keeps a sufficient pO_2 for mitochondria-rich RGC axons. As a result,

the uptake of lactate would provide an important source of energy for cells with high mitochondrial content.

Neurons are well known to be able to uptake and oxidize lactate under normal glucose supply (Larrabee, 1983). Astrocytes have been shown to release lactate and citrate that can serve as oxidative support for surrounding neurons in the adult CNS (Mächler et al., 2016; Pellerin and Magistretti, 1994; Poitry-Yamate et al., 1995). It is thus plausible to assume that citrate, and maybe lactate, both highly concentrated in the vitreous body, provide a neuroenergetic substrate for the highly oxidative RGCs undergoing axonal growth. Implication of astrocytes at these developmental stages can be excluded since Müller glial cells that are the last cell types to appear during retina neurogenesis (Doh et al., 2010; Tao and Zhang, 2014) are not yet born at stages investigated in this study. Expression of Na⁺ coupled MCTs (SMCT1 and SMCT2) has been identified in the retina and has been restricted to Müller and retinal ganglion cells (RGC-5 type) (Ganapathy et al., 2008; Martin et al., 2007). Even if we have not investigated changes in expression of this transporter, its presence would provide the mechanistic link for RGC-specific lactate uptake and oxidation.

Citrate is a well-known inhibitor of PFK1 and PFK2 (Iacobazzi and Infantino, 2014; Moreno-Sánchez et al., 2011; Pogson and Randle, 1966) and its removal from the extracellular space upon consumption is likely to provide a favorable environment for glycolytic retinal cells. Simultaneously, enhanced expression of PFK2 and PDK together with an overall dilution of mitochondrial content and activity leads to a high lactate production by the retina. This high level of lactate could in turn substitute for citrate providing sustained and uninterrupted energy support for RGC and their highly active mitochondria. A mechanism in which retina-born lactate inhibits glycolysis in RGCs for improved OXPHOS efficiency or accumulates in the vitreous to prevent auto-inhibition of glycolytic cells is also possible. Furthermore, lactic acid accumulation in the vitreous could limit the rise in pH induced by citrate uptake and favor its oxidation (Simpson, 1967). Even if we think that citrate and lactate serve as metabolic fuel, we do not exclude that this metabolic remodeling also participates in other processes important for neurogenesis. Intracellular pH modifications, histone acetylation by citrate or signaling through lactate receptor all provide interesting starting point for mechanistic investigations and could play a role in RGC maturation and axonal guidance (Kolko et al., 2016; Tatapudy et al., 2017).

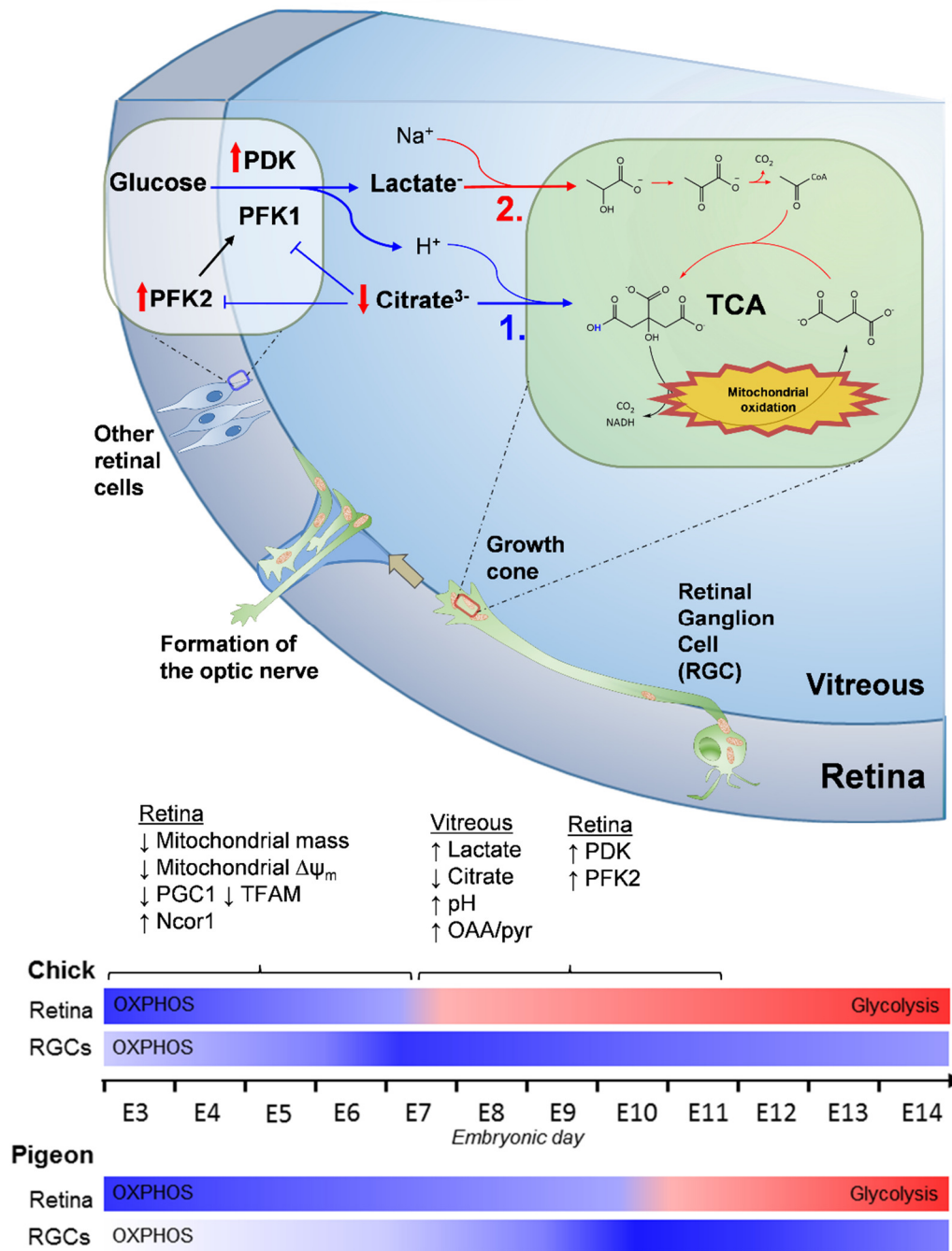


Figure 5. 14 : Summary and proposed model of neuroenergetic metabolic switch associated with retinal ganglion cell growth.

We propose that citrate in the vicinity of oxidative RGCs and their expanding axons/growth cones serves as a rapid and available energy substrate through their TCA cycle (1. blue arrows). In this early stage, high citrate concentration prevents aerobic glycolysis in surrounding cells by inhibiting PFK. Through the course of RGC growth, citrate oxidation and removal from the vitreous leads to a rise in vitreous pH. This 2-fold $[H^+]$ decrease promotes the 2-fold lactate increase from retina glycolytic activity (regulated by PDK and PFK2 expression levels) through MCT lactate/ H^+ co-transport. The transient lactate accumulation in the vitreous could serve as a new mitochondrial carbon substrate (2. red arrows), prevent an excessive rise in pH induced by citrate oxidation or serve a metabolic signaling role associated with RGC axonal outgrowth.

5.4.5 Interspecies disparities

Our study revealed major metabolic differences during avian retina development compared to what has been reported in other species, which might reflect different ratio of metabolically distinct cell subtypes. Alternatively, physical proprieties of the tissue like vascularization or layers thickness might affect nutrients and oxygen delivery and alter metabolism in a species-specific manner.

Like in the avian retina, mouse retinal progenitors have a high density of mitochondria. However, in mouse, their differentiation into RGC elicits mitophagy and a glycolytic switch (Esteban-Martínez et al., 2017). There is no evidence of mitophagy in the avian retina, and our results suggest that cell division is the main reason for mitochondria dilution in proliferating retinal progenitors. Moreover, axons of newborn RGC display a high density of mitochondria, suggesting that RGC metabolism is different between mouse and birds. As mouse retina contains almost exclusively rods, it is possible that RGCs of the rod pathway display a different metabolism compared to RGCs of the cone dominated bird retina. Low convergence of photoreceptors and the high acuity midget pathway with a high density of RGCs are characteristic of cone-dominated retinas that might explain requirement for an efficient oxidative metabolism.

On the other hand, *Xenopus* retinal progenitors strongly depend on glycolysis for proliferation and biosynthesis but can switch to oxidative phosphorylation for ATP production when glycolysis is inhibited (Agathocleous et al., 2012). Although our results do not exclude glycolysis in bird retinal progenitors, the occurrence of the glycolytic switch and vitreous lactate accumulation at the onset of neurogenesis suggest that glycolysis might not be as prominent in avian and mammalian as in amphibian retinal progenitors.

In the bird avascular retina, oxidative RGCs are located on the vitreous side furthest apart from blood nutrient delivery. Early studies have suggested that avian inner part of the retina possess little mitochondrial activity (Buono and Sheffield, 1991a; Hughes et al., 1972), explaining its high glycolytic activity at adult stage. Our Results indicate that at least during a good part of the development RGC rely on mitochondrial metabolism simultaneously with retinal overall glycolytic activity. The pecten oculi is an avian tissue which provides nutrients and oxygen supply to the inner bird retinal layers. The embryonic development of that structure has certainly adapted to the trophic needs of retina neurogenesis as a delay in pecten maturation exists between chick and pigeon (Parducci et al., 1987). While

vascularization of this tissue occurs only several days after the glycolytic switch reported here, appearance of new cells in contact with the vitreous could contribute to this evolving complex metabolic ecosystem (Gerhardt et al., 1999; Schuck et al., 2000). Prior to pecten development, RGC and their growing axon must maintain a high mitochondrial activity despite limited access to nutrients from blood. We propose that vitreous citrate and maybe lactate secreted by the glycolytic outer layers ensure RGC oxidative metabolism as well as access to oxygen from choroidal circulation. This mechanism could thus represent a particularity of avascular retinas (Poitry-Yamate et al., 1995). Interestingly, primate vascular retina displays low to none vascularization in the central high acuity fovea, the region with the highest RGC density. Thus, primate central retina metabolism might be subjected to similar metabolic challenges and adaptation as the bird embryonic retina.

Metabolic characterization of retina development in other species will provide new insight to understand metabolic diversity of this metabolically challenging tissue. Since the primate central high acuity region, the fovea, share key characteristics of bird retinas, we propose that a bird model is more representative of human fovea than a rodent model.

Chapter 6

General conclusion and perspectives

This thesis aimed at finding potential MRS biomarkers related to mood disorder and providing a mechanistic and therapeutic framework for understanding their dynamics in the brain of animal models. We have focused on two different mouse models with a genetic or environmental basis for developing depressive-like behavior. By combining molecular, biochemical and behavioral approaches with non-invasive ultra-high field MRS we have gotten insight into detailed metabolic processes associated with specific brain limbic structures. The association of neurochemical abnormalities with behavioral dysfunctions alongside the technical improvements protocol optimization has brought significant progress in the understanding of brain metabolic impairments associated with psychiatric disorders.

We have first identified alterations of the neurochemical profile in a genetically modified mouse strain lacking an important regulator of brain metabolism and function: CRTC1. We have identified that deletion of this coactivator of CREB leads to severe hippocampal neuroenergetic impairments, pointing towards a reduced glycolytic capacity, in line with an insulin-resistance phenotype. We have shown that this weakness in hippocampal metabolic resilience leads to mitochondrial allostatic load and subsequent increase in GABAergic activity. Importantly, we have noticed that the depressive-like behavior associated to this metabolic weakness is not a trait-characteristic of the mice; rather it develops according to the environment. This has led us to state that deletion of *Crtc1* generates a susceptibility to stress that is highlighted after prolonged exposure. Finally, we have been able to select a targeted treatment to protect the susceptible mice from the deleterious effects of stress.

In a second study, we have determined that other environmental factors can provide a susceptibility to chronic stress with a metabolic fingerprint in the brain. We have identified that social hierarchy in inbred mice can predict the behavioral outcome after chronic social defeat and chronic restraint stress protocols. The induced depressive-like behavior had a neuroenergetic basis in the nucleus accumbens, which we were able to quantify *in vivo* with ^1H -MRS. Finally, treatment with acetyl-L-carnitine allowed us to protect the dominant/susceptible mice from the deleterious stress effects.

Finally, the last study described the appearance of an important metabolic remodeling occurring during embryonic neurogenesis in the eye. We have observed that at the onset of neurogenesis in the avian retina, a glycolytic switch occurs in the inner eye leading to dramatic reshaping of energetic metabolism organization. Besides the technical novelty of studying

metabolism in a developing embryo inside the egg, our study provides an illustration of how metabolism adapts during ontogenesis according to the cellular needs and tissue function. Given the potential role of neurogenesis in the pathophysiology of mood disorder, our results provide new tracks for pursuing the identification of key metabolic processes associated with production or survival of newborn neurons.

Altogether, our results confirm the complex and multifactorial aspects of metabolic alterations related to mood disorders. We have identified a set of potential biomarkers and endophenotypes with clinically relevant impact. Besides the identification of given metabolites, we have identified the brain region specificities and associated environmental dependencies. The mechanisms underlying the dynamics of these potential biomarkers have been only partially resolved, particularly at the cellular level, but provide a basis for further investigations. Our results indicate that several brain limbic regions can be the target of metabolic dysfunctions and several factors, genetic or environmental, can increase the likelihood of developing behavioral abnormalities. From our results, efficient brain energetic capacity appears to be a hallmark of resilience and protection against excessive allostatic load. Whether lower energy metabolic status is the cause or the consequence of the depressive-like behavior remains to be confirmed. Nevertheless, our results are in favor of a lower energetic status preceding the induction of the behavior. While we have observed that GABAergic neurons might be particularly sensitive to energetic challenges, astrocytes appear to play an important role in metabolic resilience as well. More than astrocytes, energy substrates and trophic elements might be the key to provide protection against mood impairments, opening specific therapeutic routes. In conclusion, our results will help providing new approaches for identifying subclasses of mood disorders with a comparable pathophysiological basis and a common therapeutic window.

Several experiments can be proposed to further this research and extend the findings of this thesis. The mechanisms that lead to the metabolic impairments have been only partially elucidated. The pathological contributions of different cell types involved in brain function is certainly a point that needs to be clarified. Histological analyses can provide useful information in terms of cellular number and shape, which could be related to the metabolic differences observed in MRS. Deciphering the molecular mechanisms implicated in limbic glucose homeostasis and how they control behavior would lead to a more comprehensive

understanding of these metabolic dysfunctions and open new therapeutic strategies. Different stress protocols or behavioral measures should be performed to refine the typical brain networks affected. To the same end, electrophysiological measurements would certainly clarify the impact of metabolic unbalance on neuronal signaling. Animal models provide a fundamental tool to find potential medication, and testing more molecules related to glucose homeostasis could serve as a gateway for initiating new clinical trials. Furthermore, only male mice have been used in these studies due to limited amount of time and resources; it would be useful to replicate our findings in female mice. Finally, the clear applicability of MRS for human studies should lead to translational investigations. It is tempting to think that similar neuroenergetic dysfunctions will be observed among BPD or MDD patients. However, a similar pathophysiological profile is likely to be present only in subpopulations of both BPD and MDD diagnostics with a lot of overlap. Accordingly, our set of biomarkers could serve as selection factors for the assignment of a given treatment. Validating our findings in a human population will require facing several challenges, but can potentially bring research in psychiatric neurosciences significantly forward.

Acknowledgements

I am very grateful to all the people without whom this thesis could not have been achieved. This work consisted in several collaborative projects including groups from the Ecole Polytechnique Fédérale de Lausanne (EPFL), the Centre Hospitalier Universtaire Vaudois (CHUV) and the the University of Geneva (UNIGE).

I would like to start by thanking my thesis director, Professor Rolf Gruetter, for accepting me as a PhD student in his lab. I feel deeply grateful as you gave me a chance to realize the project I wanted to pursue from my Master thesis. When no-one could or wanted to give me a chance, you accepted me despite my limited background in physics. The high freedom and strong financial support you have provided has allowed me to thrive in the management and realization of my thesis project. Your profound knowledge and pertinent comments have been a great source of inspiration and advances in my work.

I would like to express my gratitude to my thesis co-director, Jean-René Cardinaux, as well. Thank you for having supported me and this project from the very beginning. You have always trusted me and my decisions even when the relevance of the project was questioned by peers. Thank you for having always guided my research and been available for discussing every single aspect of my thesis. Thank you for having always treated me with consideration and respect, by putting forward the importance of science being about learning rather than efficiency and yield.

I would like to thank with all my heart all the beautiful people from the Center for Psychiatric Neurosciences (CNP) at the CHUV site in Cery. Elsa Meylan and Clara Rossetti for the help with the *Crtc1*^{-/-} mice, teaching me so many molecular experiments and being always ready to help. A particular thank you goes to Anthony Carrard and Jambon. You have filled my PhD with laughter, fun and incredible memories. Apart from the Loeli/jambon's nights, thank you for having provided significant help and discussions about lactate and sometimes other things. A thank you goes to Jean-Luc Martin and Fulvio Magara for the very useful comments and discussions which have helped me at several points of my thesis.

I would like to thank Prof. Carmen Sandi for the trust she has placed in me for the collaborative project on MRS and stress. Giving me the opportunity to interact and collaborate with Bruce McEwen and Carla Nasca has been an extraordinary chance to learn from world leading experts in the field. Thanks to Thomas Larrieu for all the work done and teaching you have

brought to me during this collaboration. Thanks to Jocelyn Grosse for all the impressive amount of work and help at any time, which have made this project a success. Thanks to Joao Rodrigues, Olivia Zanoletti and Meltem Weger for your help in different aspects of the collaboration.

I would like to thank deeply Jean-Marc Matter for having followed and supervised my work since my studies in biochemistry at the University of Geneva. You have always been listening closely to all my concerns and acted as an important mentor for me. Thank you for having placed your trust in me for our collaborative project on MRS in developing avian retina. Collaborating with you has been a real source of pleasure and your competences and knowledge have significantly furthered my knowledge in neuro-biochemistry. Thanks to Laurent Brodier as well for your huge amount of work of rare quality. It has been a real pleasure tackling the challenges of embryonic MRS or the designing of potential zebra mouse experiments with you.

Among the people from CIBM I would like to warmly thank Carole Poitry-Yamate for the incredible work realized during every collaboration. Mainly I would like to thank you for all the time spent supervising, discussing, correcting, reviewing every manuscript or piece of the work I have done at the CIBM. Thank you to all the talented postdocs which have helped or supervised different aspects of my thesis at different times: Hongxia Lei, Blanca Lizarbe, Katarzyna Pierzchala, João Duarte, Nicolas Kunz and Bernard Lanz. Thanks to Lillian Vernacchio for all the administrative help, thanks to Yves Pilloud for the technical support and construction of homemade mouse cages. Thanks to all the Vet team for all the help and advice in several aspects of my thesis, in particular to Mario Lepore for the impressive quality of work and rigor. I would like to thank Emilie Baudat and Aurélien Bornet for their amazing work managing the ISIC NMR platform as well as Laure Menin for the huge work and support at the ISIC LC-MS platform.

Finally, I would like to thank particularly all the CIBM PhD students which have taught me most of spectroscopy knowledge obtained after these years. Thanks to my cochon-de-gamin Guillaume Donati for all the fondues and joking around, which were most of the time accompanied by serious discussions on spectroscopy. Thanks to Veronika Rackayová for your help and expertise in the field of spectroscopy and Krtek, which was generally accompanied by fondue as well. Thanks to Grumpy for all the biscuits and physics sessions in The cafeteria

or for deepening my knowledge about every single Japanese restaurant around the world. Non. Thanks to Yohan Boillat for being my reference person in the Palmashow science at EPFL and for being always such good company. Thanks as well to João Jr., Elise, Sarah, Emma, Dunja, Matthieu, Masoumeh, Emine and all the current or passed students of the lab for all these great times.

I would like to thank mon pote Nico for sharing the burden of a thesis at EPFL with me by having regularly payday-feasts and enjoying breaks at the “détente sportive”. I would like to thank Victor and Sueda for the time spent on an exciting project, getting my mind off my thesis.

Faezeh, this work would not have been possible without your emotional support and help. I have a great deal of admiration for your strength and patience. Your encouragements and cheerfulness have helped me bear the hard times and brought so much appeasement in this hectic PhD student life.

Finally, I would like to thank my family, in particular my parents who have been supporting me at every level since my very young age. I am very thankful for this lifelong investment you have made providing me the perfect environment to obtain a PhD. Therefore, I would like to dedicate this thesis to you.

References

References

- Abdallah, C.G., Jiang, L., De Feyter, H.M., Fasula, M., Krystal, J.H., Rothman, D.L., Mason, G.F., and Sanacora, G. (2014). Glutamate metabolism in major depressive disorder. *Am. J. Psychiatry* 171, 1320–1327.
- Abdel-Razaq, W., Kendall, D.A., and Bates, T.E. (2011). The Effects of Antidepressants on Mitochondrial Function in a Model Cell System and Isolated Mitochondria. *Neurochem. Res.* 36, 327–338.
- Acevedo-Torres, K., Berríos, L., Rosario, N., Dufault, V., Skatchkov, S., Eaton, M.J., Torres-Ramos, C.A., and Ayala-Torres, S. (2009). Mitochondrial DNA damage is a hallmark of chemically induced and the R6/2 transgenic model of Huntington's disease. *DNA Repair (Amst)*. 8, 126–136.
- Achanta, L.B., and Rae, C.D. (2017). β -Hydroxybutyrate in the Brain: One Molecule, Multiple Mechanisms. *Neurochem. Res.* 42, 35–49.
- Acharya, N.K., Goldwaser, E.L., Forsberg, M.M., Godsey, G.A., Johnson, C.A., Sarkar, A., DeMarshall, C., Kosciuk, M.C., Dash, J.M., Hale, C.P., et al. (2015). Sevoflurane and Isoflurane induce structural changes in brain vascular endothelial cells and increase blood–brain barrier permeability: Possible link to postoperative delirium and cognitive decline. *Brain Res.* 1620, 29–41.
- Adams, D.S. (2006). Early, H⁺-V-ATPase-dependent proton flux is necessary for consistent left-right patterning of non-mammalian vertebrates. *Development* 133, 1657–1671.
- Agathocleous, M., Love, N.K., Randlett, O., Harris, J.J., Liu, J., Murray, A.J., and Harris, W.A. (2012). Metabolic differentiation in the embryonic retina. *Nat. Cell Biol.* 14, 859–864.
- Agostinho, F.R., Réus, G.Z., Stringari, R.B., Ribeiro, K.F., Ferraro, A.K., Benedet, J., Rochi, N., Scaini, G., Streck, E.L., and Quevedo, J. (2011). Treatment with olanzapine, fluoxetine and olanzapine/fluoxetine alters citrate synthase activity in rat brain. *Neurosci. Lett.* 487, 278–281.
- Ali, S., Stone, M.A., Peters, J.L., Davies, M.J., and Khunti, K. (2006). The prevalence of co-morbid depression in adults with Type 2 diabetes: a systematic review and meta-analysis. *Diabet. Med.* 23, 1165–1173.
- Alisch, R.S., Van Hulle, C., Chopra, P., Bhattacharyya, A., Zhang, S., Davidson, R.J., Kalin, N.H., and Goldsmith, H.H. (2017). A multi-dimensional characterization of anxiety in monozygotic twin pairs reveals susceptibility loci in humans. *Transl. Psychiatry* 7, 1282.
- Altarejos, J.Y., Goebel, N., Konkright, M.D., Inoue, H., Xie, J., Arias, C.M., Sawchenko, P.E., and Montminy, M. (2008). The Creb1 coactivator Crtc1 is required for energy balance and fertility. *Nat. Med.* 14, 1112–1117.
- American Psychiatric Association (2013). Diagnostic and statistical manual of mental disorders (DSM-V) (Arlington: Association American Psychiatric).
- Anderson, R.M., Barger, J.L., Edwards, M.G., Braun, K.H., O'Connor, C.E., Prolla, T.A., and Weindruch, R. (2008). Dynamic regulation of PGC-1 α localization and turnover implicates mitochondrial adaptation in calorie restriction and the stress response. *Aging Cell* 7, 101–111.
- Andreazza, A.C., Shao, L., Wang, J.-F., and Young, L.T. (2010). Mitochondrial complex I activity and oxidative damage to mitochondrial proteins in the prefrontal cortex of patients with bipolar disorder. *Arch. Gen. Psychiatry* 67, 360–368.
- Arduini, A., Bonomini, M., and Zammit, V. (2016). Defining the potential antidepressant mode of action of acetyl-L-carnitine. *Proc. Natl. Acad. Sci.* 113, E5698–E5699.
- Arias-Mendoza, F., and Brown, T.R. (2004). In vivo measurement of phosphorous markers of disease. *Dis. Markers* 19, 49–68.
- Ariannur, P.S., Madhavarao, C.N., and Namboodiri, A.M.A. (2008). N-acetylaspartate synthesis in the brain: Mitochondria vs. microsomes. *Brain Res.* 1227, 34–41.
- Aston, C., Jiang, L., and Sokolov, B.P. (2004). Microarray analysis of postmortem temporal cortex from patients with schizophrenia. *J. Neurosci. Res.* 77, 858–866.
- Atsumi, T., Chesney, J., Metz, C., Leng, L., Donnelly, S., Makita, Z., Mitchell, R., and Bucala, R. (2002). High expression of inducible 6-phosphofructo-2-kinase/fructose-2,6-bisphosphatase (iPFK-2; PFKFB3) in human

cancers. *Cancer Res.* 62, 5881–5887.

Attwell, D., and Laughlin, S.B. (2001). An energy budget for signaling in the grey matter of the brain. *J. Cereb. Blood Flow Metab.* 21, 1133–1145.

Aureli, T., Miccheli, A., Ricciolini, R., Di Cocco, M.E., Ramacci, M.T., Angelucci, L., Ghirardi, O., and Conti, F. (1990). Aging brain: effect of acetyl-L-carnitine treatment on rat brain energy and phospholipid metabolism. A study by ³¹P and ¹H NMR spectroscopy. *Brain Res.* 526, 108–112.

Aureli, T., Di Cocco, M.E., Capuani, G., Ricciolini, R., Manetti, C., Miccheli, A., and Conti, F. (2000). Effect of long-term feeding with acetyl-L-carnitine on the age-related changes in rat brain lipid composition: A study by ³¹P NMR spectroscopy. *Neurochem. Res.* 25, 395–399.

Bachmann, R.F., Wang, Y., Yuan, P., Zhou, R., Li, X., Alesci, S., Du, J., and Manji, H.K. (2009). Common effects of lithium and valproate on mitochondrial functions: protection against methamphetamine-induced mitochondrial damage. *Int. J. Neuropsychopharmacol.* 12, 805–822.

Badar-Goffer, R.S., Ben-Yoseph, O., Bachelard, H.S., and Morris, P.G. (1992). Neuronal-glial metabolism under depolarizing conditions. A ¹³C-n.m.r. study. *Biochem. J.* 282, 225–230.

Bagot, R.C., Labonté, B., Peña, C.J., and Nestler, E.J. (2014). Epigenetic signaling in psychiatric disorders: Stress and depression. *Dialogues Clin. Neurosci.* 16, 281–295.

Bak, L.K., Schousboe, A., and Waagepetersen, H.S. (2006). The glutamate/GABA-glutamine cycle: Aspects of transport, neurotransmitter homeostasis and ammonia transfer. *J. Neurochem.* 98, 641–653.

Barker, P.B., Soher, B.J., Blackband, S.J., Chatham, J.C., Mathews, V.P., and Bryan, R.N. (1993). Quantitation of proton NMR spectra of the human brain using tissue water as an internal concentration reference. *NMR Biomed.* 6, 89–94.

von Bartheld, C.S., Bahney, J., and Herculano-Houzel, S. (2016). The search for true numbers of neurons and glial cells in the human brain: A review of 150 years of cell counting. *J. Comp. Neurol.* 524, 3865–3895.

Bassnett, S. (1990). Intracellular pH regulation in the embryonic chicken lens epithelium. *J. Physiol.* 431, 445–464.

Bassnett, S., and Beebe, D.C. (1992). Coincident Loss of Mitochondria and Nuclei During Lens Fiber Cell Development. *Dev. Dyn.* 194, 85–93.

Bassnett, S., Croghan, P.C., and Duncan, G. (1987). Diffusion of lactate and its role in determining intracellular pH in the lens of the eye. *Exp. Eye Res.* 44, 143–147.

Bastiaansen, J.A.M., Cheng, T., Lei, H., Gruetter, R., and Comment, A. (2015). Direct noninvasive estimation of myocardial tricarboxylic acid cycle flux in vivo using hyperpolarized ¹³C magnetic resonance. *J. Mol. Cell. Cardiol.* 87, 129–137.

Bates, T.E., Strangward, M., Keelan, J., Davey, G.P., Munro, P.M., and Clark, J.B. (1996). Inhibition of N-acetylaspartate production: implications for ¹H MRS studies in vivo. *Neuroreport* 7, 1397–1400.

Bauer, R., Plieschnig, J.A., Finkes, T., Riegler, B., Hermann, M., and Schneider, W.J. (2013). The developing chicken yolk sac acquires nutrient transport competence by an orchestrated differentiation process of its endodermal epithelial cells. *J. Biol. Chem.* 288, 1088–1098.

Baxter, L.R. (1985). Cerebral Metabolic Rates for Glucose in Mood Disorders. *Arch. Gen. Psychiatry* 42, 441.

Becker, H.M., Bröer, S., and Deitmer, J.W. (2004). Facilitated lactate transport by MCT1 when coexpressed with the sodium bicarbonate cotransporter (NBC) in *Xenopus* oocytes. *Biophys. J.* 86, 235–247.

Beckervordersandforth, R., Ebert, B., Schäffner, I., Moss, J., Fiebig, C., Shin, J., Moore, D.L., Ghosh, L., Trincherio, M.F., Stockburger, C., et al. (2017). Role of Mitochondrial Metabolism in the Control of Early Lineage Progression and Aging Phenotypes in Adult Hippocampal Neurogenesis. *Neuron* 93, 1518.

Beckmann, N., Turkalj, I., Seelig, J., and Keller, U. (1991). Carbon-13 NMR for the assessment of human brain

glucose metabolism in vivo. *Biochemistry* 30, 6362–6366.

Bednařík, P., Moheet, A., Deelchand, D.K., Emir, U.E., Eberly, L.E., Bareš, M., Seaquist, E.R., and Öz, G. (2015). Feasibility and reproducibility of neurochemical profile quantification in the human hippocampus at 3 T. *NMR Biomed.* 28, 685–693.

Befroy, D.E., Rothman, D.L., Petersen, K.F., and Shulman, G.I. (2012). ³¹P-Magnetization Transfer Magnetic Resonance Spectroscopy Measurements of In Vivo Metabolism. *Diabetes* 61, 2669–2678.

Ben-Shachar, D., Zuk, R., Gazawi, H., Reshef, A., Sheinkman, A., and Klein, E. (1999). Increased mitochondrial complex I activity in platelets of schizophrenic patients. *Int. J. Neuropsychopharmacol.* 2, 245–253.

Benjamin, A.M., and Quastel, J.H. (1972). Locations of amino acids in brain slices from the rat. Tetrodotoxin-sensitive release of amino acids. *Biochem. J.* 128, 631–646.

Berg-Johnsen, J., and Langmoen, I.A. (1990). Mechanisms concerned in the direct effect of isoflurane on rat hippocampal and human neocortical neurons. *Brain Res.* 507, 28–34.

van den Berg, C.J., and Garfinkel, D. (1971). A simulation study of brain compartments. Metabolism of glutamate and related substances in mouse brain. *Biochem. J.* 123, 211–218.

Van Den Berg, C.J., Kržalić, L., Mela, P., and Waelsch, H. (1969). Compartmentation of glutamate metabolism in brain. Evidence for the existence of two different tricarboxylic acid cycles in brain. *Biochem. J.* 113, 281–290.

Berman, R.M., Cappiello, A., Anand, A., Oren, D.A., Heninger, G.R., Charney, D.S., and Krystal, J.H. (2000). Antidepressant effects of ketamine in depressed patients. *Biol. Psychiatry* 47, 351–354.

Berton, O., McClung, C.A., Dileone, R.J., Krishnan, V., Renthal, W., Russo, S.J., Graham, D., Tsankova, N.M., Bolanos, C.A., Rios, M., et al. (2006). Essential role of BDNF in the mesolimbic dopamine pathway in social defeat stress. *Science* 311, 864–868.

Bessman, S.P., and Carpenter, C.L. (1985). The creatine-creatine phosphate energy shuttle. *Annu. Rev. Biochem.* 54, 831–862.

Bhat, A.H., Dar, K.B., Anees, S., Zargar, M.A., Masood, A., Sofi, M.A., and Ganie, S.A. (2015). Oxidative stress, mitochondrial dysfunction and neurodegenerative diseases; a mechanistic insight. *Biomed. Pharmacother.* 74, 101–110.

Bianchi, M.C., Tosetti, M., Battini, R., Manca, M.L., Mancuso, M., Cioni, G., Canapicchi, R., and Siciliano, G. (2003). Proton MR spectroscopy of mitochondrial diseases: analysis of brain metabolic abnormalities and their possible diagnostic relevance. *AJNR. Am. J. Neuroradiol.* 24, 1958–1966.

Bigio, B., Mathé, A.A., Sousa, V.C., Zelli, D., Svenningsson, P., McEwen, B.S., and Nasca, C. (2016). Epigenetics and energetics in ventral hippocampus mediate rapid antidepressant action: Implications for treatment resistance. *Proc. Natl. Acad. Sci.* 113, 7906–7911.

Bishop, P. (1996). The biochemical structure of mammalian vitreous. *Eye* 10, 664–670.

Boku, S., Nakagawa, S., Toda, H., and Hishimoto, A. (2018). Neural basis of major depressive disorder: Beyond monoamine hypothesis. *Psychiatry Clin. Neurosci.* 72, 3–12.

Bolaños, J.P. (2016). Bioenergetics and redox adaptations of astrocytes to neuronal activity. *J. Neurochem.* 139, 115–125.

Boles, R.G., Burnett, B.B., Gleditsch, K., Wong, S., Guedalia, A., Kaariainen, A., Eloed, J., Stern, A., and Brumm, V. (2005). A high predisposition to depression and anxiety in mothers and other matrilineal relatives of children with presumed maternally inherited mitochondrial disorders. *Am. J. Med. Genet. B. Neuropsychiatr. Genet.* 137B, 20–24.

Bora, E., Fornito, A., Yücel, M., and Pantelis, C. (2010). Voxelwise Meta-Analysis of Gray Matter Abnormalities in Bipolar Disorder. *Biol. Psychiatry* 67, 1097–1105.

Boumezbeur, F., Mason, G.F., de Graaf, R.A., Behar, K.L., Cline, G.W., Shulman, G.I., Rothman, D.L., and Petersen,

- K.F. (2010a). Altered Brain Mitochondrial Metabolism in Healthy Aging as Assessed by in vivo Magnetic Resonance Spectroscopy. *J. Cereb. Blood Flow Metab.* **30**, 211–221.
- Boumezbeur, F., Petersen, K.F., Cline, G.W., Mason, G.F., Behar, K.L., Shulman, G.I., and Rothman, D.L. (2010b). The contribution of blood lactate to brain energy metabolism in humans measured by dynamic ¹³C nuclear magnetic resonance spectroscopy. *J. Neurosci.* **30**, 13983–13991.
- Boumezbeur, F., Petersen, K.F., Cline, G.W., Mason, G.F., Behar, K.L., Shulman, G.I., and Rothman, D.L. (2010c). The Contribution of Blood Lactate to Brain Energy Metabolism in Humans Measured by Dynamic ¹³C Nuclear Magnetic Resonance Spectroscopy. *J. Neurosci.* **30**, 13983–13991.
- Bradley, K.A.L., Mao, X., Case, J.A.C., Kang, G., Shungu, D.C., and Gabbay, V. (2016). Increased ventricular cerebrospinal fluid lactate in depressed adolescents. *Eur. Psychiatry* **32**, 1–8.
- Brenes, J.C., Rodríguez, O., and Fornaguera, J. (2008). Differential effect of environment enrichment and social isolation on depressive-like behavior, spontaneous activity and serotonin and norepinephrine concentration in prefrontal cortex and ventral striatum. *Pharmacol. Biochem. Behav.* **89**, 85–93.
- Brenes Sáenz, J.C., Villagra, O.R., and Fornaguera Trías, J. (2006). Factor analysis of Forced Swimming test, Sucrose Preference test and Open Field test on enriched, social and isolated reared rats. *Behav. Brain Res.* **169**, 57–65.
- Breuillaud, L., Rossetti, C., Meylan, E.M., Mérinat, C., Halfon, O., Magistretti, P.J., and Cardinaux, J.-R. (2012). Deletion of CREB-Regulated Transcription Coactivator 1 Induces Pathological Aggression, Depression-Related Behaviors, and Neuroplasticity Genes Dysregulation in Mice. *Biol. Psychiatry* **72**, 528–536.
- Brindle, K.M., Blackledge, M.J., Challiss, R.A.J., and Radda, G.K. (1989). Phosphorus-31 NMR magnetization-transfer measurements of ATP turnover during steady-state isometric muscle contraction in the rat hind limb in vivo. *Biochemistry* **28**, 4887–4893.
- Broderick, Tom L, Quinney H Arthur, and D, L.G. (1992). Carnitine Stimulation of Glucose Oxidation in the Fatty. *J. Biol. Chem.* **267**, 3758–3763.
- Brown, M.F., Miljanich, G.P., and Dratz, E.A. (1977). Interpretation of 100- and 360-MHz Proton Magnetic Resonance Spectra of Retinal Rod Outer Segment Disk Membranes. *Biochemistry* **16**, 2640–2648.
- Browne, S.E., and Beal, M.F. (2004). The energetics of Huntington's disease. *Neurochem. Res.* **29**, 531–546.
- Bubb, E.J., Kinnavane, L., and Aggleton, J.P. (2017). Hippocampal–diencephalic–cingulate networks for memory and emotion: An anatomical guide. *Brain Neurosci. Adv.* **1**, 239821281772344.
- Buchsbaum, M.S., Wu, J., DeLisi, L.E., Holcomb, H., Kessler, R., Johnson, J., King, A.C., Hazlett, E., Langston, K., and Post, R.M. (1986). Frontal cortex and basal ganglia metabolic rates assessed by positron emission tomography with [¹⁸F]2-deoxyglucose in affective illness. *J. Affect. Disord.* **10**, 137–152.
- Buono, R.J., and Sheffield, J.B. (1991a). Changes in distribution of mitochondria in the developing chick retina. *Exp. Eye Res.* **53**, 187–198.
- Buono, R.J., and Sheffield, J.B. (1991b). Changes in expression and distribution of lactate dehydrogenase isoenzymes in the developing chick retina. *Exp. Eye Res.* **53**, 199–204.
- Burjanadze, G., Dachanidze, N., Kuchukashvili, Z., Chachua, M., Menabde, K., and Koshoridze, N.I. (2016). Investigation of Brain Creatine Levels Under the Mental Stress Conditions. *J. Stress Physiol. Biochem.* **12**, 5–14.
- Cao, B., Stanley, J.A., Selvaraj, S., Mwangi, B., Passos, I.C., Zunta-Soares, G.B., and Soares, J.C. (2016). Evidence of altered membrane phospholipid metabolism in the anterior cingulate cortex and striatum of patients with bipolar disorder I: A multi-voxel ¹H MRS study. *J. Psychiatr. Res.* **81**, 48–55.
- Carter, B.S., Hamilton, D.E., and Thompson, R.C. (2013). Acute and chronic glucocorticoid treatments regulate astrocyte-enriched mRNAs in multiple brain regions in vivo. *Front. Neurosci.* **7**, 139.
- Castro, J.E., Diessler, S., Varea, E., Márquez, C., Larsen, M.H., Cordero, M.I., and Sandi, C. (2012). Personality traits in rats predict vulnerability and resilience to developing stress-induced depression-like behaviors, HPA axis

- hyper-reactivity and brain changes in pERK1/2 activity. *Psychoneuroendocrinology* 37, 1209–1223.
- Cataldo, A.M., McPhie, D.L., Lange, N.T., Punzell, S., Elmiligy, S., Ye, N.Z., Froimowitz, M.P., Hassinger, L.C., Menesale, E.B., Sargent, L.W., et al. (2010). Abnormalities in mitochondrial structure in cells from patients with bipolar disorder. *Am. J. Pathol.* 177, 575–585.
- Cavassila, S., Deval, S., Huegen, C., Van Ormondt, D., and Graveron-Demilly, D. (2001). Cramér-Rao bounds: An evaluation tool for quantitation. *NMR Biomed.* 14, 278–283.
- Chakravarty, S., Reddy, B.R., Sudhakar, S.R., Saxena, S., Das, T., Meghah, V., Brahmendra Swamy, C. V, Kumar, A., and Idris, M.M. (2013). Chronic unpredictable stress (CUS)-induced anxiety and related mood disorders in a zebrafish model: altered brain proteome profile implicates mitochondrial dysfunction. *PLoS One* 8, e63302.
- Chaouloff, F. (2013). Social stress models in depression research: what do they tell us? *Cell Tissue Res.* 354, 179–190.
- Chen, R.W., and Chuang, D.M. (1999). Long term lithium treatment suppresses p53 and Bax expression but increases Bcl-2 expression. A prominent role in neuroprotection against excitotoxicity. *J. Biol. Chem.* 274, 6039–6042.
- Chen, F., Wegener, G., Madsen, T.M., and Nyengaard, J.R. (2013). Mitochondrial plasticity of the hippocampus in a genetic rat model of depression after antidepressant treatment. *Synapse* 67, 127–134.
- Chiodini, F., Matter-Sadzinski, L., Rodrigues, T., Skowronska-Krawczyk, D., Brodier, L., Schaad, O., Bauer, C., Ballivet, M., and Matter, J.-M. (2013). A Positive Feedback Loop between ATOH7 and a Notch Effector Regulates Cell-Cycle Progression and Neurogenesis in the Retina. *Cell Rep.* 3, 796–807.
- Chitty, K.M., Lagopoulos, J., Lee, R.S.C., Hickie, I.B., and Hermens, D.F. (2013). A systematic review and meta-analysis of proton magnetic resonance spectroscopy and mismatch negativity in bipolar disorder. *Eur. Neuropsychopharmacol.* 23, 1348–1363.
- Choi, I.-Y., and Gruetter, R. (2004). Dynamic or inert metabolism? Turnover of N-acetyl aspartate and glutathione from D-[1-¹³C]glucose in the rat brain in vivo. *J. Neurochem.* 91, 778–787.
- Choi, I.Y., Lei, H., and Gruetter, R. (2002). Effect of deep pentobarbital anesthesia on neurotransmitter metabolism in vivo: On the correlation of total glucose consumption with glutamatergic action. *J. Cereb. Blood Flow Metab.* 22, 1343–1351.
- Choong, E., Quteineh, L., Cardinaux, J.-R., Gholam-Rezaee, M., Vandenberghe, F., Dobrinias, M., Bondolfi, G., Etter, M., Holzer, L., Magistretti, P., et al. (2013). Influence of CRT1 polymorphisms on body mass index and fat mass in psychiatric patients and the general adult population. *JAMA Psychiatry* 70, 1011–1019.
- Chowdhury, G.M.I., Banasr, M., de Graaf, R.A., Rothman, D.L., Behar, K.L., and Sanacora, G. (2008). Chronic Riluzole Treatment Increases Glucose Metabolism in Rat Prefrontal Cortex and Hippocampus. *J. Cereb. Blood Flow Metab.* 28, 1892–1897.
- Chowdhury, G.M.I., Behar, K.L., Cho, W., Thomas, M.A., Rothman, D.L., and Sanacora, G. (2012). 1H-[¹³C]-Nuclear Magnetic Resonance Spectroscopy Measures of Ketamine's Effect on Amino Acid Neurotransmitter Metabolism. *Biol. Psychiatry* 71, 1022–1025.
- Chung, Y.-L., Madhu, B., and Griffiths, J.R. (2015). Metabolism and Metabolomics by MRS. In *EMagRes*, (Chichester, UK: John Wiley & Sons, Ltd), pp. 689–698.
- Cohen-Woods, S., Craig, I.W., and McGuffin, P. (2013). The current state of play on the molecular genetics of depression. *Psychol. Med.* 43, 673–687.
- Corrêa, C., Amboni, G., Assis, L.C., Martins, M.R., Kapczinski, F., Streck, E.L., and Quevedo, J. (2007). Effects of lithium and valproate on hippocampus citrate synthase activity in an animal model of mania. *Prog. Neuro-Psychopharmacology Biol. Psychiatry* 31, 887–891.
- Craddock, N., and Sklar, P. (2013). Genetics of bipolar disorder. *Lancet (London, England)* 381, 1654–1662.
- Cross, J.H., Gadian, D.G., Connelly, A., and Leonard, J. V (1993). Proton magnetic resonance spectroscopy studies

- in lactic acidosis and mitochondrial disorders. *J. Inherit. Metab. Dis.* **16**, 800–811.
- Cui, J., Shao, L., Young, L.T., and Wang, J.-F. (2007). Role of glutathione in neuroprotective effects of mood stabilizing drugs lithium and valproate. *Neuroscience* **144**, 1447–1453.
- Curti, C., Mingatto, F.E., Polizello, A.C., Galastri, L.O., Uyemura, S.A., and Santos, A.C. (1999). Fluoxetine interacts with the lipid bilayer of the inner membrane in isolated rat brain mitochondria, inhibiting electron transport and F1F0-ATPase activity. *Mol. Cell. Biochem.* **199**, 103–109.
- Dager, S.R., Friedman, S.D., Parow, A., Demopulos, C., Stoll, A.L., Lyoo, I.K., Dunner, D.L., and Renshaw, P.F. (2004). Brain metabolic alterations in medication-free patients with bipolar disorder. *Arch. Gen. Psychiatry* **61**, 450–458.
- Davanzo, P., Thomas, M.A., Yue, K., Oshiro, T., Belin, T., Strober, M., and McCracken, J. (2001). Decreased anterior cingulate myo-inositol/creatine spectroscopy resonance with lithium treatment in children with bipolar disorder. *Neuropsychopharmacology* **24**, 359–369.
- Deelchand, D.K., Nelson, C., Shestov, A.A., Uğurbil, K., and Henry, P.-G. (2009). Simultaneous measurement of neuronal and glial metabolism in rat brain in vivo using co-infusion of [1,6-¹³C]glucose and [1,2-¹³C]acetate. *J. Magn. Reson.* **196**, 157–163.
- DeFronzo, R.A., Tobin, J.D., and Andres, R. (1979). Glucose clamp technique: a method for quantifying insulin secretion and resistance. *Am. J. Physiol. Metab.* **237**, E214.
- Deicken, R.F., Fein, G., and Weiner, M.W. (1995). Abnormal frontal lobe phosphorous metabolism in bipolar disorder. *Am. J. Psychiatry* **152**, 915–918.
- Deranieh, R.M., and Greenberg, M.L. (2009). Cellular consequences of inositol depletion. *Biochem. Soc. Trans.* **37**, 1099–1103.
- Díaz-García, C.M., Mongeon, R., Lahmann, C., Koveal, D., Zucker, H., and Yellen, G. (2017). Neuronal Stimulation Triggers Neuronal Glycolysis and Not Lactate Uptake. *Cell Metab.* **26**, 361–374.e4.
- Doganay, S., Cankaya, C., and Alkan, A. (2012). Evaluation of corpus geniculatum laterale and vitreous fluid by magnetic resonance spectroscopy in patients with glaucoma; A preliminary study. *Eye* **26**, 1044–1051.
- Doh, S., Hao, H., Loh, S.C., Patel, T., Tawil, H.Y., Chen, D.K., Pashkova, A., Shen, A., Wang, H., and Cai, L. (2010). Analysis of retinal cell development in chick embryo by immunohistochemistry and in ovo electroporation techniques. *BMC Dev. Biol.* **10**, 8.
- Dowlati, Y., Herrmann, N., Swardfager, W., Liu, H., Sham, L., Reim, E.K., and Lanctôt, K.L. (2010). A Meta-Analysis of Cytokines in Major Depression. *Biol. Psychiatry* **67**, 446–457.
- Drevets, W.C., Price, J.L., Simpson, J.R., Todd, R.D., Reich, T., Vannier, M., and Raichle, M.E. (1997). Subgenual prefrontal cortex abnormalities in mood disorders. *Nature* **386**, 824–827.
- Dringen, R., Gebhardt, R., and Hamprecht, B. (1993). Glycogen in astrocytes: possible function as lactate supply for neighboring cells. *Brain Res.* **623**, 208–214.
- Duarte, J.M.N., and Gruetter, R. (2013). Glutamatergic and GABAergic energy metabolism measured in the rat brain by ¹³C NMR spectroscopy at 14.1 T. *J. Neurochem.* **126**, 579–590.
- Duarte, J.M.N., Lanz, B., and Gruetter, R. (2011). Compartmentalized cerebral metabolism of [1,6-¹³C]glucose determined by in vivo ¹³C NMR spectroscopy at 14.1 T. *Front. Neuroenergetics* **3**, 1–15.
- Duarte, J.M.N., Lei, H., Mlynárik, V., and Gruetter, R. (2012). The neurochemical profile quantified by in vivo ¹H NMR spectroscopy. *Neuroimage* **61**, 342–362.
- Duarte, J.M.N., Girault, F.M., and Gruetter, R. (2015). Brain energy metabolism measured by ¹³C magnetic resonance spectroscopy in vivo upon infusion of [3-¹³C]lactate. *J. Neurosci. Res.* **93**, 1009–1018.
- Duckrow, R.B., and Bryan, R.M. (1987). Regional Cerebral Glucose Utilization During Hyperglycemia. *J. Neurochem.* **48**, 989–993.

- Dunn, W.B., Broadhurst, D.I., Atherton, H.J., Goodacre, R., and Griffin, J.L. (2011). Systems level studies of mammalian metabolomes: the roles of mass spectrometry and nuclear magnetic resonance spectroscopy. *Chem. Soc. Rev.* *40*, 387–426.
- Duong, T.Q. (2011). Magnetic resonance imaging of the retina: A brief historical and future perspective. *Saudi J. Ophthalmol.* *25*, 137–143.
- Dzeja, P.P., and Terzic, A. (2003). Phosphotransfer networks and cellular energetics. *J. Exp. Biol.* *206*, 2039–2047.
- van Eijdsden, P., Behar, K.L., Mason, G.F., Braun, K.P.J., and de Graaf, R.A. (2010). In vivo neurochemical profiling of rat brain by ^1H - ^{13}C NMR spectroscopy: cerebral energetics and glutamatergic/GABAergic neurotransmission. *J. Neurochem.* *112*, 24–33.
- Emir, U.E., Raatz, S., McPherson, S., Hodges, J.S., Torkelson, C., Tawfik, P., White, T., and Terpstra, M. (2011). Noninvasive quantification of ascorbate and glutathione concentration in the elderly human brain. *NMR Biomed.* *24*, 888–894.
- Erecińska, M., and Silver, I.A. (1989). ATP and brain function. *J. Cereb. Blood Flow Metab.* *9*, 2–19.
- Esteban-Martínez, L., Sierra-Filardi, E., McGreal, R.S., Salazar-Roa, M., Mariño, G., Seco, E., Durand, S., Enot, D., Graña, O., Malumbres, M., et al. (2017). Programmed mitophagy is essential for the glycolytic switch during cell differentiation. *EMBO J.* *36*, 1688–1706.
- Fanea, L., and Fagan, A.J. (2012). Review: magnetic resonance imaging techniques in ophthalmology. *Mol. Vis.* *18*, 2538–2560.
- Fattal, O., Budur, K., Vaughan, A.J., and Franco, K. (2006). Review of the Literature on Major Mental Disorders in Adult Patients With Mitochondrial Diseases. *Psychosomatics* *47*, 1–7.
- Feier, G., Valvassori, S.S., Varela, R.B., Resende, W.R., Bavaresco, D. V, Morais, M.O., Scaini, G., Andersen, M.L., Streck, E.L., and Quevedo, J. (2013). Lithium and valproate modulate energy metabolism in an animal model of mania induced by methamphetamine. *Pharmacol. Biochem. Behav.* *103*, 589–596.
- Finsterer, J. (2004). Mitochondriopathies. *Eur. J. Neurol.* *11*, 163–186.
- Florian, C.L., Williams, S.R., Bhakoo, K.K., and Noble, M.D. (1996). Regional and developmental variations in metabolite concentration in the rat brain and eye: A study using ^1H NMR spectroscopy and high performance liquid chromatography. *Neurochem. Res.* *21*, 1065–1074.
- Folch, J., Lees, M., and Sloane Stanley, G.H. (1957). A simple method for the isolation and purification of total lipides from animal tissues. *J. Biol. Chem.* *226*, 497–509.
- Folmes, C.D.L., Dzeja, P.P., Nelson, T.J., and Terzic, A. (2012). Metabolic plasticity in stem cell homeostasis and differentiation. *Cell Stem Cell* *11*, 596–606.
- Foulds, W.S. (1987). Is your vitreous really necessary?: The role of the vitreous in the eye with particular reference to retinal attachment, detachment and the mode of action of vitreous substitutes. *Eye* *1*, 641–664.
- de Freitas, A.E., de Oliveira Balen, G., dos Santos, D.B., Farina, M., Budni, J., Severo Rodrigues, A.L., Moretti, M., and Colla, A. (2011). Ascorbic acid treatment, similarly to fluoxetine, reverses depressive-like behavior and brain oxidative damage induced by chronic unpredictable stress. *J. Psychiatr. Res.* *46*, 331–340.
- Frey, B.N., Stanley, J.A., Nery, F.G., Serap Monkul, E., Nicoletti, M.A., Chen, H.H., Hatch, J.P., Caetano, S.C., Ortiz, O., Kapczinski, F., et al. (2007). Abnormal cellular energy and phospholipid metabolism in the left dorsolateral prefrontal cortex of medication-free individuals with bipolar disorder: An in vivo ^1H MRS study. *Bipolar Disord. Suppl.* *9*, 119–127.
- Friedrich, M.J. (2017). Depression Is the Leading Cause of Disability Around the World. *JAMA* *317*, 1517.
- From, A.H.L., and Ugurbil, K. (2011). Standard magnetic resonance-based measurements of the $\text{P}_i \rightarrow \text{ATP}$ rate do not index the rate of oxidative phosphorylation in cardiac and skeletal muscles. *Am. J. Physiol. Physiol.* *301*, C1–C11.

- Fu, C., Zhang, H., Xuan, A., Gao, Y., Xu, J., and Shi, D. (2018). A combined study of 18F-FDG PET-CT and fMRI for assessing resting cerebral function in patients with major depressive disorder. *Exp. Ther. Med.* 1873–1881.
- Fujiwara, T., Anai, T., Kurihara, N., and Nagayama, K. (1993). Frequency-Switched Composite Pulses for Decoupling Carbon-13 Spins over Ultrabroad Bandwidths. *J. Magn. Reson. Ser. A* 104, 103–105.
- Fuke, S., Kametani, M., and Kato, T. (2008). Quantitative analysis of the 4977-bp common deletion of mitochondrial DNA in postmortem frontal cortex from patients with bipolar disorder and schizophrenia. *Neurosci. Lett.* 439, 173–177.
- Fung, S.J., Webster, M.J., Sivagnanasundaram, S., Duncan, C., Elashoff, M., and Weickert, C.S. (2010). Expression of Interneuron Markers in the Dorsolateral Prefrontal Cortex of the Developing Human and in Schizophrenia. *Am. J. Psychiatry* 167, 1479–1488.
- Galińska-Skok, B., Konarzewska, B., Kubas, B., Tarasów, E., and Szulc, A. (2016). Neurochemical alterations in anterior cingulate cortex in bipolar disorder: a proton magnetic resonance spectroscopy study (1H-MRS). *Psychiatr. Pol.* 50, 839–848.
- Galińska-Skok, B., Małus, A., Konarzewska, B., Rogowska-Zach, A., Milewski, R., Tarasów, E., Szulc, A., and Waszkiewicz, N. (2018). Choline Compounds of the Frontal Lobe and Temporal Glutamatergic System in Bipolar and Schizophrenia Proton Magnetic Resonance Spectroscopy Study. *Dis. Markers* 2018, 1–7.
- Gamaro, G.D., Streck, E.L., Matté, C., Prediger, M.E., Wyse, A.T.S., and Dalmaz, C. (2003). Reduction of hippocampal Na⁺, K⁺-ATPase activity in rats subjected to an experimental model of depression. *Neurochem. Res.* 28, 1339–1344.
- Gambarota, G., Mekle, R., Xin, L., Hergt, M., Van Der Zwaag, W., Krueger, G., and Gruetter, R. (2009). In vivo measurement of glycine with short echo-time 1H MRS in human brain at 7 T. *Magn. Reson. Mater. Physics, Biol. Med.* 22, 1–4.
- Ganapathy, V., Thangaraju, M., Gopal, E., Martin, P.M., Itagaki, S., Miyauchi, S., and Prasad, P.D. (2008). Sodium-coupled Monocarboxylate Transporters in Normal Tissues and in Cancer. *AAPS J.* 10, 193.
- Gardner, A., Johansson, A., Wibom, R., Nennesmo, I., von Döbeln, U., Hagenfeldt, L., and Hällström, T. (2003). Alterations of mitochondrial function and correlations with personality traits in selected major depressive disorder patients. *J. Affect. Disord.* 76, 55–68.
- Geoffroy, P.A., Etain, B., Lajnef, M., Zerdazi, E.-H., Brichant-Petitjean, C., Heilbronner, U., Hou, L., Degenhardt, F., Rietschel, M., McMahon, F.J., et al. (2016). Circadian genes and lithium response in bipolar disorders: associations with PPARGC1A (PGC-1 α) and RORA. *Genes, Brain Behav.* 15, 660–668.
- Gerhardt, H., Schuck, J., and Wolburg, H. (1999). Differentiation of a unique macroglial cell type in the pecten oculi of the chicken. *Glia* 28, 201–214.
- Gillis, L., and Kaye, E. (2002). Diagnosis and management of mitochondrial diseases. *Pediatr. Clin. North Am.* 49, 203–219.
- Golpich, M., Amini, E., Mohamed, Z., Azman Ali, R., Mohamed Ibrahim, N., and Ahmadiani, A. (2017). Mitochondrial Dysfunction and Biogenesis in Neurodegenerative diseases: Pathogenesis and Treatment. *CNS Neurosci. Ther.* 23, 5–22.
- Gong, Y., Chai, Y., Ding, J.H., Sun, X.L., and Hu, G. (2011). Chronic mild stress damages mitochondrial ultrastructure and function in mouse brain. *Neurosci. Lett.* 488, 76–80.
- de Graaf, R.A. (2007). *In Vivo NMR Spectroscopy* (Chichester: John Wiley and Sons).
- de Graaf, R.A., Brown, P.B., Mason, G.F., Rothman, D.L., and Behar, K.L. (2003). Detection of [1,6-13C₂]-glucose metabolism in rat brain by in vivo 1H-[13C]-NMR spectroscopy. *Magn. Reson. Med.* 49, 37–46.
- de Graaf, R.A., Patel, A.B., Rothman, D.L., and Behar, K.L. (2006). Acute regulation of steady-state GABA levels following GABA-transaminase inhibition in rat cerebral cortex. *Neurochem. Int.* 48, 508–514.
- de Graaf, R.A., Rothman, D.L., and Behar, K.L. (2011). State of the art direct 13C and indirect 1H-[13C] NMR

spectroscopy in vivo. A practical guide. *NMR Biomed.* 24, 958–972.

Greiner, S., André, F., Heimisch, M., Hess, A., Steen, H., Katus, H.A., and Mereles, D. (2013). Non-invasive quantification of right ventricular systolic function by echocardiography: a new semi-automated approach. *Clin. Res. Cardiol.* 102, 229–235.

Grigoriu-Serbanescu, M., Martinez, M., Nöthen, M.M., Propping, P., Milea, S., Mihailescu, R., and Marinescu, E. (1998). Patterns of parental transmission and familial aggregation models in bipolar affective disorder. *Am. J. Med. Genet.* 81, 397–404.

Gruetter, R., and Tkáč, I. (2000). Field mapping without reference scan using asymmetric echo-planar techniques. *Magn. Reson. Med.* 43, 319–323.

Gruetter, R., Novotny, E.J., Boulware, S.D., Mason, G.F., Rothman, D.L., Shulman, G.I., Prichard, J.W., and Shulman, R.G. (1994). Localized ¹³C NMR spectroscopy in the human brain of amino acid labeling from D-[1-¹³C]glucose. *J. Neurochem.* 63, 1377–1385.

Gruetter, R., Seaquist, E.R., and Ugurbil, K. (2001). A mathematical model of compartmentalized neurotransmitter metabolism in the human brain. *Am. J. Physiol. Metab.* 281, E100–E112.

Gubert, C., Stertz, L., Pfaffenseller, B., Panizzutti, B.S., Rezin, G.T., Massuda, R., Streck, E.L., Gama, C.S., Kapczinski, F., and Kunz, M. (2013). Mitochondrial activity and oxidative stress markers in peripheral blood mononuclear cells of patients with bipolar disorder, schizophrenia, and healthy subjects. *J. Psychiatr. Res.* 47, 1396–1402.

Guffanti, G., Gamaroff, M.J., Warner, V., Talati, A., Glatt, C.E., Wickramaratne, P., and Weissman, M.M. (2016). Heritability of major depressive and comorbid anxiety disorders in multi-generational families at high risk for depression. *Am. J. Med. Genet. Part B Neuropsychiatr. Genet.* 171, 1072–1079.

Guidotti, A., Auta, J., Davis, J.M., Gerevini, V.D., Dwivedi, Y., Grayson, D.R., Impagnatiello, F., Pandey, G., Pesold, C., Sharma, R., et al. (2000). Decrease in Reelin and Glutamic Acid Decarboxylase67 (GAD67) Expression in Schizophrenia and Bipolar Disorder. *Arch. Gen. Psychiatry* 57, 1061.

Gupta, D., Kurhe, Y., and Radhakrishnan, M. (2014). Antidepressant effects of insulin in streptozotocin induced diabetic mice: Modulation of brain serotonin system. *Physiol. Behav.* 129, 73–78.

Guzmán, M., and Blázquez, C. (2001). Is there an astrocyte- neuron ketone body shuttle? *Trends Endocrinol. Metab.* 12, 169–173.

Ha, J.S., Dho, S.H., Youm, T.H., Kwon, K., and Park, S.S. (2014). Astrocytic phospholipase A2 contributes to neuronal glutamate toxicity. *Brain Res.* 1590, 97–106.

Haas, R., Stumpf, D.A., Parks, J.K., and Eguren, L. (1981). Inhibitory effects of sodium valproate on oxidative phosphorylation. *Neurology* 31, 1473–1476.

Haj-Mirzaian, A., Amiri, S., Amini-Khoei, H., Rahimi-Balaei, M., Kordjazy, N., Olson, C.O., Rastegar, M., Naserzadeh, P., Marzban, H., Dehpour, A.R., et al. (2016). Attenuation of oxidative and nitrosative stress in cortical area associates with antidepressant-like effects of tropisetron in male mice following social isolation stress. *Brain Res. Bull.* 124, 150–163.

Halfter, W., Deiss, S., and Schwarz, U. (1985). The formation of the axonal pattern in the embryonic avian retina. *J. Comp. Neurol.* 232, 466–480.

Hamakawa, H., Murashita, J., Yamada, N., Inubushi, T., Kato, N., and Kato, T. (2004). Reduced intracellular pH in the basal ganglia and whole brain measured by ³¹P-MRS in bipolar disorder. *Psychiatry Clin. Neurosci.* 58, 82–88.

Hamburger, V., and Hamilton, H.L. (1992). A series of normal stages in the development of the chick embryo. 1951. *Dev. Dyn.* 195, 231–272.

Hansen, S.H., Andersen, M.L., Birkedal, H., Cornett, C., and Wibrand, F. (2006). The important role of taurine in oxidative metabolism. *Adv. Exp. Med. Biol.* 583, 129–135.

Harper, D.G., Jensen, J.E., Ravichandran, C., Perlis, R.H., Fava, M., Renshaw, P.F., and Iosifescu, D. V (2017). Tissue

- Type-Specific Bioenergetic Abnormalities in Adults with Major Depression. *Neuropsychopharmacology* 42, 876–885.
- Hashimoto, T., Bazmi, H.H., Mirnics, K., Wu, Q., Sampson, A.R., and Lewis, D.A. (2008). Conserved Regional Patterns of GABA-Related Transcript Expression in the Neocortex of Subjects With Schizophrenia. *Am. J. Psychiatry* 165, 479–489.
- Hasler, G., and Northoff, G. (2011). Discovering imaging endophenotypes for major depression. *Mol. Psychiatry* 16, 604–619.
- Hellmann, J., Vannucci, R.C., and Nardis, E.E. (1982). Blood-brain barrier permeability to lactic acid in the newborn dog: lactate as a cerebral metabolic fuel. *Pediatr. Res.* 16, 40–44.
- Hemanth Kumar, B.S., Mishra, S.K., Rana, P., Singh, S., and Khushu, S. (2012). Neurodegenerative evidences during early onset of depression in CMS rats as detected by proton magnetic resonance spectroscopy at 7T. *Behav. Brain Res.* 232, 53–59.
- Henriques-Alves, A.M., and Queiroz, C.M. (2016). Ethological Evaluation of the Effects of Social Defeat Stress in Mice: Beyond the Social Interaction Ratio. *Front. Behav. Neurosci.* 9.
- Henry, P.G., Adriany, G., Deelchand, D., Gruetter, R., Marjanska, M., Öz, G., Seaquist, E.R., Shestov, A., and Uğurbil, K. (2006). In vivo ¹³C NMR spectroscopy and metabolic modeling in the brain: a practical perspective. *Magn. Reson. Imaging* 24, 527–539.
- Homem, C.C.F., Steinmann, V., Burkard, T.R., Jais, A., Esterbauer, H., and Knoblich, J.A. (2014). Ecdysone and mediator change energy metabolism to terminate proliferation in *Drosophila* neural stem cells. *Cell* 158, 874–888.
- Hore, P.J. (1995). *Nuclear Magnetic Resonance* (Oxford: Oxford University Press).
- Hore, P.J., Jones, J.A., and Wimperis, S. (2000). *NMR: the toolkit* (Oxford: Oxford University Press).
- Howarth, C., Gleeson, P., and Attwell, D. (2012). Updated energy budgets for neural computation in the neocortex and cerebellum. *J. Cereb. Blood Flow Metab.* 32, 1222–1232.
- Hroudova, J., and Fisar, Z. (2010). Activities of respiratory chain complexes and citrate synthase influenced by pharmacologically different antidepressants and mood stabilizers. *Neuro Endocrinol. Lett.* 31, 336–342.
- Hroudova, J., Fisar, Z., and Raboch, J. (2013). Mitochondrial Functions in Mood Disorders. In *Mood Disorders*, (InTech), pp. 5–8.
- Hughes, J.T., Jerrome, D., and Krebs, H.A. (1972). Ultrastructure of the avian retina an anatomical study of the retina of the domestic pigeon (*Columba livia*) with particular reference to the distribution of mitochondria. *Exp. Eye Res.* 14.
- Hyde, C.L., Nagle, M.W., Tian, C., Chen, X., Paciga, S., Wendland, J., Tung, J., Hinds, D., Perlis, R., and Winslow, A. (2017). depression in individuals of European descent. *Nat Genet* 48, 1031–1036.
- Hyder, F., Patel, A.B., Gjedde, A., Rothman, D.L., Behar, K.L., and Shulman, R.G. (2006). Neuronal-glial glucose oxidation and glutamatergic-GABAergic function. *J. Cereb. Blood Flow Metab.* 26, 865–877.
- Iacobazzi, V., and Infantino, V. (2014). Citrate – new functions for an old metabolite. *Biol. Chem.* 395.
- Iwamoto, K., Bundo, M., and Kato, T. (2005). Altered expression of mitochondria-related genes in postmortem brains of patients with bipolar disorder or schizophrenia, as revealed by large-scale DNA microarray analysis. *Hum. Mol. Genet.* 14, 241–253.
- Jagannath, A., Butler, R., Godinho, S.I.H., Couch, Y., Brown, L.A., Vasudevan, S.R., Flanagan, K.C., Anthony, D., Churchill, G.C., Wood, M.J.A., et al. (2013). The CRTC1-SIK1 Pathway Regulates Entrainment of the Circadian Clock. *Cell* 154, 1100–1111.
- Jamshidzadeh, A., Heidari, R., Abasvali, M., Zarei, M., Ommati, M.M., Abdoli, N., Khodaei, F., Yeganeh, Y., Jafari, F., Zarei, A., et al. (2017). Taurine treatment preserves brain and liver mitochondrial function in a rat model of

fulminant hepatic failure and hyperammonemia. *Biomed. Pharmacother.* **86**, 514–520.

Jiang, B., Wang, H., Wang, J.-L., Wang, Y.-J., Zhu, Q., Wang, C., Song, L., Gao, T.-T., Wang, Y., Zhu, W.-Z., et al. (2018). Hippocampal Salt-Inducible Kinase 2 Plays a Role in Depression via the CREB-Regulated Transcription Coactivator 1–cAMP Response Element Binding–Brain-Derived Neurotrophic Factor Pathway. *Biol. Psychiatry* **1–17**.

Jornada, L.K., Moretti, M., Valvassori, S.S., Ferreira, C.L., Padilha, P.T., Arent, C.O., Fries, G.R., Kapczinski, F., and Quevedo, J. (2010). Effects of mood stabilizers on hippocampus and amygdala BDNF levels in an animal model of mania induced by ouabain. *J. Psychiatr. Res.* **44**, 506–510.

José da Rocha, A., Túlio Braga, F., Carlos Martins Maia Júnior, A., Jorge da Silva, C., Toyama, C., Pereira Pinto Gama, H., Kok, F., and Rodrigues Gomes, H. (2008). Lactate Detection by MRS in Mitochondrial Encephalopathy: Optimization of Technical Parameters. *J. Neuroimaging* **18**, 1–8.

Kan, C., Silva, N., Golden, S.H., Rajala, U., Timonen, M., Stahl, D., and Ismail, K. (2013). A Systematic Review and Meta-analysis of the Association Between Depression and Insulin Resistance. *Diabetes Care* **36**, 480–489.

Kann, O., Papageorgiou, I.E., and Draguhn, A. (2014). Highly Energized Inhibitory Interneurons are a Central Element for Information Processing in Cortical Networks. *J. Cereb. Blood Flow Metab.* **34**, 1270–1282.

Karabatsiakis, A., Böck, C., Salinas-Manrique, J., Kolassa, S., Calzia, E., Dietrich, D.E., and Kolassa, I.-T. (2014). Mitochondrial respiration in peripheral blood mononuclear cells correlates with depressive subsymptoms and severity of major depression. *Transl. Psychiatry* **4**, e397.

Kasahara, T., Takata, A., Kato, T.M., Kubota-Sakashita, M., Sawada, T., Kakita, A., Mizukami, H., Kaneda, D., Ozawa, K., and Kato, T. (2016). Depression-like episodes in mice harboring mtDNA deletions in paraventricular thalamus. *Mol. Psychiatry* **21**, 39–48.

Kasparová, S., Sumbalová, Z., Horecký, J., Bystrický, P., Mlynárik, V., Gvozdjaková, A., and Liptaj, T. (2005). New magnetic resonance spectroscopy biomarker for monitoring neurodegenerative diseases: animal models. *Biomed. Pap. Med. Fac. Univ. Palacky. Olomouc. Czech. Repub.* **149**, 373–376.

Kass, I., Hoke, D.E., Costa, M.G.S., Reboul, C.F., Porebski, B.T., Cowieson, N.P., Leh, H., Pennacchietti, E., McCoey, J., Kleinfeld, O., et al. (2014). Cofactor-dependent conformational heterogeneity of GAD65 and its role in autoimmunity and neurotransmitter homeostasis. *Proc. Natl. Acad. Sci.* **111**, E2524–E2529.

Kato, T., and Kato, N. (2000). Mitochondrial dysfunction in bipolar disorder. *Bipolar Disord.* **2**, 180–190.

Kato, T., and Takahashi, Y. (1996). Deletion of leukocyte mitochondrial DNA in bipolar disorder. *J. Affect. Disord.* **37**, 67–73.

Kato, T., Shioiri, T., Takahashi, S., and Inubushi, T. (1991). Measurement of brain phosphoinositide metabolism in bipolar patients using in vivo 31P-MRS. *J. Affect. Disord.* **22**, 185–190.

Kato, T., Takahashi, S., Shioiri, T., and Inubushi, T. (1992). Brain phosphorous metabolism in depressive disorders detected by phosphorus-31 magnetic resonance spectroscopy. *J. Affect. Disord.* **26**, 223–230.

Kato, T., Takahashi, S., Shioiri, T., and Inubushi, T. (1993). Alterations in brain phosphorous metabolism in bipolar disorder detected by in vivo 31P and 7Li magnetic resonance spectroscopy. *J. Affect. Disord.* **27**, 53–59.

Kato, T., Shioiri, T., Murashita, J., Hamakawa, H., Takahashi, Y., Inubushi, T., and Takahashi, S. (1995). Lateralized abnormality of high energy phosphate metabolism in the frontal lobes of patients with bipolar disorder detected by phase-encoded 31P-MRS. *Psychol. Med.* **25**, 557–566.

Kato, T., Winokur, G., Coryell, W., Keller, M.B., Endicott, J., and Rice, J. (1996). Parent-of-origin effect in transmission of bipolar disorder. *Am. J. Med. Genet.* **67**, 546–550.

Kato, T., Stine, O.C., McMahon, F.J., and Crowe, R.R. (1997). Increased levels of a mitochondrial DNA deletion in the brain of patients with bipolar disorder. *Biol. Psychiatry* **42**, 871–875.

Kato, T., Murashita, J., Kamiya, A., Shioiri, T., Kato, N., and Inubushi, T. (1998). Decreased brain intracellular pH measured by 31P-MRS in bipolar disorder: a confirmation in drug-free patients and correlation with white matter

- hyperintensity. *Eur. Arch. Psychiatry Clin. Neurosci.* **248**, 301–306.
- Katyare, S.S., and Rajan, R.R. (1988). Enhanced oxidative phosphorylation in rat liver mitochondria following prolonged in vivo treatment with imipramine. *Br. J. Pharmacol.* **95**, 914–922.
- Katyare, S.S., and Rajan, R.R. (1995). Effect of long-term in vivo treatment with imipramine on the oxidative energy metabolism in rat brain mitochondria. *Comp. Biochem. Physiol. C. Pharmacol. Toxicol. Endocrinol.* **112**, 353–357.
- Kemp, G.J., and Brindle, K.M. (2012). What Do Magnetic Resonance-Based Measurements of Pi-ATP Flux Tell Us About Skeletal Muscle Metabolism? *Diabetes* **61**, 1927–1934.
- Kemp, D.E., Schinagle, M., Gao, K., Conroy, C., Ganocy, S.J., Ismail-Beigi, F., and Calabrese, J.R. (2014). PPAR- γ Agonism as a Modulator of Mood: Proof-of-Concept for Pioglitazone in Bipolar Depression. *CNS Drugs* **28**, 571–581.
- Kemp, G.J., Ahmad, R.E., Nicolay, K., and Prompers, J.J. (2015). Quantification of skeletal muscle mitochondrial function by ^{31}P magnetic resonance spectroscopy techniques: a quantitative review. *Acta Physiol.* **213**, 107–144.
- Kern, T.S., and Barber, A.J. (2008). Retinal ganglion cells in diabetes. *J. Physiol.* **586**, 4401–4408.
- Ketter, T.A., Kimbrell, T.A., George, M.S., Dunn, R.T., Speer, A.M., Benson, B.E., Willis, M.W., Danielson, A., Frye, M.A., Herscovitch, P., et al. (2001). Effects of mood and subtype on cerebral glucose metabolism in treatment-resistant bipolar disorder. *Biol. Psychiatry* **49**, 97–109.
- Kiyama, T., Chen, C.-K., Wang, S.W., Pan, P., Ju, Z., Wang, J., Takada, S., Klein, W.H., and Mao, C.-A. (2018). Essential roles of mitochondrial biogenesis regulator Nrf1 in retinal development and homeostasis. *Mol. Neurodegener.* **13**, 56.
- Klein, J. (2000). Membrane breakdown in acute and chronic neurodegeneration: focus on choline-containing phospholipids. *J. Neural Transm.* **107**, 1027–1063.
- Kokavec, J., Min, S.H., Tan, M.H., Gilhotra, J.S., Newland, H.S., Durkin, S.R., Grigg, J., and Casson, R.J. (2016). Biochemical analysis of the living human vitreous. *Clin. Exp. Ophthalmol.* **44**, 597–609.
- Kolko, M., Vosborg, F., Henriksen, U.L., Hasan-Olive, M.M., Diget, E.H., Vohra, R., Gurubaran, I.R.S., Gjedde, A., Mariga, S.T., Skytt, D.M., et al. (2016). Lactate Transport and Receptor Actions in Retina: Potential Roles in Retinal Function and Disease. *Neurochem. Res.* **41**, 1229–1236.
- Konarski, J.Z., McIntyre, R.S., Kennedy, S.H., Rafi-tari, S., Soczynska, J.K., and Ketter, T.A. (2008). Volumetric neuroimaging investigations in mood disorders: Bipolar disorder versus major depressive disorder. *Bipolar Disord.* **10**, 1–37.
- Konradi, C., Eaton, M., MacDonald, M.L., Walsh, J., Benes, F.M., and Heckers, S. (2004). Molecular evidence for mitochondrial dysfunction in bipolar disorder. *Arch. Gen. Psychiatry* **61**, 300–308.
- van der Kooij, M.A., Grosse, J., Zanoletti, O., Papilloud, A., and Sandi, C. (2015). The effects of stress during early postnatal periods on behavior and hippocampal neuroplasticity markers in adult male mice. *Neuroscience* **311**, 508–518.
- Kovács, K.A., Steullet, P., Steinmann, M., Do, K.Q., Magistretti, P.J., Halfon, O., and Cardinaux, J.-R. (2007). TORC1 is a calcium- and cAMP-sensitive coincidence detector involved in hippocampal long-term synaptic plasticity. *Proc. Natl. Acad. Sci. U. S. A.* **104**, 4700–4705.
- Krishnan, V., Han, M.-H., Graham, D.L., Berton, O., Renthal, W., Russo, S.J., LaPlant, Q., Graham, A., Lutter, M., Lagace, D.C., et al. (2007). Molecular Adaptations Underlying Susceptibility and Resistance to Social Defeat in Brain Reward Regions. *Cell* **131**, 391–404.
- Kristián, T., and Siesjö, B.K. (1998). Calcium in ischemic cell death. *Stroke* **29**, 705–718.
- Krystal, J.H., Sanacora, G., Blumberg, H., Anand, A., Charney, D.S., Marek, G., Epperson, C.N., Goddard, A., and Mason, G.F. (2002). Glutamate and GABA systems as targets for novel antidepressant and mood-stabilizing

treatments. *Mol. Psychiatry* 7, S71–S80.

Kubo, H., Nakataki, M., Sumitani, S., Iga, J., Numata, S., Kameoka, N., Watanabe, S., Umehara, H., Kinoshita, M., Inoshita, M., et al. (2017). ¹H-magnetic resonance spectroscopy study of glutamate-related abnormality in bipolar disorder. *J. Affect. Disord.* 208, 139–144.

Kunz, N., Cudalbu, C., Mlynarik, V., Hüppi, P.S., Sizonenko, S. V., and Gruetter, R. (2010). Diffusion-weighted spectroscopy: A novel approach to determine macromolecule resonances in short-echo time ¹H-MRS. *Magn. Reson. Med.* 64, 939–946.

Kuratsune, H., Yamaguti, K., Lindh, G., Evengård, B., Hagberg, G., Matsumura, K., Iwase, M., Onoe, H., Takahashi, M., Machii, T., et al. (2002). Brain regions involved in fatigue sensation: Reduced acetylcarnitine uptake into the brain. *Neuroimage* 17, 1256–1265.

Lai, M., Gruetter, R., and Lanz, B. (2017). Progress towards in vivo brain ¹³C-MRS in mice: Metabolic flux analysis in small tissue volumes. *Anal. Biochem.* 529, 229–244.

Lai, M., Lanz, B., Poitry-Yamate, C., Romero, J.F., Berset, C.M., Cudalbu, C., and Gruetter, R. (2018a). In vivo ¹³C MRS in the mouse brain at 14.1 Tesla and metabolic flux quantification under infusion of [1,6- ¹³C₂]glucose. *J. Cereb. Blood Flow Metab.* 38, 1701–1714.

Lai, M., Lanz, B., Poitry-Yamate, C., Romero, J.F., Berset, C.M., Cudalbu, C., and Gruetter, R. (2018b). In vivo ¹³C MRS in the mouse brain at 14.1 Tesla and metabolic flux quantification under infusion of [1,6-¹³C₂]glucose. *J. Cereb. Blood Flow Metab.* 38, 1701–1714.

Lanz, B., Gruetter, R., and Duarte, J.M.N. (2013). Metabolic Flux and Compartmentation Analysis in the Brain In vivo. *Front. Endocrinol. (Lausanne)*. 4, 1–18.

Lanz, B., Xin, L., Millet, P., and Gruetter, R. (2014a). In vivo quantification of neuro-glial metabolism and glial glutamate concentration using ¹H-[¹³C] MRS at 14.1T. *J. Neurochem.* 128, 125–139.

Lanz, B., Poitry-Yamate, C., and Gruetter, R. (2014b). Image-Derived Input Function from the Vena Cava for ¹⁸F-FDG PET Studies in Rats and Mice. *J. Nucl. Med.* 55, 1380–1388.

Larrabee, M.G. (1982). [¹⁴C]Glucose metabolism in sympathetic ganglia of chicken embryos and in primary cultures of neurons and of other cells from these ganglia. *J. Neurochem.* 38, 215–232.

Larrabee, M.G. (1983). Lactate Uptake and Release in the Presence of Glucose by Sympathetic Ganglia of Chicken Embryos and by Neuronal and Nonneuronal Cultures Prepared from These Ganglia. *J. Neurochem.* 40, 1237–1250.

Larrabee, M.G. (1992). Extracellular intermediates of glucose metabolism: fluxes of endogenous lactate and alanine through extracellular pools in embryonic sympathetic ganglia. *J. Neurochem.* 59, 1041–1052.

Larrieu, T., and Sandi, C. (2018). Stress-Induced Depression: Is Social Rank a Predictive Risk Factor? *BioEssays* 40, 1–10.

Larrieu, T., Cherix, A., Duque, A., Rodrigues, J., Lei, H., Gruetter, R., and Sandi, C. (2017). Hierarchical Status Predicts Behavioral Vulnerability and Nucleus Accumbens Metabolic Profile Following Chronic Social Defeat Stress. *Curr. Biol.* 27, 2202–2210.e4.

Lau, T., Bigio, B., Zelli, D., McEwen, B.S., and Nasca, C. (2017). Stress-induced structural plasticity of medial amygdala stellate neurons and rapid prevention by a candidate antidepressant. *Mol. Psychiatry* 22, 227–234.

Layec, G., Bringard, A., Le Fur, Y., Vilmen, C., Micallef, J., Perrey, S., Cozzone, P.J., and Bendahan, D. (2010). Comparative determination of energy production rates and mitochondrial function using different ³¹P MRS quantitative methods in sedentary and trained subjects. *NMR Biomed.* n/a-n/a.

Lei, H., Xin, L., Gruetter, R., and Mlynárik, V. (2014). Localized Single-Voxel Magnetic Resonance Spectroscopy, Water Suppression, and Novel Approaches for Ultrashort Echo-Time Measurements. In *Magnetic Resonance Spectroscopy*, (Elsevier), pp. 15–30.

Lener, M.S., Kadriu, B., and Zarate, C.A. (2017). Ketamine and Beyond: Investigations into the Potential of

Glutamatergic Agents to Treat Depression. *Drugs* 77, 381–401.

Lenzenweger, M.F. (2013). Endophenotype, Intermediate Phenotype, Biomarker: Definitions, Concept Comparisons, Clarifications. *Depress. Anxiety* 30, 185–189.

Leong, S.F., Lai, J.C., Lim, L., and Clark, J.B. (1981). Energy-metabolizing enzymes in brain regions of adult and aging rats. *J. Neurochem.* 37, 1548–1556.

Levin, M., Thorlin, T., Robinson, K.R., Nogi, T., and Mercola, M. (2002). Asymmetries in H⁺/K⁺-ATPase and Cell Membrane Potentials Comprise a Very Early Step in Left-Right Patterning. *Cell* 111, 77–89.

Li, S., Huang, M., Wang, X., Wang, X., Chen, F., Lei, H., and Jiang, F. (2011). Retinal Metabolic Changes in an Experimental Model of Optic Nerve Transection by Ex Vivo 1H Magnetic Resonance Spectroscopy. *Neurochem. Res.* 36, 2427–2433.

Li, X., Frye, M.A., and Shelton, R.C. (2012a). Review of Pharmacological Treatment in Mood Disorders and Future Directions for Drug Development. *Neuropsychopharmacology* 37, 77–101.

Li, Y., Couch, L., Higuchi, M., Fang, J.-L., and Guo, L. (2012b). Mitochondrial Dysfunction Induced by Sertraline, an Antidepressant Agent. *Toxicol. Sci.* 127, 582–591.

Lima, T.I., Valentim, R.R., Araújo, H.N., Oliveira, A.G., Favero, B.C., Menezes, E.S., Araújo, R., and Silveira, L.R. (2018). Role of NCoR1 in mitochondrial function and energy metabolism. *Cell Biol. Int.* 42, 734–741.

Lin, D.D.M., Crawford, T.O., and Barker, P.B. (2003). Proton MR spectroscopy in the diagnostic evaluation of suspected mitochondrial disease. *AJNR. Am. J. Neuroradiol.* 24, 33–41.

Lin, K.W., Wroolie, T.E., Robakis, T., and Rasgon, N.L. (2015). Adjuvant pioglitazone for unremitted depression: Clinical correlates of treatment response. *Psychiatry Res.* 230, 846–852.

Lindner, T., Klose, R., Streckenbach, F., Stahnke, T., Hadlich, S., Kühn, J.-P., Guthoff, R.F., Wree, A., Neumann, A.-M., Frank, M., et al. (2017). Morphologic and biometric evaluation of chick embryo eyes in ovo using 7 Tesla MRI. *Sci. Rep.* 7, 2647.

Liu, W., Ge, T., Leng, Y., Pan, Z., Fan, J., Yang, W., and Cui, R. (2017). The Role of Neural Plasticity in Depression: From Hippocampus to Prefrontal Cortex. *Neural Plast.* 2017, 1–11.

Liu, Y., Ho, R.C.-M., and Mak, A. (2012). Interleukin (IL)-6, tumour necrosis factor alpha (TNF- α) and soluble interleukin-2 receptors (sIL-2R) are elevated in patients with major depressive disorder: a meta-analysis and meta-regression. *J. Affect. Disord.* 139, 230–239.

Lizarbe, B., Cherix, A., and Gruetter, R. (2018a). In vivo heteronuclear magnetic resonance spectroscopy. *Methods Mol. Biol.* 1718, 169–187.

Lizarbe, B., Cherix, A., Duarte, J.M.N., Cardinaux, J.-R., and Gruetter, R. (2018b). High-fat diet consumption alters energy metabolism in the mouse hypothalamus. *Int. J. Obes.*

Lizarbe, B., Lei, H., Duarte, J.M.N., Lanz, B., Cherix, A., and Gruetter, R. (2018c). Feasibility of in vivo measurement of glucose metabolism in the mouse hypothalamus by 1H-[13C] MRS at 14.1T. *Magn. Reson. Med.* 80, 874–884.

Lodi, R., Taylor, D.J., Tabrizi, S.J., Kumar, S., Sweeney, M., Wood, N.W., Styles, P., Radda, G.K., and Schapira, A.H. V. (1997). In vivo skeletal muscle mitochondrial function in Leber's hereditary optic neuropathy assessed by 31P magnetic resonance spectroscopy. *Ann. Neurol.* 42, 573–579.

Lu, M., Chen, W., and Zhu, X.-H. (2014). Field dependence study of in vivo brain (31) P MRS up to 16.4 T. *NMR Biomed.* 27, 1135–1141.

Lu, M., Zhu, X.H., and Chen, W. (2016a). In vivo 31P MRS assessment of intracellular NAD metabolites and NAD⁺/NADH redox state in human brain at 4 T. *NMR Biomed.* 29, 1010–1017.

Lu, Y., Day, F.R., Gustafsson, S., Buchkovich, M.L., Na, J., Bataille, V., Cousminer, D.L., Dastani, Z., Drong, A.W., Esko, T., et al. (2016b). New loci for body fat percentage reveal link between adiposity and cardiometabolic disease risk. *Nat. Commun.* 7, 10495.

- Lucca, G., Comim, C.M., Valvassori, S.S., Réus, G.Z., Vuolo, F., Petronilho, F., Gavioli, E.C., Dal-Pizzol, F., and Quevedo, J. (2009). Increased oxidative stress in submitochondrial particles into the brain of rats submitted to the chronic mild stress paradigm. *J. Psychiatr. Res.* *43*, 864–869.
- Luykx, J.J., Laban, K.G., van den Heuvel, M.P., Boks, M.P.M., Mandl, R.C.W., Kahn, R.S., and Bakker, S.C. (2012). Region and state specific glutamate downregulation in major depressive disorder: A meta-analysis of 1H-MRS findings. *Neurosci. Biobehav. Rev.* *36*, 198–205.
- Lyra e Silva, N. de M., Lam, M.P., Soares, C.N., Munoz, D.P., Milev, R., and De Felice, F.G. (2019). Insulin Resistance as a Shared Pathogenic Mechanism Between Depression and Type 2 Diabetes. *Front. Psychiatry* *10*.
- MacDonald, M.L., Naydenov, A., Chu, M., Matzilevich, D., and Konradi, C. (2006). Decrease in creatine kinase messenger RNA expression in the hippocampus and dorsolateral prefrontal cortex in bipolar disorder. *Bipolar Disord.* *8*, 255–264.
- Mächler, P., Wyss, M.T., Elsayed, M., Stobart, J., Gutierrez, R., von Faber-Castell, A., Kaelin, V., Zuend, M., San Martín, A., Romero-Gómez, I., et al. (2016). In Vivo Evidence for a Lactate Gradient from Astrocytes to Neurons. *Cell Metab.* *23*, 94–102.
- Madsen, P.L., Cruz, N.F., Sokoloff, L., and Dienel, G.A. (1999). Cerebral oxygen/glucose ratio is low during sensory stimulation and rises above normal during recovery: excess glucose consumption during stimulation is not accounted for by lactate efflux from or accumulation in brain tissue. *J. Cereb. Blood Flow Metab.* *19*, 393–400.
- Maes, M. (2011). Depression is an inflammatory disease, but cell-mediated immune activation is the key component of depression. *Prog. Neuro-Psychopharmacology Biol. Psychiatry* *35*, 664–675.
- Magistretti, P.J., and Pellerin, L. (1999). Astrocytes Couple Synaptic Activity to Glucose Utilization in the Brain. *News Physiol. Sci.* *14*, 177–182.
- Mahar, I., Bambico, F.R., Mechawar, N., and Nobrega, J.N. (2014). Stress, serotonin, and hippocampal neurogenesis in relation to depression and antidepressant effects. *Neurosci. Biobehav. Rev.* *38*, 173–192.
- Manganas, L.N., Zhang, X., Li, Y., Hazel, R.D., Smith, S.D., Wagshul, M.E., Henn, F., Benveniste, H., Djuric, P.M., Enikolopov, G., et al. (2007). Magnetic resonance spectroscopy identifies neural progenitor cells in the live human brain. *Science* *318*, 980–985.
- Manor, D., Rothman, D.L., Mason, G.F., Hyder, F., Petroff, O.A.C., and Behar, K.L. (1996). The rate of turnover of cortical GABA from [1-13C]glucose is reduced in rats treated with the GABA-transaminase inhibitor vigabatrin (γ -vinyl GABA). *Neurochem. Res.* *21*, 1031–1041.
- Marazziti, D., Rutigliano, G., Baroni, S., Landi, P., and Dell’Osso, L. (2014). Metabolic syndrome and major depression. *CNS Spectr.* *19*, 293–304.
- Markham, A., Cameron, I., Franklin, P., and Spedding, M. (2004). BDNF increases rat brain mitochondrial respiratory coupling at complex I, but not complex II. *Eur. J. Neurosci.* *20*, 1189–1196.
- Markham, A., Cameron, I., Bains, R., Franklin, P., Kiss, J.P., Schwendimann, L., Gressens, P., and Spedding, M. (2012). Brain-derived neurotrophic factor-mediated effects on mitochondrial respiratory coupling and neuroprotection share the same molecular signalling pathways. *Eur. J. Neurosci.* *35*, 366–374.
- Markham, A., Bains, R., Franklin, P., and Spedding, M. (2014). Changes in mitochondrial function are pivotal in neurodegenerative and psychiatric disorders: How important is BDNF? *Br. J. Pharmacol.* *171*, 2206–2229.
- Marmarou, A., Signoretti, S., Fatouros, P., Aygok, G.A., and Bullock, R. (2005). Mitochondrial injury measured by proton magnetic resonance spectroscopy in severe head trauma patients. *Acta Neurochir. Suppl.* *95*, 149–151.
- Martin, D.L., and Rimvall, K. (1993). Regulation of gamma-Aminobutyric Acid Synthesis in the Brain. *J. Neurochem.* *60*, 395–407.
- Martin, P.M., Dun, Y., Mysona, B., Ananth, S., Roon, P., Smith, S.B., and Ganapathy, V. (2007). Expression of the Sodium-Coupled Monocarboxylate Transporters SMCT1 (SLC5A8) and SMCT2 (SLC5A12) in Retina. *Investig. Ophthalmology Vis. Sci.* *48*, 3356.

References

- Martin, S.A., Souder, D.C., Miller, K.N., Clark, J.P., Sagar, A.K., Eliceiri, K.W., Puglielli, L., Beasley, T.M., and Anderson, R.M. (2018). GSK3 β Regulates Brain Energy Metabolism. *Cell Rep.* 23, 1922–1931.e4.
- Mason, S. (2017). Lactate Shuttles in Neuroenergetics-Homeostasis, Allostasis and Beyond. *Front. Neurosci.* 11, 43.
- Mason, G.F., Behar, K.L., Rothman, D.L., and Shulman, R.G. (1992). NMR determination of intracerebral glucose concentration and transport kinetics in rat brain. *J. Cereb. Blood Flow Metab.* 12, 448–455.
- Mason, G.F., Gruetter, R., Rothman, D.L., Behar, K.L., Shulman, R.G., and Novotny, E.J. (1995). Simultaneous determination of the rates of the TCA cycle, glucose utilization, alpha-ketoglutarate/glutamate exchange, and glutamine synthesis in human brain by NMR. *J. Cereb. Blood Flow Metab.* 15, 12–25.
- Mathers, C., Fat, D.M., Boerma, J.T., and Organization, W.H. (2008). The global burden of disease : 2004 update (Geneva).
- Mattson, M.P., Gleichmann, M., and Cheng, A. (2008). Mitochondria in Neuroplasticity and Neurological Disorders. *Neuron* 60, 748–766.
- Maurer, I.C., Schippel, P., and Volz, H.-P. (2009). Lithium-induced enhancement of mitochondrial oxidative phosphorylation in human brain tissue. *Bipolar Disord.* 11, 515–522.
- Mayberg, H.S., Liotti, M., Brannan, S.K., McGinnis, S., Mahurin, R.K., Jerabek, P.A., Silva, J.A., Tekell, J.L., Martin, C.C., Lancaster, J.L., et al. (1999). Reciprocal limbic-cortical function and negative mood: converging PET findings in depression and normal sadness. *Am. J. Psychiatry* 156, 675–682.
- McEwen, B.S. (1998). Stress, adaptation, and disease. Allostasis and allostatic load. *Ann. N. Y. Acad. Sci.* 840, 33–44.
- McEwen, B.S. (1999). Stress and Hippocampal Plasticity. *Annu. Rev. Neurosci.* 22, 105–122.
- McEwen, B.S. (2006). Protective and damaging effects of stress mediators: central role of the brain. *Dialogues Clin. Neurosci.* 8, 367–381.
- McEwen, B.S. (2008). Central effects of stress hormones in health and disease: Understanding the protective and damaging effects of stress and stress mediators. *Eur. J. Pharmacol.* 583, 174–185.
- McEwen, B.S., Bowles, N.P., Gray, J.D., Hill, M.N., Hunter, R.G., Karatsoreos, I.N., and Nasca, C. (2015). Mechanisms of stress in the brain. *Nat. Neurosci.* 18, 1353–1363.
- McIlwain, H. (1970). Metabolic adaptation in the brain. *Nature* 226, 803–806.
- McKenna, M.C., Waagepetersen, H.S., Schousboe, A., and Sonnewald, U. (2006). Neuronal and astrocytic shuttle mechanisms for cytosolic-mitochondrial transfer of reducing equivalents: Current evidence and pharmacological tools. *Biochem. Pharmacol.* 71, 399–407.
- McMahon, F.J., Stine, O.C., Meyers, D.A., Simpson, S.G., and DePaulo, J.R. (1995). Patterns of maternal transmission in bipolar affective disorder. *Am. J. Hum. Genet.* 56, 1277–1286.
- Mehta, A., Prabhakar, M., Kumar, P., Deshmukh, R., and Sharma, P.L. (2013). Excitotoxicity: Bridge to various triggers in neurodegenerative disorders. *Eur. J. Pharmacol.* 698, 6–18.
- Menke, A. (2018). Precision pharmacotherapy: psychiatry’s future direction in preventing, diagnosing, and treating mental disorders. *Pharmgenomics. Pers. Med. Volume* 11, 211–222.
- Mertens, J., Wang, Q., Kim, Y., Yu, D.X., Pham, S., Yang, B., Zheng, Y., Diffenderfer, K.E., Zhang, J., Soltani, S., et al. (2015). Differential responses to lithium in hyperexcitable neurons from patients with bipolar disorder. *Nature* 527, 95–99.
- Meylan, E.M., Halfon, O., Magistretti, P.J., and Cardinaux, J.-R. (2016a). The HDAC inhibitor SAHA improves depressive-like behavior of CRTC1-deficient mice: Possible relevance for treatment-resistant depression. *Neuropharmacology* 107, 111–121.
- Meylan, E.M., Breuillaud, L., Seredenina, T., Magistretti, P.J., Halfon, O., Luthi-Carter, R., and Cardinaux, J.

- (2016b). Involvement of the agmatinerig system in the depressive-like phenotype of the *Crtc1* knockout mouse model of depression. *Transl. Psychiatry* 6, e852–e852.
- Michael, L.F., Wu, Z., Cheatham, R.B., Puigserver, P., Adelmant, G., Lehman, J.J., Kelly, D.P., and Spiegelman, B.M. (2001). Restoration of insulin-sensitive glucose transporter (GLUT4) gene expression in muscle cells by the transcriptional coactivator PGC-1. *Proc. Natl. Acad. Sci.* 98, 3820–3825.
- Miller, M.M., Morrison, J.H., and McEwen, B.S. (2012). Basal anxiety-like behavior predicts differences in dendritic morphology in the medial prefrontal cortex in two strains of rats. *Behav. Brain Res.* 229, 280–288.
- Mlynárik, V., Gambarota, G., Frenkel, H., and Gruetter, R. (2006). Localized short-echo-time proton MR spectroscopy with full signal-intensity acquisition. *Magn. Reson. Med.* 56, 965–970.
- Mlynárik, V., Cudalbu, C., Xin, L., and Gruetter, R. (2008). ¹H NMR spectroscopy of rat brain in vivo at 14.1 Tesla: Improvements in quantification of the neurochemical profile. *J. Magn. Reson.* 194, 163–168.
- Mlynárik, V., Cacquevel, M., Sun-Reimer, L., Janssens, S., Cudalbu, C., Lei, H., Schneider, B.L., Aebischer, P., and Gruetter, R. (2012). Proton and phosphorus magnetic resonance spectroscopy of a mouse model of Alzheimer's disease. *J. Alzheimer's Dis.* 31, 87–99.
- Moore, C.M., Christensen, J.D., Lafer, B., Fava, M., and Renshaw, P.F. (1997). Lower levels of nucleoside triphosphate in the basal ganglia of depressed subjects: a phosphorous-31 magnetic resonance spectroscopy study. *Am. J. Psychiatry* 154, 116–118.
- Morash, S.C., Cook, H.W., and Spence, M.W. (1988). Phosphatidylcholine metabolism in cultured cells: catabolism via glycerophosphocholine. *Biochim. Biophys. Acta* 961, 194–202.
- Moreno-Sánchez, R., Marín-Hernández, A., Gallardo-Pérez, J.C., Quezada, H., Encalada, R., Rodríguez-Enríquez, S., and Saavedra, E. (2011). Phosphofructokinase type 1 kinetics, isoform expression and gene polymorphisms in cancer cells. *J. Cell. Biochem.* 1703, n/a-n/a.
- Morgan, J.E. (2004). Circulation and axonal transport in the optic nerve. *Eye* 18, 1089–1095.
- Morris, P., and Bachelard, H. (2003). Reflections on the application of ¹³C-MRS to research on brain metabolism. *NMR Biomed.* 16, 303–312.
- Mueller, P.L., Pritchett, C.E., Wiechman, T.N., Zharikov, A., and Hajnal, A. (2018). Antidepressant-like effects of insulin and IGF-1 are mediated by IGF-1 receptors in the brain. *Brain Res. Bull.* 143, 27–35.
- Murrough, J.W., Mao, X., Collins, K.A., Kelly, C., Andrade, G., Nestadt, P., Levine, S.M., Mathew, S.J., and Shungu, D.C. (2010). Increased ventricular lactate in chronic fatigue syndrome measured by ¹H MRS imaging at 3.0 T. II: comparison with major depressive disorder. *NMR Biomed.* 23, 643–650.
- Nabuurs, C.I.H.C., Klomp, D.W.J., Veltien, A., Kan, H.E., and Heerschap, A. (2008). Localized sensitivity enhanced in vivo ¹³C MRS to detect glucose metabolism in the mouse brain. *Magn. Reson. Med.* 59, 626–630.
- Nakazawa, T., Tachi, S., Aikawa, E., and Ihnuma, M. (1993). Formation of the myelinated nerve fiber layer in the chicken retina. *Glia* 8, 114–121.
- Narbaiz, R., Bastani, B., Galvin, N.J., Kapal, V.K., and Levine, D.Z. (1995). Ultrastructural and immunocytochemical evidence for the presence of polarised plasma membrane H(+)-ATPase in two specialised cell types in the chick embryo chorioallantoic membrane. *J. Anat.* 186 (Pt 2, 245–252.
- Nasca, C., Bigio, B., Zelli, D., Nicoletti, F., and McEwen, B.S. (2015). Mind the gap: glucocorticoids modulate hippocampal glutamate tone underlying individual differences in stress susceptibility. *Mol. Psychiatry* 20, 755–763.
- Nasca, C., Watson, K., Bigio, B., Robakis, T., Myoraku, A., Wroolie, T., McEwen, B.S., and Rasgon, N. (2019). Childhood trauma and insulin resistance in patients suffering from depressive disorders. *Exp. Neurol.* 315, 15–20.
- Naydenov, A. V, MacDonald, M.L., Ongur, D., and Konradi, C. (2007). Differences in lymphocyte electron transport gene expression levels between subjects with bipolar disorder and normal controls in response to glucose

deprivation stress. *Arch. Gen. Psychiatry* **64**, 555–564.

Nedergaard, M., Ransom, B., and Goldman, S.A. (2003). New roles for astrocytes: Redefining the functional architecture of the brain. *Trends Neurosci.* **26**, 523–530.

Nehlig, A., and Pereira de Vasconcelos, A. (1993). Glucose and ketone body utilization by the brain of neonatal rats. *Prog. Neurobiol.* **40**, 163–221.

Ngumah, Q.C., Buchthal, S.D., and Dacheux, R.F. (2006). Longitudinal non-invasive proton NMR spectroscopy measurement of vitreous lactate in a rabbit model of ocular hypertension. *Exp. Eye Res.* **83**, 390–400.

Ni, S., Huang, H., He, D., Chen, H., Wang, C., Zhao, X., Chen, X., Cui, W., Zhou, W., and Zhang, J. (2019). Adeno-associated virus-mediated over-expression of CREB-regulated transcription coactivator 1 in the hippocampal dentate gyrus ameliorates lipopolysaccharide-induced depression-like behaviour in mice. *J. Neurochem.* 1–15.

Nierenberg, A.A., Kansky, C., Brennan, B.P., Shelton, R.C., Perlis, R., and Iosifescu, D. V (2013). Mitochondrial modulators for bipolar disorder: a pathophysiologically informed paradigm for new drug development. *Aust. N. Z. J. Psychiatry* **47**, 26–42.

Nitsch, R.M., Blusztajn, J.K., Pittas, A.G., Slack, B.E., Growdon, J.H., and Wurtman, R.J. (1992). Evidence for a membrane defect in Alzheimer disease brain. *Proc. Natl. Acad. Sci. U. S. A.* **89**, 1671–1675.

Nonaka, M., Kim, R., Fukushima, H., Sasaki, K., Suzuki, K., Okamura, M., Ishii, Y., Kawashima, T., Kamijo, S., Takemoto-Kimura, S., et al. (2014). Region-Specific Activation of CRTC1-CREB Signaling Mediates Long-Term Fear Memory. *Neuron* **84**, 92–106.

Novak, I., Kirkin, V., McEwan, D.G., Zhang, J., Wild, P., Rozenknop, A., Rogov, V., Löhr, F., Popovic, D., Occhipinti, A., et al. (2010). Nix is a selective autophagy receptor for mitochondrial clearance. *EMBO Rep.* **11**, 45–51.

Öngür, D., Prescott, A.P., Jensen, J.E., Cohen, B.M., and Renshaw, P.F. (2009). Creatine abnormalities in schizophrenia and bipolar disorder. *Psychiatry Res. Neuroimaging* **172**, 44–48.

Oquendo, M.A., Ellis, S.P., Chesin, M.S., Birmaher, B., Zelazny, J., Tin, A., Melhem, N., Burke, A.K., Kolko, D., Greenhill, L., et al. (2013). Familial transmission of parental mood disorders: unipolar and bipolar disorders in offspring. *Bipolar Disord.* **15**, 764–773.

Ottersen, O.P., Zhang, N., and Walberg, F. (1992). Metabolic compartmentation of glutamate and glutamine: morphological evidence obtained by quantitative immunocytochemistry in rat cerebellum. *Neuroscience* **46**, 519–534.

Owen, O.E., Morgan, A.P., Kemp, H.G., Sullivan, J.M., Herrera, M.G., and Cahill, G.F. (1967). Brain metabolism during fasting. *J. Clin. Invest.* **46**, 1589–1595.

Oz, G., Alger, J.R., Barker, P.B., Bartha, R., Bizzi, A., Boesch, C., Bolan, P.J., Brindle, K.M., Cudalbu, C., Dinçer, A., et al. (2014). Clinical proton MR spectroscopy in central nervous system disorders. *Radiology* **270**, 658–679.

Panchal, S.K., Poudyal, H., Ward, L.C., Waanders, J., and Brown, L. (2015). Modulation of tissue fatty acids by l-carnitine attenuates metabolic syndrome in diet-induced obese rats. *Food Funct.* **6**, 2496–2506.

Parducci, F., Micali, A., La Fauci, M.A., and Puzzolo, D. (1987). [Comparative embryogenesis of the pecten oculi in chickens and pigeons]. *Arch. Ital. Anat. Embriol.* **92**, 145–158.

Park, J., Min, J.-S., Kim, B., Chae, U.-B., Yun, J.W., Choi, M.-S., Kong, I.-K., Chang, K.-T., and Lee, D.-S. (2015). Mitochondrial ROS govern the LPS-induced pro-inflammatory response in microglia cells by regulating MAPK and NF-κB pathways. *Neurosci. Lett.* **584**, 191–196.

Park, J.M., Josan, S., Grafendorfer, T., Yen, Y., Hurd, R.E., Spielman, D.M., and Mayer, D. (2013). Measuring mitochondrial metabolism in rat brain in vivo using MR Spectroscopy of hyperpolarized [2- ¹³C]pyruvate. *NMR Biomed.* **26**, 1197–1203.

Parra-Damas, A., Chen, M., Enriquez-Barreto, L., Ortega, L., Acosta, S., Perna, J.C., Fullana, M.N., Aguilera, J., Rodríguez-Alvarez, J., and Saura, C.A. (2017). CRTC1 Function During Memory Encoding Is Disrupted in Neurodegeneration. *Biol. Psychiatry* **81**, 111–123.

References

- Patel, T.B., and Clark, J.B. (1979). Synthesis of N-acetyl-L-aspartate by rat brain mitochondria and its involvement in mitochondrial/cytosolic carbon transport. *Biochem. J.* **184**, 539–546.
- Patel, A.B., de Graaf, R.A., Mason, G.F., Kanamatsu, T., Rothman, D.L., Shulman, R.G., and Behar, K.L. (2004). Glutamatergic Neurotransmission and Neuronal Glucose Oxidation are Coupled during Intense Neuronal Activation. *J. Cereb. Blood Flow Metab.* **24**, 972–985.
- Patel, A.B., de Graaf, R.A., Mason, G.F., Rothman, D.L., Shulman, R.G., and Behar, K.L. (2005). The contribution of GABA to glutamate/glutamine cycling and energy metabolism in the rat cortex in vivo. *Proc. Natl. Acad. Sci.* **102**, 5588–5593.
- Patel, A.J., Balázs, R., and Richter, D. (1970). Contribution of the GABA bypath to glucose oxidation, and the development of compartmentation in the brain. *Nature* **226**, 1160–1161.
- Pellerin, L., and Magistretti, P.J. (1994). Glutamate uptake into astrocytes stimulates aerobic glycolysis: a mechanism coupling neuronal activity to glucose utilization. *Proc. Natl. Acad. Sci. U. S. A.* **91**, 10625–10629.
- Pelvig, D.P., Pakkenberg, H., Stark, A.K., and Pakkenberg, B. (2008). Neocortical glial cell numbers in human brains. *Neurobiol. Aging* **29**, 1754–1762.
- Peng, Q., Zhang, Y., Nateras, O.S.E., van Osch, M.J.P., and Duong, T.Q. (2011). MRI of blood flow of the human retina. *Magn. Reson. Med.* **65**, 1768–1775.
- Pennington, K., Beasley, C.L., Dicker, P., Fagan, A., English, J., Pariante, C.M., Wait, R., Dunn, M.J., and Cotter, D.R. (2008). Prominent synaptic and metabolic abnormalities revealed by proteomic analysis of the dorsolateral prefrontal cortex in schizophrenia and bipolar disorder. *Mol. Psychiatry* **13**, 1102–1117.
- Petroff, O.A.C. (2002). GABA and glutamate in the human brain. *Neuroscientist* **8**, 562–573.
- Pettegrew, J.W., Withers, G., Panchalingam, K., and Post, J.F. (1988). Considerations for brain pH assessment by 31P NMR. *Magn. Reson. Imaging* **6**, 135–142.
- Pettegrew, J.W., Klunk, W.E., Panchalingam, K., Kanfer, J.N., and McClure, R.J. (1995). Clinical and neurochemical effects of acetyl-L-carnitine in Alzheimer's disease. *Neurobiol. Aging* **16**, 1–4.
- Pettegrew, J.W., Levine, J., and McClure, R.J. (2000). Acetyl-L-carnitine physical-chemical, metabolic and therapeutic properties: relevance for its mode of action in Alzheimer's disease and geriatric depression. *Mol. Psychiatry* **5**, 616–632.
- Pettegrew, J.W., Levine, J., Gershon, S., Stanley, J.A., Servan-Schreiber, D., Panchalingam, K., and McClure, R.J. (2002). 31P-MRS study of acetyl-L-carnitine treatment in geriatric depression: preliminary results. *Bipolar Disord.* **4**, 61–66.
- Pfeuffer, J., Tkác, I., Choi, I.Y., Merkle, H., Ugurbil, K., Garwood, M., and Gruetter, R. (1999). Localized in vivo ¹H NMR detection of neurotransmitter labeling in rat brain during infusion of [1-¹³C] D-glucose. *Magn. Reson. Med.* **41**, 1077–1083.
- Picard, M., McManus, M.J., Gray, J.D., Nasca, C., Moffat, C., Kopinski, P.K., Seifert, E.L., McEwen, B.S., and Wallace, D.C. (2015). Mitochondrial functions modulate neuroendocrine, metabolic, inflammatory, and transcriptional responses to acute psychological stress. *Proc. Natl. Acad. Sci.* **112**, E6614–E6623.
- Picard, M., McEwen, B.S., Epel, E.S., and Sandi, C. (2018). An energetic view of stress: Focus on mitochondria. *Front. Neuroendocrinol.* **49**, 72–85.
- Pinal, C.S., and Tobin, A.J. (1998). Uniqueness and redundancy in GABA production. *Perspect. Dev. Neurobiol.* **5**, 109–118.
- Pogson, C., and Randle, P. (1966). The control of rat-heart phosphofructokinase by citrate and other regulators. *Biochem. J.* **100**, 683–693.
- Poitry-Yamate, C.L., Poitry, S., and Tsacopoulos, M. (1995). Lactate released by Müller glial cells is metabolized by photoreceptors from mammalian retina. *J. Neurosci.* **15**, 5179–5191.

- Ponchaut, S., van Hoof, F., and Veitch, K. (1992). In vitro effects of valproate and valproate metabolites on mitochondrial oxidations. Relevance of CoA sequestration to the observed inhibitions. *Biochem. Pharmacol.* **43**, 2435–2442.
- Provencher, S.W. (2001). Automatic quantitation of localized in vivo ¹H spectra with LCModel. *NMR Biomed.* **14**, 260–264.
- Pulvirenti, G., Valerio, C., Spadaro, F., D’Agata, V., Freni, V., Nardo, L., and Drago, F. (1990). Acetylcarnitine reduces the immobility of rats in a despair test (constrained swim). *Behav. Neural Biol.* **54**, 110–114.
- Purdon, A.D., and Rapoport, S.I. (1998). Energy requirements for two aspects of phospholipid metabolism in mammalian brain. *Biochem. J.* **335** (Pt 2, 313–318.
- Qiu, S., Li, L., Weeber, E.J., and May, J.M. (2007). Ascorbate transport by primary cultured neurons and its role in neuronal function and protection against excitotoxicity. *J. Neurosci. Res.* **85**, 1046–1056.
- Quteineh, L., Preisig, M., Rivera, M., Milaneschi, Y., Castelao, E., Gholam-Rezaee, M., Vandenberghe, F., Saigi-Morgui, N., Delacrétaz, A., Cardinaux, J., et al. (2016). Association of CRT1 polymorphisms with obesity markers in subjects from the general population with lifetime depression. *J. Affect. Disord.* **198**, 43–49.
- Rager, G. (1976). Morphogenesis and physiogenesis of the retino-tectal connection in the chicken. I. The retinal ganglion cells and their axons. *Proc. R. Soc. London. Ser. B, Biol. Sci.* **192**, 331–352.
- Rahnert, J.A., Zheng, B., Hudson, M.B., Woodworth-Hobbs, M.E., and Price, S.R. (2016). Glucocorticoids Alter CRT1-CREB Signaling in Muscle Cells: Impact on PGC-1 α Expression and Atrophy Markers. *PLoS One* **11**, e0159181.
- Raison, C.L., and Miller, A.H. (2011). Is Depression an Inflammatory Disorder? *Curr. Psychiatry Rep.* **13**, 467–475.
- Rasgon, N.L., and McEwen, B.S. (2016). Insulin resistance—a missing link no more. *Mol. Psychiatry* **21**, 1648–1652.
- Regenold, W.T., Phatak, P., Marano, C.M., Sassan, A., Conley, R.R., and Kling, M.A. (2009). Elevated cerebrospinal fluid lactate concentrations in patients with bipolar disorder and schizophrenia: implications for the mitochondrial dysfunction hypothesis. *Biol. Psychiatry* **65**, 489–494.
- Regenold, W.T., Pratt, M., Nekkalapu, S., Shapiro, P.S., Kristian, T., and Fiskum, G. (2012). Mitochondrial detachment of hexokinase 1 in mood and psychotic disorders: implications for brain energy metabolism and neurotrophic signaling. *J. Psychiatr. Res.* **46**, 95–104.
- Ren, J., Sherry, A.D., and Malloy, C.R. (2015). (31)P-MRS of healthy human brain: ATP synthesis, metabolite concentrations, pH, and T1 relaxation times. *NMR Biomed.* **28**, 1455–1462.
- Rezin, G.T., Cardoso, M.R., Gonçalves, C.L., Scaini, G., Fraga, D.B., Riegel, R.E., Comim, C.M., Quevedo, J., and Streck, E.L. (2008). Inhibition of mitochondrial respiratory chain in brain of rats subjected to an experimental model of depression. *Neurochem. Int.* **53**, 395–400.
- Rezin, G.T., Furlanetto, C.B., Scaini, G., Valvassori, S.S., Gonçalves, C.L., Ferreira, G.K., Jeremias, I.C., Resende, W.R., Cardoso, M.R., Varela, R.B., et al. (2014). Fenproporex increases locomotor activity and alters energy metabolism, and mood stabilizers reverse these changes: a proposal for a new animal model of mania. *Mol. Neurobiol.* **49**, 877–892.
- Rodrigues, T., Krawczyk, M., Skowronska-Krawczyk, D., Matter-Sadzinski, L., and Matter, J.-M. (2016). Delayed neurogenesis with respect to eye growth shapes the pigeon retina for high visual acuity. *Development* **143**, 4701–4712.
- Rolfe, D.F., and Brown, G.C. (1997). Cellular energy utilization and molecular origin of standard metabolic rate in mammals. *Physiol. Rev.* **77**, 731–758.
- Rossetti, C., Sciarra, D., Petit, J., Eap, C.B., Halfon, O., Magistretti, P.J., Boutrel, B., and Cardinaux, J. (2017). Gender-specific alteration of energy balance and circadian locomotor activity in the Crt1 knockout mouse model of depression. *Transl. Psychiatry* **7**, 1269.

- Rothman, D.L., Behar, K.L., Hetherington, H.P., den Hollander, J.A., Bendall, M.R., Petroff, O.A., and Shulman, R.G. (1985). ¹H-Observe/¹³C-decouple spectroscopic measurements of lactate and glutamate in the rat brain in vivo. *Proc. Natl. Acad. Sci.* *82*, 1633–1637.
- Rothman, D.L., Novotny, E.J., Shulman, G.I., Howseman, A.M., Petroff, O.A., Mason, G., Nixon, T., Hanstock, C.C., Prichard, J.W., and Shulman, R.G. (1992). ¹H-[¹³C] NMR measurements of [4-¹³C]glutamate turnover in human brain. *Proc. Natl. Acad. Sci. U. S. A.* *89*, 9603–9606.
- Roy, C.S., and Sherrington, C.S. (1890). On the Regulation of the Blood-supply of the Brain. *J. Physiol.* *11*, 85–158.17.
- Rozovsky, I., Laping, N.J., Krohn, K., Teter, B., O’Callaghan, J.P., and Finch, C.E. (1995). Transcriptional regulation of glial fibrillary acidic protein by corticosterone in rat astrocytes in vitro is influenced by the duration of time in culture and by astrocyte-neuron interactions. *Endocrinology* *136*, 2066–2073.
- Ryan, K.M., Patterson, I., and McLoughlin, D.M. (2018). Peroxisome proliferator-activated receptor gamma co-activator-1 alpha in depression and the response to electroconvulsive therapy. *Psychol. Med.* 1–10.
- Sabunciyar, S., Kirches, E., Krause, G., Bogerts, B., Mawrin, C., Llenos, I.C., and Weis, S. (2007). Quantification of total mitochondrial DNA and mitochondrial common deletion in the frontal cortex of patients with schizophrenia and bipolar disorder. *J. Neural Transm.* *114*, 665–674.
- Sanacora, G., Treccani, G., and Popoli, M. (2012). Towards a glutamate hypothesis of depression: An emerging frontier of neuropsychopharmacology for mood disorders. *Neuropharmacology* *62*, 63–77.
- Sandi, C. (2008). Understanding the neurobiological basis of behavior: a good way to go. *Front. Neurosci.* *2*, 129–130.
- Sandi, C., and Richter-Levin, G. (2009). From high anxiety trait to depression: a neurocognitive hypothesis. *Trends Neurosci.* *32*, 312–320.
- Sapolsky, R.M. (1986). Glucocorticoid toxicity in the hippocampus: reversal by supplementation with brain fuels. *J. Neurosci.* *6*, 2240–2244.
- Saura, C.A., and Cardinaux, J. (2017). Emerging Roles of CREB-Regulated Transcription Coactivators in Brain Physiology and Pathology. *Trends Neurosci.* *40*, 720–733.
- Scaini, G., Santos, P.M., Benedet, J., Rochi, N., Gomes, L.M., Borges, L.S., Rezin, G.T., Pezente, D.P., Quevedo, J., and Streck, E.L. (2010). Evaluation of Krebs cycle enzymes in the brain of rats after chronic administration of antidepressants. *Brain Res. Bull.* *82*, 224–227.
- Schoenfeld, T.J., McCausland, H.C., Morris, H.D., Padmanaban, V., and Cameron, H.A. (2017). Stress and Loss of Adult Neurogenesis Differentially Reduce Hippocampal Volume. *Biol. Psychiatry* *82*, 914–923.
- Schrödinger, E. (1951). *Was ist Leben?: Die lebende Zelle mit den Augen des Physikers betrachtet* (University of Cornell: Lehnem).
- Schuck, J., Gerhardt, H., and Wolburg, H. (2000). The peripapillary glia of the optic nerve head in the chicken retina. *Anat. Rec.* *259*, 263–275.
- Sekeres, M.J., Mercaldo, V., Richards, B., Sargin, D., Mahadevan, V., Woodin, M.A., Frankland, P.W., and Josselyn, S.A. (2012). Increasing CR1 Function in the Dentate Gyrus during Memory Formation or Reactivation Increases Memory Strength without Compromising Memory Quality. *J. Neurosci.* *32*, 17857–17868.
- Selak, I., Skaper, S.D., and Varon, S. (1985). Pyruvate participation in the low molecular weight trophic activity for central nervous system neurons in glia-conditioned media. *J. Neurosci.* *5*, 23–28.
- Sepanjnia, K., Modabbernia, A., Ashrafi, M., Modabbernia, M.-J., and Akhondzadeh, S. (2012). Pioglitazone Adjunctive Therapy for Moderate-to-Severe Major Depressive Disorder: Randomized Double-Blind Placebo-Controlled Trial. *Neuropsychopharmacology* *37*, 2093–2100.
- Seyer, P., Vallois, D., Poitry-Yamate, C., Schütz, F., Metref, S., Tarussio, D., Maechler, P., Staels, B., Lanz, B., Grueter, R., et al. (2013). Hepatic glucose sensing is required to preserve β cell glucose competence. *J. Clin. Invest.*

123, 1662–1676.

Shalbuyeva, N., Brustovetsky, T., and Brustovetsky, N. (2007). Lithium desensitizes brain mitochondria to calcium, antagonizes permeability transition, and diminishes cytochrome C release. *J. Biol. Chem.* 282, 18057–18068.

Shannon, B.J., Vaishnavi, S.N., Vlassenko, A.G., Shimony, J.S., Rutlin, J., and Raichle, M.E. (2016). Brain aerobic glycolysis and motor adaptation learning. *Proc. Natl. Acad. Sci.* 113, E3782–E3791.

Shao, Y., Yan, G., Xuan, Y., Peng, H., Huang, Q.-J., Wu, R., and Xu, H. (2015). Chronic social isolation decreases glutamate and glutamine levels and induces oxidative stress in the rat hippocampus. *Behav. Brain Res.* 282, 201–208.

Sheikh, S., Martin, S., and Martin, D. (1999). Regional distribution and relative amounts of glutamate decarboxylase isoforms in rat and mouse brain. *Neurochem. Int.* 35, 73–80.

Shi, X., Kondo, D.G., Sung, Y., Hellem, T.L., Fiedler, K.K., Jeong, E., Huber, R.S., and Renshaw, P.F. (2012). Frontal lobe bioenergetic metabolism in depressed adolescents with bipolar disorder: a phosphorus-31 magnetic resonance spectroscopy study. *Bipolar Disord.* 14, 607–617.

Shimizu, E., Hashimoto, K., Okamura, N., Koike, K., Komatsu, N., Kumakiri, C., Nakazato, M., Watanabe, H., Shinoda, N., Okada, S., et al. (2003). Alterations of serum levels of brain-derived neurotrophic factor (BDNF) in depressed patients with or without antidepressants. *Biol. Psychiatry* 54, 70–75.

Sibille, E., Arango, V., Galfalvy, H.C., Pavlidis, P., Erraji-Benchekroun, L., Ellis, S.P., and John Mann, J. (2004). Gene Expression Profiling of Depression and Suicide in Human Prefrontal Cortex. *Neuropsychopharmacology* 29, 351–361.

Sibson, N.R., Dhankhar, A., Mason, G.F., Rothman, D.L., Behar, K.L., and Shulman, R.G. (1998). Stoichiometric coupling of brain glucose metabolism and glutamatergic neuronal activity. *Proc. Natl. Acad. Sci.* 95, 316–321.

Siciliano, G., Tessa, A., Petrini, S., Mancuso, M., Bruno, C., Grieco, G.S., Malandrini, A., DeFlorio, L., Martini, B., Federico, A., et al. (2003). Autosomal dominant external ophthalmoplegia and bipolar affective disorder associated with a mutation in the ANT1 gene. *Neuromuscul. Disord.* 13, 162–165.

Sigitova, E., Fišar, Z., Hroudová, J., Cikánková, T., and Raboch, J. (2017). Biological hypotheses and biomarkers of bipolar disorder. *Psychiatry Clin. Neurosci.* 71, 77–103.

Silva, M.F., Ruiter, J.P., Illst, L., Jakobs, C., Duran, M., de Almeida, I.T., and Wanders, R.J. (1997). Valproate inhibits the mitochondrial pyruvate-driven oxidative phosphorylation in vitro. *J. Inherit. Metab. Dis.* 20, 397–400.

Singh, N., Halliday, A.C., Thomas, J.M., Kuznetsova, O. V., Baldwin, R., Woon, E.C.Y., Aley, P.K., Antoniadou, I., Sharp, T., Vasudevan, S.R., et al. (2013). A safe lithium mimetic for bipolar disorder. *Nat. Commun.* 4, 1332.

Skowronska-Krawczyk, D., Chiodini, F., Ebeling, M., Alliod, C., Kundzewicz, A., Castro, D., Ballivet, M., Guillemot, F., Matter-Sadzinski, L., and Matter, J.-M. (2009). Conserved regulatory sequences in Atoh7 mediate non-conserved regulatory responses in retina ontogenesis. *Development* 136, 3767–3777.

Smeland, O.B., Meisingset, T.W., Borges, K., and Sonnewald, U. (2012). Chronic acetyl-L-carnitine alters brain energy metabolism and increases noradrenaline and serotonin content in healthy mice. *Neurochem. Int.* 61, 100–107.

De Smet, M.D., Gad Elkareem, A.M., and Zwinderman, A.H. (2013). The vitreous, the retinal interface in ocular health and disease. *Ophthalmologica* 230, 165–178.

Smith, E. V., Gragoudas, E.S., Kolodny, N.H., and D'Amico, D.J. (1990). Magnetic resonance imaging: An emerging technique for the diagnosis of ocular disorders. *Int. Ophthalmol.* 14, 119–124.

Soeiro-de-Souza, M.G., Otaduy, M.C.G., Machado-Vieira, R., Moreno, R.A., Nery, F.G., Leite, C., and Lafer, B. (2018). Lithium-associated anterior cingulate neurometabolic profile in euthymic Bipolar I disorder: A 1H-MRS study. *J. Affect. Disord.* 241, 192–199.

Sokoloff, L. (1981). Localization of functional activity in the central nervous system by measurement of glucose utilization with radioactive deoxyglucose. *J. Cereb. Blood Flow Metab.* 1, 7–36.

- Sonnay, S., Duarte, J.M., Just, N., and Gruetter, R. (2016a). Compartmentalised energy metabolism supporting glutamatergic neurotransmission in response to increased activity in the rat cerebral cortex: A ¹³C MRS study in vivo at 14.1 T. *J. Cereb. Blood Flow Metab.* **36**, 928–940.
- Sonnay, S., Duarte, J.M., Just, N., and Gruetter, R. (2016b). Compartmentalised energy metabolism supporting glutamatergic neurotransmission in response to increased activity in the rat cerebral cortex: A ¹³C MRS study in vivo at 14.1 T. *J. Cereb. Blood Flow Metab.* **36**, 928–940.
- Sonnay, S., Gruetter, R., and Duarte, J.M.N. (2017). How Energy Metabolism Supports Cerebral Function: Insights from ¹³C Magnetic Resonance Studies In vivo. *Front. Neurosci.* **11**, 1–20.
- Sonnay, S., Poirot, J., Just, N., Clerc, A.-C., Gruetter, R., Rainer, G., and Duarte, J.M.N. (2018). Astrocytic and neuronal oxidative metabolism are coupled to the rate of glutamate-glutamine cycle in the tree shrew visual cortex. *Glia* **66**, 477–491.
- Sonnewald, U. (2014). Glutamate synthesis has to be matched by its degradation - where do all the carbons go? *J. Neurochem.* **131**, 399–406.
- Sorrells, S.F., and Sapolsky, R.M. (2007). An inflammatory review of glucocorticoid actions in the CNS. *Brain. Behav. Immun.* **21**, 259–272.
- Sorrells, S.F., Caso, J.R., Munhoz, C.D., and Sapolsky, R.M. (2009). The stressed CNS: when glucocorticoids aggravate inflammation. *Neuron* **64**, 33–39.
- Souza, M.E., Polizello, A.C., Uyemura, S.A., Castro-Silva, O., and Curti, C. (1994). Effect of fluoxetine on rat liver mitochondria. *Biochem. Pharmacol.* **48**, 535–541.
- Stefan, D., Cesare, F. Di, Andrasescu, A., Popa, E., Lazarev, A., Vescovo, E., Strbak, O., Williams, S., Starcuk, Z., Cabanas, M., et al. (2009). Quantitation of magnetic resonance spectroscopy signals: the jMRUI software package. *Meas. Sci. Technol.* **20**, 104035.
- Steiner, J., Brisch, R., Schiltz, K., Dobrowolny, H., Mawrin, C., Krzyżanowska, M., Bernstein, H.G., Jankowski, Z., Braun, K., Schmitt, A., et al. (2016). GABAergic system impairment in the hippocampus and superior temporal gyrus of patients with paranoid schizophrenia: A post-mortem study. *Schizophr. Res.* **177**, 10–17.
- Steptoe, A., Hamer, M., and Chida, Y. (2007). The effects of acute psychological stress on circulating inflammatory factors in humans: a review and meta-analysis. *Brain. Behav. Immun.* **21**, 901–912.
- Stork, C., and Renshaw, P.F. (2005). Mitochondrial dysfunction in bipolar disorder: evidence from magnetic resonance spectroscopy research. *Mol. Psychiatry* **10**, 900–919.
- Streck, E.L., Amboni, G., Scaini, G., Di-Pietro, P.B., Rezin, G.T., Valvassori, S.S., Luz, G., Kapczinski, F., and Quevedo, J. (2008). Brain creatine kinase activity in an animal model of mania. *Life Sci.* **82**, 424–429.
- Sullivan, P.F., Neale, M.C., and Kendler, K.S. (2000). Genetic Epidemiology of Major Depression: Review and Meta-Analysis. *Am. J. Psychiatry* **157**, 1552–1562.
- Sultan Kadir, A., Georg Seland, J., Skauge, A., and Skauge, T. (2014). Nanoparticles for enhanced oil recovery: Influence of pH on aluminum-cross-linked partially hydrolyzed polyacrylamide-investigation by rheology and NMR. *Energy and Fuels* **28**, 2343–2351.
- Sun, X., Wang, J.-F., Tseng, M., and Young, L.T. (2006). Downregulation in components of the mitochondrial electron transport chain in the postmortem frontal cortex of subjects with bipolar disorder. *J. Psychiatry Neurosci.* **31**, 189–196.
- Suomalainen, A., Majander, A., Haltia, M., Somer, H., Lönnqvist, J., Savontaus, M.L., and Peltonen, L. (1992). Multiple deletions of mitochondrial DNA in several tissues of a patient with severe retarded depression and familial progressive external ophthalmoplegia. *J. Clin. Invest.* **90**, 61–66.
- Sutendra, G., Kinnaird, A., Dromparis, P., Paulin, R., Stenson, T.H., Haromy, A., Hashimoto, K., Zhang, N., Flaim, E., and Michelakis, E.D. (2014). A nuclear pyruvate dehydrogenase complex is important for the generation of acetyl-CoA and histone acetylation. *Cell* **158**, 84–97.

- Suzuki, A., Stern, S.A., Bozdagi, O., Huntley, G.W., Walker, R.H., Magistretti, P.J., and Alberini, C.M. (2011). Astrocyte-Neuron Lactate Transport Is Required for Long-Term Memory Formation. *Cell* **144**, 810–823.
- Takahashi, S., Oki, J., Miyamoto, A., and Okuno, A. (1999). Proton magnetic resonance spectroscopy to study the metabolic changes in the brain of a patient with Leigh syndrome. *Brain Dev.* **21**, 200–204.
- Tannüs, A., and Garwood, M. (1996). Improved performance of frequency-swept pulses using offset-independent adiabaticity. *J. Magn. Reson. - Ser. A* **120**, 133–137.
- Tao, C., and Zhang, X. (2014). Development of astrocytes in the vertebrate eye. *Dev. Dyn.* **243**, 1501–1510.
- Tatapudy, S., Aloisio, F., Barber, D., and Nystul, T. (2017). Cell fate decisions: emerging roles for metabolic signals and cell morphology. *EMBO Rep.* **18**, 2105–2118.
- Taylor, J.S., Vigneron, D.B., Murphy-Boesch, J., Nelson, S.J., Kessler, H.B., Coia, L., Curran, W., and Brown, T.R. (1991). Free magnesium levels in normal human brain and brain tumors: ³¹P chemical-shift imaging measurements at 1.5 T. *Proc. Natl. Acad. Sci. U. S. A.* **88**, 6810–6814.
- Terpstra, M., and Gruetter, R. (2004). ¹H NMR detection of vitamin C in human brain in vivo. *Magn. Reson. Med.* **51**, 225–229.
- Tiwari, V., Ambadipudi, S., and Patel, A.B. (2013). Glutamatergic and GABAergic TCA Cycle and Neurotransmitter Cycling Fluxes in Different Regions of Mouse Brain. *J. Cereb. Blood Flow Metab.* **33**, 1523–1531.
- Tkac, I., Henry, P., Zacharoff, L., Wedel, M., Gong, W., Deelchand, D.K., Li, T., and Dubinsky, J.M. (2012). Homeostatic Adaptations in Brain Energy Metabolism in Mouse Models of Huntington Disease. *J. Cereb. Blood Flow Metab.* **32**, 1977–1988.
- Tobe, E.H. (2013). Mitochondrial dysfunction, oxidative stress, and major depressive disorder. *Neuropsychiatr. Dis. Treat.* **9**, 567–573.
- Tochigi, M., Iwamoto, K., Bundo, M., Sasaki, T., Kato, N., and Kato, T. (2008). Gene expression profiling of major depression and suicide in the prefrontal cortex of postmortem brains. *Neurosci. Res.* **60**, 184–191.
- Toker, L., and Agam, G. (2014). Lithium, inositol and mitochondria. *ACS Chem. Neurosci.* **5**, 411–412.
- Toker, L., Bersudsky, Y., Plaschkes, I., Chalifa-Caspi, V., Berry, G.T., Buccafusca, R., Moechars, D., Belmaker, R.H., and Agam, G. (2014). Inositol-Related Gene Knockouts Mimic Lithium's Effect on Mitochondrial Function. *Neuropsychopharmacology* **39**, 319–328.
- Tsacopoulos, M., Evequoz-Mercier, V., Perrottet, P., and Buchner, E. (1988). Honeybee retinal glial cells transform glucose and supply the neurons with metabolic substrate. *Proc. Natl. Acad. Sci.* **85**, 8727–8731.
- Tymoczko, J.L., Berg, J.M., and Stryer, L. (2013). *Biochemistry: a short course* (New York, NY).
- Uchida, S., and Shumyatsky, G.P. (2018). Synaptically Localized Transcriptional Regulators in Memory Formation. *Neuroscience* **370**, 4–13.
- Uchida, T., Furukawa, T., Iwata, S., Yanagawa, Y., and Fukuda, A. (2014). Selective loss of parvalbumin-positive GABAergic interneurons in the cerebral cortex of maternally stressed Gad1-heterozygous mouse offspring. *Transl. Psychiatry* **4**, e371–e371.
- Ueno, H., Suemitsu, S., Murakami, S., Kitamura, N., Wani, K., Okamoto, M., Matsumoto, Y., and Ishihara, T. (2017). Region-specific impairments in parvalbumin interneurons in social isolation-reared mice. *Neuroscience* **359**, 196–208.
- Valvassori, S.S., Rezin, G.T., Ferreira, C.L., Moretti, M., Gonçalves, C.L., Cardoso, M.R., Streck, E.L., Kapczinski, F., and Quevedo, J. (2010). Effects of mood stabilizers on mitochondrial respiratory chain activity in brain of rats treated with d-amphetamine. *J. Psychiatr. Res.* **44**, 903–909.
- Vannucci, S.J., Koehler-Stec, E.M., Li, K., Reynolds, T.H., Clark, R., and Simpson, I.A. (1998). GLUT4 glucose transporter expression in rodent brain: Effect of diabetes. *Brain Res.* **797**, 1–11.
- Vaynman, S., Ying, Z., Wu, A., and Gomez-Pinilla, F. (2006). Coupling energy metabolism with a mechanism to

- support brain-derived neurotrophic factor-mediated synaptic plasticity. *Neuroscience* 139, 1221–1234.
- Veeraiah, P., Noronha, J.M., Maitra, S., Bagga, P., Khandelwal, N., Chakravarty, S., Kumar, A., and Patel, A.B. (2014). Dysfunctional Glutamatergic and γ -Aminobutyric Acidergic Activities in Prefrontal Cortex of Mice in Social Defeat Model of Depression. *Biol. Psychiatry* 76, 231–238.
- Videbech, P. (2000). PET measurements of brain glucose metabolism and blood flow in major depressive disorder: A critical review. *Acta Psychiatr. Scand.* 101, 11–20.
- Virmani, M.A., Biselli, R., Spadoni, A., Rossi, S., Corsico, N., Calvani, M., Fattorossi, A., De Simone, C., and Arrigoni-Martelli, E. (1995). Protective actions of L-carnitine and acetyl-L-carnitine on the neurotoxicity evoked by mitochondrial uncoupling or inhibitors. *Pharmacol. Res.* 32, 383–389.
- Volterra, A., and Meldolesi, J. (2005). Astrocytes, from brain glue to communication elements: the revolution continues. *Nat. Rev. Neurosci.* 6, 626–640.
- Wallace, D.L., Han, M.-H., Graham, D.L., Green, T.A., Vialou, V., Iñiguez, S.D., Cao, J.-L., Kirk, A., Chakravarty, S., Kumar, A., et al. (2009). CREB regulation of nucleus accumbens excitability mediates social isolation-induced behavioral deficits. *Nat. Neurosci.* 12, 200–209.
- Wallimann, T., Tokarska-Schlattner, M., and Schlattner, U. (2011). The creatine kinase system and pleiotropic effects of creatine. *Amino Acids* 40, 1271–1296.
- Walls, A.B., Waagepetersen, H.S., Bak, L.K., Schousboe, A., and Sonnewald, U. (2015). The Glutamine–Glutamate/GABA Cycle: Function, Regional Differences in Glutamate and GABA Production and Effects of Interference with GABA Metabolism. *Neurochem. Res.* 40, 402–409.
- Walsh, R.N., and Cummins, R.A. (1976). The Open-Field Test: a critical review. *Psychol. Bull.* 83, 482–504.
- Wang, F., Zhu, J., Zhu, H., Zhang, Q., Lin, Z., and Hu, H. (2011). Bidirectional control of social hierarchy by synaptic efficacy in medial prefrontal cortex. *Science* 334, 693–697.
- Wang, Q., Fan, W., Cai, Y., Wu, Q., Mo, L., and Huang, Z. (2016). Protective effects of taurine in traumatic brain injury via mitochondria and cerebral blood flow. *Amino Acids* 48, 2169–2177.
- Wang, S.-M., Han, C., Lee, S.-J., Patkar, A.A., Masand, P.S., and Pae, C.-U. (2014). A review of current evidence for acetyl-L-carnitine in the treatment of depression. *J. Psychiatr. Res.* 53, 30–37.
- Wang, W., Lu, Y., Xue, Z., Li, C., Wang, C., Zhao, X., Zhang, J., Wei, X., Chen, X., Cui, W., et al. (2015). Rapid-acting antidepressant-like effects of acetyl-L-carnitine mediated by PI3K/AKT/BDNF/VGF signaling pathway in mice. *Neuroscience* 285, 281–291.
- Ward, J., Strawbridge, R.J., Bailey, M.E.S., Graham, N., Ferguson, A., Lyall, D.M., Cullen, B., Pidgeon, L.M., Cavanagh, J., Mackay, D.F., et al. (2017). Genome-wide analysis in UK Biobank identifies four loci associated with mood instability and genetic correlation with major depressive disorder, anxiety disorder and schizophrenia. *Transl. Psychiatry* 7.
- Ward Platt, M., and Deshpande, S. (2005). Metabolic adaptation at birth. *Semin. Fetal Neonatal Med.* 10, 341–350.
- Wasserman, M.J., Corson, T.W., Sibony, D., Cooke, R.G., Parikh, S. V, Pennefather, P.S., Li, P.P., and Warsh, J.J. (2004). Chronic Lithium Treatment Attenuates Intracellular Calcium Mobilization. *Neuropsychopharmacology* 29, 759–769.
- Watson, K., Nasca, C., Aasly, L., McEwen, B., and Rasgon, N. (2018). Insulin resistance, an unmasked culprit in depressive disorders: Promises for interventions. *Neuropharmacology* 136, 327–334.
- Weber, B., and Barros, L.F. (2015). The Astrocyte: Powerhouse and Recycling Center. *Cold Spring Harb. Perspect. Biol.* a020396.
- Weinbach, E.C., Costa, J.L., Nelson, B.D., Claggett, C.E., Hundal, T., Bradley, D., and Morris, S.J. (1986). Effects of tricyclic antidepressant drugs on energy-linked reactions in mitochondria. *Biochem. Pharmacol.* 35, 1445–1451.

- Wermter, F.C., Mitschke, N., Bock, C., and Dreher, W. (2017). Temperature dependence of ¹H NMR chemical shifts and its influence on estimated metabolite concentrations. *Magn. Reson. Mater. Physics, Biol. Med.* *30*, 579–590.
- Williams, S.R., Proctor, E., Allen, K., Gadian, D.G., and Crookard, H.A. (1988). Quantitative estimation of lactate in the brain by ¹H NMR. *Magn. Reson. Med.* *7*, 425–431.
- Wong-Riley, M.T.T. (2010). Energy metabolism of the visual system. *Eye Brain* *2*, 99–116.
- Woo, T.U.W., Walsh, J.P., and Benes, F.M. (2004). Density of glutamic acid decarboxylase 67 messenger RNA-containing neurons that express the N-methyl-D-aspartate receptor subunit NR2A in the anterior cingulate cortex in schizophrenia and bipolar disorder. *Arch. Gen. Psychiatry* *61*, 649–657.
- Xia, Z., Lundgren, B., Bergstrand, A., DePierre, J.W., and Nässberger, L. (1999). Changes in the generation of reactive oxygen species and in mitochondrial membrane potential during apoptosis induced by the antidepressants imipramine, clomipramine, and citalopram and the effects on these changes by Bcl-2 and Bcl-X(L). *Biochem. Pharmacol.* *57*, 1199–1208.
- Xin, L., Lanz, B., Frenkel, H., and Gruetter, R. (2009). BISEP-based, Ultra-short TE ¹H-[¹³C] NMR Spectroscopy of the Rat Brain at 14.1 T.
- Xin, L., Mlynárik, V., Lanz, B., Frenkel, H., and Gruetter, R. (2010). ¹H-[¹³C] NMR spectroscopy of the rat brain during infusion of [2-¹³C] acetate at 14.1 T. *Magn. Reson. Med.* *64*, 334–340.
- Xin, L., Lanz, B., Lei, H., and Gruetter, R. (2015). Assessment of metabolic fluxes in the mouse brain in vivo using ¹H-[¹³C] NMR spectroscopy at 14.1 Tesla. *J. Cereb. Blood Flow Metab.* *35*, 759–765.
- Xu, S., Yang, J., and Shen, J. (2007). In vivo ¹³C saturation transfer effect of the lactate dehydrogenase reaction. *Magn. Reson. Med.* *57*, 258–264.
- Xue, Z.-C., Wang, C., Wang, Q.-W., and Zhang, J.-F. (2015). CREB-regulated transcription coactivator 1: important roles in neurodegenerative disorders. *Sheng Li Xue Bao* *67*, 155–162.
- Yadgary, L., Cahaner, A., Kedar, O., and Uni, Z. (2010). Yolk sac nutrient composition and fat uptake in late-term embryos in eggs from young and old broiler breeder hens. *Poult. Sci.* *89*, 2441–2452.
- Yamawaki, S., Kagaya, A., Tawara, Y., and Inagaki, M. (1998). Intracellular calcium signaling systems in the pathophysiology of affective disorders. *Life Sci.* *62*, 1665–1670.
- Yang, J., Li, C.Q., and Shen, J. (2005). In vivo detection of cortical GABA turnover from intravenously infused [1-¹³C]D-glucose. *Magn. Reson. Med.* *53*, 1258–1267.
- Yang, Y., Zhang, Y., Liu, X., Zuo, J., Wang, K., Liu, W., and Ge, J. (2013). Exogenous taurine attenuates mitochondrial oxidative stress and endoplasmic reticulum stress in rat cardiomyocytes. *Acta Biochim. Biophys. Sin. (Shanghai)* *45*, 359–367.
- Yildiz-Yesiloglu, A., and Ankerst, D.P. (2006). Review of ¹H magnetic resonance spectroscopy findings in major depressive disorder: A meta-analysis. *Psychiatry Res. - Neuroimaging* *147*, 1–25.
- Yu-Wai-Man, P., Griffiths, P.G., and Chinnery, P.F. (2011). Mitochondrial optic neuropathies - Disease mechanisms and therapeutic strategies. *Prog. Retin. Eye Res.* *30*, 81–114.
- Zacharoff, L., Tkac, I., Song, Q., Tang, C., Bolan, P.J., Mangia, S., Henry, P., Li, T., and Dubinsky, J.M. (2012). Cortical Metabolites as Biomarkers in the R6/2 Model of Huntington's Disease. *J. Cereb. Blood Flow Metab.* *32*, 502–514.
- Zarate, C.A., Singh, J.B., Carlson, P.J., Brutsche, N.E., Ameli, R., Luckenbaugh, D.A., Charney, D.S., and Manji, H.K. (2006). A randomized trial of an N-methyl-D-aspartate antagonist in treatment-resistant major depression. *Arch. Gen. Psychiatry* *63*, 856–864.
- Zeevalk, G.D., and Nicklas, W.J. (2000). Lactate prevents the alterations in tissue amino acids, decline in ATP, and cell damage due to aglycemia in retina. *J. Neurochem.* *75*, 1027–1034.
- Zhao, Q., Wu, X., Yan, S., Xie, X., Fan, Y., Zhang, J., Peng, C., and You, Z. (2016). The antidepressant-like effects of

pioglitazone in a chronic mild stress mouse model are associated with PPAR γ -mediated alteration of microglial activation phenotypes. *J. Neuroinflammation* **13**, 259.

Zielke, H.R., Zielke, C.L., and Baab, P.J. (2009). Direct measurement of oxidative metabolism in the living brain by microdialysis: a review. *J. Neurochem.* **109 Suppl**, 24–29.

Zubenko, G.S., Hughes, H.B., Hitchens, T.K., and Cohen, B.M. (2014). Alterations of brain anatomy in mouse model of MDD created by replacement of homologous mouse DNA sequence with an illness-associated 6-base human CREB1 promoter sequence. *Am. J. Med. Genet. Part B Neuropsychiatr. Genet.* **165**, 1–8.

Zwingmann, C., Richter-Landsberg, C., Brand, A., and Leibfritz, D. (2000). NMR spectroscopic study on the metabolic fate of [3-(13)C]alanine in astrocytes, neurons, and cocultures: implications for glia-neuron interactions in neurotransmitter metabolism. *Glia* **32**, 286–303.

van Zyl, P.J., Dimatelis, J.J., and Russell, V.A. (2016). Behavioural and biochemical changes in maternally separated Sprague-Dawley rats exposed to restraint stress. *Metab. Brain Dis.* **31**, 121–133.

Curriculum Vitae

Antoine Cherix

EPFL SB IPHYS LIFMET, CH F1 632 (Bâtiment CH), Station 6, CH-1015 Lausanne.

antoine.cherix@epfl.ch

Office: +41 21 69 30577 Mobile: +41 79 746 4452

LinkedIn: www.linkedin.com/in/antoine-cherix-5519978b

ORCID: <https://orcid.org/0000-0002-4168-8273>

Education

*Currently, since
11.2014*

PhD Student at the Doctoral School in Neuroscience of the Ecole Polytechnique Fédérale de Lausanne (EPFL), in the Laboratory for Functional and Metabolic Imaging (LIFMET) under supervision of Prof. Rolf Gruetter (defense date: February 2019).

2011-2014

MSc. Biochemistry, University of Geneva, Section of Biochemistry, Geneva, Switzerland.

2008-2011

BSc. Biochemistry, University of Geneva, Section of Biochemistry, Geneva, Switzerland.

2005-2008

High-School of Burier, Option biology-chemistry, Burier, Switzerland.

Employment

*Currently, since
11.2014*

Teaching Assistant at the Department of Physics of the Ecole Polytechnique Fédérale de Lausanne (EPFL), under responsibility of Prof. Rolf Gruetter.

Teaching experience

2014-2017

Teaching assistant at the Ecole Polytechnique Fédérale de Lausanne (EPFL)

- General Physics I for Biologists (210 hours, french).
- General Physics I for Life Scientists (95 hours, french).
- General Physics I for Engineers (190 hours, german).

2010-2013

Substitute teacher at the Secondary School of Bex, Switzerland (200 hours).

- German, Sciences, French, Mathematics, Music

Since 2010

Group instructor at the Civil Defense of State of Vaud, Switzerland.

Active scientific societies memberships

- Society for Neuroscience (SFN), Student Member 2018 ID 210726908
- International Society for Magnetic Resonance in Medicine (ISMRM), Trainee Member 2018 ID 79681
- International Society for Neurochemistry (ISN), ID 22635

Award and distinctions

- LIMNA (Lausanne Integrative Metabolism and Nutrition Alliance) 2018, Travel Award stipend to attend SFN annual meeting in San Diego (USA)
- ICBEM Valdivia 2018, Student presentation Award
- ICBEM Valdivia 2018, Travel Award
- ISMRM 25th Annual Meeting & Exhibition, 2017; Educational Stipend
- ISMRM « Magna Cum Laude » Merit Award 2017
- ISMRM 24th Annual Meeting & Exhibition, 2016; Educational Stipend

Research skills

- Spectroscopy: ^1H - and ^{13}C -MRS on animals at 14.1 Tesla and spectra quantification
- Animal behavioural experimentation and surgery: FST, TST, OF, vein cannulation, intracardiac perfusion
- Molecular biology: immunohistology, PCR - genotyping/gene expression analysis
- Biochemistry: tissue metabolite extractions, $^1\text{H}/^{31}\text{P}$ HR-NMR, fluorometric assays
- Experience in ethical animal authorisation and grant proposal writing

Other skills

Languages

- Bilingual in French and German
- Fluent in English

Computer Literacy

- Proficient with Word, Excel and Powerpoint.
- Skills in JMRUI, LCModel, MATLAB, and GraphPad
- Good knowledge in ImageJ, Adobe Photoshop and Illustrator

MS Office

Data analysis

Image processing

Other experience

Sept-Oct 2012

- **Internship** at Department of Organic Chemistry, University of Geneva. Synthesis of phthalocyanine derivatives for surface initiated polymerization (SOSIP) towards double channel photo-systems. (Pr Stefan Matile, Giuseppe Sforazzini PhD)

Oct-Nov 2012

- **Internship** at Department of Human Protein Science CMU and Department of Organic Chemistry, University of Geneva: Single molecule study of the photostability of novel fluorescent helicene and triangulene derivatives. (Alexandre Fuerstenberg PhD, Pr Jérôme Lacour, Pr Oliver Hartley)

August 2014

- **Research assistant volunteering** with Fauna Forever organisation for scientific research and conservation in the Peruvian Amazon, Puerto Maldonado, Peru.

Since 2010

- **Group leader (Caporal) and Specialist in Radioprotection** at the State detachment of the Civil Defense of State of Vaud, Switzerland

1996-2011

- **Piano Diploma** from the Association Vaudoise des Conservatoires et Ecoles de Musiques (AVCEM)

Publications and Conference Proceedings

Publications in peer-reviewed scientific journals

Cherix, A., Larrieu T., Grosse J., Rodrigues J., McEwen B., Nasca C., Gruetter R., Sandi C. "Metabolic signature in nucleus accumbens for antidepressant-like effects of acetyl-L-carnitine", *eLife, in revision*. Available on the BioRxiv preprint repository; doi: <https://doi.org/10.1101/690768>

Cherix, A*, Brodier*, L., Poitry-Yamate, C., Matter J.-M., Gruetter, R. "The appearance of the Warburg effect in the developing avian eye using characterized *in ovo*: how neurogenesis can remodel neuroenergetics", *IOVS, submitted*.

Cherix A., Donati G., Lizarbe B., Poitry-Yamate C., Lei H., Gruetter R. "Excitatory/inhibitory neuronal metabolic balance in mouse hippocampus upon infusion of [U-¹³C₆]Glucose", *Journal of Cerebral Blood Flow and Metabolism (JCBFM), in revision*.

Cherix A., Poitry-Yamate C., Lanz B., Zanoletti O., Grosse J., Sandi C., Gruetter R., Cardinaux J.-R. "Deletion of *Crtc1* is associated with strong neuroenergetic dysfunctions leading to depressive-like behaviour". *Manuscript in preparation*

Larrieu, T., **Cherix, A.**, Duque, A., Rodrigues, J., Lei, H., Gruetter, R., & Sandi, C. (2017). Hierarchical Status Predicts Behavioral Vulnerability and Nucleus Accumbens Metabolic Profile Following Chronic Social Defeat Stress. *Curr Biol*, 27(14), 2202-2210 e2204. doi:10.1016/j.cub.2017.06.027
<https://www.sciencedirect.com/science/article/pii/S0960982217307297?via%3Dihub>

Lizarbe, B., Lei, H., Duarte, J. M. N., Lanz, B., **Cherix, A.**, & Gruetter, R. (2018). Feasibility of in vivo measurement of glucose metabolism in the mouse hypothalamus by (1)H-[(13)C] MRS at 14.1T. *Magn Reson Med*. doi: 10.1002/mrm.27129
<https://onlinelibrary.wiley.com/doi/abs/10.1002/mrm.27129>

Lizarbe, B., **Cherix, A.**, Duarte, J.M.N., Cardinaux J.-R. & Gruetter, R. (2018) High-fat diet consumption alters energy metabolism in the mouse hypothalamus. *IJO*, doi:10.1038/s41366-018-0224-9
<https://www.nature.com/articles/s41366-018-0224-9>

Publications in peer-reviewed books

Lizarbe, B., **Cherix, A.**, & Gruetter, R. (2018). In Vivo Heteronuclear Magnetic Resonance Spectroscopy. *Methods Mol Biol*, 1718, 169-187. doi: 10.1007/978-1-4939-7531-0_11
https://link.springer.com/protocol/10.1007%2F978-1-4939-7531-0_11

Publications in peer-reviewed conference proceedings

- 1) **Cherix, A.**, Gruetter, R., Lei, H. and Cardinaux J.-R (2015). MRI and MRS characterization of *Crtc1* knockout mice limbic structures: investigating neurobiology of mood disorders. (traditional poster at the Annual Meeting of the Society for Neurosciences (SFN) in Chicago (USA))
- 2) **Cherix A.**, Poitry-Yamate C., Grosse J., Sandi C., Gruetter R. and Cardinaux J.-R. (2018). Deletion of *CRTC1* is associated with strong neuroenergetic dysfunctions in a mouse model of mood disorders. (traditional poster at the Annual Meeting of the Society for Neurosciences (SFN) in San Diego (USA))
- 3) **Cherix, A.**, Donati, G., Lizarbe, B., Lei, H., Poitry-Yamate, C., Cardinaux J.-R. and Gruetter, R. (2017) Investigating mitochondrial biomarkers and function using magnetic resonance spectroscopy at 14.1

- Tesla in a mouse model of mood disorders. *J. Cereb. Blood Flow Metab.*, **37**, 494-494. ([traditional poster](#) at the 28th Symposium on Cerebral Blood Flow, Metabolism and Function in Berlin (DE))
- 4) **Cherix, A.**, Donati, G., Lizarbe, B., Lei, H., Poitry-Yamate, C., Cardinaux J.-R. and Gruetter, R. (2017) Investigating mitochondrial biomarkers and function using magnetic resonance spectroscopy at 14.1 Tesla in a mouse model of mood disorders. *J. Neurochem.*, **142**, 197-198. ([traditional poster](#) at the International Society for Neurochemistry (ISN) biennial Meeting in Paris (FR))
 - 5) **Cherix, A.**, Donati, G., Lizarbe, B., Lei, H., Poitry-Yamate, C., Cardinaux J.-R. and Gruetter, R. (2018) Deletion of CRTCL1 is associated with strong neuroenergetic dysfunctions in a mouse model of mood disorders. ([traditional poster](#) and [oral presentation](#) at the 13th International Conference on Brain Energy Metabolism (ICBEM) in Valdivia (CL))
 - 6) **Cherix, A.**, Cardinaux, J.-R, Gruetter, R., and Lei, H. (2015). MRI and MRS characterization of *Crtcl* knock-out mice limbic structures: investigating neurobiology of mood disorders. *Proc. Intl. Soc. Mag. Reson. Med.* 23 ([oral presentation](#) at the International Society for Magnetic Resonance in Medicine (ISMRM) in Toronto (CA))
 - 7) **Cherix, A.**, Lizarbe, B., Lei, H., and Gruetter, R. (2016). In vivo measurement of metabolic fluxes in mouse dorsal hippocampus using ¹H-[¹³C] NMR spectroscopy at 14.1 Tesla. *Proc. Intl. Soc. Mag. Reson. Med.* 24 ([electronic poster](#) at the International Society for Magnetic Resonance in Medicine (ISMRM) in Singapore)
 - 8) **Cherix, A.**, Bordier, L., Matter, J.-M. & Gruetter, R. (2017b). In vivo measurement of metabolic changes associated with chick embryo development using ¹H-NMR spectroscopy at 14.1 Tesla. *Proc. Intl. Soc. Mag. Reson. Med.* 25 ([electronic poster](#) at the International Society for Magnetic Resonance in Medicine (ISMRM) in Honolulu (USA))
 - 9) **Cherix, A.**, Larrieu, T., Duque Moreno, A., Lei, H., Moléon, S., Sandi, C. & Gruetter, R. (2017a). Individual metabolic differences in murine nucleus accumbens (NAc) measured by ¹H-MRS at 14.1 Tesla is associated with trait-anxiety levels. *Proc. Intl. Soc. Mag. Reson. Med.* 25 ([electronic poster](#) at the International Society for Magnetic Resonance in Medicine (ISMRM) in Honolulu (USA))
 - 10) **Cherix, A.**, Donati, G., Lizarbe, B., Lepore, M., Lei, H., Poitry-Yamate, C., Cardinaux J.-R. and Gruetter, R. Deletion of CRTCL1 is associated with strong neuroenergetic dysfunctions in a mouse model of mood disorders. *Proc. Intl. Soc. Mag. Reson. Med.* 25 (power pitch [oral presentation](#) and [electronic poster](#) at the International Society for Magnetic Resonance in Medicine (ISMRM) in Paris (FR) 2018)